
Development of an electronic monitor for the determination of individual radon and thoron exposure

Josef Irlinger



2014

Aus dem Helmholtz Zentrum München
German Research Center for Environmental Health
Vorstand: Prof. Dr. Günther Wess

Development of an electronic monitor for the determination of individual radon and thoron exposure

Josef Irlinger

Dissertation
zum Erwerb des Doktorgrades der Naturwissenschaften
an der Medizinische Fakultät
der Ludwig-Maximilians-Universität
München

vorgelegt von
Josef Irlinger
aus Berchtesgaden, Deutschland

2014

Mit Genehmigung der Medizinische Fakultät der Universität München

Erstgutachter: Prof. Dr. Werner Rühm

Zweitgutachter: Prof. Dr. Gunnar Brix

Dekan: Prof. Dr. med. Dr. hc. M. Reiser, FACR, FRCR

Tag der mündlichen Prüfung: 11.06.2015

Contents

Abstract	ix
Zusammenfassung	xi
1 Introduction	1
2 Theory on Radon	5
2.1 Appearance and origin	5
2.2 Radon, Thoron and progenies	5
2.2.1 Radon decay chain	6
2.2.2 Thoron decay chain	9
2.3 Radon transport	10
2.3.1 Diffusion at thin barriers	13
2.3.2 Diffusion in media	14
2.4 Indoor Radon occurrence	15
2.4.1 Concentration in German homes	15
2.4.2 Indoor distribution	15
2.5 Thoron occurrence	17
2.5.1 Concentration in German homes	18
2.5.2 Indoor distribution	18
2.6 Exposure to dose conversion	18
2.6.1 Potential alpha energy concentration	19
2.6.2 Equilibrium-equivalent concentration	19
2.6.3 Equilibrium factor F	19
2.6.4 Exposure	20
2.6.5 Dose conversion factors	20
2.7 Health effects of Radon	22
2.7.1 Epidemiological studies on miners	23
2.7.2 Epidemiological studies on residential exposure	24
2.7.3 Summary	25

3	Principle and design of the exposimeter	27
3.1	Measurement principles	27
3.1.1	Discrimination methods	28
3.2	Electronic design	29
3.2.1	Voltage generator	29
3.2.2	Detectors	30
3.2.3	Amplifier	32
3.2.4	Comparator	35
3.2.5	Micro controller	36
3.3	SPICE simulation	39
3.3.1	JFET signal model	39
3.3.2	SPICE parameters	40
3.3.3	Amplification stage output	40
3.4	Setup	44
3.4.1	Geometry 1, small exposimeter	44
3.4.2	Geometry 2, large exposimeter	45
4	Calibration	47
4.1	Basic Principles	48
4.2	Calibration chamber setup	49
4.2.1	Geometry	50
4.2.2	Radioactive sources	50
4.2.3	Humidity	50
4.3	Radon calibration	51
4.3.1	Reference device comparison	51
4.3.2	Calibration factors	52
4.3.3	Spectrum	55
4.3.4	Calibration factor concentration dependence	56
4.4	Thoron calibration	57
4.4.1	Quality assurance	57
4.4.2	Spectrum	61
4.5	Filters	62
4.6	Mixed concentrations	65
4.6.1	Acquired spectra	66
4.6.2	Evaluation methods	68
4.6.3	Concentration calculation and detection limits	73
5	Monte-Carlo simulations	79
5.1	Model	81
5.1.1	Fundamentals	81
5.1.2	Environmental parameters	81
5.1.3	Assumptions	82
5.1.4	Geometry	85

5.2	Transport code result comparison	86
5.3	Results	90
5.3.1	Radon calibration factors	90
5.3.2	Thoron calibration factors	96
5.3.3	Radon: calibration factor environmental dependence	98
5.3.4	Thoron: calibration factor environmental dependence	106
5.3.5	Geometry dependence	112
6	Application	117
6.1	Prague 2013 Intercomparison	117
6.2	Radon galleries Bad Gastein	118
6.2.1	Comparison to AlphaGuard	119
6.2.2	Exposure	120
6.3	Salt mine Berchtesgaden	121
6.3.1	Comparison to AlphaGuard	121
6.3.2	Exposure	122
6.4	Thoron field measurements	123
6.4.1	HMGU thoron house	123
6.4.2	Bavarian clay house	127
7	Conclusions and outlook	129
	Bibliography	133
	List of Figures	155
	List of Tables	156
	Acknowledgments	157
	Publications	159

Abstract

The carcinogenic effect of the radio isotope ^{222}Rn of the noble gas radon and its progeny, as well as its residential distribution, are well studied. In contrast, the knowledge about the effects and average dwelling concentration levels of its radio isotope ^{220}Rn (“thoron”) is still limited. Generally, this isotope has been assumed to be a negligible contributor to the effective annual dose. However, only recently it has been pointed out in several international studies, that the dose due to thoron exceeds the one from ^{222}Rn under certain conditions. Additionally, radon monitors may show a considerable sensitivity towards thoron which was also not accounted for in general. Therefore a reliable, inexpensive exposimeter, which allows to distinguish between decays of either radon and thoron, is required to conduct further studies.

The scope of this thesis was to develop an electronic radon/thoron exposimeter which features small size, low weight and minimal power consumption. The design is based on the diffusion chamber principle and employs state-of-the-art alpha particle spectroscopy to measure activity concentrations. The device was optimized via inlet layout and filter selection for high thoron diffusion. Calibration measurements showed a similar sensitivity of the monitor towards radon and thoron, with a calibration factor of $cf_{^{222}\text{Rn}} = 16.2 \pm 0.9 \text{ Bq m}^{-3}/\text{cph}$ and $cf_{^{220}\text{Rn}} = 14.4 \pm 0.8 \text{ Bq m}^{-3}/\text{cph}$, respectively. Thus, the radon sensitivity of the device was enhanced by a factor two compared to a previous prototype. The evaluation method developed in this work, in accordance with ISO 11665 standards, was validated by intercomparison measurements. The detection limits for radon and thoron were determined to be $C_{^{222}\text{Rn}}^{\#} = 44.0 \text{ Bq m}^{-3}$ and $C_{^{220}\text{Rn}}^{\#} = 40.0 \text{ Bq m}^{-3}$, respectively, in case of a low radon environment, a one-hour measurement interval, and a background count rate of zero. In contrast, in mixed radon/thoron concentrations where the ^{212}Po peak must be used for thoron concentration determination, a calibration factor of $cf_{^{220}\text{Rn}} = 100 \pm 10 \text{ Bq m}^{-3}/\text{cph}$ was measured, yielding a detection limit of $C_{^{220}\text{Rn}}^{\#} = 280 \text{ Bq m}^{-3}$.

Further, Monte Carlo (MC) simulations were performed by means of various codes including Geant4, to study the effect of the variation of parameters influencing the calibration factors. The results showed reasonable agreement between simulated and acquired spectra, with differences being below 8%, thus validating the employed simulation model. The simulations indicated a significant impact of environmental parameters, such as temperature

and pressure, on the measured spectra and accordingly on the calibration factor. Therefore the calibration factor was quantified as a function of temperature, relative humidity and pressure as well as chamber volume. For devices with increased detection volume a considerable influence of air density changes, corresponding to altitudes from 0-5000 m , and temperatures from -25 to 35 $^{\circ}C$, on the calibration factor of up to 32% was observed. In contrast, for devices with standard housing the calibration factor changed only up to 4%. When increasing the detection volume compared to the employed standard housing by at least a factor of four, a maximum increase of the sensitivity of about 20% was found, at the expense of device portability. On the contrary, when reducing the height of the housing by 10 mm , which yields 40% less volume, a decrease of sensitivity by 30% and 41% for radon and thoron was observed, respectively.

Finally, devices were used and tested at different realistic conditions, such as mines, radon spas, and dwellings with mixed ^{222}Rn and ^{220}Rn environments. Measurements in a salt mine with the device developed within the framework of this thesis revealed maximum radon concentrations of up to 1.0 $kBq m^{-3}$. In the *Bad Gastein Heilstollen*, ^{222}Rn concentrations up to 24.3 $kBq m^{-3}$ were found, in agreement with an AlphaGuard reference device. First measurements in radon/thoron environments of about 200 $Bq m^{-3}$ each, in a clay model house at the Helmholtz Center Munich, showed reasonable agreement with reference devices, thus validating the introduced evaluation method. First measurements in a private Bavarian clay house revealed a low thoron concentration of about $C_{^{220}Rn} = 13.0 \pm 3.0 Bq m^{-3}$, in comparison to a high radon concentration of $C_{^{222}Rn} = 200 \pm 70 Bq m^{-3}$.

Zusammenfassung

Die krebserregende Wirkung des Radioisotops ^{222}Rn des Edelgases Radon und dessen Folgeprodukte sowie deren Verbreitung in Wohnräumen sind gut untersucht. Im Gegensatz dazu ist der Kenntnisstand über die gesundheitlichen Auswirkungen und die durchschnittliche Raumluft-Konzentration des Radioisotops ^{220}Rn („Thoron“) in Wohnungen noch begrenzt. Für dieses Isotop wurde angenommen, dass es einen vernachlässigbaren Beitrag zur effektiven Jahresdosis der Bevölkerung liefert. Vor kurzem wurde jedoch in mehreren internationalen Studien gezeigt, dass die Lungendosis durch Thoron unter bestimmten Bedingungen höher sein kann als die durch ^{222}Rn (im Folgenden als „Radon“ bezeichnet). Zudem können Radon-Messgeräte eine erhebliche Empfindlichkeit gegenüber Thoron zeigen, die meist vernachlässigt wird, was zu einer Verfälschung einer Radonmessung führen kann.

Das Ziel dieser Arbeit war es daher, ein elektronisches Messgerät zu entwickeln, das zwischen Radon und Thoron unterscheiden kann, und das sich durch eine geringe Größe, ein geringes Gewicht und einen minimalen Stromverbrauch auszeichnet, und das die Bestimmung von Radon- und Thoronkonzentrationen in Echtzeit ermöglicht. Das Design des Geräts basiert auf dem Diffusionskammern-Prinzip und verwendet die Technik der Alpha-Teilchen-Spektroskopie, um Aktivitätskonzentrationen von Radon und Thoron über die bei deren Zerfall emittierten Alphateilchen und deren Energien zu messen. Das Gerät wurde mittels eines neuen Konzepts für Einlass-Löcher und Filterauswahl für eine hohe Thoron Diffusion optimiert. Kalibriermessungen zeigten eine ähnliche Empfindlichkeit des Messgeräts für Radon und Thoron, mit Kalibrierfaktoren von $cf_{^{222}\text{Rn}} = 16,2 \pm 0,9 \text{ Bq m}^{-3}/\text{cph}$ und $cf_{^{220}\text{Rn}} = 14,4 \pm 0,8 \text{ Bq m}^{-3}/\text{cph}$. Somit wurde die Radon Empfindlichkeit des Messsystems im Vergleich zu einem vorherigen Prototyp um den Faktor 2 verbessert. Die in dieser Arbeit unter Verwendung der ISO-Norm ISO 11665 entwickelten Auswerteverfahren, wurden mittels Vergleichsmessungen validiert. Die Nachweisgrenze des neuen Geräts für Radon beträgt $C_{^{222}\text{Rn}}^{\#} = 44,0 \text{ Bq m}^{-3}$, die für Thoron für den Fall einer vernachlässigbaren vorhandenen Radonkonzentration beträgt $C_{^{220}\text{Rn}}^{\#} = 40,0 \text{ Bq m}^{-3}$, in beiden Fällen jeweils für eine einstündige Messung und einer Untergrund Zählrate von Null. Im Falle einer gemischten Radon/Thoron-Konzentration muss dagegen der ^{212}Po Peak für die Thoron Konzentrationsbestimmung benutzt wird, wodurch sich ein Thoron-Kalibrierfaktor von $cf_{^{220}\text{Rn}} = 100 \pm 10 \text{ Bq m}^{-3}/\text{cph}$ ergibt, was einer Nachweisgrenze von $C_{^{220}\text{Rn}}^{\#} = 280 \text{ Bq m}^{-3}$ entspricht.

Ferner wurden mit verschiedenen Programmen einschließlich GEANT4 Monte Carlo (MC)-Simulationen durchgeführt, um den Einfluss von Detektionsvolumen und sich verändernden Umweltparametern auf den Kalibrierfaktor zu untersuchen. Die Ergebnisse zeigten gute Übereinstimmung zwischen Simulation und gemessenen Spektren, mit Abweichungen von weniger als 8%, wodurch das verwendete Simulationsmodell validiert wurde. Die Simulationen zeigten eine deutliche Auswirkung von Umgebungsparametern wie Temperatur und Luftdruck auf die gemessenen Spektren und dementsprechend auf den Kalibrierfaktor. Daher wurde der Kalibrierfaktor als eine Funktion von relativer Luftfeuchte, Temperatur und Luftdruck sowie des Kammervolumens quantifiziert. Bei Geräten mit größerer Diffusionskammer war ein größerer Einfluss der Luftdichte festzustellen als bei Geräten mit kleinerer Diffusionskammer, wobei Luftdruck-Änderungen (entsprechend einer Höhe über dem Meeresspiegel von 0 bis 5.000 m) und Temperaturänderungen von -25 bis 35 $^{\circ}C$ simuliert wurden. Dabei war eine Änderung des Kalibrierfaktors für Radon und Thoron von bis zu 32% zu beobachten. Dagegen änderte sich für Geräte mit Standardgehäuse der Kalibrierfaktor nur um bis zu 4%. Bei Vergrößerung der Diffusionskammer im Vergleich zu dem üblich verwendeten Standardgehäuse um mindestens einen Faktor vier wurde eine maximale Zunahme der Empfindlichkeit von etwa 20% gefunden, auf Kosten der Tragbarkeit des Geräts. Im Gegensatz dazu ergab sich bei einer Verringerung der Höhe der Diffusionskammer um 10 mm was einem ca. 40% geringeren Volumen entspricht, eine Abnahme des Kalibrierfaktors um 30% und 41% für Radon bzw. Thoron.

Schließlich wurden die Geräte unter verschiedenen natürlichen Bedingungen, zum Beispiel in einem Salz-Bergwerk, einem Radon-Heilstollen und in Wohnungen mit gemischten ^{222}Rn und ^{220}Rn Umgebungen getestet. Messungen in einem Salzbergwerk zeigten eine maximale Radonkonzentrationen von bis zu $1,0$ $kBq\ m^{-3}$. Im *Heilstollen Bad Gastein* wurden mit dem im Rahmen dieser Arbeit entwickelten und gebauten Gerät ^{222}Rn Konzentrationen von bis zu $24,3$ $kBq\ m^{-3}$ gemessen, in Übereinstimmung mit den Messergebnissen, die mit einem AlphaGuard Referenzgerät erzielt wurden. Erste Messungen in gemischten Radon/Thoron-Umgebungen von etwa je 200 $Bq\ m^{-3}$ in dem Tonmodell-Haus am Helmholtz Zentrum München zeigten gute Übereinstimmung mit Messergebnissen von Referenzgeräten, wodurch unter anderem die angewandte Auswertungsmethode validiert wurde. Erste Messungen in einem privaten bayerischen Lehm Haus ergab eine niedrige Thoron-Konzentration von etwa $C_{220Rn} = 13,0 \pm 3,0$ $Bq\ m^{-3}$, im Vergleich zu einer hohen Radonkonzentration von $C_{222Rn} = 200 \pm 70$ $Bq\ m^{-3}$.

Chapter 1

Introduction

The human organism is exposed to ionizing radiation from natural and artificial sources throughout the entire life span. Using this distinction, for the majority of the population the natural exposure exceeds that from man-made sources. The main contributors to natural radiation exposure are high-energy cosmic radiation and radioactive nuclides emanating from the earth's crust [192]. The principal source for radiation exposure of the inner body originates from the ubiquitous, radioactive and inert noble gas radon. The radioisotope ^{222}Rn (in the following called "radon") is a decay product of the naturally occurring primordial isotope ^{238}U . The radon progeny have been identified to increase the excess relative risk for lung cancer [29, 178] and are, after smoking, the main cause responsible for that disease [210]. This was, amongst others, deduced from epidemiological studies, in which the radon concentration at homes [29, 202] and in uranium mines [178, 199, 90] had been correlated to increased lung cancer rates. It is noted, however, that indoor epidemiological studies are necessarily based on retrospective dose estimation of lung-cancer diseased persons. The data were derived from measurements of ^{222}Rn activity concentrations in the air of sleeping and living rooms. Accordingly, a persons' mobility was not taken into account, which can influence the persons' exposure to radon considerably, thus adding to the uncertainty in the deduced excess risk estimates.

In order to quantify the radon exposure of an individual, a portable electronic radon exposure meter has been developed at the Helmholtz Center Munich (HMGU) [79]. This device allows for a realistic and on-line evaluation of a persons' radon exposure and, consequently, allows prevention against high exposure when constantly worn. But despite these efforts to determine the health risk of radon exposure, the effects of the decay products of another radon isotope, ^{220}Rn , commonly called thoron, have not yet been adequately taken into account. Thoron is considered to contribute about 4% to the annual effective dose of natural radiation [192], and cannot be neglected [166, 180]. In fact, worldwide studies suggest that under certain conditions, the annual effective lung dose of thoron can exceed that of radon [187, 111, 203, 163, 155, 109]. In contrast to radon, the gas concentration of the short lived ^{220}Rn isotope (half-life $\tau_{1/2} = 55.6\text{ s}$) is difficult to measure and advanced methods have to be applied [123]. It also has been pointed out, that passive sampling radon monitors

are also sensitive to thoron exposure, thus overestimating the radon exposure [120, 181, 171] at times considerably. In order to address the mentioned issues, recent developments already combine radon and thoron gas measurements [182, 183]. However, most devices are not designed as personal exposure monitors, or do not allow on-line evaluation, and thus cannot help to prevent exposure.

In this work a radon/thoron monitor was developed, allowing simultaneous measurements of the activity concentrations of ^{222}Rn and ^{220}Rn . It is based on the previously developed radon exposimeter prototype, and features small size, low weight and minimal power consumption. The successive steps for its usage as a radon/thoron on-line monitor were improving its sensitivity for radon via new detectors and amplifier design, followed by the implementation of an alpha-particle-spectrometer, realized by a new embedded digital circuit design. The development was facilitated by use of electronic design automation software, granting the optimization and complete modeling via SPICE simulations of the employed components. A new diffusion chamber design was established for which several filter materials were investigated, to identify the most suitable material for fast thoron diffusion into the measurement volume. An approach based on the necessity for a high thoron sensitivity of the device. Additionally, any progeny must be kept out of the diffusion chamber by the filter element. The new device was calibrated in high radon and thoron concentrations within a closed chamber, where the variation of the ^{220}Rn calibration factor was intensively studied. The accuracy of the device was validated by participating in an international intercomparison measurement campaign. An evaluation method based on the recently released ISO 11665 standard for measurement of radioactivity in the environment [69] was developed and verified by comparison measurements in mixed $^{222}\text{Rn}/^{220}\text{Rn}$ gas environments. Decision threshold and detection limit were evaluated based on background count rates and calibration factors [68]. Further, simulation programs were developed to study the effects of environmental parameters such as humidity, temperature and pressure as well as diffusion chamber size on the calibration factors. These programs are employing Monte Carlo methods and are based on an analytic and on the Geant4 transportation code. The alpha particle spectroscopy newly implemented in the device as part of this theses, offered the unique opportunity to explicitly study and compare the change of the spectral shape of the measured signal due to different measurement conditions, with the results of the developed simulations. In addition, the simulations were validated by intercomparison of transportation codes, own measurement results and findings reported in literature.

In Chapter 2 information on radon and thoron, with respect to origin, decay properties, transport in air, indoor distribution and health effects is summarized. An in-depth presentation of the working principle and the electronic design of the developed device can be found in Chapter 3. The sensitivity of the device for various filter materials and geometries was also extensively studied, and results are presented in Chapter 4 and 5. In particular the diffusion constant of the employed filter as well as its ability to prevent progeny from entering the diffusion chamber, are reviewed. Also the employed evaluation method is introduced and verified. The sensitivity of the common HMGU radon monitor towards ^{220}Rn

is also discussed in this chapter. Various parameters influencing the functionality of the device, including variations in air density, temperature, and housing size, are considered on a theoretical basis via Monte Carlo simulations in Chapter 5. The developed devices were finally tested in realistic exposure scenarios with radon and thoron exposures, such as a salt mine, radon spa and a clay house (Chapter 6). In conclusion the developed hardware, methods, models and simulation tools provide the ideal basis for further development of alpha particle measurement systems for radon/thoron monitoring.

Chapter 2

Theory on Radon

Only a few years after the discovery of radioactivity in the early 1900 Ernest Rutherford observed apart from the ionizing radiation from alpha and beta decay an additional ionizing gas diffusing from thorium compounds [151, 153], which was called thoron. In the same year Fritz Dorn found a similar radioactive gas emanating from radium salts to which was referred as radon [35, 127]. Nowadays it is known that both are isotopes of the same element, where radon generally refers to ^{222}Rn while ^{220}Rn is commonly nominated as thoron. Another isotope is ^{219}Rn actinon and all are the respective products of the three radioactive decay chains of uranium, thorium and actinium occurring in nature [189]. In this chapter some physical aspects of ^{222}Rn and ^{220}Rn are described.

2.1 Appearance and origin

^{222}Rn and ^{220}Rn are color- and odorless, chemically inert noble gases with no stable isotopic form. Both are naturally occurring and originate from radium and thorium present in rock and soil. These two long lived mother nuclides are ubiquitous with a concentration of ^{232}Th in the earth crust which is about 4 times larger than that of ^{238}U equal to 2.7 mg kg^{-1} [152]. Due to the abundance of uranium and ^{222}Rn 's long half-life of 3.8 days it has the highest activity concentration of the three stated isotopes in air and is widely distributed. It therefore contributes the major part to the human natural exposure. Additionally the short lived (55.6 s) ^{220}Rn , which to most parts already decays in the earth before emanating to the atmosphere, can still significantly contribute to the radiation exposures in homes and even exceed the contribution of ^{222}Rn . On the other hand actinon is because of the lack of its natural parent ^{235}U and its short half-life (3.96 s) not available in notable concentrations in the air and hence of no interest to radiation protection.

2.2 Radon, Thoron and progenies

The three main transport mechanisms important for ^{222}Rn migration are transport from solid to either gas or liquid in porous spaces, molecular diffusion in the material or con-

vection flow in gas or liquid [24]. The process of gaseous ^{222}Rn transport from the solid is called emanation, where the emanation coefficient is defined as ratio of atoms which escaped the solid over the ones produced in the material. Hence the emanation rate is dependent on the soil composition, humidity and porosity. Thus the ground ^{222}Rn and ^{220}Rn gas concentrations are depending on the soil's uranium and thorium concentration and the emanation rate. Due to this geogenic dependence there is a large variation in ground ^{222}Rn gas concentrations, for example in Germany in the domain of $10 - 500 \text{ kBq m}^{-3}$ [82], but generally speaking in areas with high ground concentrations a higher indoor concentration is to be expected [52, 88].

Isotopes of ^{222}Rn and ^{220}Rn progenies are heavy metals such as polonium, lead, bismuth and thallium as shown in the decay chain in Figures 2.1 and 2.3. They share similar chemical and aerodynamically properties if belonging to the same element or sharing alike atomic mass. Normally when of airborne origin these progeny are positive ionized due to recoil or the interaction of the alpha particles with the electronic shell [25]. Such ions are quickly adsorbed by water molecules or trace gases, shaping into clusters with diameters between 0.3 to 4 nm, denoted as unattached fraction f_p [143]. These clusters are highly reactive and shortly deposit on aerosol or dust particles in the environment, where the rate depends on the aerosol size distribution and their density in air [136]. The size diameter of this attached fraction is approximately equal for progenies of both decay series [135] and was found to be in range of 20 – 3000 nm [55] in real indoor environments. These properties influence the effective dose which a person receives and are discussed in Section 2.6.

2.2.1 Radon decay chain

All ^{222}Rn isotopes are radioactive and disintegrate either by alpha or beta particle decay, where the decay rate is characterized by the half-life $\tau_{1/2}$, which defines the period after which only half of the initial quantity of radioactive atoms is still present. The stochastic process of radioactive decay is regarded as Poisson distributed [165, 96] and is describe by:

$$\frac{dN(t)}{dt} = -\lambda N(t) \quad (2.1)$$

where N is the time dependent number of atoms, t the time and λ the decay constant which equals $\ln(2)/\tau_{1/2}$ by definition. To this quantity one also refers as activity $A = -\lambda N(t)$ generally stated in the unit of Becquerel, which are decays per second ($Bq = 1/s$). Equation 2.1 can be used to relate the radioactive growth and decay of successive nuclides such as depicted in Figure 2.1. Here it is done exemplary for $^{226}\text{Ra} \rightarrow ^{222}\text{Rn} \rightarrow ^{218}\text{Po} \rightarrow ^{214}\text{Pb} \rightarrow ^{214}\text{Bi} \rightarrow ^{214}\text{Po}$ which are described by a set of coupled differential equations:

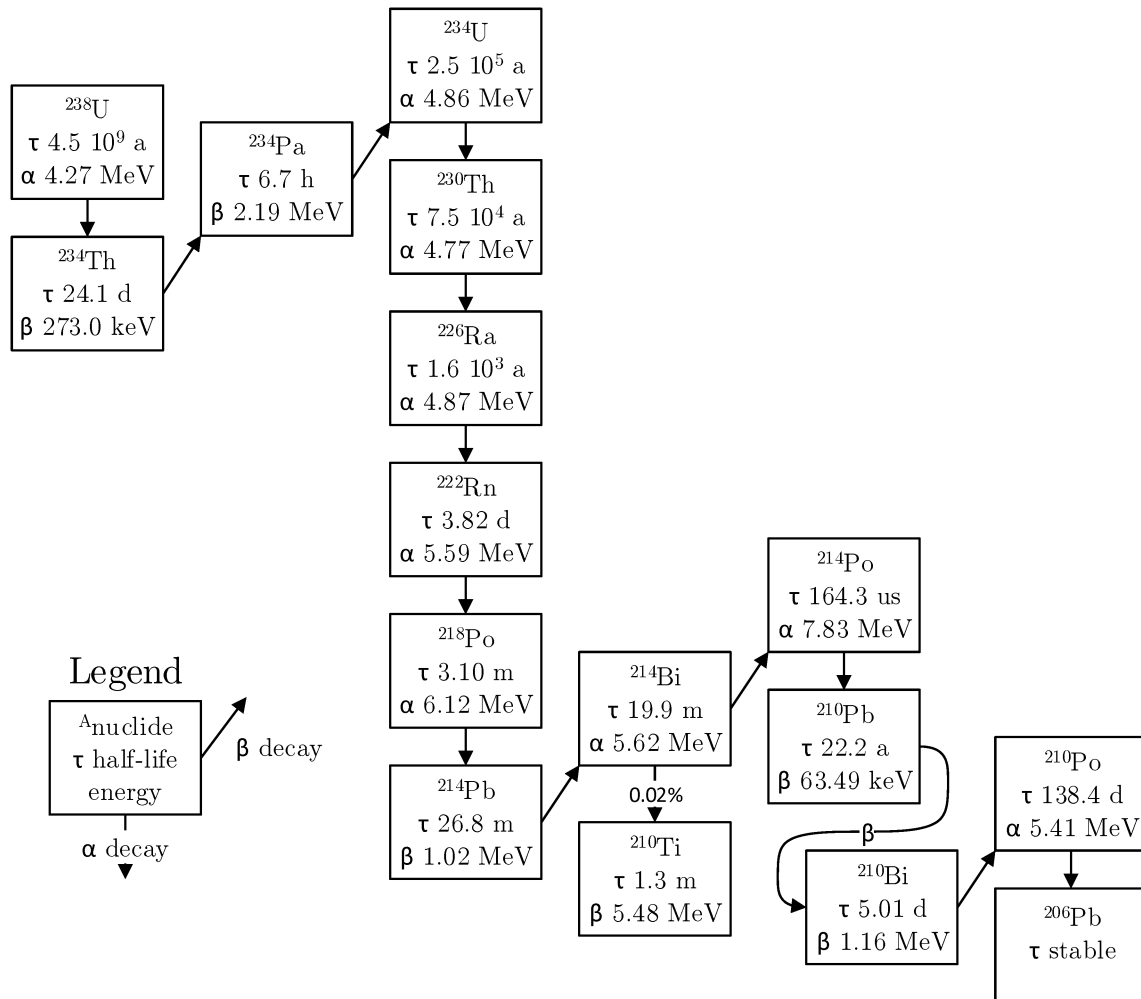


Figure 2.1: Simplified ^{238}U decay series, including radon ^{222}Rn and its progenies. Only the major decay branches with the respective decay modes, energies and half-lives are shown. See also Table 2.2.

$$\frac{dN_{222Rn}(t)}{dt} = -\lambda_1 N_{222Rn}(t) + \lambda_0 N_{226Ra}(t) \quad (2.2a)$$

$$\frac{dN_{218Po}(t)}{dt} = -\lambda_2 N_{218Po}(t) + \lambda_1 N_{222Rn}(t) \quad (2.2b)$$

$$\frac{dN_{214Pb}(t)}{dt} = -\lambda_3 N_{214Pb}(t) + \lambda_2 N_{218Po}(t) \quad (2.2c)$$

$$\frac{dN_{214Bi}(t)}{dt} = -\lambda_4 N_{214Bi}(t) + \lambda_3 N_{214Pb}(t) \quad (2.2d)$$

$$\frac{dN_{214Po}(t)}{dt} = -\lambda_5 N_{214Po}(t) + \lambda_4 N_{214Bi}(t) \quad (2.2e)$$

where N_n and λ_n refer to the number of atoms and decay constant of the respective atom in the subscript. It is assumed here that there is a radium source term and zero concentration of its daughters at $t = 0$. The solution to Equations 2.2 is rather lengthy but a general equation for this kind of problem was found by Bateman [17, 8]:

$$N_n(t) = \prod_{j=0}^{j=n-1} \lambda_j \sum_{i=1}^n \sum_{j=i}^n \frac{N_i(0)e^{-\lambda_j t}}{\prod_{p=i, p \neq i}^n (\lambda_p - \lambda_j)} \quad (2.3)$$

which also can be expanded with daughter source terms and decay branches [106], which are in this case however of no interest. Equation 2.3 can be implemented into a computer program but if $\lambda_p \approx \lambda_j$ isotope pair cancellation can lead to computational errors. The solution to Equation 2.1 is $N(t) = N_0 e^{-\lambda t}$, with N_0 being the initial number of atoms. Hence the relative activity for a single radionuclide behaves as in Table 2.1, i.e. after a period of six half-lives either a 98% relative activity is reached or atoms have decayed from the initial amount N_0 . After eleven half-life's the activity is at a total of 100% with 1‰ accuracy.

Equations 2.2 have been implemented in a Mathematica program and solved numerically in order to plot the individual activities under the assumption of a constant ^{222}Rn source, with a value of $N_1 = (\ln(2)/\lambda_1)^{-1}$. Each solution of equations 2.2 is then multiplied by its corresponding decay constant λ_n yielding the respective activity. Figure 2.2 demonstrates that the progeny enter a so called secular equilibrium, which occurs if the half-life of the mother nuclide is much larger than that of their daughters [26]. Here after 4 hours the equilibrium for all depicted progenies is reached and beyond this point all have the same decay rate, i.e. at this time the activity of the short lived decay products and ^{222}Rn are the same. It can also be seen in Figure 2.2 that the activity of ^{218}Po increases rapidly as it is the case in a closed vessel or in a building subjected to ^{222}Rn entry. Within 10 minutes almost 90% equilibrium between radon and its first decay product is reached. Next the ^{220}Rn decay series is discussed.

Table 2.1: Radioactive decay relative change

time	relative activity [%]
0	0
1 $\tau_{1/2}$	50.0
2 $\tau_{1/2}$	75.0
3 $\tau_{1/2}$	87.5
4 $\tau_{1/2}$	93.8
5 $\tau_{1/2}$	96.9
6 $\tau_{1/2}$	98.4
7 $\tau_{1/2}$	99.2
8 $\tau_{1/2}$	99.6
9 $\tau_{1/2}$	99.8
10 $\tau_{1/2}$	99.9
11 $\tau_{1/2}$	100.0

2.2.2 Thoron decay chain

The ^{220}Rn thoron decay chain can be seen in Figure 2.3 and decay parameters of both isotopes can also be found in Table 2.2. The activity can be again modeled by Formula 2.1 resulting in,

$$\frac{dN_{220\text{Rn}}(t)}{dt} = -\lambda_1 N_{220\text{Rn}}(t) + \lambda_0 N_{224\text{Ra}}(t) \quad (2.4a)$$

$$\frac{dN_{216\text{Po}}(t)}{dt} = -\lambda_2 N_{216\text{Po}}(t) + \lambda_1 N_{220\text{Rn}}(t) \quad (2.4b)$$

$$\frac{dN_{212\text{Pb}}(t)}{dt} = -\lambda_3 N_{212\text{Pb}}(t) + \lambda_2 N_{216\text{Po}}(t) \quad (2.4c)$$

$$\frac{dN_{212\text{Bi}}(t)}{dt} = -\lambda_4 N_{212\text{Bi}}(t) + \lambda_3 N_{212\text{Pb}}(t) \quad (2.4d)$$

$$\frac{dN_{212\text{Po}}(t)}{dt} = -\lambda_5 N_{212\text{Po}}(t) + 0.64 \lambda_4 N_{212\text{Bi}}(t) \quad (2.4e)$$

with the assumption of zero concentration at start for all elements except ^{224}Ra . Equations 2.2 are very similar to the ones above (Eq. 2.4), which can be also solved by Bateman's solution 2.3. In 2.4e the branching of ^{212}Bi into two nuclides with different alpha-particle decay energies has been taken into account. Equations 2.4 were also solved in Mathematica and plotted in Figure 2.4. ^{220}Rn is assumed to be at a constant level here and its first daughter, polonium, is in equilibrium in about one second, hence both lines overlap in drawing 2.4. Under such conditions a secular equilibrium is reached in about 60 hours after starting a measurement. However in real indoor environments such equilibrium conditions are hardly achieved since the airborne decay products concentrations are influenced by indoor aerosol concentrations, ventilation and entry rates as discussed in 2.1. However after the gas diffused into the measurement chamber of a $^{222}\text{Rn}/^{220}\text{Rn}$ monitor the influence

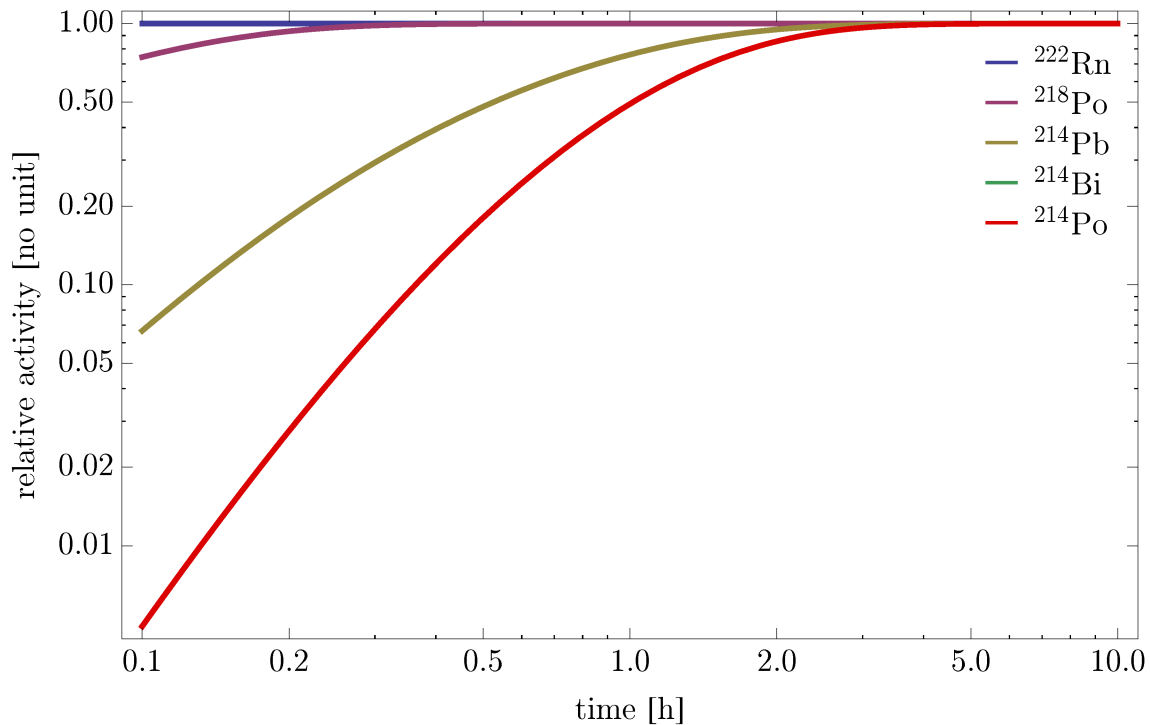


Figure 2.2: Relative activities of ^{222}Rn and its immediate progenies. Here it is assumed that only ^{222}Rn is present initially and is also constant. Lines of bismuth and polonium overlap due to the short half-life of ^{214}Po .

is eliminated and build up is exactly as described. The basic principles of diffusion are discussed next.

2.3 Radon transport

The main ways for ^{222}Rn to enter a dwelling are as discussed in section 2.2 by soil-gas or water-gas emanation, flow transport through cracks and joints in places such as basements driven by pressure differences caused by convection currents, the influence of outdoor wind and of course diffusion, which is the migration of the gas relative to a solid, liquid or gas. It is the dominant transport mechanism [144, 18] by which ^{222}Rn gas migrates through an intact media. Therefore basements often are observed to have high average ^{222}Rn concentration which then decreases significantly with the floor levels [117]. Also since the ^{222}Rn flow into an enclosure is influenced by a pressure gradient between in- and outdoors, for example arising through a temperature gradient due to indoor heating or also wind, one can typically notice seasonal changes in the indoor concentrations. The main transport mechanism of ^{222}Rn into an exposure monitor is however by diffusion. Thus it shall be discussed in more detail in this section.

Table 2.2: Radon/Thoron Decay Series

Nuclide	Half-Life ¹	E_α ¹ (MeV)	$\sum E_\alpha$ (PAE) (MeV)	rel. EEC ²
^{222}Rn	3.82 d	5.59	19.53	-
^{218}Po	3.10 min	6.11	13.94	0.105
^{214}Pb	26.8 min	-	7.83	0.516
^{214}Bi	19.9 min	-	7.83	0.379
^{214}Po	164.3 μs	7.83	7.83	0.00
^{210}Pb	22.2 a	-	-	-
^{220}Rn	55.6 s	6.40	21.27	-
^{216}Po	145 ms	6.91	14.87	0.00
^{212}Pb	10.64 h	-	7.96	0.913
^{212}Bi	60.6 min	6.21	7.96	0.087
^{212}Po	299 ns	8.95	5.73	0.00

¹[40, 43], ²[190]

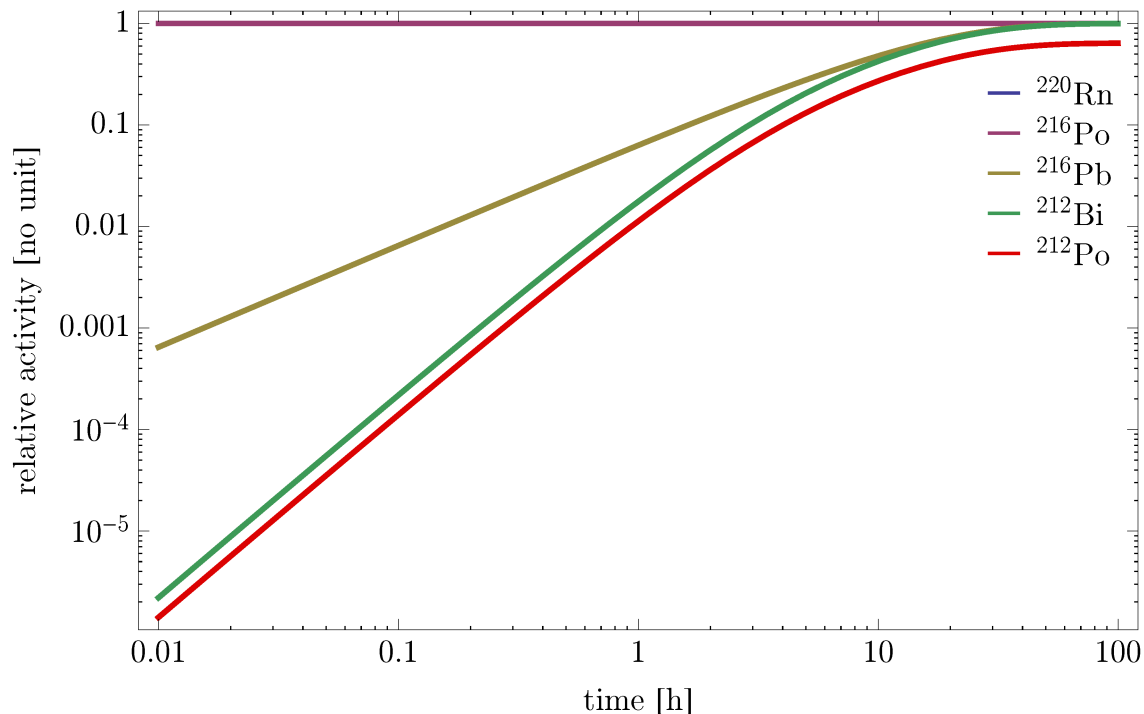


Figure 2.4: Relative activities of ^{220}Rn and its immediate progenies. Here it is assumed that only thoron is present initially and at a constant level. Lines of thoron and polonium overlap due to the short half-life of ^{216}Po .

sinks of particles have not to be considered. The diffusion coefficient in air is significantly affected by pressure, temperature [27], humidity and aerosol particle size [59]. Of course gas diffusion is fastest in other gases as compared to diffusion in liquids or solids, where the diffusion coefficient is several order of magnitudes smaller.

2.3.1 Diffusion at thin barriers

One important aspect of diffusion chamber based devices to consider is its applied filter. It influences the time dependence of the ^{222}Rn concentration build up in the measurement chamber as well as how much ^{220}Rn is able to enter it. The time dependence is described by Fick's second law (Eq. 2.6) and taking into account the decay law (Eq. 2.1) which leads to [146],

$$\frac{\delta C(\vec{x}, t)}{\delta t} = D\vec{\nabla}^2 C(\vec{x}, t) - \lambda C(\vec{x}, t) \quad (2.7)$$

with λ being the decay constant and the others parameters as in Equation 2.6. If one considers Cartesian coordinates with x, y being the floor plane vectors and z being the height, diffusion along x and y axes is negligible as it does not change concentration along the chamber height, where the inlets are located. Thus considering diffusion only along the z -axis and using the finite element method Equation 2.7 can be rewritten to [141]:

$$\frac{\delta C(z, t)_{in}}{\delta t} = -\lambda C(z, t)_{in} + \gamma [C(z, t)_{in} - C(z, t)_{out}] \quad (2.8)$$

where $C(z, t)_{in}$ is the concentration (activity length⁻³) inside the measurement chamber, $C(z, t)_{out}$ the outside concentration at the filter surface and γ the air exchange rate (time⁻¹),

$$\gamma = \frac{DA}{\Delta x V} \quad (2.9)$$

with A being the effective area (length²) of the membrane, Δx the thickness of the filter (length), and V the interior volume of the monitor (length³). The one dimensional state equation 2.8 can either be solved numerically [73] or analytically when $\delta C(z, t)_{in}/\delta t = 0$, i.e. if the exposure time is long enough $t \gg (\lambda + \gamma)^{-1}$ [182] and a steady state equilibrium is achieved. This can only be reached by a stable ^{222}Rn concentration and distribution within the measurement chamber. Then the ratio R of the concentration inside to outside the monitor is given by:

$$R = \frac{C_{in}}{C_{out}} = \frac{\gamma}{\lambda + \gamma} \quad (2.10)$$

The dimensionless ratio in 2.10, also called infiltration rate [160], is in the range from 0 to 1, where 0 indicates no diffusion into the chamber, while 1 is the ideal case with no concentration difference. The higher R the better is the sensitivity of the device for ^{220}Rn . Thus according to Equation 2.9 the sensitivity of a monitor from a diffusion viewpoint mainly depends on the diffusion constant and thickness of the filter, the area of inlets on the device and its volume. The diffusion process of ^{222}Rn and ^{220}Rn in a filter is exactly

Table 2.3: Typical diffusion coefficients

Medium	Diffusion coefficient m^2s^{-1}	Diffusion length		Reference
		^{222}Rn	^{220}Rn	
Air	$9.98 \cdot 10^{-6}$	2.18 <i>m</i>	2.83 <i>cm</i>	[118]
Soil	$3.16 \cdot 10^{-6}$	1.23 <i>m</i>	1.59 <i>cm</i>	[18]
Coarse sand	$4.37 \cdot 10^{-6}$	1.44 <i>m</i>	1.87 <i>cm</i>	[118]
Concrete	$4.30 \cdot 10^{-8}$	0.14 <i>m</i>	1.86 <i>mm</i>	[195]
Polyethylene	$4.10 \cdot 10^{-12}$	1.40 <i>mm</i>	18.1 μm	[107]

similar as the diffusion coefficient of atoms or molecules in porous media is proportional to $M^{1/2}$, with M being the mass of the atom or molecule [159, 205].

2.3.2 Diffusion in media

The ^{222}Rn gas distribution in indoor air can be described by the mass balance model [70, 138], which is however not applicable to ^{220}Rn due to its short half-life. Instead for thoron also diffusion has to be considered and its spacial distribution can be described by introducing an effective diffusion coefficient [208], which expresses the diffusion in a room macroscopically. Solving Equation 2.8 with the appropriated boundary conditions the concentration $C(z)$ versus the distance z from the emanating surface is then given by [185]:

$$C(z) = C_0 e^{-z/L} \quad (2.11)$$

where C_0 is the concentration at zero distance from the wall, i.e. the maximum ^{220}Rn concentration at the entry. The parameter L is the so called diffusion length,

$$L = \sqrt{\frac{D}{\lambda}} \quad (2.12)$$

which is the characteristic distance traversed by ^{222}Rn or ^{220}Rn atoms during one half-life. In Table 2.3 some diffusion coefficients and diffusion lengths, calculated via Equation 2.12, for radon and thoron are given for typical materials. Values in Table 2.3 are valid for stagnant conditions where other transport processes such as advection can be neglected. In that case a large spread for the permeability of the materials for ^{222}Rn is notable. Concrete has the smallest diffusion coefficient as compared to other building materials such as sand or soil. In general the ^{222}Rn diffusion through soil and sand reduces with decrease in their grain size [18, 118], due to increased packing density. The high density polyethylene membrane shows the best capability for ^{222}Rn mitigation by blocking its entry. Such types of foils can be used to seal basements of houses to reduce ^{222}Rn gas concentration in the building. It has to be noted that other publications have found diffusion lengths for ^{220}Rn to be in the range of 3.0 – 3.5 *cm* [157, 185] and about 2.4 *m* for radon [24], however these are within the error boundaries of the values in Table 2.3.

2.4 Indoor Radon occurrence

Only recently the Joint Research Centre (JRC) of the European Commission (EC) started collecting data for indoor ^{222}Rn concentrations (IRC). The goal is a European Atlas of Natural Radiation, not limited only to ^{222}Rn , with the main objective to inform the public of its natural radioactive environment [37]. Though most European National Authorities agreed to contribute to a European map for IRC there are many challenges to be solved as type and number of available data varies significantly. While some countries introduced ^{222}Rn monitoring programs decades ago and already finished them, others, such as Germany, have not even started yet. So for example in Sweden about 500,000 dwellings were already monitored compared to Germany with less than 50,000, pooled together from individual studies. Nevertheless most European countries provide an estimated annual mean level for IRC which varies from 20 – 140 Bq m^{-3} [36]. Even though the representation of ^{222}Rn levels in form of a map greatly helps to identify areas that are prone to ^{222}Rn , one has to keep in mind that there may be huge variations even at a certain location. The individual IRC of a dwelling is influenced by a great number of variables such as type of building and foundation, year of construction, floor level, outdoor temperature [94] and living habits of the inhabitants, just to name a few.

2.4.1 Concentration in German homes

In Figure 2.5 the distribution of IRC in German dwellings is illustrated. It is based on about 75,000 ^{222}Rn readings in approximately 28,000 residences [169]. Each individual ^{222}Rn measurement was weighted according to the corresponding measurement interval and corrected for seasonal variations. In areas in which the number of available measurements was too low the data-set was increased by adding random concentrations of dwellings with similar soil-gas concentrations, leading to a total number of about 32,000 habitats. In the areas Brandenburg, Mecklenburg-Vorpommern, Sachsen-Anhalt and Schleswig-Holstein the number of measurements was still too small so no regional conclusion could be drawn. However, when taking into account the number of residence in the respective area, the construction time and floor levels of the buildings, an arithmetic mean of 49 Bq m^{-3} for Germany could be estimated. At this IRC level about 1,900 deaths per year due to lung cancer, or about 5% of the all annual deaths connected to former, may be attributed to ^{222}Rn in Germany [112].

2.4.2 Indoor distribution

In early discussions generally a homogeneous gas distribution of indoor ^{222}Rn and ^{220}Rn , as well as of their progenies, in a room by complete mixing was assumed [70, 138]. This hypothesis relies on the transport mechanism of advection, i.e. air currents caused by temperature gradients in a room by either heating or cooling. A critical review of the refined Porstendörfer model [138] for indoor ^{222}Rn levels showed that it quite accurately predicts equilibrium factors and unattached fractions (f_p) [119]. The main physical pro-

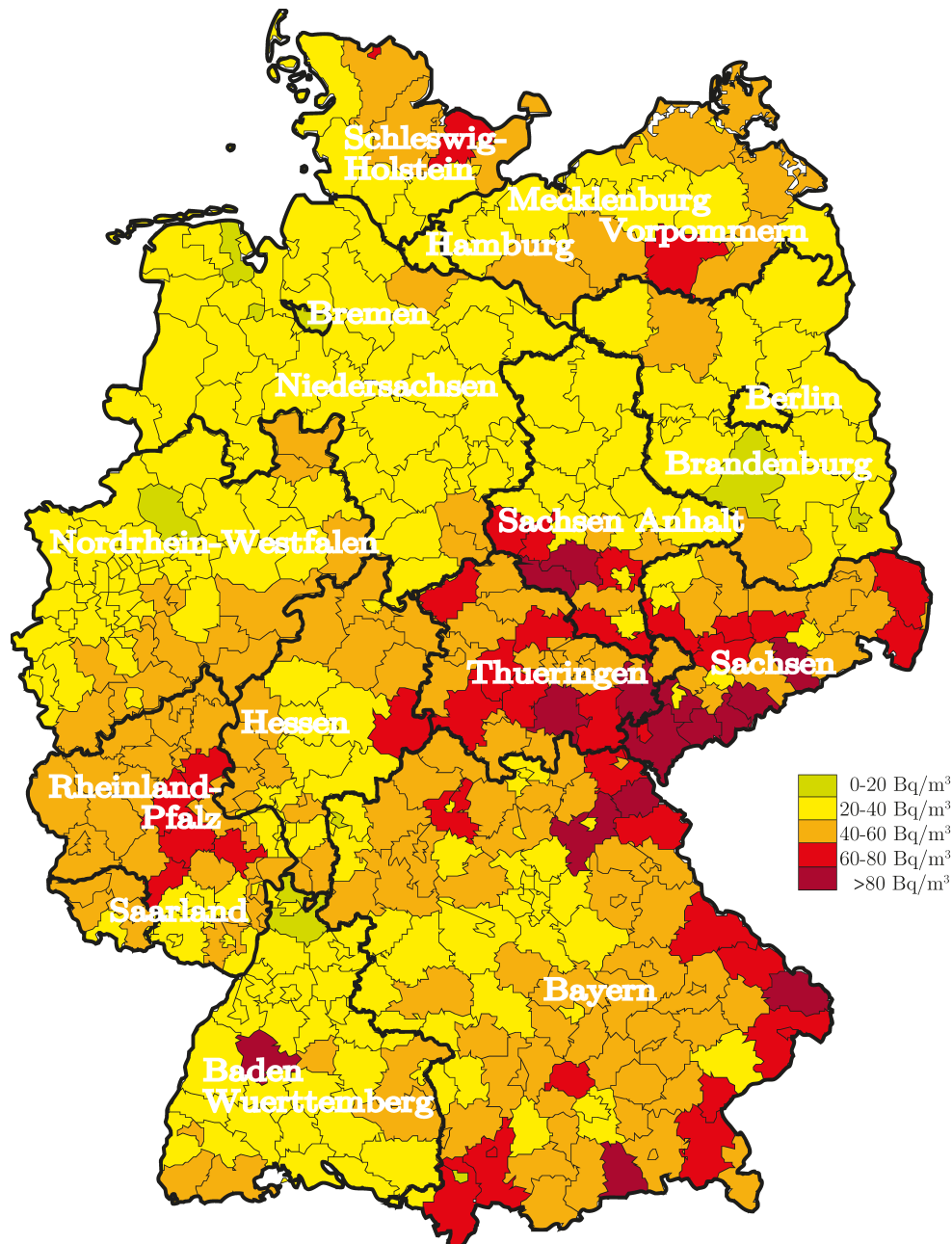


Figure 2.5: Average ^{222}Rn concentration in dwellings in the Federal Republic of Germany [112], adapted from [15].

cesses involved in that model are radioactive decay, attachment of nuclides to aerosols, or recoil from aerosols through decay, deposition on surfaces, for the unattached progeny the so called plate-out and removal by ventilation. Such a model, however, is not necessarily true, especially for the short-lived ^{220}Rn , in rooms with a spatially inhomogeneous radioactive source. However, considering the large diffusion length of ^{222}Rn as discussed in Section

2.3.2, an almost homogenous indoor distribution of ^{222}Rn and its progeny can be in most of the cases reached. Detailed simulations concerning that matter show a maximum 11% deviation in the room center compared to the concentration close to the source in the walls, under the assumption of moderate ventilation [196]. This implies that the only condition for placing a ^{222}Rn monitor in a room should be that it is not close to a sink such as a window or door as this could bias the measurement towards lower exposure levels. For ^{220}Rn , however, the gas concentration behaves differently as discussed in the next section.

2.5 Thoron occurrence

Very little is known about the concentration distribution of indoor ^{220}Rn levels compared to those for ^{222}Rn . This can be attributed to mainly two effects, which both originate from the short half-life of ^{220}Rn . On one hand thoron gas is difficult to measure and devices for that purpose are therefore hard to calibrate, and on the other hand, due to its short diffusion length (see Table 2.3), the origin of ^{220}Rn in the atmosphere is almost entirely limited to sources in the top few centimeters of soil or building material. Also early estimates indicated that under typical atmospheric conditions the potential alpha particle energy concentration (PAEC) from ^{220}Rn progenies would only deliver one tenth of the dose to the lung compared to an equivalent PAEC of ^{222}Rn [3]. Thus exposure due to ^{220}Rn seemed negligible and hence no epidemiological data to that subject exists [180], although it was already pointed out earlier that the role of ^{220}Rn as an air pollutant needs to be investigated [153]. Still only scarce data is available for European indoor thoron concentrations [166], mostly due to the lack of cost effective ^{220}Rn progeny measurement equipment. Only recently the topic again gained momentum when several studies in different parts of the world discovered increased thoron concentrations [203, 163, 155, 109]. For example the year 2000 Chinese study investigated mainly cave dwellings and adobe brick houses showing a significant ^{220}Rn influence on the total annual effective dose with a ^{220}Rn contribution of 1.7 mSv y^{-1} and $4.8 - 14.4 \text{ mSv y}^{-1}$ respectively, highly exceeding the dose rates of ^{222}Rn from 1.0 mSv y^{-1} to 2.3 mSv y^{-1} [203]. Similar results were obtained for India where the highest ^{220}Rn concentrations were found in dwellings with mud floors [163], with mean ^{220}Rn concentrations of $143 \pm 83 \text{ Bq m}^{-3}$. These findings are not exclusively limited to developing countries, since for example also in Europe one can find dwellings (7 – 14% of investigated houses) in which exposure due to ^{220}Rn exceeds that of ^{222}Rn [109]. Therefore, indoor ^{220}Rn progeny doses are not always of negligible radiological importance. These results also led to the development of mathematical models which allow assessment of the annual effective dose due to ^{220}Rn in certain mud building types [111]. Key factors which influence the indoor ^{220}Rn concentration are the air exchange rate, the aerosol concentration, the specific ^{232}Th activity, ^{220}Rn emanation rates plus the room dimensions and material properties. Also in Germany the ^{220}Rn issue is again a topic as discussed in the next section.

2.5.1 Concentration in German homes

Already in the early 1980's a survey in 150 dwellings and 100 outdoor areas took place acquiring the indoor ^{222}Rn and ^{220}Rn progeny concentrations as well as ^{222}Rn gas concentrations [81]. The ^{222}Rn activity concentration was found to have a median value of 26.0 Bq m^{-3} , while median PAEC value for its daughters was $1.7 \cdot 10^{-3} \text{ W.L.}$ which equals an EEC of 3.4 Bq m^{-3} . For ^{220}Rn the median PAEC value was determined to be $0.9 \cdot 10^{-3} \text{ W.L.}$, corresponding to an ECC of 0.5 Bq m^{-3} . The outdoor concentration was found to be lower by a factor of 3 – 4. In conclusion the study showed that the ^{220}Rn progeny concentration is only about 14% of that of ^{222}Rn . However, the study did not take into account the building materials used. More recent studies considering very common adobe houses in Germany show that ^{220}Rn progeny concentrations range between $2 - 10 \text{ Bq m}^{-3}$ [49]. Accordingly the resulting annual effective dose of $0.6 - 4 \text{ mSv a}^{-1}$ due to ^{220}Rn can exceed that of ^{222}Rn for such types of houses, meaning that ^{220}Rn is an issue for radiation protection and thus needs to be accounted for in further studies.

2.5.2 Indoor distribution

Large-scale studies with passive detectors as conducted for ^{222}Rn gas concentration are not so easily applicable for ^{220}Rn . The main issue here is the inhomogeneous ^{220}Rn gas distribution in a room. Simulations and measurements show [212, 196] that the ^{220}Rn gas concentration decreases exponentially with distance from the source walls (Equation 2.11). This originates from the short half-life of ^{220}Rn as it shares the same transport processes as ^{222}Rn . For ^{220}Rn complete mixing can only be achieved by unrealistically high ventilation rates (60 h^{-1}) [119], meaning that ^{220}Rn is generally in an incomplete mixing state. Therefore, due to the inhomogeneity of ^{220}Rn gas, its first decay product and the unattached fraction of the following bismuth and lead isotopes are also not evenly spread in a room [110]. However, if ^{220}Rn emanates from all room walls, the attached fraction of ^{212}Pb is distributed homogeneously, as demonstrated by measurements and simulations [212, 196, 111]. All these effects have to be taken into account when using devices for indoor ^{220}Rn concentration measurements.

2.6 Exposure to dose conversion

In order to be able to compare health effects due to ^{222}Rn exposure with other sources of radiation, the International Commission on Radiological Protection (ICRP) introduced the dose conversion convention [64], which allows calculation of the effective dose from an exposure. For this several quantities were introduced with the most important ones being discussed in the following.

2.6.1 Potential alpha energy concentration

The potential alpha energy (PAE) E_{pj} is the sum of alpha energies emitted by an atom decaying through its entire radioactive series, for ^{222}Rn or ^{220}Rn for example up to ^{210}Pb or ^{208}Pb (Table 2.2). It describes the energy which could be potentially released in the lung if an atom experienced all decays there. The PAE of all nuclei of a nuclide j with decay constant λ_j and activity A_j is therefore $A_j E_{pj} / \lambda_j$.

The potential alpha energy concentration (PAEC) C_p is defined as the sum of the PAE of all daughter nuclides present per volume of air [135]:

$$C_p = \sum_j C_{pj} = \sum_j C_j E_{pj} / \lambda_j \quad (2.13)$$

where C_j (Bq m^3) is the activity concentration of the corresponding decay product. The unit commonly used for the PAEC is (J m^{-3}) in the SI-system. An older unit still often encountered is the working level [WL] which can be converted via Equation 2.14 [24]:

$$1 \text{ WL} = 1.3 \cdot 10^5 \text{ MeV L}^{-1} = 2.08 \cdot 10^{-5} \text{ J m}^{-3} \quad (2.14)$$

2.6.2 Equilibrium-equivalent concentration

The equilibrium-equivalent concentration (EEC) equals an ^{222}Rn concentration which is in equilibrium with its daughters and which has the same PAEC as a non-equilibrium mixture. Only alpha decays are considered, because other decays are radio-biologically less important. This then leads by definition to the following relation [134]:

$$C_{eq} = \sum_j k_{pj} C_j \text{ with } k_{pj} = \frac{E_{pj}}{\lambda_j} / \sum_j \frac{E_{pj}}{\lambda_j} \quad (2.15)$$

Its unit is also Bq m^{-3} and the EEC is used to calculate the accumulated exposure and convert that to an effective dose.

For ^{222}Rn , ^{220}Rn and their short-lived daughters Equation 2.15 transforms to:

$$C_{eq,Rn} = 0.105 C_{218Po} + 0.516 C_{214Pb} + 0.379 C_{214Bi} \quad (2.16a)$$

$$C_{eq,Tn} = 0.913 C_{212Pb} + 0.087 C_{212Bi} \quad (2.16b)$$

where C_j Bq m^{-3} are the individual progeny concentrations in air. The individual factors for all progenies with PAE are also shown in Table 2.2, however, only those given in Equation 2.15 are relevant for dose estimation. In the case when only gas measurements are available, the EEC can be calculated via the equilibrium factor, as discussed next.

2.6.3 Equilibrium factor F

The equilibrium factor describes the disequilibrium between the progeny mixture and the mother nuclide with respect to PAE. It is defined as the ratio between EEC (C_{eq}) to the

activity concentration of its parent in air C_0 [64]:

$$F = \frac{C_{eq}}{C_0} \quad (2.17)$$

Measurements of the equilibrium factor for indoor ^{222}Rn yield a range from 0.1 to 0.9 but for most cases it is possible to use an equilibrium factor of 0.4 [64, 191, 190, 178]. In mines without diesel engines polluting the air a factor of 0.2 is recommended [34]. For ^{220}Rn the determination of the equilibrium factor is much more difficult, due to its large spacial variation (Section 2.5.2). Latest results show values between 0.02-0.03 for indoor ^{220}Rn , which are subjected to large uncertainties [190]. Therefore it is arguable to use ^{220}Rn gas measurements as domestic exposure estimation.

2.6.4 Exposure

For radiation dose estimation the equilibrium equivalent exposure E_{eq} is required which is defined as the integral of the activity concentration over a certain exposure time T , $E_{eq}(T) = \int_0^T C_{eq}(t) dt$, with unit ($Bq h m^{-3}$). Another definition is the integral over the PAEC yielding a potential α -energy exposure E_p with units ($J h m^{-3}$) or the historical unit *WLM* (working level month), which corresponds to an exposure of 1 *WL* during a reference working period of 1 month (170 *h*) at a EEC for ^{222}Rn of $3700 Bq m^{-3}$. With Equation 2.14 the unit can be converted into the SI-system via,

$$1 \text{ WLM} = 2.08 \cdot 10^{-5} J m^{-3} \times 170 h = 3.54 mJ h m^{-3} \quad (2.18)$$

which can be also transferred into E_{eq} with the relation $C_{eq}/C_p = [(5.79 + 28.5 + 21.0 + 2.9 \cdot 10^{-6}) \cdot 10^{-10} J Bq^{-1}]^{-1} = 1.80 \cdot 10^8 J^{-1} Bq$, where the factors are the PAE per unit of activity ($MeV Bq^{-1}$), which were converted to units of ($10^{-10} J Bq^{-1}$) [64]. Hence this leads to a ^{222}Rn equilibrium-equivalent activity exposure of,

$$1 \text{ WLM} = 3.54 mJ h m^{-3} \times 1.80 \cdot 10^8 J^{-1} Bq = 6.37 \cdot 10^5 Bq h m^{-3} \quad (2.19)$$

and for ^{220}Rn ,

$$1 \text{ WLM} = 3.54 mJ h m^{-3} \times 1.32 \cdot 10^7 J^{-1} Bq = 4.67 \cdot 10^4 Bq h m^{-3} \quad (2.20)$$

These conversions factors can be of value as in many publications the older *WLM* unit is still used to simplify comparison with former findings.

2.6.5 Dose conversion factors

The absorbed dose of tissue from inhalation of ^{222}Rn , ^{220}Rn and their daughters cannot be measured. Instead it needs to be calculated by either numerically modeling the sequence of inhalation, deposition, clearance, retention and decay of the radionuclides, or, as an alternative approach, ICRP introduced a conversion convention based on the equality

Table 2.4: Dose conversion factors (DCFs) for exposure of adults to ^{222}Rn daughters

Nuclide	Group	DCF	DCF ¹	Reference
		$nSv/Bq\ h\ m^{-3}$	mSv/WLM^{-1}	
^{222}Rn	Public	7.7	4.9	[65]
	Worker	10.4	6.6	[65]
^{220}Rn	Public	39	1.82	[62]
	Public	40	1.87	[191]

¹Multiplied by a factor of $6.37 \cdot 10^5$ (^{222}Rn daughters) or $4.67 \cdot 10^4$ (^{220}Rn daughters).

of detriments from epidemiological studies [64]. In 1993 the nominal lifetime lung cancer risk for ^{222}Rn for the average population was taken to be $8 \cdot 10^{-5}$ per $mJ\ h\ m^{-3}$ ($2.83 \cdot 10^{-4}\ WLM^{-1}$), while the detriment per unit effective dose, was chosen to be $5.6 \cdot 10^{-4}\ mSv^{-1}$ for workers and $7.3 \cdot 10^{-4}\ mSv^{-1}$ for the public [64]. This led to conversion factors of $8 \cdot 10^{-5}/5.6 \cdot 10^{-4} = 1.43\ nSv\ (mJ\ h\ m^{-3})^{-1}$ for workers and $8 \cdot 10^{-5}/7.3 \cdot 10^{-4} = 1.10\ nSv\ (mJ\ h\ m^{-3})^{-1}$ for the general population [191]. The factors can be converted via Equations 2.19 and 2.20 to $7.9\ nSv\ (Bq\ h\ m^{-3})^{-1}$ and $6.0\ nSv\ (Bq\ h\ m^{-3})^{-1}$ respectively. The difference in the values originates from parameters like age structure, exposure time, aerosol concentration, smoking behavior etc. for the two different groups. Recently the detriment per unit effective dose was updated in ICRP 103 changing the effective dose conversion factors (DCF) for ^{222}Rn to $10.4\ nSv\ (Bq\ h\ m^{-3})^{-1}$ ($6.6\ mSv\ WLM^{-1}$) for workers and $7.7\ nSv\ (Bq\ h\ m^{-3})^{-1}$ ($4.9\ mSv\ WLM^{-1}$) for the public [65]. With the newly proposed lifetime excess absolute risk (LEAR) in the recent ICRP 115 [178] of $14 \cdot 10^{-5}\ mJ\ h\ m^{-3}$ ($5.0 \cdot 10^{-4}\ WLM^{-1}$) the effective dose conversion factors for ^{222}Rn would almost double to $19\ nSv\ (Bq\ h\ m^{-3})^{-1}$ for workers and $14\ nSv\ (Bq\ h\ m^{-3})^{-1}$ for the public [108].

In the most recent ICRP statement on ^{222}Rn it was concluded that radon and its progeny should be treated in the same way as other radionuclides within the ICRP system of protection, i.e. doses should be calculated using ICRP biokinetic and dosimetric models [178]. Calculation of dose conversion coefficients depend on the aerosol activity median diameter, the unattached-to-aerosol-attached progeny fraction f_p , breathing rates and the used model [137]. Based on recent publications the favored model seems to be the Human Respiratory Tract Model (HRTM) [63]. It divides the human respiratory tract into four anatomic regions that act as filters for inhaled materials. The deposition of the ^{222}Rn or ^{220}Rn decay products in the different regions depend on aerosol characteristics, such as particle diameters or the attached fraction f_p , and thus also the simulated received dose. Values from dosimetric calculations yield dose conversion factors in a range of $9.4 - 31\ nSv\ (Bq\ h\ m^{-3})^{-1}$, or in historic units of $6 - 20\ mSv\ WLM^{-1}$ [16]. While for ^{222}Rn an ample set of epidemiological data is available, no such data exists for ^{220}Rn . Thus conversion factors for ^{220}Rn originate from model calculations. Based on the indoor equilibrium factor of 0.02 (see Section 2.6.3) UNSCEAR recommends a value of $40\ nSv\ (Bq\ h\ m^{-3})^{-1}$ ($1.87\ mSv\ WLM^{-1}$) for dose estimation [191], while ICRP suggests

a factor of $39 \text{ nSv } (Bq \text{ h } m^{-3})^{-1}$ ($1.82 \text{ mSv WLM}^{-1}$) [62]. More recent publications suggest the conversion factors to be in the range of $81.0 - 116 \text{ nSv } (Bq \text{ h } m^{-3})^{-1}$ [12]. In Table 2.4 the current recommended dose conversion factors for both radon isotopes are listed.

The effective dose D_{eff} (Sv) an individual receives is then calculated via,

$$D_{eff} = f_{DCF} \int_0^T C_{eq}(t) dt = f_{DCF} F \int_0^T C(t) dt \quad (2.21)$$

where f_{DCF} is the dose conversion factor ($\text{nSv } (Bq \text{ h } m^{-3})^{-1}$), C_{eq} the equivalent equilibrium concentration ($Bq \text{ m}^{-3}$), F the equilibrium factor, $C(t)$ the gas activity concentration ($Bq \text{ m}^{-3}$) and T the exposure time (h).

2.7 Health effects of Radon

While ^{222}Rn was discovered in the early 20th century, symptoms due to its exposure have been known since the sixteenth century as mountain sicknesses, leading to an increased fatality rate of miners [24]. 300 years later in 1879 two physicians revealed that most of these deaths were related to lung cancers [50], and ^{222}Rn was suspected as possible cause some decades later [105]. Then, in the 1950s, it was recognized that one possible cause for bronchial carcinoma is a high lung dose due to the inhalation and deposition of short-lived ^{222}Rn daughter atoms [156, 6, 7]. In the wake of this development intense research started relating exposure versus incidence which indicated a correlation between added lung cancer risk and ^{222}Rn exposure.

One possibility to do so is by epidemiological investigations of radiation effects, which are usually conducted either as a cohort study or as a case-control study. For a cohort study, a defined population with a wide range of exposures is repeatedly examined for a long period of time to record the occurrence of effects. That type of study can be performed either prospectively by following a current cohort into the future, or retrospectively. In that case a cohort of living persons at some point in the past is constructed and followed prospectively, generally to the current time. In a case-control study, the cases and controls, i.e. people with and without a specified disease, are compared, to examine differences in exposures. Generally this is done for ^{222}Rn with retrospective dose estimation of lung cancer diseased persons, while controls are chosen on comparable socio-demographic parameters. Hence epidemiology is rather observational than experimental in nature and greatly relies on the quality of a study. Important parameters are potential bias or confounding by unmeasured factors, statistical power, radiation dose estimation, available data on potential con-founders and modifiers of radiation risk, and data availability and quality of cancer incidences and subtypes [191]. Results of epidemiological studies on radiation-exposed groups are often stated as estimates of excess relative risk (ERR). Additionally they may be expressed per unit concentration, e.g. ERR per $Bq \text{ m}^{-3}$ when these values have been derived based on a linear dose-response assumption. The ERR represents the increased cancer rate relative to an unexposed group. It is defined as the quotient of the excess

absolute risk $E = R_1 - R_0$, with R_1 being the risk for a population exposed to some risk factor (e.g. radiation or smoke), and R_0 being that of an identical population not exposed (spontaneous incidence), i.e. $ERR = E/R_0$ by definition [46]. For example, an ERR of 1 corresponds to a doubling of the cancer rate.

2.7.1 Epidemiological studies on miners

The first large meta-analysis combining eleven underground miner studies was published in 1994 [102]. It included data from 68000 miners which in average worked 5.7 years in a mine with a lung cancer incidence of 2700 cases. The mean cumulative ^{222}Rn exposure was determined to be 164 WLM ($108.0 \text{ MBq h m}^{-3}$). This would be comparable to a persons domestic exposure living at a ^{222}Rn concentration level of about 2000 Bq m^{-3} for 20 years, assuming an 80% indoor exposure with an equilibrium factor of 0.4. These results were also discussed in the BEIR VI report [10] which suggested a linear increase of lung cancer risk per unit exposure without a threshold value, see Table 2.5. However, no significant increase of extrapulmonary cancers due to ^{222}Rn exposure could be observed [28]. One problem with such pooled studies is the heterogeneity of data with respect to the quality of exposure assessment and the influence of confounding factors such as arsenic and dust pollution, tobacco smoke as well as lifestyle and genetic factors. A notable miner study in this context is the one on Wismut miners. Between 1946 and 1990 about 200,000 people were employed in the former Wismut AG, of which about 156,000 were exposed to high ^{222}Rn concentrations between 1946 to 1955 of about 150 WLM a^{-1} [41]. The main strengths of this study are its size, wide range of exposures, long duration and large number of lung cancers cases with additional information on dust and arsenic exposure available [91]. In the most recent publication [90] it was evaluated that of the 58,987 individuals in observation from 1946 to 2003, 20,920 (35.5%) had died. From these deaths 3,016 (14.4%) were attributable to lung cancers. A total number of 50,773 persons were exposed to ^{222}Rn with a person-year-weighted mean cumulative exposure of 218 WLM a^{-1} and an external gamma radiation dose of 30 mSv a^{-1} . The results indicated a statistically significant increase in risk for lung cancer of 0.19% (95% CI : 0.17 – 0.22%) ERR/WLM for ^{222}Rn , where ERR is the excess relative risk. No association between leukemia and cumulative ^{222}Rn exposure could be discovered. Other relations such as those between ^{222}Rn exposure and cancers of the extra-thoracic airways are limited due to low statistical power [89]. A potential drawback of the Wismut cohort is its limited information on smoking and the validity of retrospective dose assessment in the years before 1955. However, there are several additional miner studies available.

An overall summary of several international miner studies was recently released in the UNSCEAR 2009 report [190], which reports a combined ERR of 0.59% (95% CI : 0.35 – 1.0%) per WLM , comparable to that reported by Lubin et al. of 0.49% (95% CI : 0.2 – 1.0%) per WLM [102]. Further published results are presented in Table 2.5 as simple linear estimates of the excess relative risk per exposure. The three large-scale analyses that have summarized most of the currently available information provide very similar estimates of the correlation between accumulated WLM exposure and the risk of lung cancer. The

Table 2.5: Summary of excess relative risk (ERR) for lung cancer incidence per working level month (WLM) from combined analysis of miner studies [179].

Reference	Cohorts	Miners	Person-years	ERR/WLM	95% CI
[64]	7	31,486	635,022	1.34%	0.82–2.13%
[102]	11	60,570	908,903	0.49%	0.20–1.00%
[10]	11	60,705	892,547	0.59%	
[190]	9	125,627	3,115,975	0.59%	0.35–1.00%
[184]	2	10,100	248,782	1.60%	1.00–2.30%

variations in the estimates may be explained by differences in the cohorts with respect to duration of follow-up, attained age, duration of work, exposure levels, and background rates of lung cancer. One problem is to apply the results of miner studies to the common population because gender, age and duration of exposure is completely different as well as the aerosol and ^{222}Rn concentrations influencing the accumulated absorbed alpha particle energy. Thus also the influence of ^{222}Rn on lung cancer risk in low indoor concentrations of the general public had to be assessed.

2.7.2 Epidemiological studies on residential exposure

Studies to estimate the risk of lung cancer incidence directly associated with residential ^{222}Rn exposure have been conducted in many countries. There are over 22 individual studies and 6 pooled analyses listed in the recent UNSECEAR report [190]. Case-control studies prior to the year 2000 are well described in [103]. It included 4,236 cases and 6,612 controls, and reported a relative risk of 1.14 at 150 Bq m^{-3} ^{222}Rn gas in indoor air, that corresponds to an ERR of 0.09 per 100 Bq m^{-3} (95% CI : 0.0 – 0.2), which was similar to model-based extrapolations from miner studies. A pooled German study with data of 2,963 incident lung cancer cases and 4,232 population controls yielded an ERR of 0.10 per 100 Bq m^{-3} (95% CI : 0.02 – 0.30) [202]. More studies with higher statistical power due to pooling of several individual studies have been recently published. They show firm evidence that residential ^{222}Rn acts as a cause of lung cancer in the general population [104, 29, 30, 93, 92]. In the pooled Chinese study of Lubin et al. a total of 1,050 lung cancer cases and 1,996 controls were included. Residential ^{222}Rn concentrations were measured in one home for each subject by means of two alpha-track detectors placed in the bed- and living room for at least one year. The mean ^{222}Rn level in Shenyang dwellings was 115.7 Bq m^{-3} while for the Ganso region it was 222.9 Bq m^{-3} . Thus individual exposure was determined based on indoor ^{222}Rn levels, with dependence on coverage, i.e. the time staying indoors at the same house. The evaluation of the ERR for ^{222}Rn with respect to sex, indoor smokiness and cigarette smoking showed no significant variation. It was found to be 0.133 per 100 Bq m^{-3} (95% CI : 0.01 – 0.36).

The European pooled study by Darby et al. based on the data of 7,148 individuals with lung cancer and 14,208 controls. Mean ^{222}Rn concentrations were 104 Bq m^{-3} for the

Table 2.6: Summary of ERR per unit concentration or exposure from combined residential ^{222}Rn studies [190].

Reference	Cases	Controls	ERR/ $Bq\ m^{-3}$	ERR/WLM ¹
[202]	2963	4232	0.10%	0.8%
[104]	1050	1996	0.133%	1.01%
[30]	7148	14208	0.16%	1.21%
[92]	3662	4966	0.11%	0.83%

¹Converted from $(Bq\ m^{-3})^{-1}$ to WLM^{-1} by dividing with $13.2\ WLM / 100\ Bq\ m^{-3}$

cases while the controls had $97\ Bq\ m^{-3}$. Before correcting for uncertainties in ^{222}Rn concentrations the reported ERR was about 0.08 (95% *CI* : 0.03 – 0.16) per $100\ Bq\ m^{-3}$ which corresponds to an ERR of 0.16 (95% *CI* : 0.05 – 0.31) per $100\ Bq\ m^{-3}$, when taking into account uncertainties ^{222}Rn level measurements. Again no evidence was found that the ERR varied with age, sex, or smoking history. This study is classified as high quality as it was able to improve data homogeneity by using a common format and consistent analysis of the pooled studies.

The combined analysis of 7 North-American studies by Krewski et al. retained a total of 3,662 cases and 4,966 controls and focused on a time window 5 to 30 years before the interview date. Here retrospective ^{222}Rn dosimetry was based on long-term monitoring with alpha-track detectors which measured the concentration of ^{222}Rn progeny in indoor air in the living area for 12 months. Concentration varied from lowest in New Jersey ($25\ Bq\ m^{-3}$) to highest in Winnipeg ($131\ Bq\ m^{-3}$). The overall estimate of the ERR for lung cancer was 0.11 (95% *CI* : 0.00 – 0.28) per $100\ Bq\ m^{-3}$ which is consistent with the ERR of 0.12 (95% *CI* : 0.02 – 0.25) per $100\ Bq\ m^{-3}$ based on data of low-exposed miners [10]. Also the authors reported that no significant difference in the ERR with sex, education level or smoking status could be found. An analysis to a restricted subset with presumed better quality of ^{222}Rn measurements resulted in an increase of the ERR to 0.18 (95% *CI* : 0.02 – 0.43) per $100\ Bq\ m^{-3}$. These values are also listed in Table 2.6. The conversion between ERR per ^{222}Rn concentration to ERR per *WLM* is based on a procedure assuming 30 years of exposure with 7000 hours spent at home per year and an equilibrium factor of 0.4. Then the miner-based conversion factor is $0.4 \times 100\ Bq\ m^{-3} \times 7000\ h \times 30 \times (6.37 \cdot 10^5)^{-1} = 13.2\ WLM$ per $100\ Bq\ m^{-3}$ [61], see also Equation 2.19 for conversion between *WLM* and $Bq\ h\ m^{-3}$.

2.7.3 Summary

The main pooled ^{222}Rn studies on miners (Table 2.5) and the public (Table 2.6) indicate a significant association between risk of lung cancer and exposure to ^{222}Rn . The difference between risk estimates for residential and occupational exposure can be attributed to the lack of information on smoking behavior for the latter, which is a potential confounding factor in both study types. There is far more data on smoking history available for the resi-

dential studies. However, with a joint analysis of three European miner case-control studies with a restricted data set including only individuals with low exposure (< 300 *WLM*) and known smoking behavior the results are consistent [61]. Despite this strong evidence there is still controversy regarding the results of the case-control studies, as large ecologic studies such that of Cohen [20, 19] showed an inverse relationship between ERR and ^{222}Rn exposure. In addition all studies failed to show a significant effect on health for low level ^{222}Rn concentrations below 150 Bq m^{-3} . The inverse correlation revealed in the ecological studies was attributed to smoking as confounding factor, because in rural regions, where higher indoor ^{222}Rn concentrations were measured, people tend to smoke more. Other methodological challenges of ecological study types are their inability to adjust for individual mobility [167, 168]. Thus, they are considered of limited value in assessing the risk from ^{222}Rn because of their dependence on grouped data and confounding [57]. On the other hand, it is argued that the results indicating a significant increase in lung cancer risk are biased since cases tend to underestimate their actual cigarette consumption, in particular after being diagnosed with lung cancer. Hence retrospective smoking history is largely unreliable and health effects of ^{222}Rn are blurred by cancer incidence due to smoking [9]. This author also emphasized that far more studies have been conducted on an anti-radon attitude with the support of governmental agencies, while studies questioning the official linear non-threshold (LNT) theory are hardly supported, leading to an imbalance of published data.

Nonetheless, the current consensus of several institutions like the ICRP, the United Nations Scientific Committee on the Effects of Atomic Radiation (UNSCEAR), the International Atomic Energy Agency (IAEA), the National Council on Radiation Protection and Measurements (NCRP) and the Environmental Protection Agency (EPA) is to consider ^{222}Rn as a significant risk factor for lung cancer. An ERR of 0.16 (95% *CI* : 0.05 – 0.31) per 100 Bq m^{-3} is suggested as an appropriate and possible conservative estimate of lifetime risk from residential ^{222}Rn [190].

Chapter 3

Principle and design of the exposimeter

Different techniques for radon and thoron detection have been elaborated in the past decades and new ones are still being developed. Here only airborne radon/thoron measurement principles shall be discussed because devices based on progeny sampling [130, 48, 113, 114] are not topic of this thesis.

3.1 Measurement principles

In general a radon/thoron monitor consists at least of a detector or collector (e.g., active charcoal) and a diffusion chamber or something similar where the components are mounted. Such airborne monitors are separated into two sampling methods, namely active, when a pressure difference is generated, or passive, relying only on natural diffusion, and two cycling methods, as depicted in Figure 3.1. They either allow for a one time cycle, so called integrated or grab sampling, and continuous sampling, which means repeated cycling. For latter electronic components are required, while integrated devices often use solid-state nuclear track detectors (SSNTD) based typically on cellulose nitrate (LR 115) or allyl diglycol carbonate (CR-39) [71]. These types of detectors are cost effective, easy to handle and transport and hence often employed for radon and thoron gas measurements. Activated charcoal detectors have the same features, however, they suffer from temperature and humidity dependence [75, 197], and thus can only be used for short periods. All are proportional counters requiring a so called calibration factor (CF) to determine the radon or thoron concentration. In this work a diffusion chamber type device was developed, because bare detectors without filter have serious disadvantages since their CF is dependent on the progeny deposition rates influenced by humidity, aerosol concentration, airflow and equilibrium factor of the environment [5, 121, 113]. With a diffusion chamber monitor this problem is omitted because a filter applied to the diffusion inlets grants only undisturbed diffusion of the inert radon and thoron gas [209, 164], and the counts/tracks generated by the alpha decays from radon and its progeny are then proportional to the respective gas activity concentration. Due to its smaller dependence on environmental parameters, this method has also been set as default method by the recently released ISO standards [69]

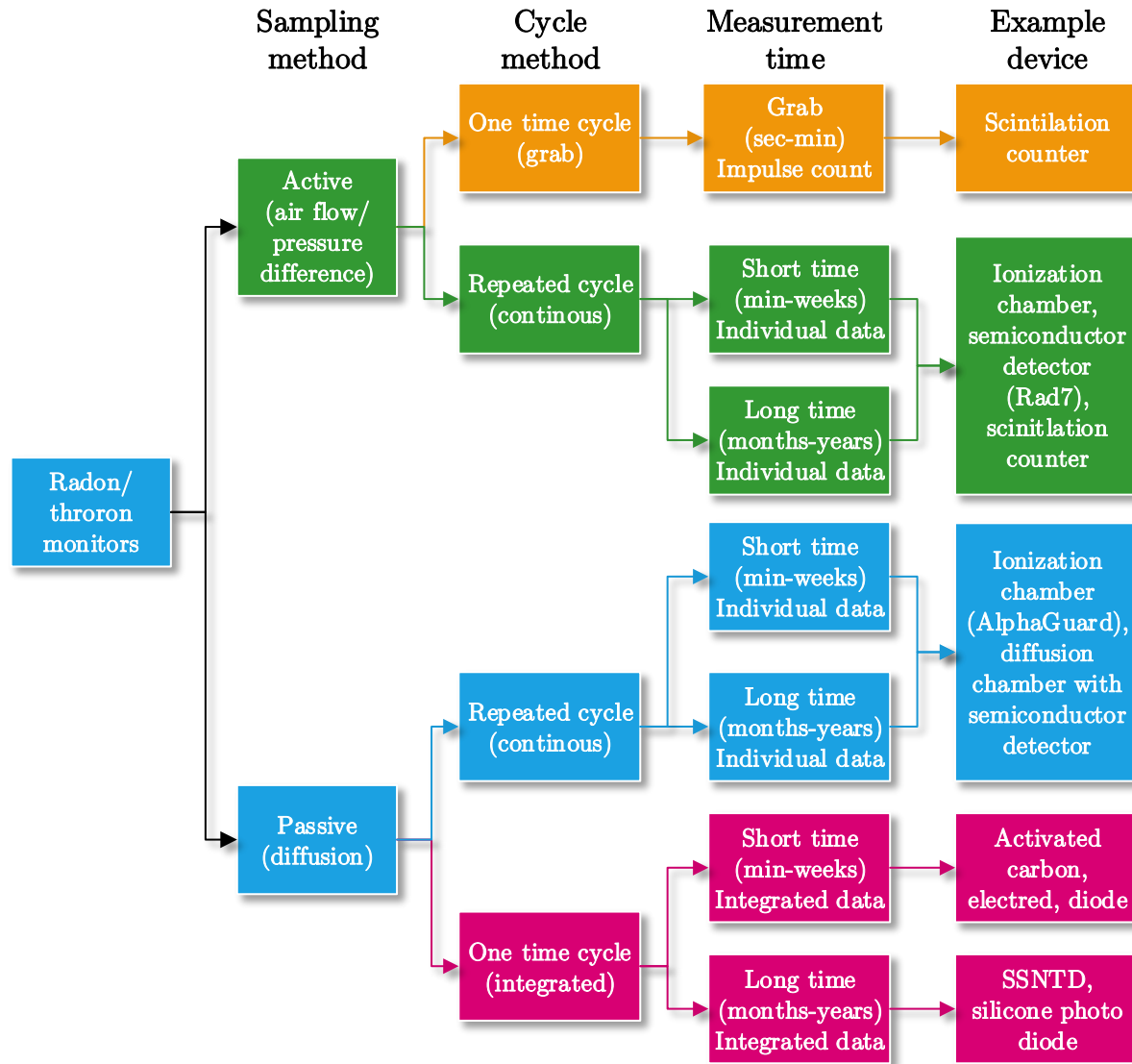


Figure 3.1: Categories for radon and thoron measurement methods, adapted from [71]. The developed device belongs to the blue group.

for passive devices.

3.1.1 Discrimination methods

Several methods allow to differentiate between radon and thoron, for example by parallel measurements with the two filter method [173, 158, 213, 183], where one chamber only measures radon, by preventing thoron to diffuse inside its measurement volume, while the other permits both. The difference in counts is then related to the thoron concentration. Another approach is to switch between active and passive sampling which results in differ-

ent count rates for either mode, for example realized with an electronic detector such as a scintillation cell [182], which usually requires a large acquisition apparatus and high power consumption.

The third approach measures the individual energy of each alpha particle decay, using ionization chambers or semiconductor detectors [47]. Ion-implanted silicon detectors are standard equipment and widely used for alpha-particle spectrometry. They can be used in hand-held devices with low power consumption while allowing for discrimination of radon and thoron by definition of different regions of interest [13, 45]. A commonly used [161, 170] semiconductor detector is the DurrIDGE Rad7, which utilizes a pump for active sampling and additionally electrostatic collection. It was also used in this work as reference for radon/thoron measurements.

The passive discriminative monitor developed in this work employs alpha-particle spectroscopy, to determine the gas activity concentration.

3.2 Electronic design

In this section the electronic parts of the exposure meter partly developed in the frame of this thesis are described. The amplifier and shaper design employed by an in house developed Neutron dosimeter [204] were adapted and used for the present monitor. The different stages of the device are discussed in detail, as well as simulation results to characterize the circuit behavior under changing component values and temperatures.

3.2.1 Voltage generator

The device is powered by an 1/2 AA Lithium battery with a capacity of 1200 *mAh* and a voltage of 3.6 *V*. The battery output voltage is stabilized by an integrated circuit (IC) voltage regulator, locking the operating voltage at 3.3 *V*. In order to achieve full detector depletion, necessary to ensure near linear energy absorption, an additional high voltage generator is needed. As low power consumption was a requirement, a charge pump circuit has been chosen for that purpose, which features very high efficiencies in the range of 90 – 95 % [126]. Figure 3.2 demonstrates the charge pump used for this device¹. It is built from Schottky diodes denoted as *Dn*, which feature a low forward voltage drop U_D (0.1 *V*), and capacitors denoted as *Cn*, where *n* is the part number. The net label *Vdig* refers to the input voltage U_{in} of 3.3 *V*, while *pulse* refers to a 50 *Hz* rectangular signal generated by the microcontroller, used to pump the voltage generator. The pulse rail voltage V_{pulse} is periodically switched between two states, 0 *V* and 3.3 *V* respectively. In state one *C9* is charged to $V_{in} - V_D$, while in state two the first diode of *D1* is in reverse and the second in forward direction, and the charge of *C9* is forced off in direction of *C1* which is hence charged to $V_{in} + V_{pulse} - 2V_D$. This means that after each stage *k* of a diode and a capacitors

¹Original design by B. Haider.

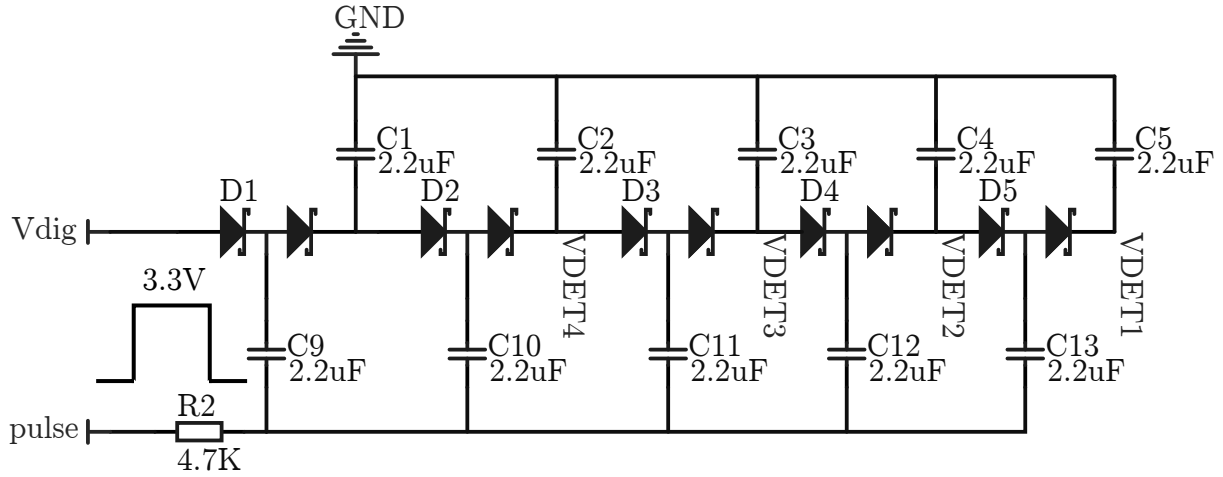


Figure 3.2: Schematic of voltage generator used in current exposimeter version.

pair, the output voltage V_k can be approximated by [140]:

$$V_k = V_{dig} + k \times (V_{dig} - V_D) \quad (3.1)$$

where V_{dig} is the digital input voltage of 3.3 V and V_D the diode voltage drop. This leads to approximate output voltages of 19.3 V, 16.1 V, 12.9 V and 9.7 V for the indicated net labels $VDET1$, $VDET2$, $VDET3$, $VDET4$ respectively, assuming no load is connected to the pump. These four different voltages can be set as reverse voltage for the detector. The ripple voltage originating from the oscillating voltage V_{pulse} can be reduced by using a large output capacitance, which in turn leads to longer times needed to reach the maximum output voltage.

3.2.2 Detectors

A new detector for the special requirements of alpha-particle detection has been developed at the Institute of Electron Technology in Warsaw [200]. It is a silicone pin-diode detector build from four $p^+ - i - n^+$ structures which are assembled on a ceramic base and connected in parallel. The detector features an active detection area of approximately 467 mm^2 , covered with a 400 nm thick aluminum layer acting as cathode, and a depleted active layer thickness of 110 μm . All important parameters are also stated in Table 3.1. This ensures that charges from ionizing alpha-particles with energies of less than or equal to 10 MeV, which have a maximum penetration depth of 70 μm according to SRIM [214] calculations, are fully collected.

Before assembly in the exposimeter all detectors were tested several days in a reverse bias voltage setup to assure that none exceeds the dark current given in Table 3.1. Further the employed detectors have been tested for their energy absorption behavior, which in

Table 3.1: Design and electrical parameters of detector

Parameter	Value
Active layer thickness	$110 \pm 10 \mu m$
$p^+ - i$ junction dimensions	$10.8 \times 10.8 mm$
Active surface Al thickness	$400 nm$
Average breakdown voltage	$100 V$
Average depletion voltage	$9 V$
Maximum dark current	$79 nA$

a first order approximation can be assumed to be linear. For this the monitoring system has been put into a low pressure environment at $13 mbar$, and 6 detectors were individually exposed with alpha-particles from an Americium-Curium-Plutonium source, with fixed detector-source distance ($19.2 mm$). The obtained spectra were, apart statistical fluctuations similar, and therefore summed up for evaluation. The expected peaks originating from alpha particles with energies of $5.24 MeV$, $5.49 MeV$ and $5.90 MeV$ were clearly visible. Each was fitted by a Gaussian function, resulting in a mean channel number per incident energy. The linear regression of the obtained values yielded a coefficient of determination of $R^2 = 0.974391$, confirming the assumption of an almost linear energy absorption. Of course the energy absorption of alphas in the aluminum layer is highly nonlinear. However, due to the low energy resolution of the whole system, this effect has only a minor impact on the linear relationship between incident energy and output amplitude. This can be also seen in Table 3.2, where the difference $\Delta E = dE_\beta - dE_\gamma$ of the energy loss dE of alpha particles incident at two different angles, namely $\beta = 60^\circ$ and $\gamma = 0^\circ$, is stated. The values calculated for transitions through Aluminum with a $400 nm$ thickness show that the difference in energy absorption is in the same range as the energy resolution of the electronics. Therefore only alpha particles with low energy and greater incidence angle are affected by a higher energy loss difference, which, however, perishes due to limited events in statistical fluctuations.

For the monitoring system, two of the detectors are connected in parallel with a reverse bias voltage of $14 V$ and a capacitance of about $470 pF$ each. As an approximation the voltage drop at the detectors, due to currents generated by electron-hole pair production

Table 3.2: Energy loss difference $\Delta E = dE_{60^\circ} - dE_{0^\circ} MeV$ for alpha particles incident under two different angles (60° and 0°) for different energies E_α .

E_α	MeV	0.1	1	2	3	4	5	6	7	8	9	10
dE_{0°	MeV	0.07	0.14	0.11	0.09	0.07	0.07	0.06	0.05	0.05	0.04	0.04
dE_{60°	MeV	0.09	0.28	0.22	0.18	0.15	0.13	0.12	0.11	0.1	0.09	0.08
ΔE	MeV	0.02	0.14	0.11	0.09	0.08	0.07	0.06	0.05	0.05	0.05	0.04

of the absorbed alpha-particles, can be calculated via Eq. 3.2:

$$\Delta U = \frac{E_\alpha e}{E_{ehp} C} \quad (3.2)$$

where ΔU is the induced voltage drop, E_α the alpha particle energy, e the elementary charge, E_{ehp} the electron-hole-pair production energy and C the combined capacitance of the detectors. With an energy of 3.63 eV per electron-hole pair in *Si* [84] the voltage drop for the targeted α -particle energy range between 1 – 10 MeV approximately spans from 47 – 470 μV , and is therefore too small to be measured directly. Equation 3.2 also implies that it is absolute necessary for the detector capacitance to remain constant during operation. This is ensured by applying a high reverse voltage leading to full depletion of the detector. For this new requirements a new amplifier had to be developed with high gain and linear amplification which is discussed next.

3.2.3 Amplifier

The amplification system uses three stages for amplifying and shaping the signal produced by an α -particle. The system is entirely built from discrete components to allow for a maximum optimizability concerning power consumption and gain. The pre- and main amplifier employ n-channel field effect transistors (FETs), which are characterized by a high input impedance along with low output noise [76].

Preamplifier

Preamplifiers are employed to enhance very small signals from detectors, in order to be able to transmit the waveform to other equipment. Therefore, preamplifiers are normally located as close as possible to the detector electronics to ensure reduced cable length and low parasitic effects from electromagnetic fields, thus improving the signal-to-noise-ratio [162]. In general three basic types of preamplifier exist, such as voltage, current

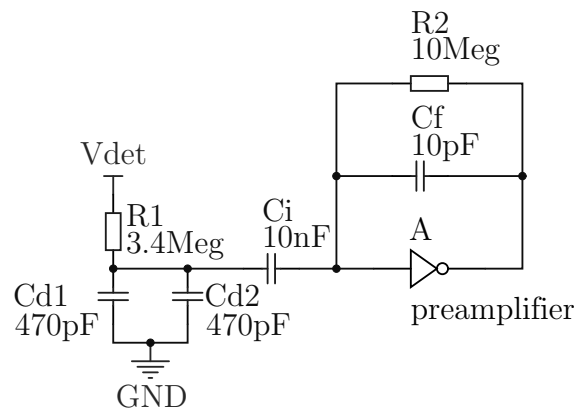


Figure 3.3: Schematic drawing of charge sensitive preamplifier.

or charge sensitive setups. Due to the temperature dependent capacity of the employed semiconductor detectors [98] a charge sensitive preamplifier was developed for this device. It is built from three FET cascades, hence an inverting amplifier, which are ideally suited for small input signals such as those described in Section 3.2.2. The schematic circuit in Figure 3.4 depicts the working principle of the preamplifier. It uses a negative feedback through C_f to stabilize its gain with a RC time constant of $\tau = 100 \mu s$. So R_2 is needed to restore initial operating conditions. The detector and amplifier circuits are decoupled via C_i due to the high detector voltage V_{det} , as discussed in Section 3.2.1. The gain A of the preamplifier is in general determined by the relation between the feedback and input resistances. In this case, however, capacities are used because coupling impedances behave as $X_C = 1/2\pi fC$. The gain of the amplifier in figure 3.4 is then [98]

$$A = \frac{C_{d1} + C_{d2} + C_f}{C_f} \quad (3.3)$$

where C_d is the capacity of one detector. The amplification of the preamplifier is thus determined by the feedback capacitor C_f (Equation 3.3). However, a much higher gain A is required for the preamplifier as in this example here. High gain can be achieved by reducing the coupling capacitor C_f further. The output voltage V_o of the preamplifier is then given by [98]

$$V_o = \frac{q}{C_f} \quad (3.4)$$

where q is the charge generated by incoming alpha particles, with $q = E_\alpha/E_{ehp} e$, as in Equation 3.2. So for example a $1 MeV$ alpha particle generates approximately a charge of $44 fC$ which results with Equation 3.4 in an output amplitude of about $22 mV$, when $C_f = 2 pF$. Thus the closed-loop amplification is in the order of $A \approx 500$, which is used for the radon exposimeter not featuring spectrum acquisition. For the combined radon/thoron exposimeter, allowing for spectrum analysis, a $C_f = 6 pF$ was chosen, resulting in a preamplifier output voltage range of $7 - 70 mV$ for an energy range of $1 - 10 MeV$.

Shaper

In order to prevent pile-ups from successive signals and improve the signal-to-noise ratio (SNR), a RLC shaping unit is employed, transforming the signal to semi-Gaussian shape. This kind of filter is used in most read out systems dealing with spectral measurements, because it provides an voltage pulse which response is proportional to the incident particle energy [86]. The serial RLC circuit is designed to work near the critically damped response where the signal decay time is at the minimum while at the same time avoiding oscillations. The damping constant ξ is given by [201]

$$\xi = \frac{R_1}{2} \sqrt{\frac{C}{L_1}} \quad (3.5)$$

In the current design Equation 3.5 results in $\xi \approx 0.83$, with $R_1 = 523 \Omega$, $L = 1 mH$ and $C = 10 nF$. As final step in the shaping circuit an inductance with $L_2 = 4.7 mH$,

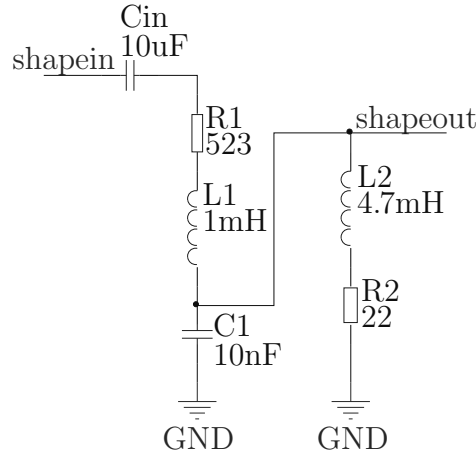


Figure 3.4: Schematic drawing of pulse shaper stage.

for shorting low frequencies signals to ground, and a resistor $R_2 = 22 \Omega$ for pole-zero cancellation is employed, which is crucial to ensure correct voltage amplitude of successive signals [77]. The resulting signal shape has a full-width-half-maximum (FWHM) pulse width of about $14 \mu s$ and an output voltage range of $4.3 - 43 mV$ for $1 - 10 MeV$. As this signal is still too small to be measured accurately a final amplification stage is needed.

Main-amplifier

The last closed-loop amplification stage is also built from discrete FET cascades and boosts the signal to its final output voltage range of approximately $70 - 700 mV$ for energies of $1 - 10 MeV$, respectively. Typically the noise has an amplitude of about $\pm 5 mV$ from the baseline output of the amplification system, thus the signal-to-noise ratio is in the domain of about $SNR \approx 70/5 = 14$, and thus deemed acceptable. The linearity of the whole system has been checked via the pulser method, which electronically induces voltage drops at the detectors as calculated in Equation 3.2. A linear regression of one of the obtained output voltage amplitudes with respect to the input energy in MeV of one particular device yields a slope of $73.0 mV MeV^{-1}$ with a coefficient of determination of $R^2 = 0.999887$. The final gain of the whole system is determined by the distribution of absolute values of the used components. In order to ensure best reproducibility, each component is chosen, if possible, to have a 1% tolerance and small thermal dependence, for example capacitors should have NP0 classification. This means, however, that each device needs to be individually calibrated for its energy dependence.

The total current consumption of the amplifier system is approximately $375 \mu A$ in idle state.

3.2.4 Comparator

In order to detect signals above a certain energy threshold, a comparator in a Schmitt-trigger setup, as depicted in Figure 3.5, is employed. For this circuit the integrated comparator in the microprocessor is used, thus allowing the digital detection of an impulse via interrupts. The trigger uses the inverting mode [56], allowing for two voltage thresholds V_{low} and V_{high} at which the comparator output will be switched from high to low and vice versa. The corresponding threshold voltages are calculated via:

$$V_{low} = V_{CC} \times \frac{R_1}{(R_1^{-1} + R_2^{-1})^{-1} + R_2} \quad (3.6)$$

$$V_{high} = V_{CC} \times \frac{(R_2^{-1} + R_3^{-1})^{-1}}{(R_2^{-1} + R_3^{-1})^{-1} + R_1} \quad (3.7)$$

For the resistor values given in Figure 3.5 the detector will switch its output $CAOUT$ to 0 V at $V_{low} = 72 \text{ mV}$ calculated with Equation 3.6, and to 3.3 V at $V_{high} = 32 \text{ mV}$ as by Equation 3.7. Hence there is a 40 mV hysteresis between the two switching limits thus avoiding possible oscillations at the thresholds. V_{low} was chosen such that the energy threshold for alpha particles is about 1 MeV. These thresholds are however not equal for every device, as the reference voltage is not the same due to differences in resistors. Additionally there exists an input offset voltage which is different for every comparator. The offset voltage is comparable to a voltage source applied in series with one input of an ideal comparator, hence changing the voltage at which the comparators toggles its state. For the used internal comparator this offset can reach up to 30 mV with a response time to switch from high to low of 2.2 μs [175]. This means that for all devices the threshold voltage will be in the domain from 40 – 100 mV. To solve this issue a software threshold is implemented, depending on each device's individual energy calibration, allowing for an exact energy threshold.

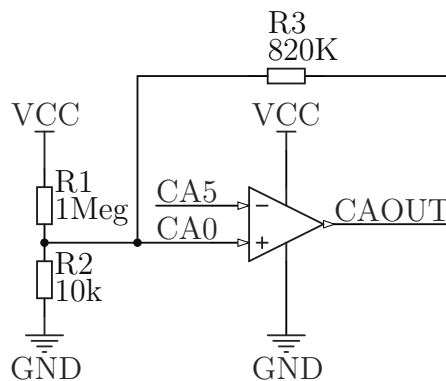


Figure 3.5: Schematic of Schmitt-trigger circuit with microcontroller pin designators.

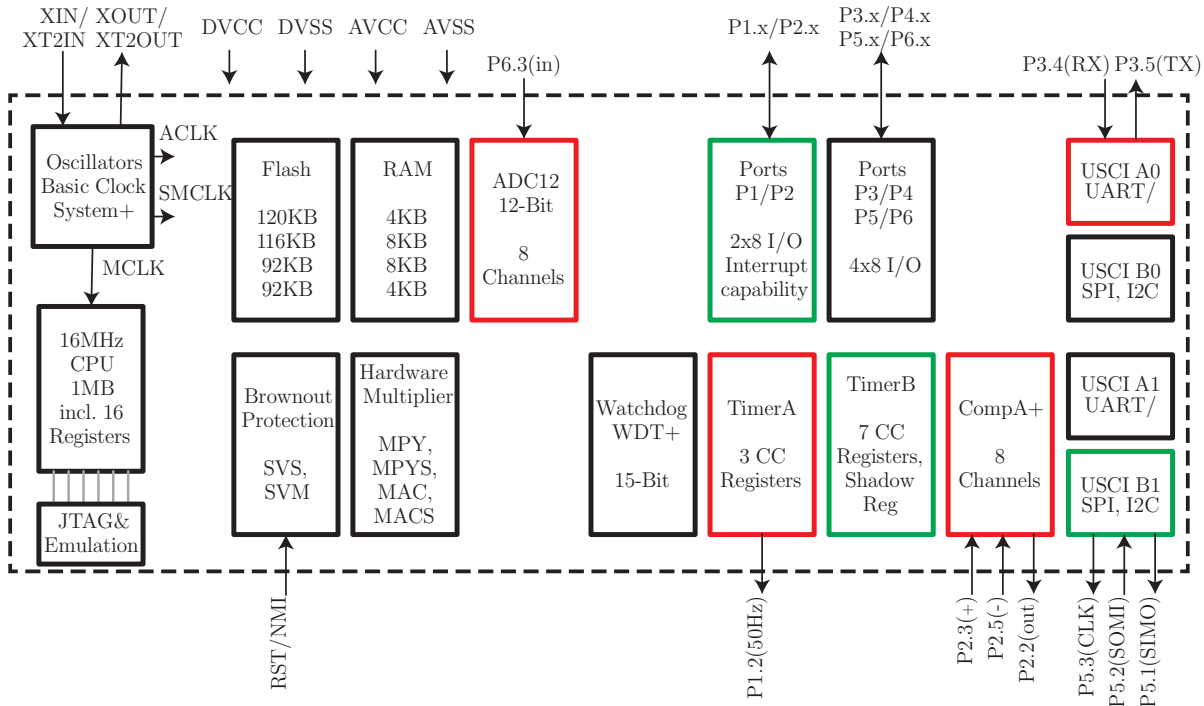


Figure 3.6: Functional block diagram with pin assignment of most important components (red) and optional future features (green), adapted from [175].

3.2.5 Micro controller

As new micro controller unit (MCU) a MSP430 F2419 was utilized. This MCU has several advantages compared to the previously used PIC16F88 MCU as it offers a 16-bit reduced instruction set computing (RISC) architecture with 16 MHz clock frequency, 12-bit analog-to-digital converter (ADC), 4 kB of random access memory (RAM) and 120 kB of flash memory. It features low power modes that require only a minimum current in the range of $10 \mu A$ for data retention. However, due to the non-deterministic source of the signal, the ADC reference voltage has to be switched on all the time requiring a relative huge steady input current, typically in the order of $0.5 mA$. Further it features several high precision timers which can be used for delayed coincidence measurements. Data transfer is bidirectional, using universal asynchronous receiver/transmitter (UART) protocol with a universal serial bus (USB) converter at speeds of $115 kbaud$. Measurement interval and start can be set via a PC, acquired data is not lost in case of power failure. The total current consumption of the chip and its dependencies is approximately $545 \mu A$ in idle state.

Block diagram

The Texas Instruments MSP430 micro controller (MCU) family offers regular features such as programmable input/output (I/O) ports, an ADC, real-time clocks, communication in-

interfaces and, for software development, a background debugger plus embedded emulator. With respect to comparable processors on the market it is very power and resource efficient[174]. In Figure 3.6 the units functionality is depicted. In the following only the essential features of the exposimeter are described [176]:

- System Clocks (CLK): Main system clock (MCLK) - runs at 16 *MHz*, equals the frequency of the central processing unit (CPU)
Sub system clock (SMCLK) - runs at 2 *MHz*, used to drive TimerB for microsecond timing
Auxilliary clock (ACLK) - external low speed clock with 32.768 *kHz* needed for low power modes
- Flash/Ram Memory to store program, acquired data and variables
- ADC12 Successive-approximation-register (SAR) analog-to-digital converter - acquires voltage amplitude, 12-bit and more than 200k-samples-per-second
- COMPA+ Internal comparator - used in Schmitt-trigger setup as described in Section 3.2.4 - interrupt starts ADC acquisition
- TimerA Timer - used for generation of time base (register CCR0) and voltage (Section 3.2.1, register CCR1), ACLK source clock with 1/8 divider, i.e. 4096 *Hz*
- USCI A0 Universal serial communication interface (USCI) module - for support of serial bidirectional communication, SMCLK clock, speed 115.2 kbps, interrupt for command reception

With these modules the basic functionality of the device is secured. Additional features have also been implemented in the final prototype, which are not yet fully supported. This includes support for a display, a SD card slot for increased memory storage and user input by push-buttons. The modules indicated by green frames in Figure 3.6 are:

- TimerB Timer - used for generation of microsecond delays, SMCLK source clock with 1/4 divider, i.e. 500 *kHz*, integrated in driver to address display
- USCI B1 USCImodule in serial peripheral interface (SPI) mode - SMCLK clock, speed 256 kbps, addresses display and memory card
- Ports P1/P2 Digital I/O ports - interrupt for user event capture on button push

Program

The main program is a buffered interrupt-driven state-machine. This is a common design pattern for multiple producer and single consumer tasks. The multiple producers here are the different interrupts feeding the main program with information such as the comparator interrupt starting the sampling of the signal or the timer for the generation of the time base. The states are stored in a ring buffer which allows for parallel feeding while the main program can process the different events in series. In this way no event is missed as

long as generation of new states is below execution time of the main program. The main loop executes all states before returning to idle state again. The most important states are:

- Idle When the queue is empty the program adds an idle state which sets the MCU into low power mode 3 (LPM3), and enables the comparator interrupt if a measurement is running
- Event Is executed when the terminal character (“;”) on the serial line (RX) is received; compares the received ASCII string with the available commands, such as start/stop or transfer data, used for communication with the device
- ADC Is executed after a pulse was sampled, checks if the event happened in the coincidence time window, and invokes state for storing
- Store Saves data to flash with two available memory banks, FLASH1 starts at address 0x4100 with a length of 48639 bytes, and FLASH2 at 0x10000 with a length of 65536 bytes, thus allowing a total number of 57087 16-bit integers to store
- Transmit Reads the stored data from FLASH and sends it in ASCII code to the PC via TX line
- InitFlash Erases flash memory banks used for data storage

This means that the MCU is most of the time in idle state thus requiring only a small amount of power to generate the ADC reference voltage of 1.5 V (typical requiring 0.5 mA). This consumption can be even further reduced by using an external reference. To wake up from LPM3 and continue the main loop takes approximately 1 μ s. In case the flash is full the program stops acquisition. Further when there is a power loss during the measurement and a new battery is inserted the program won’t start measuring but the user has to send the command externally thus ensuring data persistence for readout.

Analog to Digital conversion

The 12-bit successive-approximation-register ADC uses a 5 MHz source clock (ADC12OSC). When the enable conversion (ENC) bit is set an acquisition takes place which requires at least 4 cycles to sample and hold the input signal and then 13 cycles to convert the voltage to a bit sequence [176]. This means at this clock speed the minimum time for one conversion is 3.4 μ s. Measurements showed that when the pulse is sampled 4 times by the ADC the sampling interval is approximately 3.6 μ s. The slightly bigger interval time is caused by an additional synchronizing time between sampling and conversion. The resulting acquired number is proportional to the pulse area, and therefore to the incident α -particle energy. The ADC uses its internal 1.5 V reference voltage, resulting in a voltage resolution of 0.4 mV per channel which corresponds to an energy of 6 keV per channel. But as the whole system is subjected to noise, the measured energy resolution, which is the FWHM of the acquired Gaussian peaks during pulser calibration, corresponds to $\Delta E \approx 100$ keV.

3.3 SPICE simulation

In order to predict the behavior of the electronic design in detail with changing components a simulation program with integrated circuit emphasis (SPICE) was employed. SPICE is generally used when analog circuits are to be developed. It relies on Kirchhoff rules, differential and integral equations describing the components, and discrete models to calculate the transfer function of a specific circuit. The different analysis options like direct current, alternating current, transient, noise and Monte-Carlo simulation allow to evaluate the design with respect to power consumption, frequency response, parasitic effects, temperature dependence and component tolerance boundaries [83]. The result of the simulation crucially depends on the validity of the models used for capacitors, resistors, diodes and JFETS. Therefore, special attention was paid to the JFET model in SPICE.

3.3.1 JFET signal model

In general a single field effect transistor has 3 contacts denoted as source, gate and drain. For the n-channel-FET used in the present design two voltages applied to this connections are important. The gate-source voltage V_{GS} , which determines the working point of the JFET, the drain-source voltage V_{DS} regulating the drain current I_D , and the threshold voltage V_{Th} , where a drain current can only flow if $V_{Th} < V_{GS}$. Its output characteristic is described by a $V - I$ curve which can be separated into three regions:

- $V_{GS} > V_{Th}$ Cutoff region: the conduction channels is depleted, no current flows $I_D = 0$
- $V_{GS} \geq V_{Th}, 0 \leq V_{DS} \leq V_{GS} - V_{Th}$ Ohmic region: linear dependence of I_D on the drain-source voltage V_{DS}
- $V_{GS} \geq V_{Th}, V_{DS} \geq V_{GS} - V_{Th}$ Saturation region: almost constant current flow I_D even with increasing V_{DS}

The corresponding formulas for this regions are [177]:

$$I_D = \begin{cases} 0 & \text{Cutoff region,} & (3.8a) \\ \beta V_{DS} (V_{GS} - V_{Th} - \frac{V_{DS}}{2})(1 + \frac{V_{DS}}{V_A}) & \text{Ohmic region,} & (3.8b) \\ \frac{\beta}{2} (V_{GS} - V_{Th})^2 (1 + \frac{V_{DS}}{V_A}) & \text{Saturation region.} & (3.8c) \end{cases}$$

where β is the transconductance and V_A the so called Early voltage which is the inverse of the channel length modulation parameter $\lambda = V_A^{-1}$. Normally V_{GS} is chosen such that the working point of a JFET amplifier lies in the saturation mode and I_D is then described by the small signal model via linearization of Equation 3.8c [177].

3.3.2 SPICE parameters

In order to simulate the amplifier circuit, the parameters as described in Section 3.3.1 have to be known for the mathematical model. Some parameters can be read directly from the data sheet [124] while others are found via parameter extraction [54, 95, 177]. The Early Voltage V_A is identified via a linear fit of the saturation current I_{DS} versus V_{DS} for several output characteristic curves, i.e. for different gate-source voltages V_{GS} applied. The acquired lines intersect approximately all in one point. With λ known one can fit the V-I curves with Equation 3.8c to find β . The obtained parameters for the JFET in the simulation model were:

Table 3.3: JFET SPICE parameters

Parameter	Description	Value	Unit
β	transconductance coefficient	30.6 ± 0.6	$mA V^{-2}$
β_{TCE}	β exponential temperature coefficient	-0.5	$^{\circ}C^{-1}$
λ	channel-length modulation	27.3 ± 0.4	kV^{-1}
V_{Th}	threshold voltage	-0.6	V
V_{ThTC}	V_{Th} temperature coefficient	-2.5	$mV ^{\circ}C^{-1}$
I_S	gate p-n saturation current	114.5	fA
I_{SR}	recombination parameter	1.091	pA
α	ionization coefficient	1.0	MV^{-1}
C_{GD}	zero-bias gate-drain capacitance	7.3485	pF
C_{GS}	zero-bias gate-source capacitance	7.0000	pF

Other parameters not set in the model take the default value in the corresponding SPICE implementation. However, with the values stated in Table 3.3, it is possible to simulate the static and dynamic behavior of the circuit.

3.3.3 Amplification stage output

The analog circuit, including preamplifier, shaper and main-amplifier, has been implemented in OrCAD Capture, an electronic design software using a PSPICE kernel. In Figure 3.7 the result of a simulation and a measurement of the actual output is drawn. The measurement was obtained using the shaper circuit design of the previously developed exposimeter prototype [78] demonstrating a good agreement of shape and amplitude between simulated and real signal. This validates the parameters stated in Table 3.3. Note however, that the precise amplitude agreement of the signals might be pure coincidence, since the total gain of the system is very dependent on the tolerances of the used components. Monte-Carlo simulations performed in the present work with OrCAD Capture, using a Gaussian distribution for varying component values, have shown that even with the optimistic assumption of a 1% tolerance for all components, (note that the inductors have a 20% tolerance) an amplitude range of 68.3 – 81.8 mV is to be expected, which means at least a 16% relative deviation. Figure 3.8 shows the amplitude output range in dependence

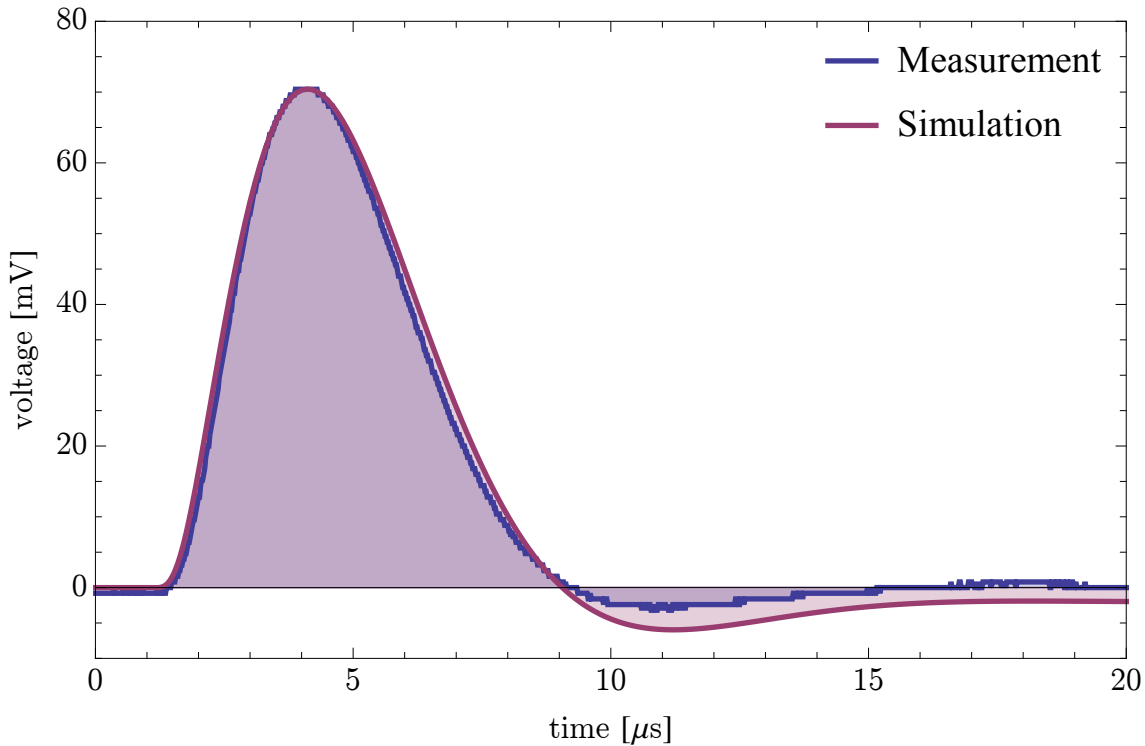


Figure 3.7: Comparison of simulated and measured voltage output of amplifier.

on the tolerance of the coupling capacitance and resistor of the preamplifier (Figure 3.4), while all other components have ideal behavior (0% tolerance). The maximum voltage of the whole amplification stage output is about 901 mV , thus for the desired energy range the maximum output has to stay below this threshold. In this example a signal corresponding to a 10 MeV alpha particle is simulated and the spread between minimum and maximum output amplitude is indicated by the error bars. Figure 3.8 demonstrates that at least a 2% component tolerance is necessary as otherwise the signal of high energy alphas could be truncated since the amplification stage might be in saturation. The mean value of the amplitude of $744.7 \pm 2.7\text{ mV}$ hardly changes as expected for Gaussian tolerance distribution.

An even higher uncertainty applies to the FWHM pulse width in the range of $11.4\text{--}16.2\ \mu\text{s}$, which is a 30% deviation, due to the large tolerances of the inductors. On the other hand temperature variations between $-50\text{ to }50\text{ }^\circ\text{C}$ have no significant influence on the output, less than 1% on the final amplitude, as the temperature coefficients for the components are in the parts per million (ppm) domain. However, due to these effects it is of importance to select only high quality components for this crucial part of the device.

The simulation tool was then utilized to adapt the shaper, to deliver a longer output signal, because the one depicted in Figure 3.7 cannot be sampled by the ADC due to its shortness (see section 3.2.5) with an approximate FWHM of $4\ \mu\text{s}$. In order to simulate the charge deposited by alphas in the detectors a voltage divider followed by a capacitor of 10 pF is

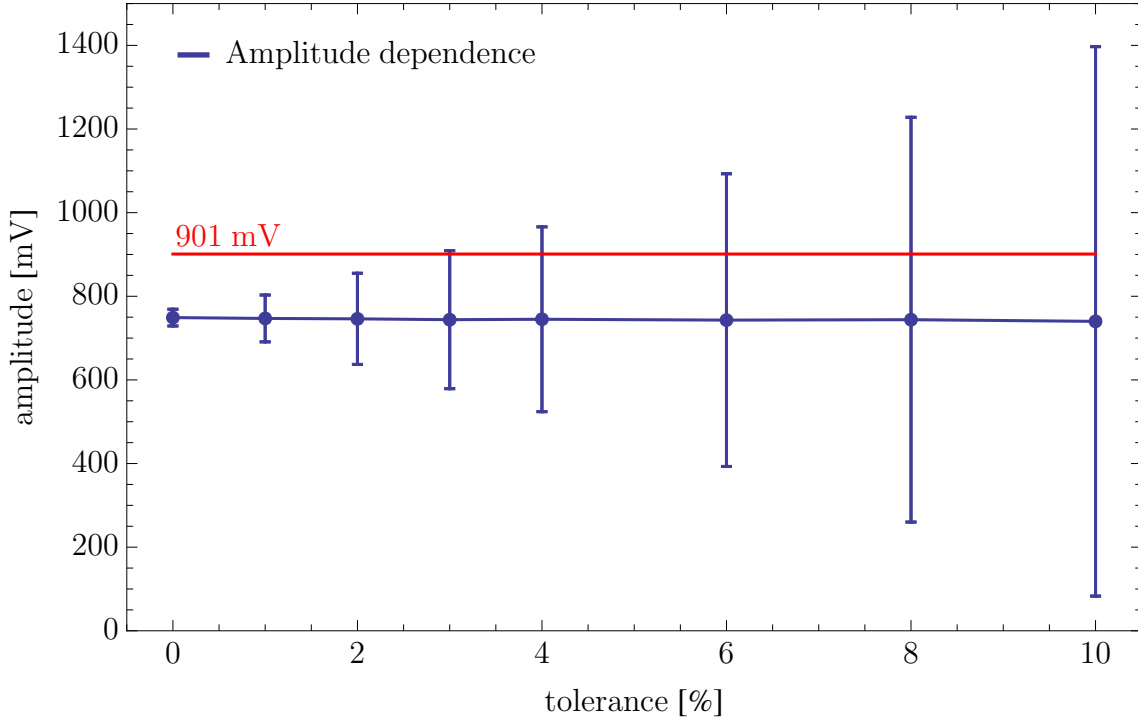


Figure 3.8: Dependence of amplifier output amplitude, for a signal corresponding to a 10 MeV alpha, on tolerance of coupling components. Threshold (red) should not be exceeded.

applied. As the approximate charge generated by a 1 MeV alpha particle is approximately $\Delta Q = 44 \text{ fC}$ according to Equation 3.2, a voltage change of $\Delta U = 4.4 \text{ mV}$ is required for the given capacitor. Hence the resistors were chosen to have $100 \text{ k}\Omega$ and $22.4 \text{ k}\Omega$, to induce a ΔQ proportional to a rectangular pulse signal. This so called attenuator is also employed in the pulser energy resolution measurement and produces charges at the detectors which correspond to alpha particle energies between 1 – 10 MeV for voltages of 1 – 10 V, not taking into account energy absorption effects before the depletion region. In the SPICE simulation the rectangular pulse generating the signal, had an voltage amplitude of -1 V , which corresponds to an 1 MeV alpha particle, and a rise/fall time of $1.0 \mu\text{s}$, because shorter times caused convergence problems in the transient analysis simulation. In Figure 3.9 the result for the different stages of the whole amplifier system are shown. It is not possible to measure the preamplifier and shaper output because a probe distorts the electronic signal. The first voltage pulse starts after a delay of $1 \mu\text{s}$, the second after $51 \mu\text{s}$, where the input voltage at the preamplifier (green line) is just too small to recognize as it only had a maximum amplitude of $40 \mu\text{V}$. For the preamplifier output one recognizes the expected pile up for successive events, which are of no concern after passing the shaper. This means that the system can handle successive signals with a minimum time difference of $50 \mu\text{s}$.

Hence the overall timing behavior of the amplifier system is the limiting factor, since the

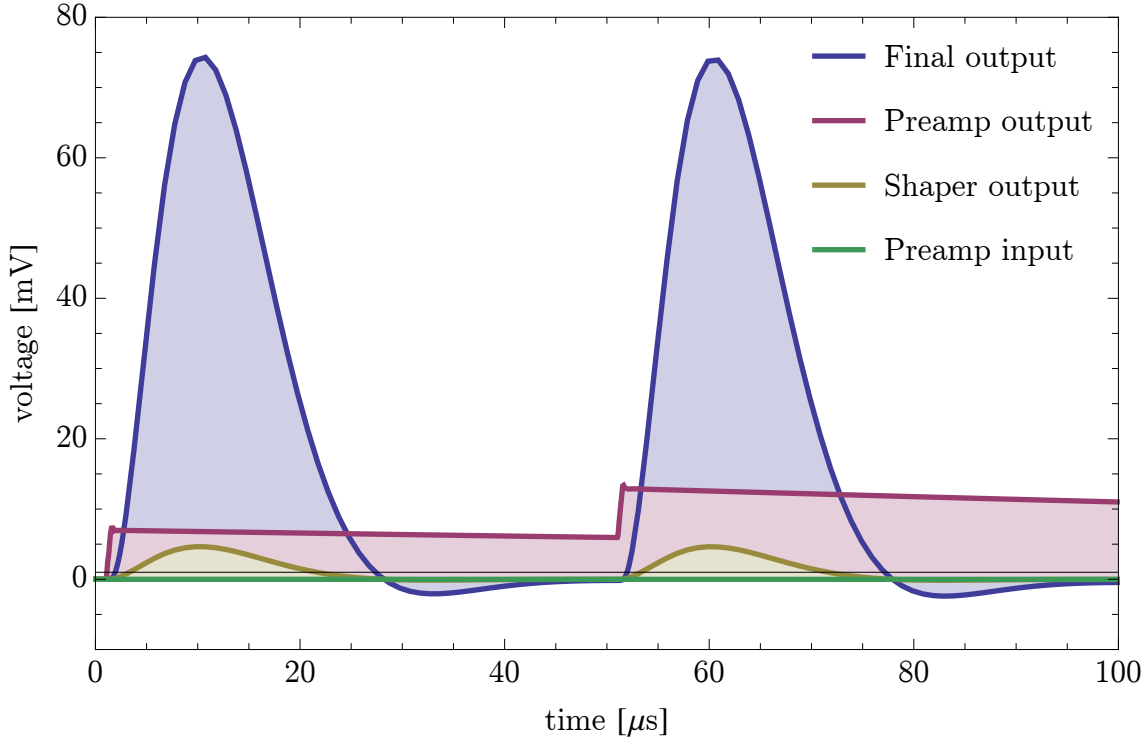


Figure 3.9: Simulated signals for preamplifier, shaper and final output, corresponding to an input signal of an 1 MeV alpha particle.

maximum charge collection time $t = d^2 / \mu V$ [162], where d is the depletion layer thickness (100 μm), μ the hole mobility at 300 K room temperature ($473 \text{ cm}^2 \text{ V}^{-1} \text{ s}^{-1}$) [60] and V the reverse bias voltage (9 V), is with approximately 24 ns a 1000 times faster for the slowest carrier than the pile-up limitation. For electrons the collection time is about 9 ns , due to their higher mobility. As the charge carrier life-time of the material is not known, it could be possible that some of the induced electron-hole pairs recombine before reaching the contacts. However due to the small collection time in the ns domain the impact on the variation of the collected charge and thus the output amplitude can be considered negligible since the energy resolution is mainly determined by the amplifier system.

The frequency with which signals may be detected is thus not limited by the detector. With the given RC time constant of 100 μs the system stability can only be obtained when the capacitor has enough time to recharge after each signal, i.e. at least 600 μs . This means the maximum frequency of a constant signal generated by a source would be 277 Hz . This still allows for either radon or thoron concentrations to rise beyond 10 $MBq \text{ m}^{-3}$ before an electrical constraint would occur.

The measurement of the output signal with an adapted circuit yielded an amplitude of 64.4 mV with an FWHM pulse width of 13.1 μs . Comparing this to the simulation with 74.4 mV and 13.1 μs FWHM pulse width shows again very good agreement within the error boundaries for the voltage amplitude of at least 13% and pulse width of 30%.

3.4 Setup

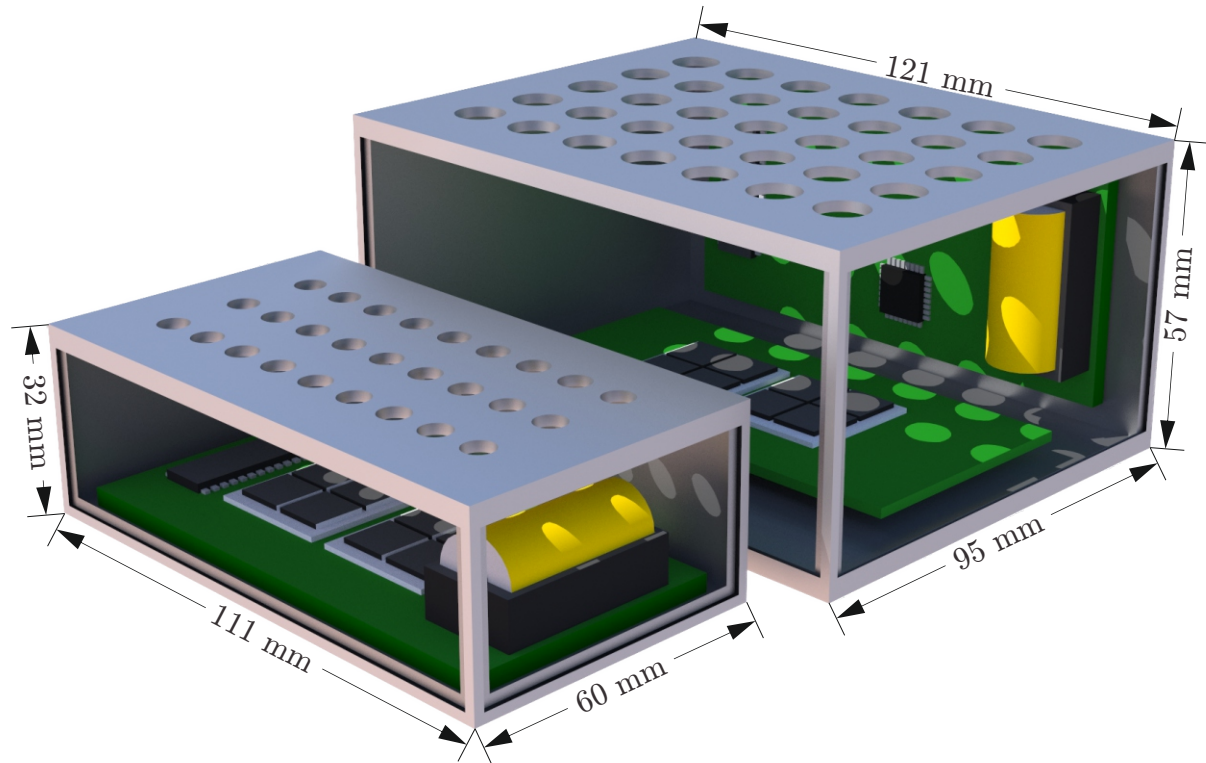


Figure 3.10: Rendered CAD drawing of both geometries showing size and PCB position differences. In final setup the side walls are complete, and the top inlets are covered with a filter.

The geometry of the diffusion chamber influences the calibration factor of the device and the shape of the acquired spectrum. Both is discussed in chapter 5. For experimental purposes two casing geometries, as depicted in Figure 3.10, have been realized.

3.4.1 Geometry 1, small exposimeter

This is the original geometry for radon gas measurements [79]. The two detectors and all electronic components are placed on the same printed circuit board (PCB). The board is fixed on the cover of a casing (Hammond Electronics 27134PSLA, length: 11.1 cm; width: 6.0 cm; height: 3.2 cm), which is made of aluminum to shield the electronics and ensure electromagnetic compatibility (EMC). In the cover 6 holes with 4 mm diameter were drilled, and in between the cover plate and the fixed PCB an electro-conductive sponge was compressed for filtration. The conductive material also ensures that no surface charges are generated on the walls thus allowing for a homogeneous collection efficiency for radon decay products [194].

For the measurements in a mixed radon/thoron atmosphere, the dimensions were the

same, but instead of diffusion holes in the cover plate, the top plate of the casing itself was perforated, see Figure 3.10. In this setup the detectors directly faced the inlets, to minimize the diffusion path between inlet and detection area.

3.4.2 Geometry 2, large exposimeter

In the second setup for parallel radon/thoron gas concentration measurements, the analog and digital part are assembled on different PCBs, which are fixed within a bigger aluminum casing (Hammond Electronics 26908PSLA, length: 12.1 cm; width: 9.5 cm; height: 5.7 cm), as shown in Figure 3.10. Setup one can be easily carried on a person, while setup two is for on-site measurements only at the time being.

Chapter 4

Calibration

Metrology relies on standards that define a relationship between a unit of measurement and a physical quantity [125]. There are three different quality levels known as primary, secondary and reference calibration standard. The primary calibration standard should have long-term stability, sufficient accuracy and should allow transfer of calibration to other measuring instruments [193]. The latter is then called secondary standard, i.e. it is a device or method calibrated against the national primary standard and thus a very close approximation to that. A so called working standard is a device, generally commercially available, which has a traceable relationship to secondary and primary standards. It is normally routinely used to calibrate or check measures. Finally, the reference standard is referred to as having the highest metrological quality available at a certain location or organization [14].

For the generation of radon reference atmospheres, two different primary methods have been developed. One is the radon-in-air activity standard [132, 32] which allows absolute activity measurements for example by counting alpha particles emitted from condensed ^{222}Rn at a defined solid angle. In this method the radon gas activity concentration in the reference atmosphere decreases due to radioactive decay. The second uses an emanation source which allows for a constant reference atmosphere after a build-up period [101]. In this case the traceability of the activity concentration is given by the radium source activity, the emanation coefficient and the reference volume. This method also allows to generate low-level constant activity concentrations down to 150 Bq m^{-3} . For thoron only recently a primary standard based on emanation sources has been established [149]. Gas activity standards are not feasible here as no reasonable thoron activity can be produced with such. Apart from gas standards it is often required to produce reference atmospheres for radon progeny with the control of temperature, humidity, air pressure and aerosol size distribution [128, 148]. This enables traceable calibrations of devices measuring radon, thoron and all of their progenies, when environmental parameters and the respective radon gas and progeny activity concentration are monitored. Such systems also allow to investigate the behavior of the equilibrium factor F and the attached fraction f_p . It is controlled via the aerosol size distribution [97], and when particle density is low also F is low while f_p is high. This is of course natural as with clean air less progeny can attach to aerosols while also

there is an increased plate-out rate of unattached progenies to chamber walls (no equilibrium reached). The effect is vice versa for high aerosol concentrations ($F \rightarrow 1, f_p \rightarrow 0$) [128].

In 1999 the mutual recognition arrangement (MRA) was introduced to allow for international comparisons of national metrology institutes and calibration laboratories [87]. As the standard atmosphere for radon cannot be transported, typically a transfer standard is employed [147], which is usually a secondary standard. In an European inter-comparison the transfer device was an ionization chamber based monitor, which is commercially available (Saphymo AlphaGuard) [150]. In this study twelve institutes participated using standard calibration procedures with three different activity concentrations (1, 3 and 10 $kBq m^{-3}$). All results were consistent within the assigned uncertainties, demonstrating the high quality and capability of available calibration facilities. Also it is generally advisable for all radon monitors to participate in such comparisons to ensure that measured absolute values are correct and not biased by systematic errors [72].

4.1 Basic Principles

In this work calibrations are conducted in similar manner as described in the recently released ISO standard for radon measurements [69]. The exception is that the devices are calibrated against a reference device and not a primary standard. The two reference devices used in the present work are a Saphymo AlphaGuard, exclusively employed for radon calibrations, and a DurrIDGE Rad7 for radon and thoron calibrations. All calibrations in this work were conducted in a standard procedure applying the emanation method. The exposure meter and the radioactive source are placed within a closed vessel, and depending on the reference devices it is either placed within the same or is externally connected to it. The activity A (Bq) build up in such a vessel is then described by [119]:

$$A = \frac{E}{\lambda^*} (1 - e^{-\lambda^* t}) \quad (4.1)$$

where E is the total exhalation rate ($Bq h^{-1}$) and $\lambda^* = \lambda + \lambda_b$ is the effective decay constant which is corrected for first-order removal of radon by back diffusion and leakage denoted as λ_b . The exhalation rate per unit area E_d ($Bq m^{-2} h^{-1}$) is given by [119]:

$$\begin{aligned} E_d &= \epsilon f L \tanh(d / 2L) \\ &= I \lambda \rho \eta L \tanh(d / 2L) \end{aligned} \quad (4.2)$$

where $f = (\epsilon^{-1} \lambda I \rho \eta)$ is the radon production rate ($Bq h^{-1} m^{-3}$), ϵ and ρ the porosity and density ($kg m^{-3}$) of the material, I the specific parent concentration ($Bq kg^{-1}$) of ^{226}Ra (for radon) or ^{224}Ra (for thoron) and η the emanation coefficient. The value of η is the quotient of released ^{222}Rn from soil into air over the parent nuclide ^{226}Ra concentration, or $^{220}Rn / ^{224}Ra$ for thoron. For typical rocks and soils it ranges from about 0.05 to 0.70, with an average suggested value of 0.22 [154]. The emanation coefficient increases linearly

with increasing surface area-to-volume ratio (the specific surface).

In conclusion this means that the achievable activity concentration in a vessel depends on the characteristics of the used source (Equation 4.2), the tightness of the chamber (Equation 4.1), its volume, since $C = A/V$ with A being the activity, and the surface area A_{src} of the source, since the emanation is $E = E_d A_{src}$. Hence in a completely tight vessel with a semi-permeable source, i.e. $\lambda_b = 0$, a stable radon concentration would be reached only after about 23 days. However the less airtight the calibration chamber the faster an equilibrium between emanation of the source and loss through leakage is reached [119]. In the present work, calibration measurements were always conducted in stable gas concentration environments.

The reading of the reference device and the quantity measured by the radon monitors, which are counts per interval, a count rate, is related by the so called calibration factor cf via,

$$cf = \frac{1}{n} \sum_{i=1}^n \frac{C(t_i)}{N(t_i)} \quad (4.3)$$

with $C(t_i)$ being the gas activity concentration ($Bq\ m^{-3}$) at interval i and $N(t_i)$ the number of counts (c) recorded by the exposure meter in that time. The unit generally used for the calibration factor is then activity concentration over counts per time interval ($Bq\ m^{-3} / cph$), with cph being counts per hour. For continuous monitors an annual calibration is recommended [122]. Along with calibration at elevated radon gas concentration levels also a background measurement has to be performed for quality assurance [42], in order to acquire a reliable instrument background and check instrument operation. Background signals originate mainly from the alpha decays of ^{210}Po , a daughter nuclide of ^{210}Pb , which is accumulated within the detection chamber and on the detectors, with a half-life of 22.2 years. Due to its long half life the background signal can be seen as constant when the measurement periods are much smaller. A high background means that a device was either exposed to very high radon concentrations beforehand or that there is an electronic error present. A detailed discussion can be found in Section 4.6.3.

4.2 Calibration chamber setup

At the HMGU no accredited calibration chamber is available. For large scale calibrations normally a big steel chamber with a volume of $1\ m^3$ is used. For day-to-day measurements however, this is not very applicable, especially not for thoron, and smaller volumes are more feasible. They reach constant atmospheres faster (see Section 4.1), allow for a spatially more homogenous thoron concentration and are quicker accessible. All chambers used in the present work were made of conductive metals, in order to avoid generation of charged surfaces which could influence distribution and deposition of gas and progeny.

4.2.1 Geometry

For the calibrations performed within this thesis two chamber geometries were employed. When radon and thoron were measured, a small aluminum box with following specifications was used,

- Manufacturer: ROSE
- Type: 012333180
- Dimensions: $18\text{ cm} \times 23\text{ cm} \times 33\text{ cm}$ ($h \times w \times l$)
- Volume: 13.5 l

It features additional two fans inside the chamber, needed for thoron mixing, 3 BNC connectors for online readout of the exposure meter, 1 BNC input for voltage supply and 4 tube-connectors, which allow to attach external pumps, sources or reference devices. Also the two 80 mm fans have been replaced in some cases by a 200 mm fan at the top, to increase thoron homogeneity. For radon calibrations it is possible to employ a bigger chamber geometry, due to the long diffusion length of ^{222}Rn . For example a cylindrical steel pot is available

- Dimensions: $46\text{ cm} \times 33\text{ cm}$ ($\varnothing \times h$)
- Volume: 53.5 l

which also features 4 tube-connectors, 2 fans and a pipe network within, allowing for active thoron distribution. For radon however no active air mixing is required. Also the chamber geometries are less crucial as long as they are significantly smaller than the radon diffusion length of 2.2 m (see Table 2.3).

4.2.2 Radioactive sources

As emanation source for the generation of radon gas a uranite rock, also commonly called pitchblende, was used. A gamma-spectrometric analysis of a 0.538 g sample showed a specific ^{226}Ra activity of $23.0 \pm 0.4\text{ Bq g}^{-1}$. The emanation coefficient was not measured. As thoron source thorium containing lantern mantles have been applied. The specific ^{232}Th activity of a 29.2 g probe (10 mantles) was determined to be $47.98 \pm 0.77\text{ Bq g}^{-1}$. The stated values are not valid for all source rocks or mantles as these are subjected to natural variations. Typical values for soil containing these nuclides are 41.0 Bq kg^{-1} for ^{226}Ra and 36.0 Bq kg^{-1} for ^{232}Th [119].

4.2.3 Humidity

Humidity is controlled via saturated salt solutions using potassium carbonate (K_2CO_3). Its solubility is about 112 g per 100 ml at $20\text{ }^\circ\text{C}$. At this temperature the solution reaches a

humidity equilibrium of about 43% *RH* [44]. Thus using about 200 *g* potassium carbonate per 100 *ml* water provides a sufficiently saturated solution which keeps the humidity at a constant level during calibration measurements at realistic indoor *RH* values. Humidity control is mainly important to keep thoron emanation from lantern mantels constant.

4.3 Radon calibration

The new radon exosimeters with improved sensitivity were calibrated in a radon atmosphere in order to allow for a comparison to the previously developed devices.

4.3.1 Reference device comparison

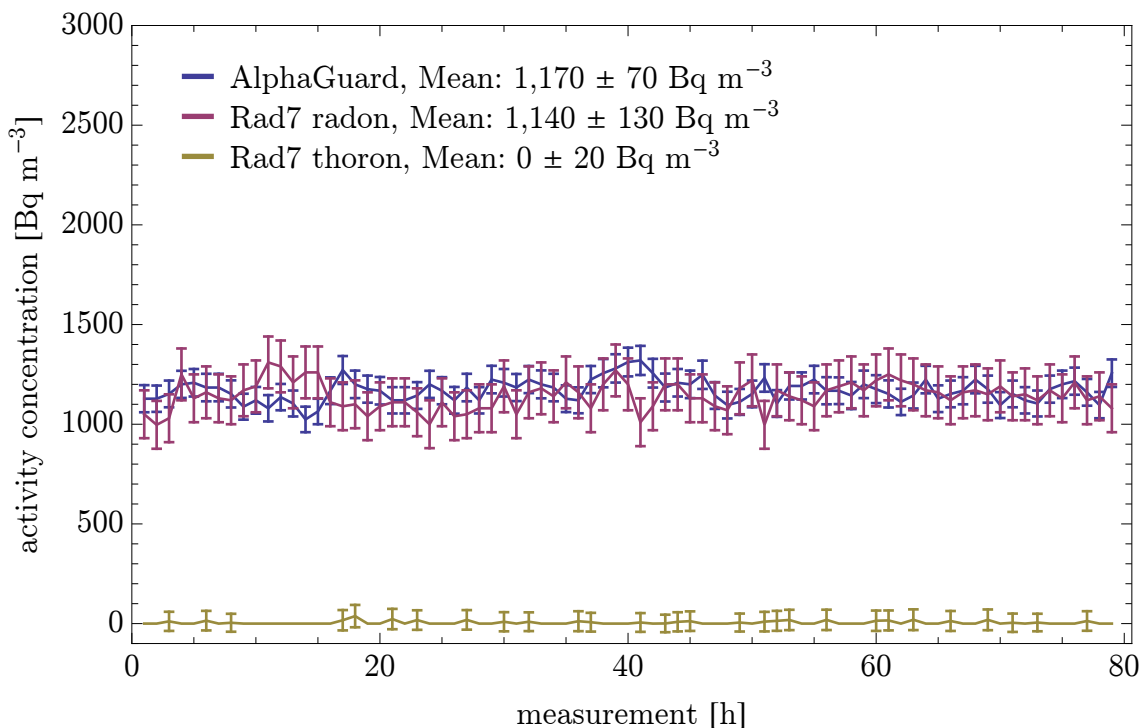


Figure 4.1: Reference device comparison, absolute radon activity concentrations determined by an AlphaGuard and a Rad7. Error bars include 1σ statistical uncertainty only.

As for previous radon calibrations an AlphaGuard was employed, which does not allow for thoron measurements, hence it had to be ensured that a Rad7 shows similar radon concentrations under equal conditions. Otherwise any calibration performed with the Rad7 as reference would not be comparable to the ones performed with the AlphaGuard. Therefore a device comparison measurement was realized in the 54 *l* steel pot with the AlphaGuard placed within the vessel, plus an additional pitchblende rock acting as radon source. The Rad7 was externally connected with tubes and its flow rate was determined to

be $650 \text{ cm}^3 \text{ min}^{-1}$, i.e. 0.65 l min^{-1} , in exact agreement with the value given in the user manual [39]. After 35 hours a stable radon concentration was reached and the comparison measurement run a total time of 79 hours after that. The mean environmental parameters during the measurement were 46% relative humidity, 21° C ambient temperature and 951.9 hPa absolute pressure. The mean radon concentration stated by the AlphaGuard was $1,170 \pm 67.8 \text{ Bq m}^{-3}$ while the Rad7 gave a value of $1,140 \pm 125 \text{ Bq m}^{-3}$, see also Figure 4.1. The relative difference between both values is thus about $2.3 \pm 1.4 \%$, where the error has been calculated via error propagation and the stated 1σ device uncertainties. As this is less than the measurement uncertainty of the AlphaGuard, which is one of the most sensitive devices available on the market, and also less than the accuracy achieved by the PTB [148], the measurement results of both devices are essentially equal. Hence no correction factor for comparison of calibration factors between the two devices has to be used. The individual acquired data is also shown in Figure 4.1, and reveals no thoron was present (yellow line). When there is no thoron measurement indicated in the graph it means that the Rad7 did give a 0 for the concentration and the error, and not that the value is missing.

4.3.2 Calibration factors

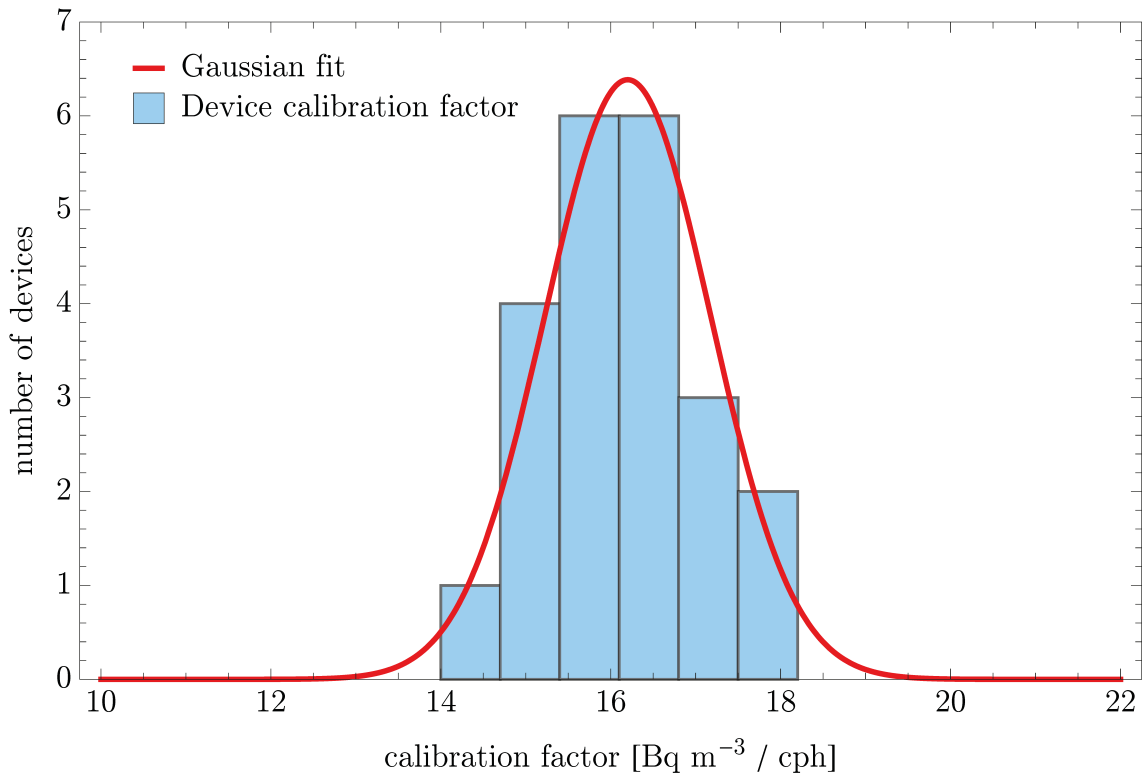


Figure 4.2: Distribution of calibration factors with bin width of 0.7 and Gaussian fit (solid line), resulting from a measurement with 22 radon monitors.

With the improved amplifier and detector layout 22 new Radon monitor prototypes in geometry 1 (standard housing) have been built. The devices have been calibrated in a high radon concentration environment (up to $2,300 \text{ Bq m}^{-3}$) within a closed vessel, using an uranite rock (see Section 4.2.2) as radon source. As reference device an AlphaGuard was used. The measurement period was 9 days and 21 hours, with environmental conditions being at 65% relative humidity, 18.1° C ambient temperature and 959.0 hPa absolute pressure. The comparator energy threshold for the devices was set to 1.8 MeV . Generally the uncertainty associated with the calibration factor of a single device is governed by the number of counts detected. In the present experiment this uncertainty was about 8.8% with a mean count rate of 128 cph . Figure 4.2 shows the distribution of the obtained calibration factors. With a mean value of $cf_{222\text{Rn}} = 16.2 \pm 0.9 \text{ Bq m}^{-3}/\text{cph}$ (mean \pm standard deviation), the calibration factor of the device, compared to the previous one of $29.9 \pm 1.4 \text{ Bq m}^{-3}/\text{cph}$, was almost doubled. All individual acquired factors are stated in Table 4.1. After the calibration also a 46 h background check was performed by opening the box and putting it in a ventilation shaft, where the mean radon concentration was determined to be $35.8 \pm 19.0 \text{ Bq m}^{-3}$. The excess counts were then calculated by subtracting the reference concentration from the one determined by the exposimeter and dividing the difference by the individual calibration factor. It yielded a mean value for the background count rate of $cr_0 = 0.29 \text{ cph}$ for the 22 new prototypes and thus background correction can be disregarded and proper functionality is proven. This was to be expected as the devices were newly assembled with unexposed detectors and cases. The background measurement can be improved by putting the devices in a calibration chamber which is flushed with pure nitrogen to reduce radon gas concentrations to zero. Figure 4.2 also demonstrates that the device can be built in a reproducible manner within a small error boundary. Hence, for a series of devices it may be sufficient to calibrate only one instead of each individual device, and to assume that the resulting calibration factor is representative for the other devices, although an individual calibration is preferred.

Table 4.1: Device calibration factors (cf) with 1σ standard deviation as uncertainty (std) for exosimeters of first ($V1xx$) and third ($V3xx$) generation in a ^{222}Rn environment.

Device (1 detector)	$cf \pm std$ $Bq\ m^{-3} / cph$	Device (2 detectors)	$cf \pm std$ $Bq\ m^{-3} / cph$
V101	29.4 ± 3.2	V306	15.3 ± 2.0
V102	29.1 ± 3.2	V309	14.4 ± 1.9
V104	29.0 ± 2.9	V310	15.2 ± 2.0
V108	29.4 ± 2.5	V311	16.1 ± 2.2
V109	29.6 ± 2.8	V312	16.9 ± 2.3
V111	28.5 ± 2.2	V313	15.4 ± 2.0
V112	28.3 ± 2.6	V314	15.7 ± 2.1
V113	29.8 ± 3.0	V315	15.5 ± 2.1
V114	28.8 ± 2.5	V317	15.3 ± 2.0
V115	29.9 ± 2.9	V318	18.1 ± 2.5
V121	30.4 ± 2.9	V319	17.8 ± 2.5
V122	32.5 ± 3.0	V320	16.2 ± 2.2
V123	33.3 ± 3.5	V321	17.4 ± 2.4
V124	31.2 ± 2.8	V322	15.6 ± 2.1
V127	29.7 ± 2.8	V323	16.5 ± 2.2
		V324	16.4 ± 2.2
		V325	17.1 ± 2.3
		V326	15.8 ± 2.1
		V327	15.6 ± 2.1
		V328	16.7 ± 2.3
		V330	16.6 ± 2.2
		V331	15.8 ± 2.1
		V301	15.6 ± 1.3
Mean:	29.9 ± 1.4		16.2 ± 0.9

4.3.3 Spectrum

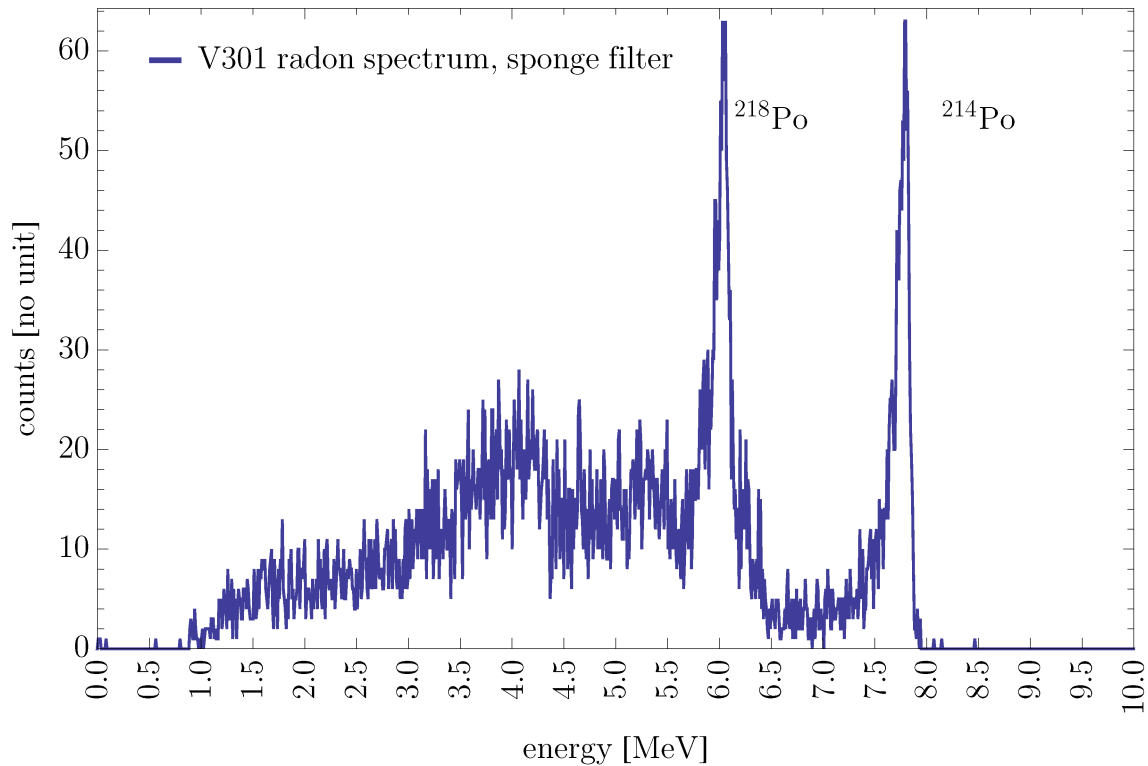


Figure 4.3: Typical alpha particle spectrum acquired in a radon environment for the small housing (geometry 1). In the summed spectrum (hours 10-50) the characteristic alpha peaks of two progeny are clearly visible.

The most significant improvement of the new devices is however the possibility to acquire additional information on each decay via alpha spectroscopy. Figure 4.3 depicts a typical energy spectrum acquired in a high radon gas environment with mean activity concentration of $3,310 \pm 250 \text{ Bq m}^{-3}$. Environmental conditions during the calibration in the small calibration were 47.6% *RH*, 19.8 °C and 968.1 *hPa*. As expected two peaks can be identified, which belong to the immediate radon daughters which decay via alpha particle emission (see also Figure 2.1). These decays measured at energies of approximately 6 and 7.8 *MeV* originate from particles deposited directly on the detector surface. This allows counting of alpha particles with smallest energy loss before entering the detectors' sensitive volume, as they only need to pass the thin aluminum coating on top of the detector of about 400 *nm*. The other signals in the spectrum are a superposition of decays registered from radon gas and progeny decomposition, originating from the volume and housing walls. The spectral form is thus influenced by the environmental conditions, as they change alpha-particle energy absorption in air, and the geometry of the device. The geometry determines the path lengths alpha particles can traverse and the fraction of detector surface to total inner housing surface, which influences the number of direct deposited progenies on the

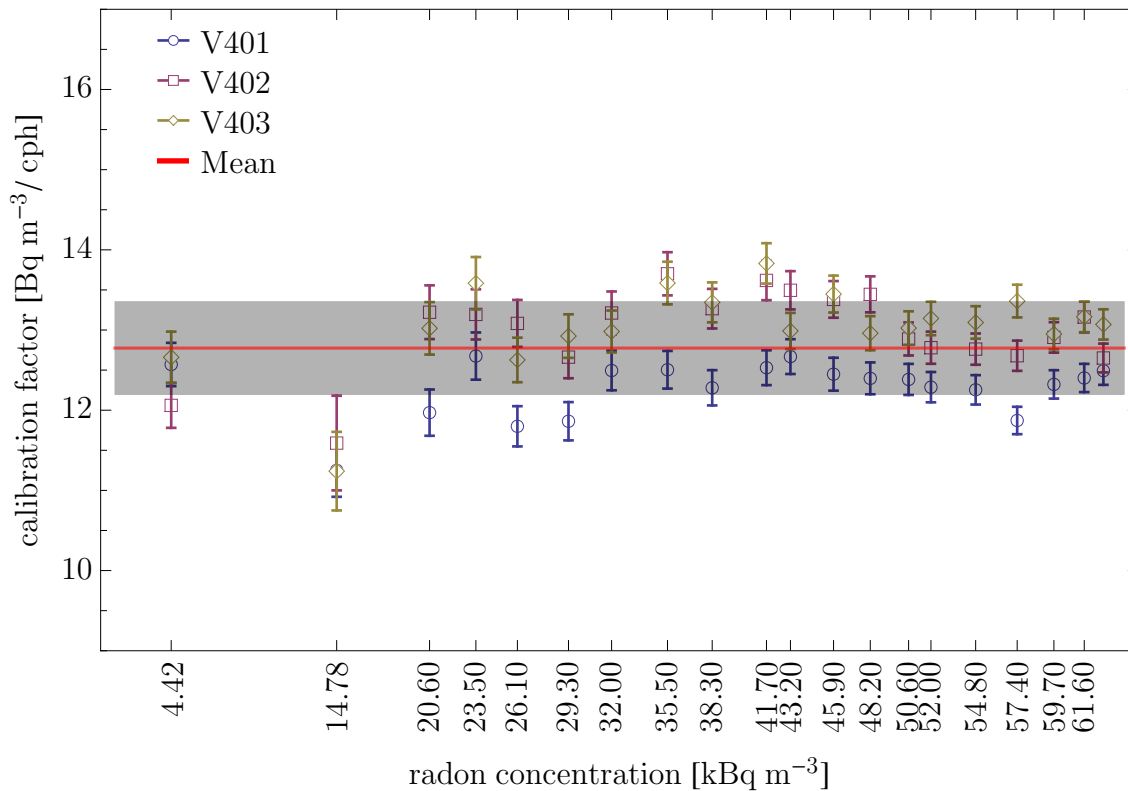


Figure 4.4: Radon calibration factors obtained by three devices for a linear increasing radon concentration. Error bars include 1σ statistical uncertainty only. The mean was found to be $12.8 \pm 0.6 \text{ Bq m}^{-3}/\text{cph}$ (red line, standard deviation as gray shade), hence a 4.5% relative standard deviation.

detector area. This is however discussed in detail in Chapter 5 by comparing measurements with simulations. The calibration factor is then found by summing all counts from $1 - 10 \text{ MeV}$ each hour and dividing the reference concentration with the found value. The resulting calibration factor for device V301 was determined to be $15.6 \pm 1.3 \text{ Bq m}^{-3}/\text{cph}$ and thus lies within the range of previous determined factors (Table 4.1) for this geometry.

4.3.4 Calibration factor concentration dependence

Another important aspect is the linear behavior of the calibration factor with increasing concentration. In order to test this 3 devices with geometry 2, denominated $V40x$, were exposed to a linear increasing radon concentration within the small calibration chamber. Concentrations varied between $20.6 - 65.4 \text{ kBq m}^{-3}$ at a mean RH of 49%, 24.5° C and 960.3 hPa . The resulting calibration factors from the high radon concentration calibration, plus two additional measurement at lower concentrations preceding those, are shown in Figure 4.4. It demonstrates that a linearity over the concentration range can be established.

The mean was found to be $12.8 \pm 0.6 \text{ Bq m}^{-3}/\text{cph}$, meaning the relative standard deviation is only about 4.5%. This independence of the calibration factor on the concentration was to be expected, since the electronic restriction, due to the setup of the amplifier, is well above 10 MBq m^{-3} (see Section 3.3.3), while the microprocessor allows to store a maximum number of 2^{16} events per time interval, which corresponds to a maximum concentration of 838 kBq m^{-3} with the stated calibration factor and hourly measurements.

4.4 Thoron calibration

While a radon calibration is straightforward and a high accuracy, less than 6% deviation, can be achieved with respect to the variation of the calibration factors, this is much less trivial for thoron. The minor variation of the radon calibration factor can be attributed to two facts, firstly the homogenous distribution of ^{222}Rn and secondly the reproducible assembly of pin-diode based monitors (see Figure 4.2). On the other hand, reason for a possible inhomogeneous thoron distribution is the short half-life of ^{220}Rn and therefore its small diffusion length L of about 3 cm (Table 2.3). This means that at a distance of 6 cm ($2 L$) from the ^{220}Rn source, only about 13.5% of the original concentration C_0 remains (Equation 2.12). Therefore active air stirring by means of ventilators or pumps has to be employed within a small calibration volume to achieve an almost homogenous distribution. Still the total uncertainty of such a system can be in the range of 10-15% where a 4.15 l reference chamber was used [115]. Measurements at the National Institute of Radiological Sciences (NIRS), within a 150 l pot with active ventilation and at 5 cm from the bottom, indicate a ^{220}Rn concentration deviation of less than 10% relative standard deviation for active sampling devices, such as the Rad7 [161]. However, calibrations performed with a passive sampling device, such as the RADUET monitor, at the same institute show a variation of the thoron calibration factor of up to 30% for the high air-exchange rate chamber type ($1,800 - 2,400 \text{ cts cm}^{-2}$) and 34% ($41 - 55 \text{ cts cm}^{-2}$) for the low air-exchange chamber type. Less variation is seen when calibrating the devices in a radon atmosphere with ranges of 24% ($3,900 - 5,100 \text{ cts cm}^{-2}$) and 20% ($4,400 - 5,500 \text{ cts cm}^{-2}$) for the corresponding chamber type respectively [183]. Intercomparison measurements with the RADUET monitor at the PTB facility yielded discrepancies of more than 50% [161]. Therefore special attention to the thoron distribution during calibrations has to be paid.

4.4.1 Quality assurance

To determine the calibration factor for thoron, over 25 measurements have been performed by 3 devices assembled in geometry 2 (Section 3.4.2), the large housing. Each thoron calibration was performed in the small calibration chamber, with thorium mantles acting as source and emanation control via humidity regulation. The reference device in all cases was the externally connected Rad7 with consistent setup and without the use of a drying tube, as a constant humidity level within the chamber is required.

The ^{220}Rn levels determined by the Rad7 have to be corrected depending on the setup,

h

Table 4.2: Mean thoron calibration measurement conditions

Test ¹	Fans	²²⁰ Rn Concentration <i>Bq m⁻³</i>	Humidity <i>RH</i>	Temperature <i>°C</i>	Pressure <i>hPa</i>
1	2 × 80 <i>mm</i> fans	9963 ± 421	45%	23.7	961.6
2	2 × 80 <i>mm</i> fans	10734 ± 436	47%	23.0	962.0
3	2 × 80 <i>mm</i> fans	11085 ± 460,	49%	23.9	961.9
4	2 × 80 <i>mm</i> fans	5428 ± 328,	47%	24.1	953.2
5	1 × 200 <i>mm</i> fan	3339 ± 202	23%	25.5	962.4
6	1 × 200 <i>mm</i> fan	3916 ± 259	44%	24.7	961.0
7	1 × 200 <i>mm</i> fan	4075 ± 264	46%	24.0	960.6
8	1 × 200 <i>mm</i> fan	4449 ± 291	45%	23.9	961.0
9	1 × 200 <i>mm</i> fan	5561 ± 316	55%	24.3	961.1
10	1 × 200 <i>mm</i> fan	6971 ± 374	56%	25.3	956.1

¹Evaluation in the period from hours 60-85

since the volume of the connecting tubes V and the flow rate q of the device determine the loss of thoron, before it reaches the inlet of the Rad7. The activity concentration C at the inlet depends on the original thoron concentration C_0 in the chamber via Equation 4.4 [161],

$$C = C_0 e^{-\lambda V / q} \quad (4.4)$$

where λ is the decay constant of ²²⁰Rn (0.748 min^{-1}), V the sampling tube volume, which was determined from a 121 *cm* pipe length with 4 *mm* diameter to be 15.2 *cm*³, and q the flow rate of the Rad7 ($650 \text{ cm}^3 \text{ min}^{-1}$). Hence about 98.3% of the original thoron gas reaches the reference device. Since the device was calibrated at the manufacturer with a sampling volume of 50 *cm*³ [39], which leads to a higher thoron loss ($C = 0.944 C_0$), the resulting concentration values for ²²⁰Rn are overestimated and thus must be corrected by a factor $f = 1.0174/1.0559 = 0.963$. In Table 4.2 the environmental conditions during the calibration measurements are shown. Humidity and temperature were logged by the Rad7 while the absolute pressure was recorded with a *testo 511* barometer, featuring an accuracy of $\pm 3 \text{ hPa}$.

Calibration factors reproducibility

All devices under test were equipped with a sponge filter and had the same inlet area and geometry. The calibration factor for ²²⁰Rn has been calculated in equilibrium conditions, generally between hours 60 and 85, and from counts in the energy range of 1 – 10 *MeV*. In the high concentration calibration two thorium lantern mantels were employed while in the low level concentration calibration only one was used. Figure 4.5 shows the obtained values for each corresponding setup as described in Table 4.2. With a mean value of $8.4 \pm 1.6 \text{ Bq m}^{-3}/\text{cph}$ (mean $\pm 1\sigma$ standard deviation), the sensitivity of the device,

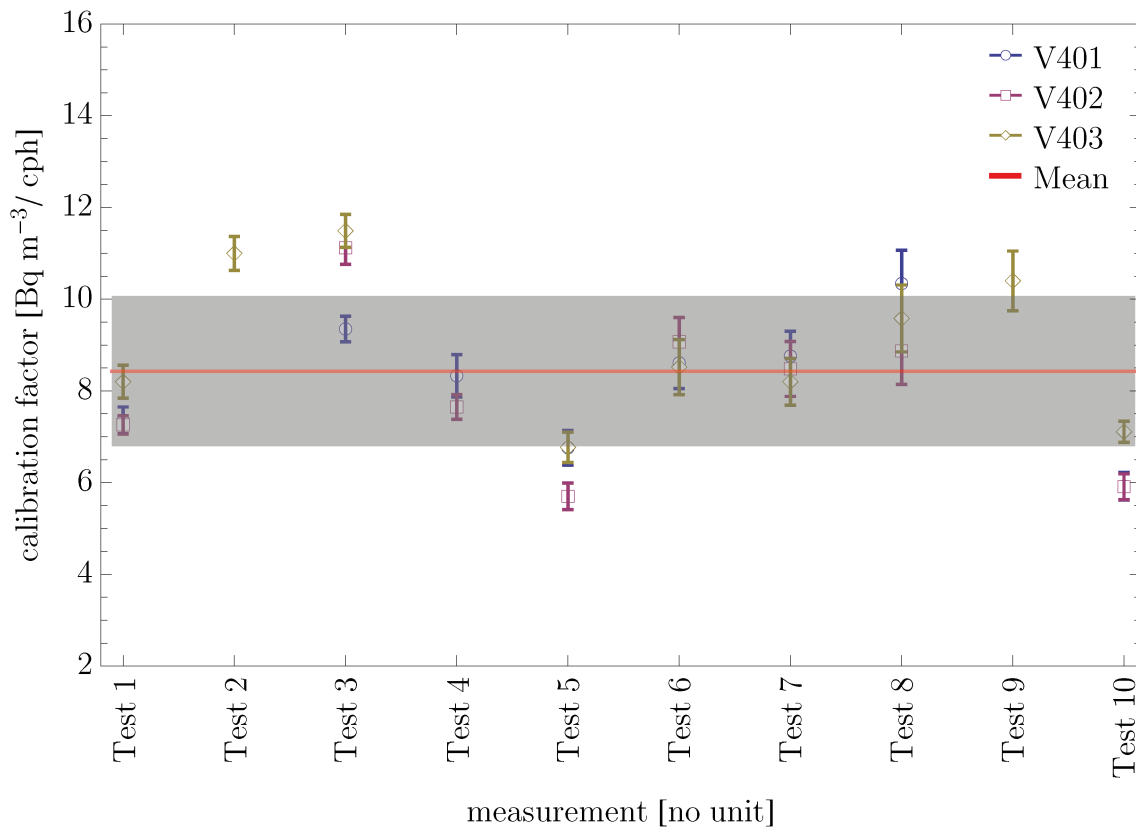


Figure 4.5: Thoron calibration factors obtained by three similar devices under varying conditions (Table 4.2). Error bars include 1σ statistical uncertainty only. The mean was found to be $8.4 \pm 1.6 \text{ Bq m}^{-3} / \text{cph}$ (red line, standard deviation as gray shade).

compared to the one for radon of $12.85 \pm 0.5 \text{ Bq m}^{-3} / \text{cph}$, is similar. A smaller calibration factor was to be expected since the alpha particle emitters of ^{220}Rn and its daughters have higher energies. Thus the energy loss before the alphas reach the detectors is overall less in comparison to the ^{222}Rn decay series. There a higher fraction of alpha particle energies is below the comparator threshold, due to energy losses by transition through air (see also Chapter 5), resulting in a reduced sensitivity.

The relative standard deviation of the calibration factor for thoron with about 17% is significantly larger than that for ^{222}Rn of about 4%. This is probably attributable to the difficulty of establishing a reproducible and homogenous ^{220}Rn distribution within the calibration chamber as described in Section 4.4. The standard deviation of the calibration factor in each setup ranges from $1.14 - 0.28 \text{ Bq m}^{-3} / \text{cph}$ with a mean of $0.59 \text{ Bq m}^{-3} / \text{cph}$ which is only about a 7% deviation. The relative difference in each calibration measurement is therefore less subject to variations compared to the repeated test under similar conditions, where one notices a maximum deviation of about a factor of two in Figure 4.5. In the low level concentration environment the mean count rate for a one hour measure-

ment was about 487 *cph* and thus the relative statistical error was about 4.5%, while the total count number was well over 10^4 , hence a statistical error of less than 1%. This means the uncertainty of the calibration factor is not governed by the statistical error here.

Thoron sensitivity of HMGU radon monitor

It has been pointed out, that passive sampling radon monitors might be sensitive to thoron exposure, thus overestimating the radon exposure [120, 181]. Until now a negligible influence of thoron on the HMGU radon monitor was assumed [78], due to the long diffusion path through the filter, that is mounted on the back of PCB where also the inlets are positioned. The thoron sensitivity of the previously developed device was investigated in the framework of a Diploma thesis [51] and revealed a calibration factor of about $cf_{220Rn} = 690 \pm 20 \text{ Bq m}^{-3}/\text{cph}$. Results, however, were inconclusive, since the calibration factor showed no dependence on the employed filter material, indicating an inhomogeneous thoron distribution in the used calibration chamber. Therefore another interference test with devices with standard dimensions (Geo1) was performed to determine the calibration factor of the radon HMGU monitor for ^{220}Rn . During the measurement in an high thoron gas environment the mean activity concentrations of $C_{220Rn} = 9,520 \pm 570 \text{ Bq m}^{-3}$ and $C_{222Rn} = 150 \pm 250 \text{ Bq m}^{-3}$ were reached. Thus approximately 9 *cph* will be attributable to radon decays. Environmental conditions during the calibration in the small calibration chamber were 52.0% *RH*, 24.5 °C and 959.0 *hPa*. Three devices with standard housing size (Geo1) were calibrated, namely V311, V315 and V305, where the last one was a newly developed combined radon/thoron monitor. Table 4.3 shows the evaluated calibration factors, where the contribution of radon to the count rate has been considered. For the calculation of the calibration factor all counts in the energy domain of 1 to 10 *MeV* have been considered for V305, while the other devices do not allow for a discrimination. While the combined monitor shows the same sensitivity for radon and thoron (similar calibration factor), the radon exposimeter is about a factor 6 to 9 less effective in detecting thoron. Therefore the sensitivity is, however, much higher than the previously determined estimate, where a ratio was found of $cf_{220Rn}/cf_{222Rn} \approx 690/30 = 23$. The results in Table 4.3 indicate a sensitivity of about 12% to 16% of the radon HMGU monitor towards thoron, in agreement with other similar devices [120, 181, 171], which show for passive ^{222}Rn devices also about a 10% thoron sensitivity. This means that at elevated ^{220}Rn activity concentration levels the sensitivity of the HMGU radon monitor to thoron, and thus the excess

Table 4.3: Calibration factors for ^{222}Rn and ^{220}Rn for radon (V311, V315) and combined radon/thoron (V305) exposimeter.

Gas	V311	V315	V305
	<i>Bq m</i> ⁻³ / <i>cph</i>	<i>Bq m</i> ⁻³ / <i>cph</i>	<i>Bq m</i> ⁻³ / <i>cph</i>
^{220}Rn	99.5 ± 9.8	134.5 ± 20.6	16.6 ± 1.0
^{222}Rn	16.1 ± 2.2	15.5 ± 2.1	17.0 ± 2.1

counts, have to be considered.

4.4.2 Spectrum

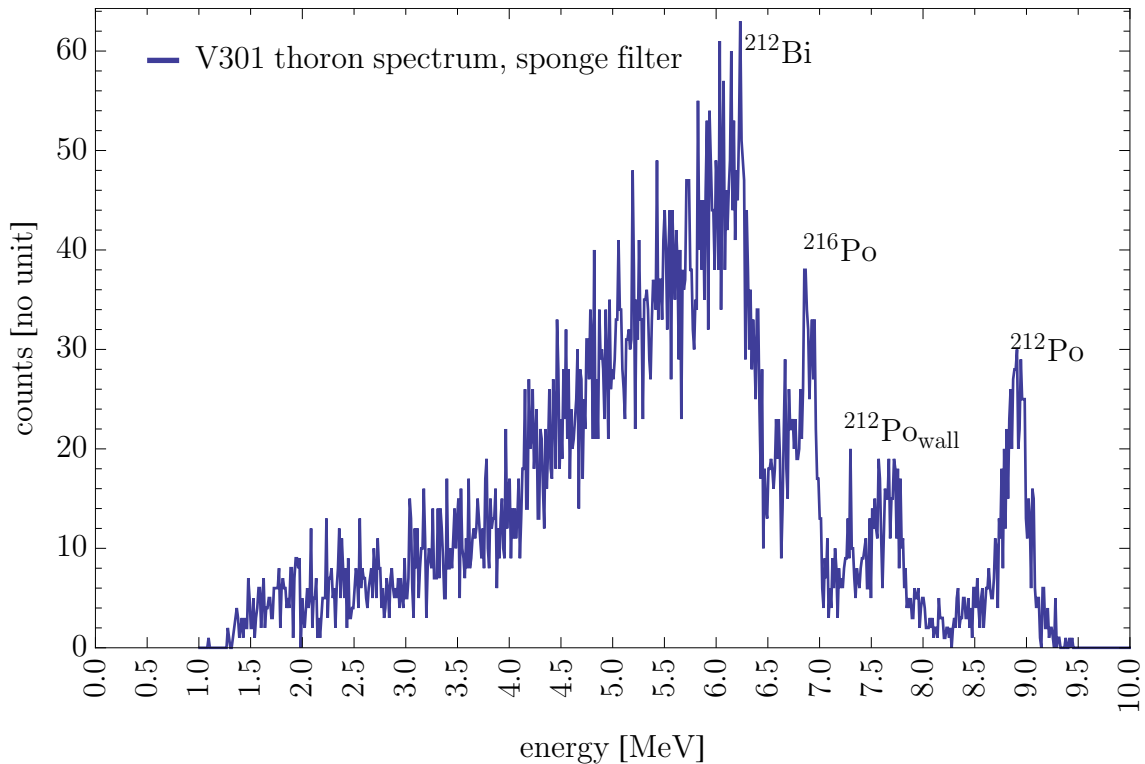


Figure 4.6: Typical alpha particle spectrum acquired in a thoron environment for the standard housing (geometry 1). In the summed spectrum (hours 60-85) the characteristic alpha peaks of two progeny are clearly visible.

Figure 4.6 shows a typical energy spectrum acquired in a high thoron gas environment with mean activity concentration of $8,280 \pm 330 \text{ Bq m}^{-3}$. Environmental conditions during the calibration in the small calibration chamber were 46.0% *RH*, 23.4 °C and 968.6 *hPa*. Again two progeny peaks can be identified which belong to the thoron daughters ^{212}Bi and ^{212}Po which decay via alpha particle emission (see also Figure 2.3). These decays measured at energies of approximately 6.2 and 8.9 *MeV* originate from particles deposited directly on the detector surface. The energy loss by transition through the thin aluminum coating on top of the detector (400 *nm*) was considered for the stated energies (see in Chapter 5). The other signals in the spectrum are a superposition of events registered from thoron gas, volume decays of ^{216}Po and of course from progeny deposited on inner walls. Specifically one notices in Figure 4.6 a peak between energies 7 and 8 *MeV* which is a result of alphas originating from ^{212}Po which was deposited on the inner surface of the housing, indicated as $^{212}\text{Po}_{\text{wall}}$. The calibration factor has been calculated by summing all counts from 1 – 10 *MeV* each hour and dividing it by the reference concentration. The resulting

calibration factor for device V301 was determined to be $cf_{220Rn} = 14.4 \pm 0.8 \text{ Bq m}^{-3}/\text{cph}$ and thus is close to but below of the corresponding range of previously determined ^{222}Rn calibration factors (Table 4.1) for this geometry. The higher thoron sensitivity can be again explained by the fact that due to higher decay energies more alpha particles are able to reach the detector. This effect, with respect to the difference between radon and thoron calibration factors, is more dominant in bigger cases, i.e. the calibration factor for thoron is smaller than for radon with increased geometrical size (see Section 4.4.1), up to certain threshold (see Section 5.1.4).

4.5 Filters

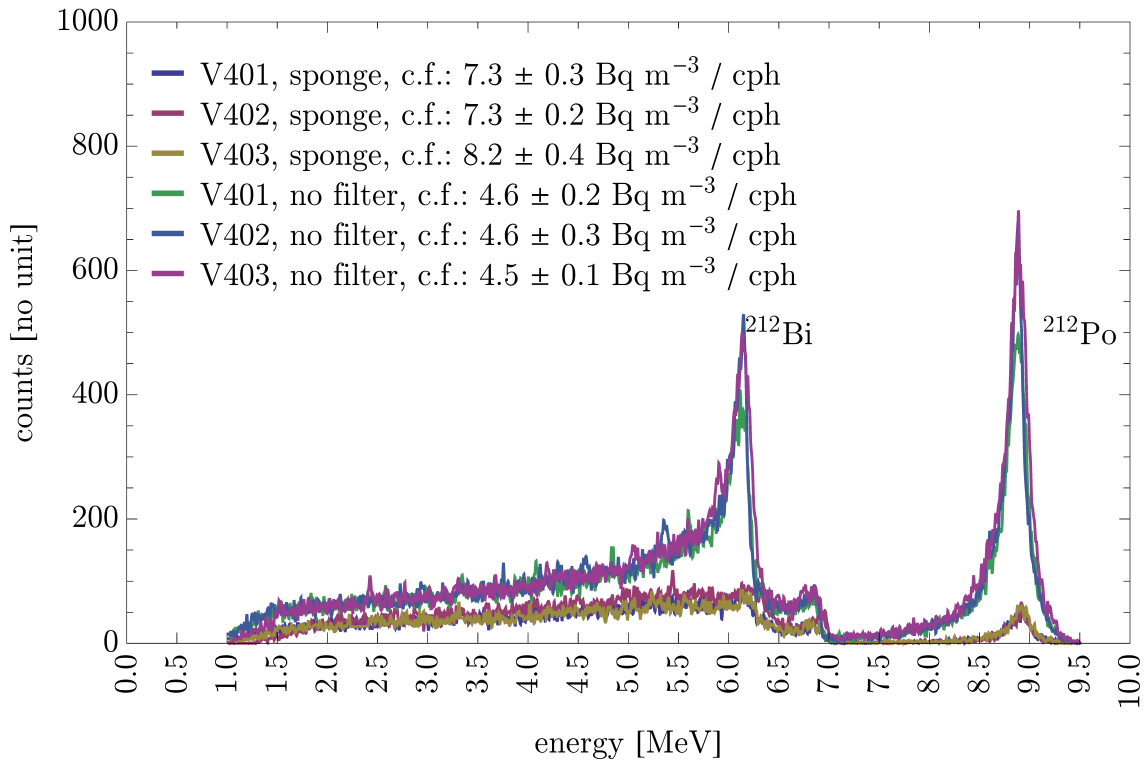


Figure 4.7: Typical alpha particle spectrum acquired in a thoron environment for the monitor with large housing (geometry 2). In the summed spectrum (hours 60-85) with no filter applied the characteristic alpha peaks of two progeny are clearly visible.

The primary goal of using a filter is to stop air-based ^{222}Rn and ^{220}Rn progenies from entering the diffusion chamber. This is necessary to ensure independence on environmental conditions such as aerosol particle size distribution and deposition rates, as discussed in Section 3.1. Filter efficiency can be measured for example with thoron infused aerosol gas mixtures and is depended on particle size and velocity [209]. Usually with particle velocities below 5 cm s^{-1} , diffusion is considered to be the dominant filtering mechanism,

and in this domain the Whatman 41 filter shows 100% collection efficiency for particle sizes of $2 \mu m$ [164], decreasing up to 60% with $0.3 \mu m$ diameter. This filter is also commonly used for thoron monitors and is considered to allow for better thoron gas diffusion than the Millipore MF-AA filter [213]. Even newer versions use electroconductive sponges instead of filter paper [183], which increase the sensitivity of the thoron monitor further. Using a polyethylene sponge also reduces the dependence problem of the filter material on humidity, as cellulose based filters are hydrophile and can accumulate water within their pores, effectively decreasing thoron diffusion. Measurements show that water absorption is linearly increasing with relative humidity, where filter paper absorbs about 10 times more water than sponge filters [160]. Water molecules accumulate in filter pores, and change the diffusion constant of the filter in an undesired manner.

Progeny filtration

In order to determine whether the filter hinders diffusion of progeny into the chamber, a comparison measurement with and without filter was performed. In this test the small calibration chamber, with active fans for stirring the air, was employed. The newly developed thoron monitor prototypes in the larger housing, namely geometry 2, were used and covered with 8 inlets of $10 mm$ diameter at the top. As tracer gas ^{220}Rn was utilized as it offers, in terms of half lives, the longest decay chain. Hence ^{212}Bi and ^{212}Po have enough time for diffusion and adsorption. For both evaluations only counts acquired in hours 60 to 85 were considered and three monitors were exposed with identical setup. In the run without filter a mean thoron concentration of $11,890 \pm 490 Bq m^{-3}$ at 48% RH, $23.3 ^\circ C$ and $962.1 hPa$ was reached. The second test, with filter, attained a stable thoron concentration of $10,650 \pm 440 Bq m^{-3}$ at 45% RH, $23.7 ^\circ C$ and $961.6 hPa$. Figure 4.7 shows the obtained spectra which clearly demonstrate the significant influence of the applied sponge filter by reducing the corresponding progeny in the diffusion chambers. The total number of counts in the ROI from $7 - 10 MeV$, which are purely attributable to ^{212}Po , sum up to 20,534, 21,161 and 24,270 (mean $21,988 \pm 2,001$) for the three devices without filter. When the filter is applied under similar conditions only 2,025, 1,729 and 2,088 (mean $1,947 \pm 192$) counts are acquired, i.e. progeny are reduced by more than a factor of ten. Considering the thoron concentration measured by the reference device and the volume and detection area of the used devices it is possible to estimate the expected N_{212Po} counts via,

$$N_{212Po} = \frac{1}{2} k_b f_{det} V C_{220Rn} T \quad (4.5)$$

where it is assumed that the progeny are homogeneously deposited on all areas within the diffusion chamber and that a steady equilibrium has been reached. Here the factor $1/2$ originates from the fact of isotropy, thus only half of the decays have the chance to be detected by the pin-diodes, while $k_b = 0.64$ is the branching fraction of ^{212}Po , f_{det} is the quotient of detector area over total inner housing area, V the diffusion chamber volume (m^3), C_{220Rn} the mean thoron concentration ($Bq m^{-3}$) and T the exposure time (s). With the stated conditions and Equation 4.5 this leads to an estimated number of

3,426±380 and 2,185±217 counts for the non filter and filter setup respectively. The error has been calculated via error propagation and assuming an uncertainty of 1.0 mm in the geometric dimensions. Hence a well agreement between measured and estimated events can be deduced within the error limit for the case of employing the sponge filter, with a slightly smaller number of counts than in the estimation. This can be attributable to the fact that, due to the diffusion process (see Section 2.3.1), some thoron gas already decays before entering the chamber, effectively lowering the concentration within the diffusion chamber. On the other hand the number of counts without filter is extremely high compared to the estimate, which is due to the fact that also progeny from within the calibration chamber have enough time to attach to the inner device area, enormously increasing the effective collection volume. Now that it is established that the sponge filter is reasonable tight for the air-borne progeny the question of diffusion effectiveness remains.

Filter efficiency

Therefore those three filters, which are commonly employed, have been tested for their thoron diffusivity. Two are cellulose based, the Whatman Grade 41 (W41, \varnothing 90 mm, pore size 25 μ m, thickness 220 μ m) and the Millipore membrane filter SMWP (MM, \varnothing 90 mm, pore size 5 μ m, thickness 135 μ m), while as sponge filter a Vermason L210633 (SP, thickness 6 mm) polyether polyurethane foam was chosen.

A characteristic value to describe a filter is its diffusion constant D over its thickness Δx from Equation 2.9, $D/\Delta x$, which can be interpreted as diffusion velocity. The W41 and MM filter have estimated values of $790 \pm 210 \text{ cm h}^{-1}$ and 209 cm h^{-1} respectively [213, 53]. A sponge filter used by the Raduet thoron monitor developed at NIRS has a $D/\Delta x$ value of $179 \pm 96 \text{ cm h}^{-1}$ [160]. The higher the value the better is the diffusion speed and thus the infiltration rate (Equation 2.10). Three devices equipped with the three different filters have been put inside the small calibration chamber with two active 80 mm fans and have been exposed to thoron gas at a concentration of $12,560 \pm 480 \text{ Bq m}^{-3}$ with 47% RH, 23.2 °C and 961.9 hPa. All devices had the same geometry with 8 inlet holes of 10 mm diameter and thus an total opening area of $A = 6.3 \cdot 10^{-4} \text{ m}^2$ and an approximate volume of $V = 116 \cdot 91 \cdot 53 \text{ mm}^3 = 5.6 \cdot 10^{-4} \text{ m}^3$. Under equilibrium conditions in between hours 60-85 the total counts in the ROI from 1 to 10 MeV accumulated to 10,730 for the W41, 11,493 for the MM and 25,436 for the SP filter. This means that the cellulose filters only have about 42% or 45% of the efficiency compared to the employed Vermason filter, which is a significant improvement.

A follow-up measurement under different conditions ($4,816 \pm 300 \text{ Bq m}^{-3}$, 50% RH, 23.6 °C, 961.0 hPa, small chamber with one 200 mm fan) but equal time window showed the same tendency with counts between 4,951, 4,518 and 14,316, thus a 35% and 32% efficiency of the W41 and MM filter respectively. The difference to the previous measurement can be explained by the thoron gas inhomogeneity in the chamber of up to 20%. From both measurements it can be concluded that the sponge filter, which has a much higher influence on the count number than gas inhomogeneity, is at least by a factor of 2 better for thoron gas diffusion. Unexpected is the similar behavior of the W41 and MM filter,

since the W41 should have, under these conditions, a 3.5 higher infiltration rate (Equation 2.10) and thus measured counts, which is not observable.

Diffusion through sponge filter

The diffusion constant of a filter can be determined by fitting Equation 2.7 to the time dependent concentration behavior of ^{222}Rn build-up through a filter material in a sealed vessel [73], which however takes a long measurement time, special setup equipment and numerical solving algorithms. A simpler method is to employ thoron which allows the use of the stationary diffusion equation due to its short half-life [146]. In the present work three identical thoron monitors were used with the sponge filter material, but varying inlet area. The effective area has been reduced by sealing part of the 8 holes with tape to change the original area A by a factor of 1/4, 1/2 and 1. By comparing the number of counts in each device it is possible to estimate the diffusion constant D via Equation 4.6 [160],

$$\frac{N_1}{N_2} = A_1 \left(\frac{A_2 D}{\Delta x V} + \lambda \right) / A_2 \left(\frac{A_1 D}{\Delta x V} + \lambda \right) \quad (4.6)$$

where N_i denotes the number of counts measured by device i with inlet area A_i (m^2), λ (s^{-1}) is the decay constant of thoron, Δx the filter thickness (m) and V the monitor volume (m^3). Equation 4.6 is derived from equation 2.10 for different C_i and γ_i by division of the two equations. The devices have been put into the small calibration chamber with 2 active fans and a constant thoron gas concentration of $10,940 \pm 460 \text{ Bq m}^{-3}$ at 45% RH, 23.9 °C and 968.6 hPa. The total number of counts in the time window between hour 138 to 160 were for areas $A_{1/4}$, $A_{1/2}$ and A_1 exactly 3,914, 14,483 and 25,158 respectively. The estimated $D/\Delta x$ value via Equation 4.6 for the used SP filter yields $1,417 \pm 587 \text{ cm h}^{-1}$, where the error was calculated via error propagation and assuming a length uncertainty of 0.1 mm. This is in well agreement with the relative efficiency measurements performed in Section 4.5. There the sponge filter achieved a more than factor two better count rate, which under equal monitor geometries translates to an increased diffusion velocity $D/\Delta x$. Since the W41 filter has an estimated $D/\Delta x$ of $790 \pm 210 \text{ cm h}^{-1}$ [213] the found value of the sponge filter is within the expected domain and uncertainty. The expected value for a count number relation of 2/1 between the sponge and W41 filter would result with this geometry in a value of $1,972 \text{ cm h}^{-1}$ (Equation 2.10). This means the sponge filter introduces no measurable obstacle for the thoron diffusion process and can be assumed to be as permeable as air.

4.6 Mixed concentrations

The results in Sections 4.3 and 4.4 show that the calibration factor for both isotopes ^{222}Rn and ^{220}Rn is quite similar for both geometries employed. However, when both isotopes are present in the atmosphere and it is necessary to distinguish either one from the other, another evaluation approach is necessary. This is due to the continuity of the spectra, which

Table 4.4: Mean radon and thoron mixed concentrations measurement conditions

Test ¹	Ratio	²²² Rn Conc. <i>Bq m⁻³</i>	²²⁰ Rn Conc. <i>Bq m⁻³</i>	Humidity <i>RH</i>	Temperature <i>°C</i>	Pressure <i>hPa</i>
1	1/26	220 ± 110	5,790 ± 340	48%	23.8	958.6
2	1/1	1,150 ± 210	1,480 ± 110	48%	24.7	960.0
3	5/1	6,300 ± 300	1,260 ± 100	49%	24.5	957.3
4	3/1	17,730 ± 630	5,980 ± 350	48%	24.7	960.0
5	7/1	65,960 ± 1,190	9,050 ± 510	49%	24.6	960.0

¹Evaluation in the period from hours 60-85

mainly interfere in the energy domain from 1 to 8 MeV. Only the region of interest (*ROI*) between 8 to 10 MeV, denominated here as *ROI₄*, is free from any ²²²Rn contribution, as there is no element in the decay chain of radon with such high energies (see Figure 2.1). Other regions to distinguish radon and thoron effectively and without dependence on environmental parameters are not available, as discussed in Chapter 5. In this section measurements of different concentration mixtures between radon and thoron are presented and discussed. Again as reference device a Rad7 was employed and measurements were executed in such a way that equilibrium conditions for both isotopes would settle. In order to allow for a maximum consistency of the reference concentration values determined by the Rad7, this time the thoron activity was calculated via the raw output of the device. This is necessary since the formula to calculate the corresponding activity concentrations in the proprietary *Capture* software is unknown. The Rad7 also determines the concentrations by use of a ROI, where the ²¹²Po peak lies within the so called *ROI_D*. The calibration factor for this ROI was determined in 10 measurements at high thoron concentrations to be about $cf_{ROI_D} = 3.67 \pm 0.19 \text{ Bq m}^{-3}/\text{cph}$, where the error is the standard deviation. Hence the relative standard deviation is about 5%, which is about the accuracy that is assumed for the Rad7 [39] for thoron measurements. In the following cf_{ROI_D} is used as the equilibrium calibration factor for ²¹²Po and the Rad7 reference device between hours 60 to 85 and for a relative humidity of about 46% - 49%. This method ensures that there is no interference from signals originating from ²²²Rn, as the Rad7 usually calculates the thoron concentration on basis of *ROI_B* (²¹⁶Po).

4.6.1 Acquired spectra

In order to test whether the newly developed device allows discrimination between radon and thoron decays, several measurements in mixed concentrations have been performed. All measurements were performed in the small calibration chamber with one 200 mm fan at the top and sources position at the center of the chamber below the ventilator. The Rad7 was connected via a tube externally as described in Section 4.4.1. In Table 4.4 the conditions of the different tests are stated. The measurements were conducted consecutively and the same time frame, thus ensuring quite stable environmental conditions. The relative fraction of the concentration mixture for ²²²Rn/²²⁰Rn was thus about 1/26, 1/1, 5/1, 3/1 and 7/1

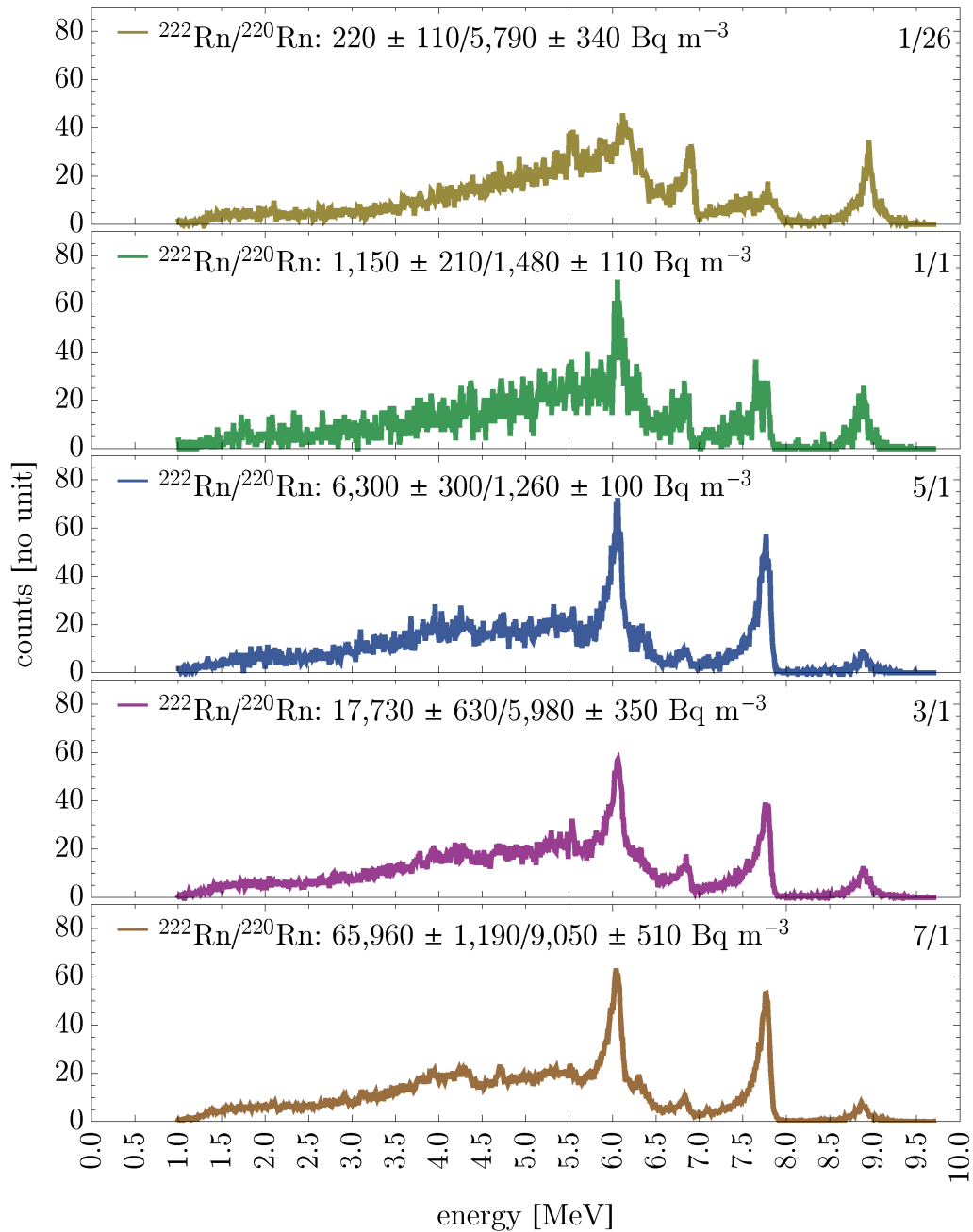


Figure 4.8: Spectra in mixed ^{222}Rn and ^{220}Rn concentrations acquired by device V305 with standard housing (Geo1) and improved ADC circuit. Spectra are normalized with respect to total count number.

respectively. The device employed for these measurements was built with the standard housing dimensions (Geo1), and used the new improved 12-bit ADC, just as the new devices with geometry 2. For this device V301 was modified, the battery was removed, and the digital part was disconnected from any power source. The microprocessor and power supply were situated on a second, external PCB in another housing. Both boxes were taped together and the amplifier output line was connected via a shielded coaxial cable. Thus the only difference to standard geometry 1 is the removed battery, and thus about 3.6% more volume inside the diffusion chamber ($V_{bat} = 5.78 \cdot 10^{-6} \text{ mm}^3$). The device was denoted V305. The acquired spectra for all five test measurements under the conditions given in Table 4.4 for V305 are shown in Figure 4.8, with lowest to highest radon concentration from top to bottom. Due to the differences in mixed concentration all the spectra were normalized to their total count rate and then multiplied by a factor 10^4 . At all times the ^{212}Po is clearly visible. Other progeny peaks such as ^{216}Po and ^{212}Bi are decreasing and finally vanishing under the higher number of counts due to radon decays. One notices that with this geometry counts generated by decays originating from $^{212}\text{Po}_{wall}$ wall decays interfere with ^{214}Po detector decays and $^{214}\text{Po}_{wall}$ with ^{216}Po decays. Their influence on each other renders it very difficult to determine the origin of a count register in the respective regions. Additionally energy loss of decays originating from walls is influenced by environmental parameters, thus shifting the energy spectrum. This is in detail discussed in Section 5.3.4. Here this effect is just noted and taken into consideration when choosing an appropriate evaluation method for discrimination.

4.6.2 Evaluation methods

In order to determine the individual contribution from either radon or thoron to the measured counts of the exposimeter, two methods for the calculation of the activity concentration are discussed here.

Region of interest

Due to the interference of thoron and radon decays in the energy domain of 1-8 MeV , in addition to the coupled influence of environmental parameters on the calibration factor (see Chapter 5), the best method for discrimination in a single chamber device is by integration of counts over certain region of interests (ROI). A detailed explanation of the effects affecting the calibration factor is given in Section 5.3.4. For the evaluation of the acquired spectra obtained in mixed concentrations two ROIs are considered, namely ROI_1 in the domain from 1 – 8 MeV and ROI_4 from 8 – 10 MeV . The ^{220}Rn concentration $C_{220\text{Rn}}$ is calculated from count rate cr in the ROI_4 where no radon interference is expected since there all progeny decay energies are below 8 MeV (see Figure 2.1). Then, of course, one has to consider the number of counts registered in ROI_1 due to thoron quantified by the factor f . This fraction f , determined in high thoron concentrations, is given by the quotient of the respective count rates cr in the regions, i.e. cr_{ROI_1}/cr_{ROI_4} , which are a measure for the ^{220}Rn concentration. These have to be subtracted from counts in ROI_1 ,

and the difference is used for the determination of the ^{222}Rn concentration $C_{222\text{Rn}}$. This methodology leads to following formulas for the concentration calculations,

$$C_{220\text{Rn}} = cf_{220\text{Rn}} cr_{ROI_4} \quad (4.7a)$$

$$C_{222\text{Rn}} = cf_{222\text{Rn}} (cr_{ROI_1} - f cr_{ROI_4}) \quad (4.7b)$$

where the calibration factor cf is given in activity concentration per counts per time interval ($Bq\ m^{-3}/cpt$) and the resulting concentration in $Bq\ m^{-3}$.

In independent calibration measurements following values have been determined for device V305:

- V305: $cf_{222\text{Rn}} = 17.0 \pm 2.1\ Bq\ m^{-3}/cph$, $cf_{220\text{Rn}} = 95.1 \pm 11.1\ Bq\ m^{-3}/cph$, $f = 11.79 \pm 2.67$ and $cr_0 = 0.03\ cph$

where the fraction f has been calculated by evaluating 6 high thoron concentration calibrations with the error stating the standard deviation. The background count rate cr_0 has been determined in a low thoron environment, but is assumed here to be zero. The radon calibration factor $cf_{222\text{Rn}}$ is in well agreement with the previous result for this type of device (Section 4.3.3). Further the ^{212}Po calibration factor $cf_{220\text{Rn}}$ for thoron yields a similar value as the one determined by a simulation performed for this device, which resulted in a value of $106.9 \pm 2.1\ Bq\ m^{-3}/cph$.

With the stated values and the counts obtained from the spectra in Figure 4.8, it is possible to calculate the corresponding mean activity concentrations measured with V305 via Equations 4.7 and compare them to the reference concentrations determined by the Rad7 (Table 4.4).

Figure 4.9 shows that in most cases the results agree within their respective 1σ uncertainty. The error of the concentration determined by V305 is calculated via Gaussian error propagation of Equations 4.7, taking into consideration the statistical error, which was taken to be the square root of the number of counts $u(cr) = \sqrt{ct}/t_m$, and the respective error of the involved constants, assuming a negligible error of the time interval t_m . This can result in quite large relative errors of up to 12% in this evaluation. In general the error mainly depends on the precision of the employed calibration factors and the number of obtained counts. The reasonable agreement between reference and calculated values demonstrate that this evaluation method is valid and can be employed to discriminate ^{222}Rn and ^{220}Rn . Further it is also the standard method for calculation of the activity concentration defined by the recently released ISO standard for measurement of radioactivity in the environment [69].

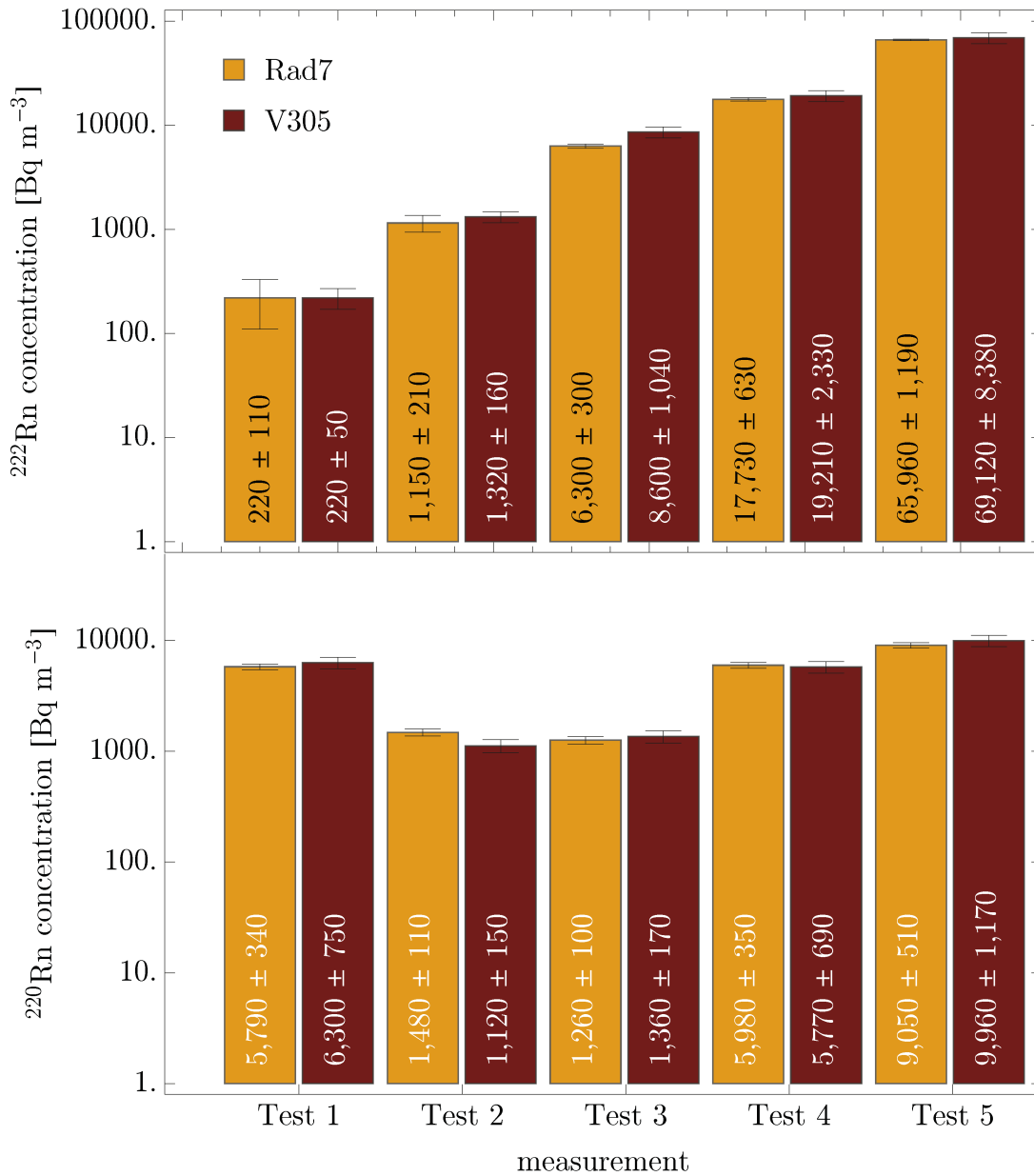


Figure 4.9: Comparison of reference activity concentration with calculated values from device V305 with standard housing (Geo1). Note that concentration is plotted on a logarithmic scale. Uncertainties refer to 1σ .

Least square fitting

The second evaluation method takes advantage of the spectral information acquired by the exosimeter. It employs the method of least square approximation, where the fitting parameters are the constants of a linear combination of normalized spectra, which were acquired during calibration in either high radon or thoron concentrations. Under ideal conditions any spectrum acquired in a $^{222}\text{Rn}/^{220}\text{Rn}$ mixed atmosphere should be just a linear combination of the spectra of individual concentrations. However, this is only valid as long as there is no influence on the spectral shape due to environmental influences. The measured spectrum S_{meas} can then be expressed by a combination of the single contribution spectra,

$$S_{meas} = a S_{222\text{Rn}}^N + b S_{220\text{Rn}}^N \quad (4.8)$$

where a, b are the respective concentrations and S_i^N are the normalized spectra. The spectra are normalized with respect to the reference concentration. This means that during a calibration for each measurement interval t all channels of the spectrum are divided by the reference concentration of the isotope under investigation. The arithmetic mean of the all acquired spectra yields then the normalized spectra ($cpt/Bq\ m^{-3}$). This requires that during the calibration measurement either ^{222}Rn or ^{220}Rn is only present insignificantly with respect to the other. Given an acquired spectrum S_{meas} one can determine the radon and thoron concentrations by determining parameters a and b . The data presented in Figure 4.8 was fitted via Equation 4.8 by employing the respective normalized calibration spectra ($cph/Bq\ m^{-3}$). The unit of the acquired sum spectra S_{meas} was a count rate in time interval $t = 25\ h$, ie. cpt , therefore the resulting fit parameters (unit $Bq\ m^{-3}$) have to be divided by t or the normalized spectra have to be multiplied by $t \cdot S_i^N$ before fitting, in order to ensure equality of units. The fitting function employed was the *LinearModelFit* in *Wolfram Mathematica 9.0.1*, using weights $w_x = 1/u(x)$ for each channel x , where the error $u(x) = \sqrt{ct_x}$ is taken to be the statistical uncertainty. Hence the error variance for counts ct_x in channel x is assumed to be σ^2/w_i . This means that the fit function considers channels of the spectrum with high count number more than others, since there the residuals are weighted higher. The resulting fitted spectra and calculated activity concentrations are shown in Figure 4.10, where the error of the calculated concentration is the standard error for the parameter estimates. Comparing the trend in spectral form and absolute count number per channel between measured and fitted spectrum one notes reasonable agreement for all five measurements. This is to be expected as the environmental conditions hardly changed during the calibration campaign in the laboratory. The value and error found with this method however show larger deviations from the reference mean values as with the *ROI* evaluation method. For example in test 1 the ^{222}Rn is overestimated by a factor of 5, and the ^{220}Rn by a factor 1.3. Also for test 3, 4 and 5 the determined ^{220}Rn concentration differs from the reference value by more than a factor of 2. Only in the case of test 2 and a 1/1 ratio the fit results are similar to the reference concentration. This is most likely due to the fact that in the region from 1-6 MeV is a lot of interference between radon and thoron decays, which, considering the additional statistical uncertainty, offers potential for large

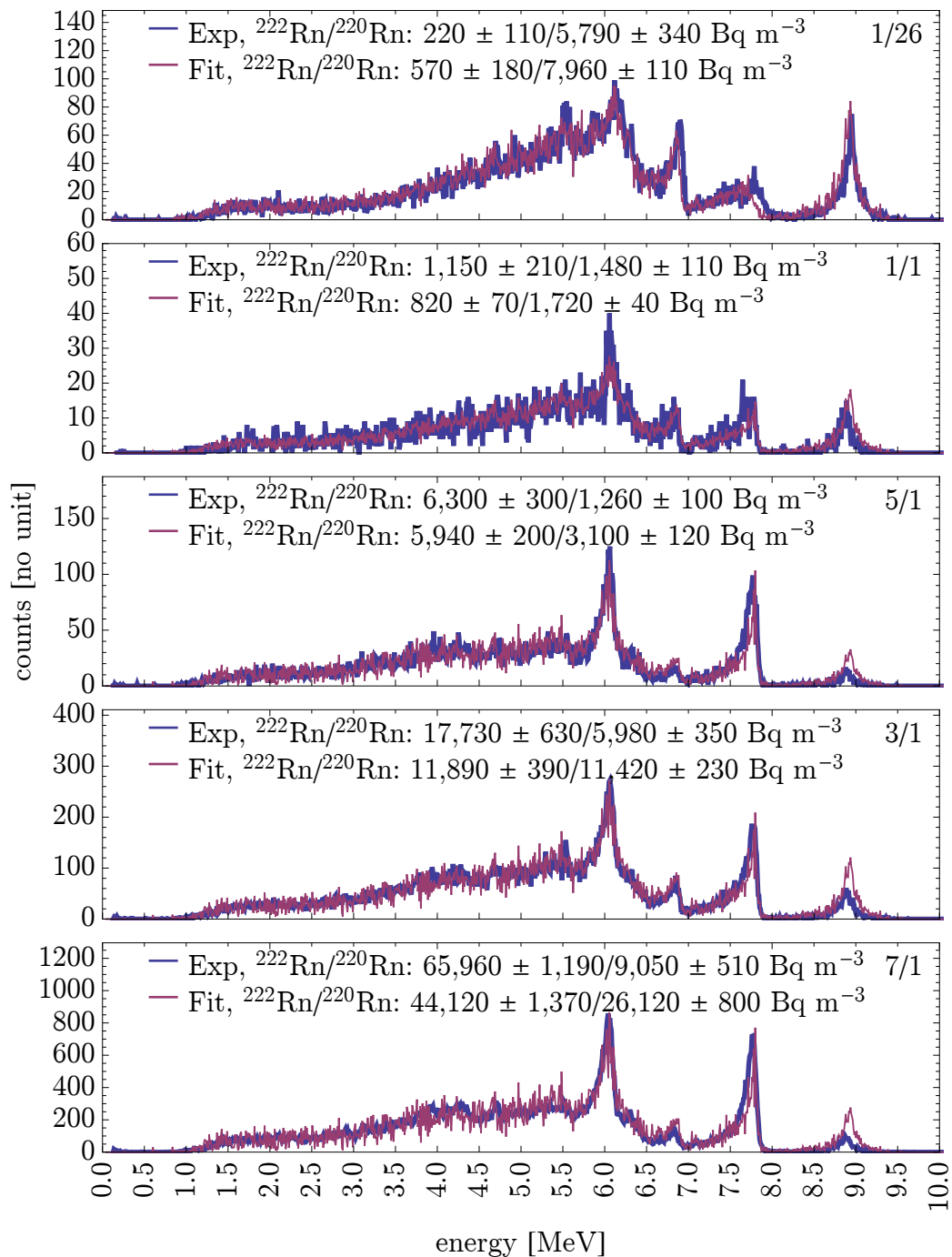


Figure 4.10: Experimentally acquired spectra in mixed ^{222}Rn and ^{220}Rn concentrations and fit of linear combination of normalized spectra. Trend shows good agreement, however, calculated concentrations differ largely.

variations of the fitting parameters. This indicates that the least squares fitting method is not very well suited for evaluation of mixed gas environments, especially when no a priori information on the ratio is known, and thus if the method works reliable.

4.6.3 Concentration calculation and detection limits

The recently released ISO standards for measurement of radioactivity in the environment for radon [69] state that the activity concentration C shall be calculated via,

$$C = (cr - cr_0) cf \quad (4.9)$$

where cr is the measured count rate cph , cr_0 the background count rate and cf the calibration factor $Bq\ m^{-3}/cph$. Due to the high energy threshold of the detection system of about $1\ MeV$ and the stability of the amplifier, generally a background count rate of zero due to electronic noise can be assumed ($cr_0 = 0$). Another source for background counts are the immediate short-lived daughter products. These can be ignored as long as the time between consecutive measurements is significantly larger than the longest half-life, which is from the ^{212}Po progeny. In contrast the long-lived daughters cannot be ignored and their influence on the background count rate can only be kept small on the condition of low total cumulative exposure of the device.

Background estimation

In general, the main physical background contribution, which needs to be considered, are alpha decays from the radon progeny ^{210}Po ($\tau_{1/2} = 138.4\ d$, $E_\alpha = 5.41\ MeV$), that are attached to the chamber and detector surface. It is the daughter nuclide of ^{210}Pb , which accumulates in the chamber during exposure to radon, and due to its long half-life ($\tau_{1/2} = 22.3\ a$), ^{210}Pb is present for a long time, compared to the life-cycle of such a device. When considering a long-term time scale at a constant radon exposure, one can calculate the ^{210}Po atoms present by continuing the ^{222}Rn decay chain for $^{214}Pb \rightarrow ^{210}Pb \rightarrow ^{210}Bi \rightarrow ^{210}Po$, according to Equations 2.2. At equilibrium conditions the number of radon atoms N_{222Rn} in the measurement volume is given by

$$N_{222Rn} = \lambda_{222Rn}^{-1} C_{222Rn} V \quad (4.10)$$

where V is the chamber volume, C_{222Rn} the radon activity concentration and λ_{222Rn} the radon decay constant. Assuming that all progeny will distribute homogeneously on the surface of the device, a detector will register counts due to ^{210}Po decays originating from chamber walls and the detector surface. Simulations showed that the detection efficiency for this decay is about $\eta = 0.046$ for geometry 1 and STP conditions. Thus when knowing the number of ^{210}Po atoms present in the volume, the background count rate can be calculated via Equation 4.11,

$$cr_0 = \eta \lambda_{210Po} N_{210Po} \quad (4.11)$$

h

Table 4.5: Relative difference of N_{210Po} atoms calculated with Equation 4.12 and with the decay chain implementation in *Mathematica*.

Time	1	2	3	4	5	6	7	8	9	10
a	%	%	%	%	%	%	%	%	%	%
ΔN	3.1	1.3	0.8	0.6	0.4	0.3	0.3	0.2	0.2	0.2

where the number of ^{210}Po atoms was calculated numerically in *Wolfram Mathematica 9.0.1*. In the numerical model of the decay chain the ^{214}Po decay step was ignored, as its short half-life caused numerical overflow and thus oscillation of the solution in the considered time frame.

The number of N_{210Po} atoms was also estimated in a simplified approach by ignoring all short lived daughters and just considering $^{222}Rn \rightarrow ^{210}Pb \rightarrow ^{210}Po$, which leads to following equation for the number of ^{210}Po atoms,

$$N_{210Po}(t) = \frac{\lambda_{222Rn} N_{222Rn} (\lambda_{210Pb} - \lambda_{210Po} e^{-\lambda_{210Po} t} + \lambda_{210Po} (e^{-\lambda_{210Pb} t} - 1))}{\lambda_{210Po} (\lambda_{210Pb} - \lambda_{210Po})} \quad (4.12)$$

Results obtained by use of Equation 4.12 are within 3.1% similar to those of the accurate numerical solution implemented in *Mathematica*. Table 4.5 shows the relative difference ΔN between the estimated N_{210Po} and the accurately calculated number of atoms as a function of time. Thus, for the considered time frame the difference is negligible.

This means with Equations 4.11 and 4.12 an estimate of the background count rate due to ^{210}Po atoms in the chamber can be calculated. Assuming a relatively low radon concentration of 10 Bq m^{-3} and an exposure of 10 years, the number of ^{210}Po atoms in the volume $V = 1.6 \cdot 10^{-4} \text{ m}^3$ (Geo1) is about $N_{210Po} = 7,125$. This yields a background count rate of $cr_0 = 0.065 \text{ cph}$, which is in general negligible. If the radon exposimeter was situated in a ^{222}Rn atmosphere with $C_{222Rn} = 1 \text{ kBq m}^{-3}$ for ten years, the resulting additional background would be about $cr_0 = 6.5 \text{ cph}$, and thus quite considerable. However as long as there is no fault in the electronics or the detector, the background count rate can be safely assumed to be almost zero, provided that no exposure in high radon concentrations had occurred, or that the detector and housing are new.

In the following a stable ^{222}Rn activity concentration is assumed, which results in a constant number of radon atoms present in the diffusion chamber according to Equation 4.10.

The background count rate is important when estimating the decision threshold, detection limit and limits of the confidence interval [68]. These so called characteristic limits are defined as:

- the decision threshold is the threshold whether a real physical effect due to the measurand is present or not
- the detection limit is the smallest value which can be detected with the employed measurement method.
- the limits of confidence interval state a confidence interval which contains the true value of the measurand with a chosen probability.

Standard uncertainty

The uncertainty u of the activity concentration (Eq. 4.9) is calculated via Gaussian error propagation and yields [68],

$$u(C) = \sqrt{cf^2 [u^2(cr) + u^2(cr_0)] + [cr - cr_0]^2 u^2(cf)} \quad (4.13a)$$

$$= \sqrt{\left[\frac{C}{cf t_m} + cr_0 \left[\frac{1}{t_m} + \frac{1}{t_0} \right] \right] cf^2 + C^2 u_{rel}^2(cf)} \quad (4.13b)$$

$$= \sqrt{\left[\frac{C}{cf} + 2 cr_0 \right] \frac{cf^2}{t_m} + C^2 u_{rel}^2(cf)} \quad (4.13c)$$

where $u^2(cr) = (\sqrt{ct}/t_m)^2$ is the statistical error of the acquired count rate, with ct being the count number and $t_m = t_0$ the measurement time, of which the uncertainty is considered negligible and $u_{rel}^2(cf) = u^2(cf)/cf^2$.

Decision threshold

The decision threshold C^* is obtained from Equation 4.13b for $C = 0$,

$$C^* = k_{1-\alpha} u(0) = k_{1-\alpha} cf \sqrt{cr_0 \left[\frac{1}{t_m} + \frac{1}{t_0} \right]} = k_{1-\alpha} cf \sqrt{\frac{2 cr_0}{t_m}} \quad (4.14)$$

where $k_{1-\alpha}$ is the $(1 - \alpha)$ -quantile of the standard normal distribution and $t_m = t_0$ the measurement time. The probability α of the PDF is the part which is unlikely to be within the limit of the true value of the concentration. Generally a 95% confidence interval is desired, thus yielding an $\alpha = 0.05$ and $k_{1-\alpha} = 1.645$.

Detection limit

The detection limit $C^\#$ is calculated as given in Equation 4.15,

$$C^\# = C^* + k_{1-\beta} u(C^\#) \quad (4.15)$$

where generally again a confidence interval of 95% is chosen. $C^\#$ is obtained from solving Equation 4.15 for $C^\#$ and Equation 4.13c for $u(C^\#)$, one usually starts by iteration using the approximation $C^\# = 2 C^*$, which yields,

$$C^\# = \frac{2 C^* + k^2 cf t_m^{-1}}{1 - k^2 u_{rel}^2(cf)} \quad (4.16)$$

where $\alpha = \beta = 0.05$ and hence $k_{1-\alpha} = k_{1-\beta} = k = 1.645$.

Limits of the confidence interval

In the case that $C \geq 4 u(C)$ the symmetric approximation for both limits is valid which are given by,

$$C^\pm = C \pm k_{1-\gamma/2} u(C) \quad (4.17)$$

where often a $\gamma = 0.05$ with $k_{1-\gamma/2} = 1.96$ is chosen. This means according to ISO standards one should use almost a 2σ uncertainty by default.

Application to developed devices

Given the calibration factor determined in Section 4.3.2 the detection limit for radon can be calculated via Equation 4.15. The value found for the calibration factor was $cf_{222Rn} = 16.2 \pm 0.9 Bq m^{-3}/cph$, and assuming an $cr_0 = 0 cph$ in case of a new device with time interval $t_m = 1 h$, this yields a detection limit of,

$$C_{222Rn}^\# = \frac{2 \cdot 0 + 1.645^2 \cdot 16.2}{1 - 1.645^2 \cdot (0.9/16.2)^2} = 44.0 Bq m^{-3} \quad (4.18)$$

However one has to keep in mind that the background count rate could not be determined in a zero radon concentration environment. The background count rate stated in Section 4.3.2 was calculated from counts obtained at low but non-zero ^{222}Rn concentration levels resulting in the excess count rate $cr_0 = 0.29$, when compared to counts that should have occurred according to a reference device. For a new and unexposed device $cr_0 = 0 cph$ can be safely assumed.

When using the estimated value of $cr_0 = 0.065 cph$ calculated via Equation 4.11 ($C_{222Rn} = 10 Bq m^{-3}$, $T = 10 a$), one gets for $C_{222Rn}^* = 10.0 Bq m^{-3}$ and for the detection limit $C_{222Rn}^\# = 64.0 Bq m^{-3}$. This would be the minimum detection limit achievable with Geol and the stated calibration factor for devices used for long times, and in a one hour time interval ($t_m = 1 h$).

For high-level thoron activity concentrations, and negligible radon concentrations, the whole spectrum can be used for evaluation and the detection limit, with a calibration factor of $cf_{220Rn} = 14.4 \pm 0.8 \text{ Bq m}^{-3}/\text{cph}$ (Section 4.4.2), again with a background count rate $cr_0 = 0 \text{ cph}$, is then about,

$$C_{220Rn}^{\#} = \frac{2 \cdot 0 + 1.645^2 \cdot 14.4}{1 - 1.645^2 \cdot (0.8/14.4)^2} = 40.0 \text{ Bq m}^{-3} \quad (4.19)$$

in case of the standard housing and with $t_m = 1 \text{ h}$. Note, however, there will be always some sort of radon contribution to the total count rate, depending on the concentration relation between ^{222}Rn and ^{220}Rn , which has to be considered.

For mixed radon/thoron concentrations and the standard housing the mean calibration factor in ROI_4 was found to be about $cf_{220Rn} = 100 \pm 10 \text{ Bq m}^{-3}/\text{cph}$, and with a $cr_0 = 0.0 \text{ cph}$ and $t_m = 1 \text{ h}$, Equation 4.16 yields a detection limit of,

$$C_{220Rn}^{\#} = \frac{2 \cdot 0 + 1.645^2 \cdot 100.0}{1 - 1.645^2 \cdot (10.0/100.0)^2} = 280.0 \text{ Bq m}^{-3} \quad (4.20)$$

When using the experimentally determined value of $cr_0 = 0.03 \text{ cph}$, found in a low thoron gas environment, the result for the detection threshold is $C_{220Rn}^* = 40.0 \text{ Bq m}^{-3}$ and for the detection limit $C_{220Rn}^{\#} = 360.0 \text{ Bq m}^{-3}$.

Detection limit and time intervall

The detection limits can be reduced by increasing the integration time to a new value $t'_m = f t_m$. According to Equations 4.14 and 4.16 one gets,

$$C^{\#} = \frac{2 k cf \sqrt{cr_0 (f^{-1} t_m^{-1} + t_0^{-1})} + k^2 cf f^{-1} t_m^{-1}}{1 - k^2 u_{rel}^2(cf)} \quad (4.21)$$

For example, for a 6 hour sampling period $f = 6$, the limit reduces to $C_{222Rn}^{\#} = 7.0 \text{ Bq m}^{-3}$ according to Equation 4.21 with $cr_0 = 0.0 \text{ cph}$, or $C_{220Rn}^{\#} = 6.5 \text{ Bq m}^{-3}$ for thoron with $cr_0 = 0.0 \text{ cph}$.

Chapter 5

Monte-Carlo simulations

Monte Carlo simulations related to ^{222}Rn monitors have been performed already very early [194], where also diffusion into the chamber has been considered, to calculate the calibration factor on a theoretical basis. Another approach uses a SRIM based transportation code to simulate alpha-particle spectra [145] in dry air, while a recent study employs Geant4 to investigate the effect of environmental changes on the calibration factor [211]. All studies focused, however, on passive etch-track detectors and therefore could not provide a good agreement of simulated and measured spectrum. With the new device developed within the framework of this thesis this was for the first time possible.

Monte Carlo can be considered as a statistical sampling method using pseudo-random number generation and numerical calculations. It focuses on repetitive trials, forming a so called history for a large number of runs, and tries to find an estimated solution to a given problem [38]. A typical application for the Monte Carlo method is the problem of radiation transport, which refers to the transport of particles such as electrons, protons, ions, photons etc. through some medium. The interaction of particles within the medium is a purely statistical process and thus Monte Carlo simulations are a well suited tool which allow prediction of the average behavior of particles traversing a volume.

Within the framework of this thesis the Geant4 toolkit (version 9.5.2) was employed, which is an open source C++ code, originally developed for high energy physics [1]. It covers an ample set of particles and energy ranges from a few eV to the TeV scale. The implementation of the geometry and the physics model (electromagnetic, hadronic, transportation, decay, optical, photolepton-hadron, parametrization) [21] are the most important aspects in any Geant4 simulation and are the sole responsibility of the application developer. Depending on the problem at hand the required physic models have to be chosen.

In general the transportation process in Geant4 is performed in discrete distances [23], where at the end of each step a physical interaction takes place. The distance between physical interactions is called mean free path λ and depends on the cross section for a particular process and the number of possible interaction atoms, and is given by,

$$\lambda(E) = \left(\sum_i n_i \cdot \sigma(Z_i, E) \right)^{-1} \quad (5.1)$$

which is the sum over all elements i forming the material, with n_i being the density of atom species i and $\sigma(Z_i, E)$ the total cross section. The term $\sum_i n_i \cdot \sigma(Z_i, E)$ in Equation 5.1 is also called macroscopic cross section. The number of atoms per volume is given by $n = N_A/V$ with N_A being the Avogadro constant, where the molar volume is given by $V = M/\rho$ and the mass of a single atom $m_i = M_i/N_A$. Then, for example, for an isotope i with mass m_i , fractional mass $w_i = m_i/m_{tot}$ within a material of density ρ and the interaction cross-section $\sigma(E)$, the mean free path can then be calculated via,

$$\lambda(E) = \left(\sum_i \frac{N_A w_i \rho \sigma_i(E)}{M_i} \right)^{-1} = \left(\rho \sum_i \frac{w_i \sigma_i(E)}{m_i} \right)^{-1} \quad (5.2)$$

Thus the mean free path for a particle with energy E and a given process depends on the medium it is traversing. In a heterogeneous structure a material independent value is employed instead, the so called number of mean free paths n_λ (Equation 5.3),

$$n_\lambda(l) = \int_0^l \frac{dx}{\lambda(x)} \quad (5.3)$$

The probability of a particle traversing a distance l that has no interaction somewhere along its path is then

$$P(l) = 1 - e^{-n_\lambda(l)} \quad (5.4)$$

which is material and energy independent. Further the total number of free paths before a particle reaches its interaction point can be sampled with a random number $\eta \in [0, 1]$ from a uniform distribution via Equation 5.5 [22],

$$n_\lambda = -\ln \eta \quad (5.5)$$

which is updated after each step Δx with Equation 5.6

$$n'_\lambda = n_\lambda - \frac{\Delta x}{\lambda(x)} \quad (5.6)$$

up to the final step originating from $s(x) = n_\lambda \lambda(x)$, determining the next interaction. This method is called the differential approach, which requires that the cross section is almost constant along the finite step size, ie. the energy is small. Hence the step size is determined by the energy of the particle and the material, but also by the geometry, as a step may not cross a boundary. Also it is possible to define a maximum step size. In general the smaller the step size the more accurate the simulation but the more computation power or time is needed.

The methods introduced allow the generation of random tracks, where the state of a particle is defined by its position $\vec{x} = (x, y, z)$, its energy E and its direction of flight via a unit vector $\vec{d} = (u, v, w)$. The history of a track is then a series of states $\vec{r}_n, E_n, \vec{d}_n$, which are the position, energy and direction after the n -th scattering event. The changes to the states are randomly generated from the corresponding probability density functions which

are depending on the scattering processes, the cross section and the particle energy. For example the length s to the next collision is sampled via $s = -\lambda \ln \eta$ and thus the position of the next interaction is $\vec{r}_{n+1} = \vec{r}_n + s \vec{d}_n$. The track continues stepwise until it either leaves the simulation volume or its energy becomes smaller than a certain cut off energy, where the particle is assumed to have been stopped in the material.

The Monte Carlo approach should provide answers to several questions, namely the dependence of the calibration factor on geometry and on environmental parameters, thus granting a complete understanding of the detection mechanisms.

5.1 Model

5.1.1 Fundamentals

An alpha particle decay is random in nature, with an isotropic angular distribution and a stochastic spatial origin. Only decay energies are known which are a constant input parameter for the simulation (see also Table 2.2). The energy spectrum an exposimeter will acquire thus depends on its geometry, which determines the possible distances between source and detector as well as the density and composition of air, which influences the energy loss experienced by an alpha particle traversing the medium. Alpha particles suffer mostly energy loss due to inelastic collisions with shell electrons, producing so called δ electrons, which is commonly referred to as ionization. The mean energy loss per distance traveled can be calculated via the Bethe-Bloch formula for heavier particles like ions [98],

$$-\frac{dE}{dx} = \frac{4\pi n z^2}{m_e v^2} \cdot \left(\frac{e^2}{4\pi\epsilon_0} \right)^2 \cdot \left[\ln \left(\frac{2m_e v^2}{I} \right) \right] \quad (5.7)$$

where n is the electron density of the target, z the incident particle charge, v its velocity, m_e and e the electron mass and charge, ϵ_0 the vacuum permittivity and I the mean excitation potential. One should note that Equation 5.7 does not apply to electrons nor protons, while for latter a corrected version of Formula 5.7 exists, which takes into account quantum mechanical effects [172]. Since the electron density of the medium $n = N_A Z \rho / A M_u$, with Z being the atomic number, A its atomic mass and N_A the Avogadro constant, depends on the composition and density ρ of the material, in our case air, one has to consider the parameters influencing it.

5.1.2 Environmental parameters

The composition of air, considering its most important constituents, is, for example, defined by the National Institute of Standards and Technology (NIST) at a standard temperature and pressure (STP) of 0% relative humidity (*RH*), 20 °C and 1,013.25 *hPa*, with a density of 1.20479 *mg cm*⁻³. The relative fraction by weight and the molecular composition of air and water vapor for its individual nuclides are given in Table 5.1. In the case of a gas mixture, for example with water vapor, Dalton's law of partial pressure can be applied to

calculate the individual composition. This law states that total pressure p_t is the sum of partial pressures [142]

$$p_t = p_{air} + p_{water} \quad (5.8)$$

According to the ideal gas law $pV = nRT$, the fractional number of air (n_{air}) and water (n_{water}) molecules in a volume can be calculated via Equations 5.9

$$n_{air} = (p_t - p_{water}) / p_t \quad (5.9a)$$

$$n_{water} = p_{water} / p_t \quad (5.9b)$$

where the partial pressure of water vapor depends on the relative humidity, which is defined as the ratio of the partial pressure over the saturated vapor pressure $RH = p_{water} / p_{vapor}$. For a known temperature the saturation vapor pressure can be calculated via the Goff-Gratch equation [116],

$$\begin{aligned} \log_{10}(p_{vapor}) = & 8.13 \left(10^{-3.49 \left(\frac{373.16}{T} - 1 \right)} - 1 \right) \cdot 10^{-3} - 1.38 \left(10^{11.34 \left(1 - \frac{T}{373.16} \right)} - 1 \right) \\ & \cdot 10^{-7} - 7.90 \left(\frac{373.16}{T} - 1 \right) + 5.03 \log_{10} \left(\frac{373.16}{T} \right) + \log_{10}(1, 013.25) \end{aligned} \quad (5.10)$$

where T is the temperature in Kelvin and the resulting pressure is given in Pascal. Figure 5.1 demonstrates the very good agreement of Equation 5.10 with actual experimental data. Therefore, using Equations 5.9 and 5.10, it is possible to calculate the fractional number of molecules, which, when multiplied by the values given in Table 5.1, leads to the individual nuclide percentage the medium, in this case air, is composed of. ^{222}Rn itself has in general no significant fractional part of air. For example consider a relatively high ^{222}Rn concentration of $C = 1 \text{ kBq m}^{-3}$ that leads to a total number of $n = C / \ln(2) \lambda^{-1} = 476 \text{ cm}^{-3}$ of ^{222}Rn atoms per unit volume. Its density is then about $\rho = n M_{Rn} / N_A = 4.76 \times 10^2 \text{ cm}^{-3} \cdot 222 \text{ g mol}^{-1} / 6.022 \times 10^{23} \text{ mol}^{-1} = 0.176 \text{ pg m}^{-3}$. Hence ^{222}Rn contributes only insignificantly to the general composition of air ($\rho_{air} = 1.2 \text{ kg m}^{-3}$) and is therefore a negligible constituent, for radiation transport simulations.

The second input parameter Geant4 requires for defining a material is its density. The ideal gas law $pV = nRT$, combined with Dalton's law, yields Equation 5.11 for the calculation of the air density ρ ,

$$\rho = \frac{p_{air} M_{air}}{R T} + \frac{p_{water} M_{water}}{R T} \quad (5.11)$$

where M_{index} is the molecular mass of the respective gas. Equation 5.11 is sufficiently accurate, since a comparison to the recently revised air density formula of the Comité International des Poids et Mesures (CIPM) [131], shows a deviation of less than 1‰ for temperatures between -20 and $100 \text{ }^\circ\text{C}$.

5.1.3 Assumptions

The developed simulation is time-independent, which means at static conditions without diffusion processes and the precondition of a equilibrium between mother and daughter

Table 5.1: Composition of dry air and water vapor at standard temperature and pressure (STP)

Nuclide	Atomic number	Mass fraction
C	6	0.000124
Ar	18	0.012827
N	7	0.755267
O	8	0.231781
H	1	0.111894
O	8	0.888106

nuclides. For ^{222}Rn this is reached after about 7 h and for ^{220}Rn after 70 h (see Section 2.2). Only the decay of alpha-particle emitters is considered, i.e. $^{222}\text{Rn} \rightarrow ^{218}\text{Po} \rightarrow ^{214}\text{Po}$ for radon and $^{220}\text{Rn} \rightarrow ^{216}\text{Po} \rightarrow ^{212}\text{Bi} \rightarrow ^{208}\text{Tl}$ and $^{212}\text{Po} \rightarrow ^{208}\text{Pb}$ for thoron. For ^{222}Rn the ratio is 1:1:1 and for ^{220}Rn 1:1:0.36:0.64 respectively. Beta decays and δ -electrons are disregarded, since their deposited energies are in general way below the energy threshold of the detection system of approximately 1 MeV, and even when exceeding it, assumed to contribute mainly to the electronic noise. The radioactive and inert gas is assumed to decay within the volume, while the progeny alphas are assumed to originate from the wall and detector surfaces (except ^{216}Po). The deposition fraction of progeny on housing walls for cylindrical dimension up to 100 mm (height, diameter) is mostly > 0.9 for ^{218}Po and unity for ^{214}Po , ^{212}Po and ^{212}Bi [139], depending on the employed diffusion coefficient. For common detector geometries, which generally have a small volume, all deposition fractions are essentially equal to one [211]. All simulations performed in the framework of this thesis assume a unity deposition fraction for ^{218}Po , ^{214}Po , ^{212}Po and ^{212}Bi . The ^{216}Po progeny, with a half-life of about 150 ms, has insufficient time for deposition on the surfaces, and it is more likely to decay within the volume. In conclusion the following nuclides are considered:

- ^{222}Rn , ^{220}Rn and ^{226}Po randomly decay, with respect to origin and direction, within the simulation volume as well as the surfaces.
- ^{218}Po , ^{214}Po , ^{212}Bi and ^{212}Po randomly decay on the surfaces of the volume, including detector surfaces.

Accordingly ^{222}Rn and most of its progeny are therefore distributed via a uniform probability density function (PDF) within the volume and the surface.

$$P(x)_u = \begin{cases} 1 / (x_{max} - x_{min}) & \text{if } x_{min} \leq x \leq x_{max} \\ 0 & \text{otherwise} \end{cases} \quad (5.12)$$

where $P(x)_u$ is the PDF. For thoron and its first progeny (^{216}Po), which immediately follows its decay, the diffusion length L has to be considered, as the concentration decreases exponentially from the entry point (Equation 2.11). The function to generate values subject

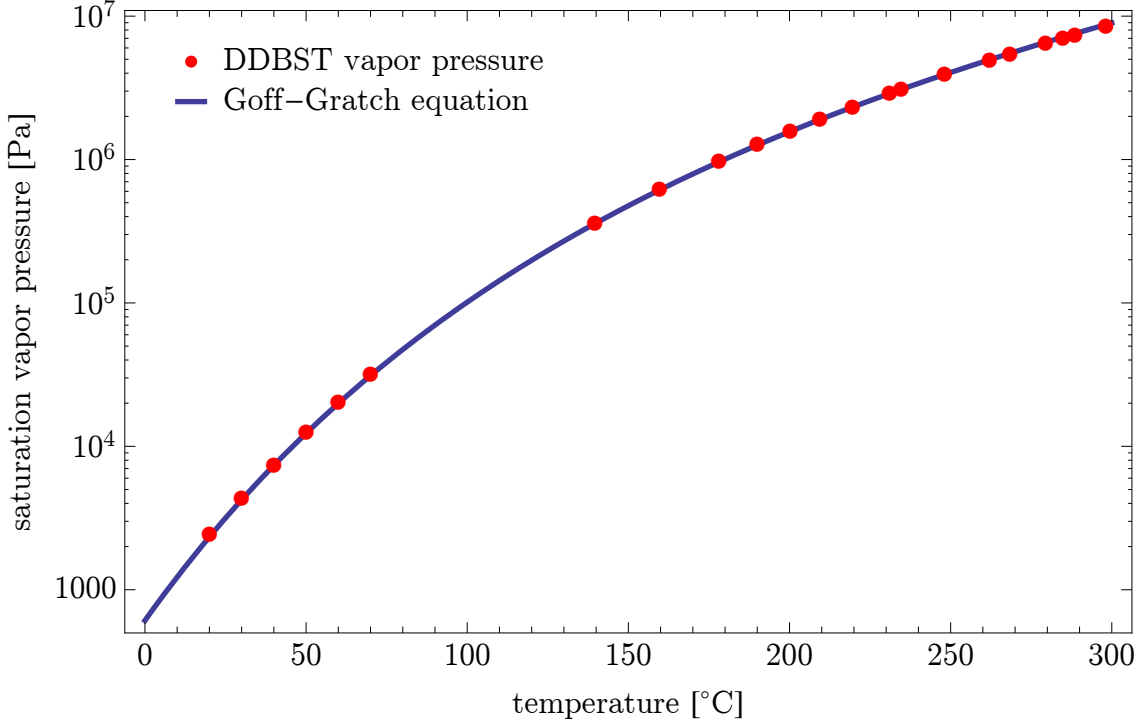


Figure 5.1: Goff-Gratch approximation (Equation 5.10) used for the simulation described below and experimental data [31] of saturated vapor pressure are in well agreement.

to an exponential PDF can be inferred by using an uniform PDF via equating it to the inverse exponential cumulative distribution function (CDF), the so called inverse transform technique [33], which yields,

$$f(x_{max}) = -1/\lambda \log_{10}[1 - (1 - e^{-x_{max} \lambda}) u] \quad (5.13)$$

where $u \in [0, 1]$ and $\lambda = 1 / L$. Equation 5.13 generates random values between 0 and x_{max} in a truncated form, which is necessary to simulate volumes with boundaries.

The generation of arbitrary angles for the polar angle θ and azimuthal angle ϕ , which populate a sphere uniformly, can be achieved by choosing u and v to be random variates on $[0, 1]$, where

$$\phi = 2 \pi u \quad (5.14)$$

$$\theta = \cos^{-1}(2 v - 1) \quad (5.15)$$

since the area element $d\Omega = \sin\phi d\theta d\phi$ is a function of ϕ and thus a uniform sampling of $\theta \in [0, \pi]$ and $\phi \in [0, 2\pi]$ would be incorrect. In order to save computation time it is possible to only consider particles decaying into to direction of the detectors, thus into a 2π solid angle. The only change necessary is $v \in [0, 0.5]$, which means that only half of the number of real decays needs to be calculated in the simulation.

The histogram of all resulting values, i.e. the energies deposited in the detector, yields a simulated spectrum with a discrete number of energies. In order to achieve a better agreement between simulation and measurement, however, one has to consider the energy broadening introduced by the amplification stage (Section 3.2.5). This is generally done by applying the Gaussian energy broadening (GEB) method [207], via multiplication of each individual energy bin value with a normalized Gaussian function. The one dimensional function is given by,

$$f(E) = \frac{1}{\sqrt{2\pi}\sigma} e^{-\frac{E^2}{2\sigma^2}} \quad (5.16)$$

where σ is the standard deviation, which is related to the *FWHM* energy resolution ΔE of the detector system via $\Delta E = 2\sqrt{2 \ln 2} \sigma$ [133]. After equation 5.16 has been applied to each value, only the total in each energy bin of the overlying functions has to be taken,

$$S(E) = \sum_{i=1}^n \frac{1}{\sqrt{2\pi}\sigma} e^{-\frac{(E-E_i)^2}{2}\sigma^2} N_i \quad (5.17)$$

where n is the number channels, E_i the respective energy of the channel and N_i its accumulated number of events. Equation 5.17 results in a smoothed and realistic version of the simulated spectrum. The corresponding energy resolution ΔE has been determined in Section 3.2.5.

5.1.4 Geometry

The two device geometries, which were realized, were also implemented in the Monte Carlo simulation. Only the volume of the inner housing is considered, which has the following approximate dimensions:

- Geometry 1: 108 mm × 57 mm × 26 mm (length × width × height)
- Geometry 2: 116 mm × 90.5 mm × 47 mm (length × width × height)

which are the dimensions stated in Figure 3.10, where the housing wall thickness was subtracted. In the simulation only the distance between the detector surface and upper housing wall are relevant for the height, since all decays lower to it, as for example from progeny attached to the bottom or gas below the printed circuit board (PCB), are very unlikely able to reach the detector, and thus generate a significant amount of events. This is due to the low cross section of elastic nuclear scattering of alphas, and simulations with a source at the detector bottom hardly produces events. For example a simulation with $1.5 \cdot 10^5$ events each from ^{218}Po and ^{212}Po decaying at the bottom in upward direction only produced a total of 5 counts, which is negligible compared to the over 15,000 counts when considering the top wall of geometry 1 as source. Most probably these 5 counts were generated from decays entering the sensitive detector volume from the side or from below, as the particle scorer does not discriminate between decay directions, and not from scattering on air molecules. Therefore these decays were not simulated further, the area and

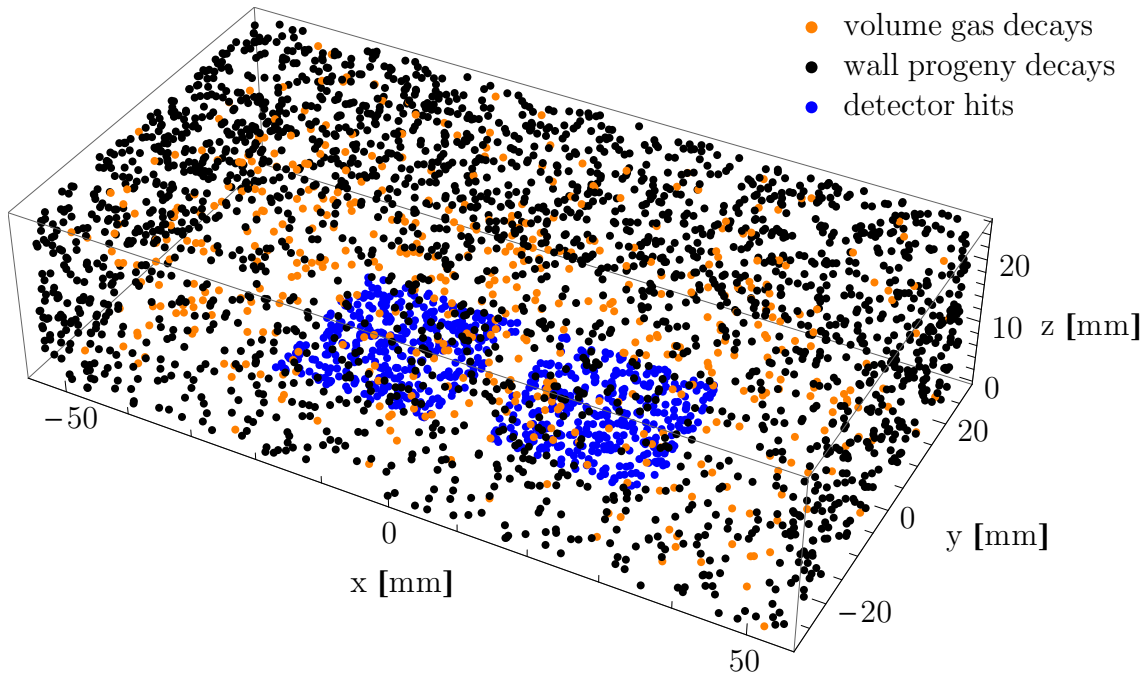


Figure 5.2: Schematic representation of exposimeter geometry 1 with random decay origins from volume and walls. Decays from the bottom area are not calculated since these cannot hit the detectors.

volume, however, is still considered when weighting the progeny deposition. The geometry was parametrized with a single rectangular form, as shown in Figure 5.2. The detector is modeled as a combination of two materials. At its top is a 400 nm layer of aluminum followed by a 0.5 mm thick silicon bulk. The width and length of the detector was set to 24.8 mm . When an alpha particle enters the detector its energy deposition within the volume is scored and saved for output. The histogram of events, using a fixed energy bin width and applying a Gaussian smooth function (Eq. 5.17), accounting for the energy resolution of the system, then results in the alpha spectrum detected by the device.

5.2 Transport code result comparison

The Geant4 simulation framework is a proven and valuable tool for development tasks in various fields such as detector development for space and medicine applications [4]. To model alpha particle energy loss as described by Equation 5.7, Geant4 relies on data driven models, which use ICRU 49 data [66] as hard-coded tables. The transport process also considers statistical fluctuations in the rate of the interactions what is seen as “straggling”, i.e. a distribution of particle ranges. The electro-magnetic interactions with the nuclei cause Rutherford scattering and are seen as small (and occasionally large) changes in the direction. However, the more frequent interactions occur with the shell electrons, that are

Table 5.2: Individual contributions to the sum spectra of Figure 5.3 for the two different transport codes in Geant4 (G4) and Analytic (AN) (ASTAR based) simulation.

Simulation	Nuclide	²²² Rn	²¹⁸ Po	²¹⁴ Po		Sum
G4	counts	15,785	10,498	11,150		37,433
	fraction	0.42	0.28	0.3		1
AN	counts	19,423	9,499	10,050		38,972
	fraction	0.5	0.24	0.26		1
	Nuclide	²²⁰ Rn	²¹⁶ Po	²¹² Bi	²¹² Po	Sum
G4	counts	16,043	15,973	4,211	7,911	44,137
	fraction	0.36	0.36	0.1	0.18	1
AN	counts	19,058	19,361	4,385	8,283	51,086
	fraction	0.37	0.38	0.09	0.16	1

the dominant processes contributing to the kinetic energy loss, which is seen as quite a steady energy loss. The Geant4 simulation developed in the framework of this thesis uses the QGSP_BERT_HP physics list, which is recommended for low energy dosimetric applications. While there is little doubt about the accuracy of the calculations performed by Geant4, the final result is still prone to errors due to the many options and thus possible flaws the application developer can introduce.

In order to cross check any possible issues also an analytic simulation relying on the NIST alpha stopping power and range (ASTAR) database [11] was developed, which itself is a program based on the ICRU 49 report [129]. Therefore a comparison of simulation results at STP conditions should yield similar results, thus implying correctness of the Geant4 calculations within the boundaries of the introduced assumptions. This verification method is in general suggested for Monte Carlo simulations concerning alpha particle transport [47].

The analytical program, implemented in *Wolfram Mathematica 9.0.1*, uses the same starting conditions as the Geant4 simulation, with random generation of alpha particle sources in volume and on walls as well as random decay directions into the 2π solid angle facing the detector. However, particle transport is based on an analytic approach, meaning an energy loss is only calculated along the straight line through air and aluminum from the origin to the entry point at the detector. All decays not hitting the detector are not calculated. The kinetic energy loss dE is approximated by linear iterative steps along the ASTAR stopping power dE/dx . Again the simulation is more accurate the smaller the step length, as a constant energy loss per step is required. Using the available NIST values, however, denies the possibility to change the air composition. Only the air density can act as parameter on the stopping power. A total number of $n = 150,000$ events per decay energy was simulated and all results were smoothed via Equation 5.17, with $\Delta E = 150 \text{ keV}$, to account for the Gaussian energy broadening of the electronics.

Figure 5.3 demonstrates the overall good agreement of the simulated spectra. The progeny

peaks lie at the same energy bins and there is a general amplitude correspondence over the whole energy range. In Table 5.2 the individual events composing the simulated spectra are stated. There is a good agreement between the surface progeny decay counts between both simulations, while for volume based decays one finds a deviation of about 23% for ^{222}Rn , 19% for ^{220}Rn and 21% for ^{216}Po . This is due to the fact that the analytic simulation does not consider range (longitudinal) nor directional (lateral) straggling, which has more influence with the long distances in air, thus leading to more registered events, due to the made simplification of straight movement paths. Straggling and scattering are less dominant for short paths, as for example in the aluminum layer, where the values of both codes are essentially the same within the 95% confidence interval of the involved statistical uncertainty.

With the stated number of events and the volume of geometry 1 ($V = 1.6 \cdot 10^{-5} \text{ m}^3$), the concentration of either ^{222}Rn or ^{220}Rn is given by $c_n = n V^{-1}$. The theoretical time interval t can be chosen freely, since the simulation has no time dependence, thus the activity concentration is $C = n V^{-1} t^{-1}$. The number of accumulated events c is assigned the unit counts per time interval (cpt), i.e. $c t^{-1}$, where the calibration factor cf is then calculated via $cf = C/c = n V^{-1} t^{-1}/c$ with units $\text{Bq m}^{-3}/\text{cpt}$. For convenience one hour ($t = 3600 \text{ s}$) is used here, since generally the calibration coefficient is stated per counts per hour (cph). Accordingly the activity concentration in the performed simulation was $C = 520651 \pm 33811 \text{ Bq m}^{-3}$, where the error has been calculated via error propagation and assuming a geometric length uncertainty of 1 mm . The resulting calibration factors for ^{222}Rn at STP are then, when integrating over the whole energy spectrum, $17.77 \pm 1.16 \text{ Bq m}^{-3}/\text{cph}$ and $17.07 \pm 1.11 \text{ Bq m}^{-3}/\text{cph}$ according to the Geant4 and Analytic simulations respectively, i.e. only a deviation of about 4% is noted. For thoron the according calibration factors are $14.68 \pm 0.96 \text{ Bq m}^{-3}/\text{cph}$ and $13.02 \pm 0.85 \text{ Bq m}^{-3}/\text{cph}$, meaning the deviation is approximately 13%. However, within their error boundaries the stated values are essentially the same. The absolute amplitude and energy correspondence of both simulations suggests that there are no major uncertainties in the applied Geant4 simulations. Additionally, measurement results and Geant4 simulations are compared in the next section.

In terms of computing time the analytic approach is much more efficient, as it requires only about 4 minutes to finish one simulation run, while Geant4 takes about 130 minutes to complete, i.e. about 30 times more. This is to be expected as in Geant4 all decays, whether or not they produce an event in the detectors, are calculated. In addition the energy loss calculation is much more complex.

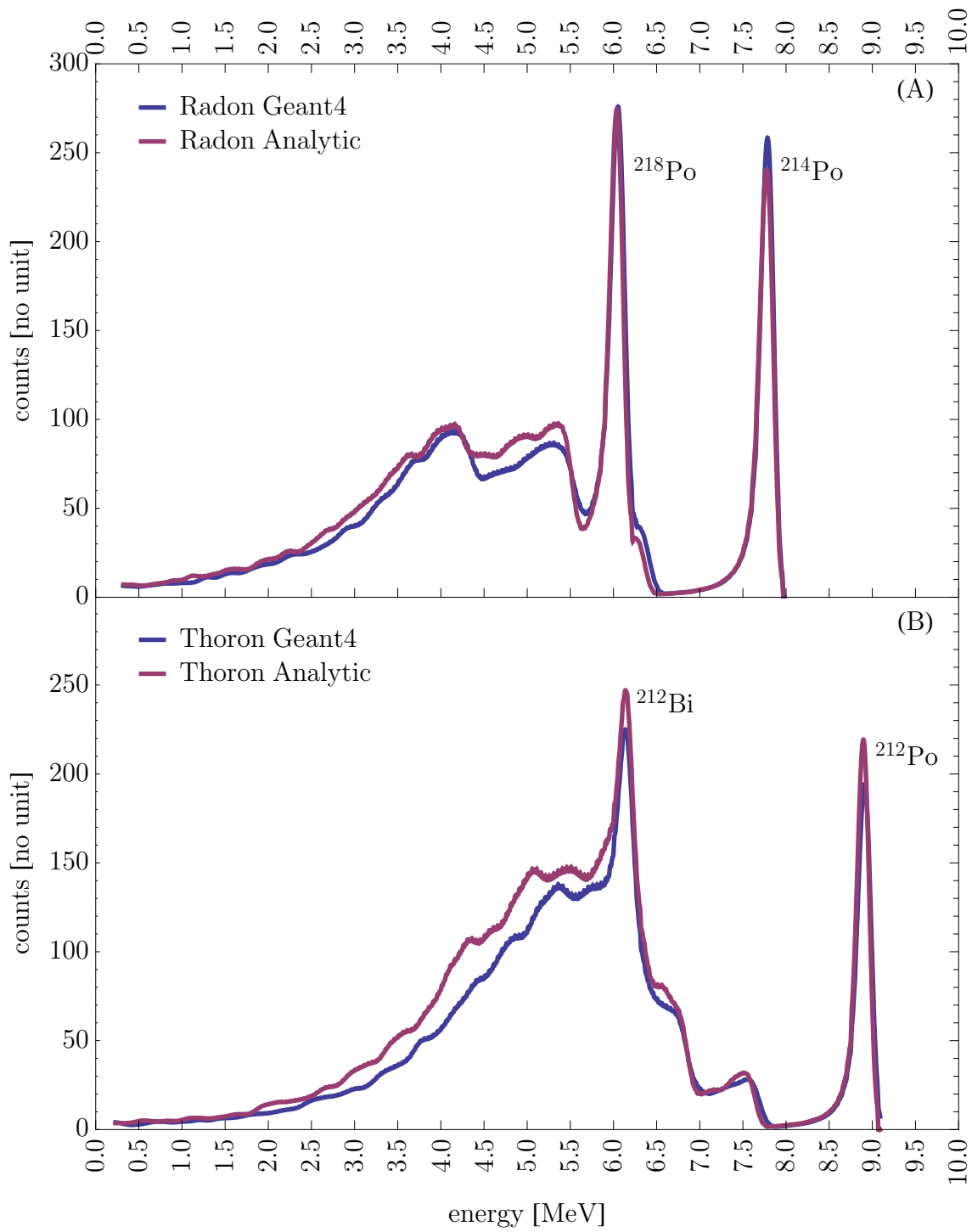


Figure 5.3: Simulated spectra for ^{222}Rn (A) and ^{220}Rn (B) environments at STP for geometry 1, show reasonable agreement between Geant4 and Analytic transport code.

5.3 Results

The main goal of the simulations performed was to reproduce the alpha particle spectra measured in either a ^{222}Rn or ^{220}Rn rich environment. The normalization factor to compare simulation and measurement spectra depends on the total count number ct and the decays/events N that occurred. If all other relevant influencing parameters are considered in the simulation, one is able to model the measurement conditions realistically. Then the quotient of the observed count number ct over the number of total decays is the same as in the simulation,

$$\frac{ct_m}{N_{actual}} = \frac{ct_s}{N_{sim}} \quad (5.18)$$

where ct_m and ct_s are the counts in the measurement and the simulation, respectively. The total number N_{actual} of airborne ^{222}Rn or ^{220}Rn decays in Equation 5.18 can be estimated from the known reference concentration $C(t)$ via,

$$N_{actual} = V \int C(t) dt \quad (5.19)$$

where V is the chamber volume of the exposimeter. Hence according to Equation 5.18 a simulated spectrum needs to be multiplied by N_{actual}/N_{sim} , when comparing absolute count numbers per channel, where the number of decays is calculated via Equation 5.19. The calibration factor for a simulated spectrum, on the other hand, depends on the events, the volume and the count number. The simulated activity concentration C_s is given by,

$$C_s = \frac{N_{sim}}{V t} \quad (5.20)$$

where the time interval t can be chosen freely for any $t > 0$, since the simulation is time independent. The simulated observed counts ct_s are assigned the unit counts per time interval (cpt). The calibration factor cf is then calculated according to Equation 4.3 via,

$$cf_{sim} = \frac{C_s}{ct_s} = \frac{N_{sim}}{V t ct_s} \quad (5.21)$$

In the following t is set to 3600 seconds for ease of comparison, which yields a calibration factor unit of $Bq m^{-3}/cph$. In all the results presented the number of simulated decays was $1.5 \cdot 10^5$ directed into the 2π solid angle facing the detectors, which equals an actual decay number of $N_{sim} = 3 \cdot 10^5$ when considering the 4π solid angle.

5.3.1 Radon calibration factors

Several calibration measurements in standard laboratory conditions were performed. Temperature and pressure were not controllable but continuously monitored. Here the typical acquired spectra for two different geometries in a ^{222}Rn environment are discussed. The mean environmental conditions during the calibration period between hour 85 to 115 were

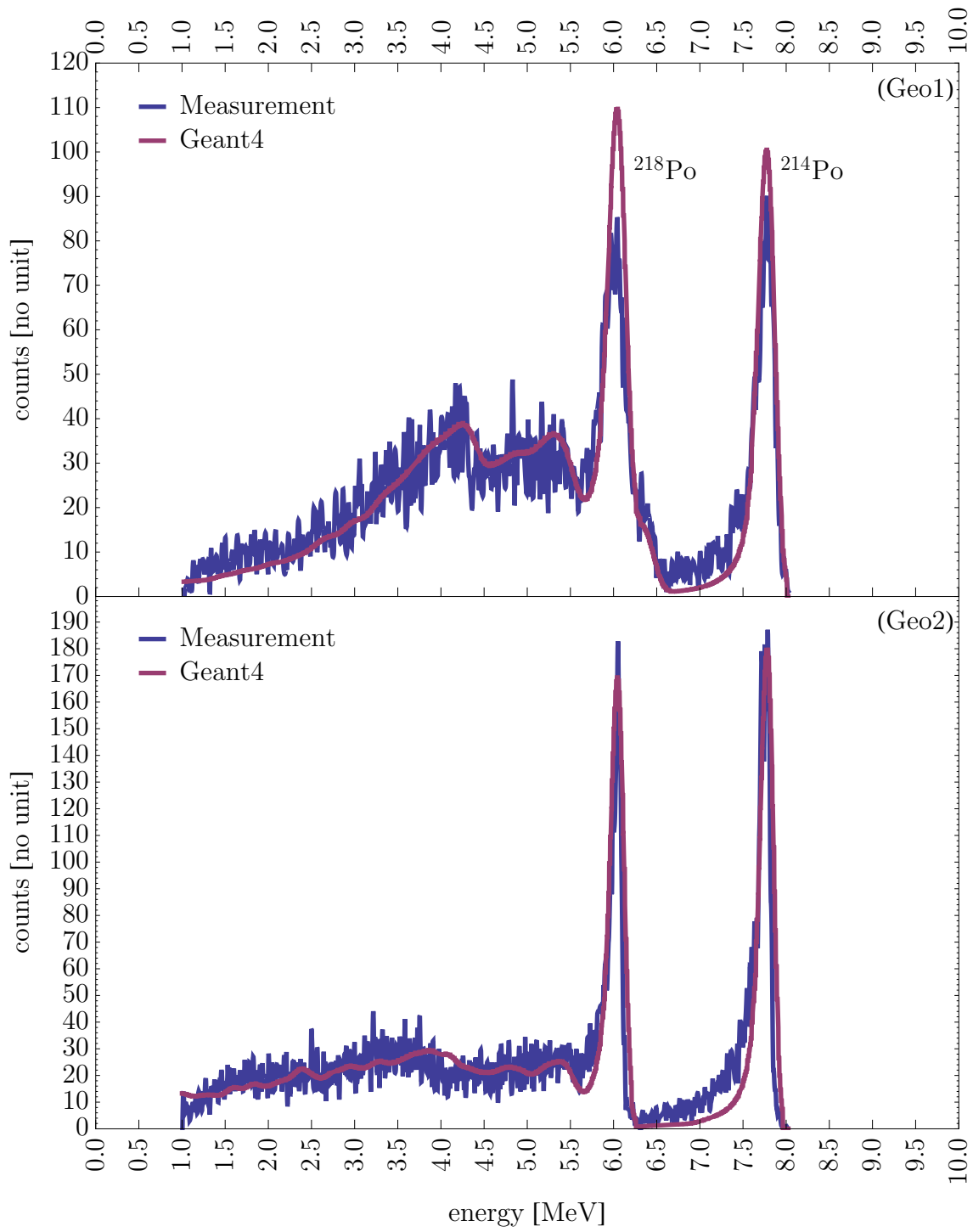


Figure 5.4: Simulated and measured spectra in a ^{222}Rn environment for geometries 1 (Geo1) and 2 (Geo2).

45% RH , 16.3 °C and 96,836 Pa . The mean ^{222}Rn concentration was $6,866 \pm 331 Bq m^{-3}$ while only negligible ^{220}Rn was present ($7 \pm 27 Bq m^{-3}$). The total exposure due to ^{222}Rn was $212,830 \pm 1,845 Bq h m^{-3}$. Two exposure meters with standard and large dimensions, named geometry 1 and 2 (see Section 5.1.4), have been calibrated to demonstrate the influence of housing size. Geometry 1 has a volume of $124.4 cm^3$ and geometry 2 of about $493.4 cm^3$. Therefore the number of occurred decays N during the measurement within the respective volume and the given ^{222}Rn concentration can be calculated via Equation 5.19, which are $N_{geo1} = 122,633$ and $N_{geo2} = 378,042$. The normalization factor for comparing measurement and simulation is calculated via equation 5.18. The total number of measured and simulated counts as function of energy are shown in Figure 5.4. Energy calibration was performed by evaluating the channel number of the clearly visible progeny peaks, assigning the energy according to the calculated value, and assuming a linear energy-channel relationship.

One finds a reasonable agreement between absolute counts per channel as well as in the general energy dependence. This is particularly noteworthy since the simulation was not adjusted via any least-squares fit, but only via the factor N_{geo}/N_{sim} , where the number of simulated events was $N_{sim} = 3 \cdot 10^5$, and the number of occurred decays N_{geo} depends on the values measured by the reference device. This indicates that the most important factors influencing the shape and count number of the acquired spectrum have been considered. The characteristic quantity of a radon monitor is, however, its calibration factor, which for any simulation can be calculated via Equation 5.21. The simulated calibration factor is completely independent on any reference concentration measurements. The number of simulated counts ct_s is integrated from 1 to 10 MeV , using the same energy bin width as the corresponding measurement device. For geometry 1 the measured calibration factor was $cf_{meas} = 16.9 \pm 0.2 Bq m^{-3}/cph$ (mean±std) which is very close the simulated one of $cf_{sim} = 16.8 \pm 0.7 Bq m^{-3}/cph$, where the error was calculated via Gaussian error propagation, assuming a geometric uncertainty of 1 mm . For geometry 2 the measurement yielded values $cf_{meas} = 11.3 \pm 0.5 Bq m^{-3}/cph$ and $cf_{sim} = 10.7 \pm 0.3 Bq m^{-3}/cph$. The relative differences are hence about 1% and 6%, respectively, which is acceptable.

In an additional experiment, an external membrane pump was connected to the small calibration chamber, to lower the pressure inside the calibration chamber, thus mimicking a different altitude level. The environmental condition reached stable values between hours 7-61 of about 24% RH , 23.9 °C and 77,259 Pa which equals an approximate height of 2229 m according to the international barometric formula [58] that also accounts for the temperature altitude dependence. The mean ^{222}Rn concentration was $1,462 \pm 154 Bq m^{-3}$ while the ^{220}Rn concentration was $182 \pm 97 Bq m^{-3}$, which was considered to be negligible. The radon exposure according to the Rad7 reference device was about $90,630 \pm 1,214 Bq h m^{-3}$ resulting in estimated occurred decays during that time of $N_{geo1} = 52,221$ and $N_{geo2} = 160,983$. Dividing this number by the simulated events N_{sim} yields the factor with which the simulation has to be multiplied. The resulting spectra are shown in Figure 5.5, where again one notices a very good agreement in shape and amplitude. For geometry 1 the measured calibration factor was $cf_{meas} = 17.6 \pm 0.3 Bq m^{-3}/cph$ (mean±std), again very close the

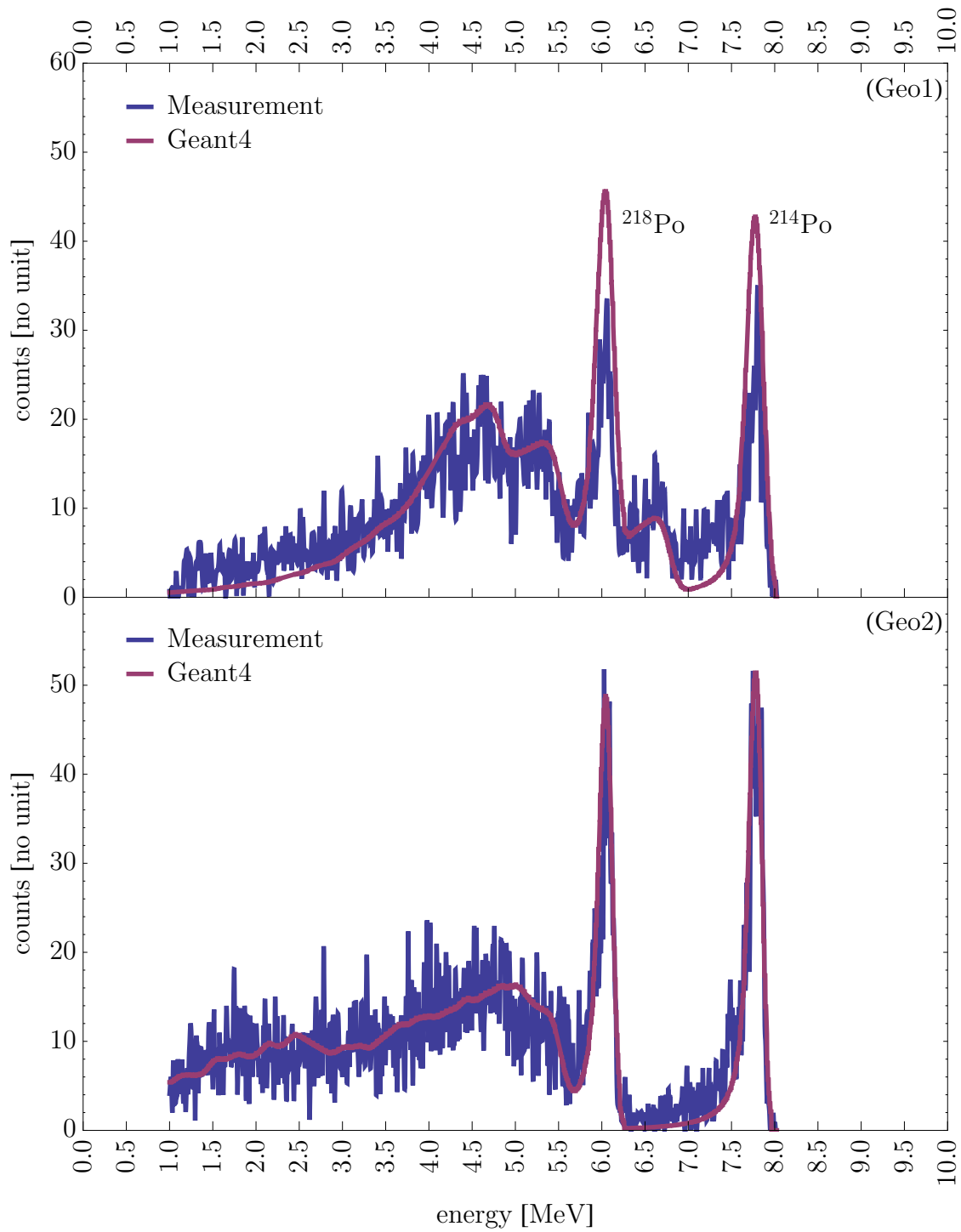


Figure 5.5: Simulated and measured spectra in a ^{222}Rn environment at an altitude equivalent of about 2229 m for geometries 1 (Geo1) and 2 (Geo2).

simulated one of $cf_{sim} = 16.4 \pm 0.7 \text{ Bq m}^{-3}/\text{cph}$ while for geometry 2 results yielded factors of $cf_{meas} = 11.3 \pm 0.2 \text{ Bq m}^{-3}/\text{cph}$ and $cf_{sim} = 11.2 \pm 0.3 \text{ Bq m}^{-3}/\text{cph}$. The relative differences are about 7% and 2%, respectively, and are of the same order of magnitude as the calculated error of the simulation. This means that the simulation can accurately determine the calibration factor for dimensional and environmental changes with sufficient accuracy.

As examples, in Figure 5.6 the individual contributions of the various involved alpha-emitters to the spectra under the different ambient pressures of Figures 5.4 and 5.5 for geometry 1 are shown. Lowering the ambient pressure causes a decrease in air density (Equation 5.11) which in turn reduces the energy loss of alphas traversing the volume according to Equation 5.7. This is to be expected as a lower number of air molecules implies less chances of occurring interactions and thus less ionization energy losses. The result is a shift to higher energies of all alphas reaching the detector that were either of airborne origin or deployed on surfaces other than the detector itself. In Figure 5.6 this is most recognizable for progeny decays $^{218}\text{Po}_{wall}$ and $^{214}\text{Po}_{wall}$ from volume surfaces. In contrast, direct decays on the detector surface are not influenced by environmental changes since the aluminum layer determining the energy loss hardly changes its dimension. The thermal expansion coefficient of aluminum is about $24 \cdot 10^{-6} \text{ K}^{-1}$ and for a temperature change of 50 K the thickness of 400 m changes about 0.48 nm , i.e. about 0.1% of the total thickness. Due to uniform expansion in all directions, the density of the material remains the same. Thus the energy absorbing behavior of the top layer is not influenced at all by ambient temperature, pressure or relative humidity changes as long as no water condensates on the surface.

In Table 5.3 the count number for the two geometries and pressures of the simulation results are stated. Here, the count number is the actual total number of registered events. The main contribution to the total count number arises from airborne ^{222}Rn decays for both devices and is about 40%. While the composition and absolute number of the registered event changes only little for geometry 1, the bigger housing is more influenced by environmental changes. This is of course due to the longer paths that alpha particles have to cross in the larger housing. The sum differs about 3% for Geo1 and 19% for Geo2. Higher count rates in low density environments are also to be expected as this enables more alpha particles reaching the detector above the threshold energy of 1 MeV . One has to note that the absolute number of counts is less in geometry 2 since the number of simulated events N_{sim} was in both the same resulting in a lower concentration for larger volumes. With equal concentrations the number of counts would be actually higher for Geo2 than for Geo1, due to the lower calibration factor for geometry 2.

Further one notices somewhat broader peaks for Geo1. The difference originates from the characteristic properties of the employed amplification system of the individual devices. The electronics in Geo2 used updated hardware with better ADC resolution and less noise, thus having a improved energy resolution. The FWHM of the applied Gaussian energy broadening was $\Delta E = 200 \text{ keV}$ for Geo1 and $\Delta E = 150 \text{ keV}$ for Geo2.

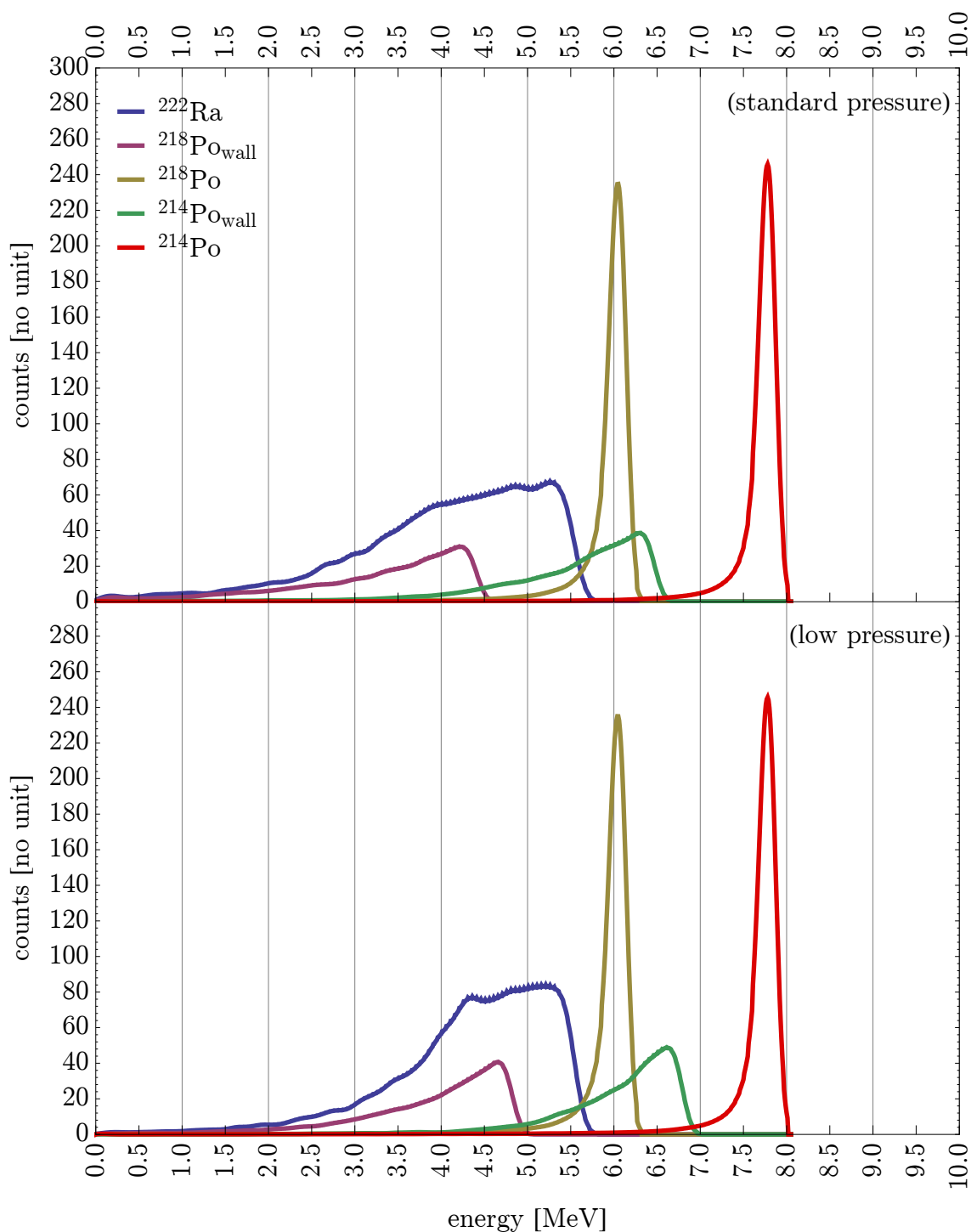


Figure 5.6: Individual contributions to simulated spectrum in a ^{222}Rn environment at equal concentrations but different ambient pressures (96,836 Pa and 77,259 Pa) for standard housing (Geo1). Lower air density causes energy shift to the right for decays traversing the volume. Index *wall* denominates contributions of progeny decays from surfaces of the housing.

Table 5.3: Individual contributions to the spectra of Figure 5.6 for the standard housing and different pressures, as well as for geometry 2.

Geo1	Nuclide	^{222}Rn	^{218}Po	^{214}Po	Sum
96,836 Pa	counts	16,040	11,765	12,262	40,067
	fraction	0.40	0.29	0.31	1
77,259 Pa	counts	16,569	12,183	12,339	41,092
	fraction	0.40	0.30	0.30	1
Geo2	Nuclide	^{222}Rn	^{218}Po	^{214}Po	Sum
96,836 Pa	counts	5,507	3,478	5,222	14,206
	fraction	0.39	0.24	0.37	1
77,259 Pa	counts	6,905	4,488	5,567	16,960
	fraction	0.41	0.26	0.33	1

5.3.2 Thoron calibration factors

In principle the simulation for ^{220}Rn is similar as that for ^{222}Rn except a different diffusion length has to be considered for ^{220}Rn . The activity concentration decreases exponentially from the inlet area as described in Section 5.1. The higher decay energies, however, lead to a fundamentally different spectrum. Again two measurements are compared with the corresponding simulation for the two available housing geometries. The standard housing (Geo1) spectrum was acquired under environmental conditions of about 46% RH, 23.4 °C and 96,861 Pa between hours 60-77 at a mean activity concentration of $8,263 \pm 332 \text{ Bq m}^{-3}$ for ^{220}Rn and $91 \pm 130 \text{ Bq m}^{-3}$ for ^{222}Rn . The exposure due to thoron was thus about $148,724 \pm 331 \text{ Bq h m}^{-3}$ resulting in estimated decays that occurred during that time of $N_{geo1} = 85,695$. The resulting spectrum (Fig. 5.7) is the same as shown in Figure 4.6. The bigger housing (Geo2) was calibrated during hours 60-85 at 44% RH, 24.2 °C, 96,100 Pa and a mean ^{220}Rn concentration of $3,916 \pm 259 \text{ Bq m}^{-3}$ (^{222}Rn : $69 \pm 117 \text{ Bq m}^{-3}$) was present. The thoron exposure measured by the reference device was about $101,811 \pm 1323 \text{ Bq h m}^{-3}$ and therefore $N_{geo2} = 180,842$. In Figure 5.7 the acquired spectra plus the corresponding simulation is shown. The simulated spectra are again in well agreement with those measured. However, the ^{216}Po progeny peak is more visible than expected while the ^{212}Po is overestimated and $^{212}\text{Po}_{wall}$ underestimated. The reason for this is most probably the complex diffusion behavior of decay products, which is not considered in the static simulation. Nevertheless, energy position and amplitude are considered to be reasonably simulated. Further one can recognize some counts beyond the right edge of the ^{212}Po peak at 9.16 MeV. Actually these originate from pileups due to the β^- decay (2.25 MeV) of ^{212}Bi which is directly followed by a ^{212}Po alpha decay ($\tau_{1/2} = 298 \text{ ns}$, see also Figure 2.3). If by coincidence an β^- , which has enough energy to generate a signal within the detector, is followed by an alpha decay, both signals are in superposition and add to an amplitude which is higher than the one which would be induced by a single alpha. As explained in Chapter 3 the distance between successive signals needs to be about 50 μs , that they can be distinguished, which is about 166 times

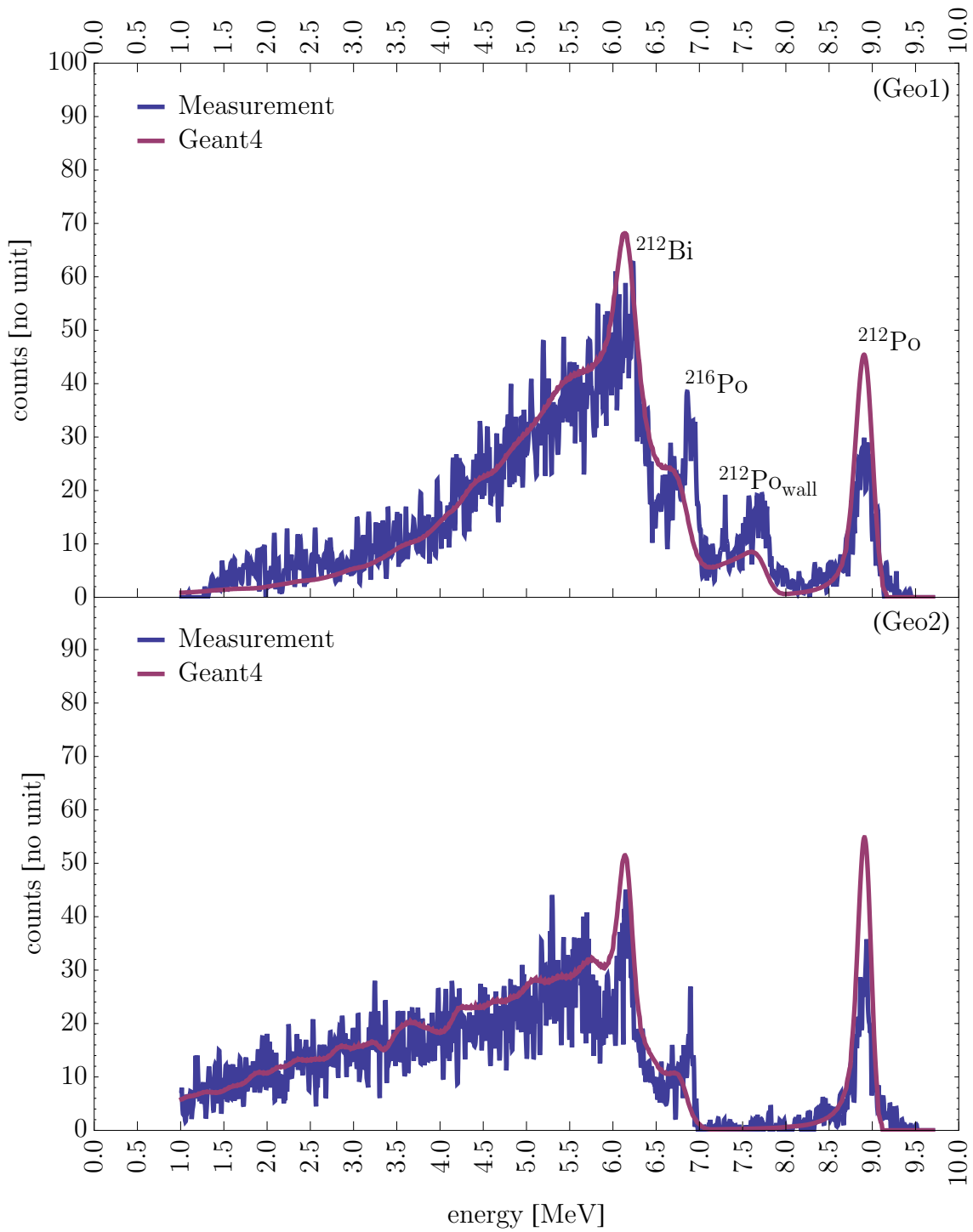


Figure 5.7: Simulated and measured spectra in a ^{220}Rn environment for geometries 1 (Geo1) and 2 (Geo2).

Table 5.4: Individual contributions to the spectra of Figure 5.6 for the different housings.

Case	Nuclide	^{220}Rn	^{216}Po	^{212}Bi	^{212}Po	Sum
Geo1	counts	16,463	16,609	4,276	7,867	45,216
	fraction	0.36	0.37	0.09	0.17	1
Geo2	counts	6,910	7,513	1,304	4,917	20,644
	fraction	0.33	0.36	0.06	0.24	1

the half-life of ^{212}Po . This favors the probability of pileups. For geometry 1 the measured calibration factor was $cf_{meas} = 14.4 \pm 0.8 \text{ Bq m}^{-3}/\text{cph}$ (mean \pm std), which again is very close to the simulated one of $cf_{sim} = 14.3 \pm 0.6 \text{ Bq m}^{-3}/\text{cph}$. On the other hand for geometry 2 the measured calibration factor was $cf_{meas} = 9.1 \pm 0.5 \text{ Bq m}^{-3}/\text{cph}$ while the simulated one was $cf_{sim} = 8.4 \pm 0.2 \text{ Bq m}^{-3}/\text{cph}$. The relative differences are hence only about 1% and 8% respectively, which is considered sufficiently accurate, given the general calibration accuracy. However, one has to keep in mind the high variation of the thoron calibration factor and thus the final amplitude of the acquired spectra, which can be in fact up to 17% in difference (Section 4.4.1). Accordingly, other measurement not shown here revealed higher difference of up to 12% between the simulated and the measured calibration factor. This however only affects the absolute count number per channel, and not the shape of the simulated spectrum. This is of course to be expected according to the results in Section 4.4.1.

In Figure 5.8 the individual contribution of the involved alpha-emitters to the spectra given in Figure 5.7 are shown, while the absolute numbers are stated in Table 5.4. The superposition of all individual parts composes the final spectrum, where airborne decays of ^{220}Rn and ^{216}Po contribute the major part to the total count number for both dimensions with about 73% and 69%, respectively. From an analytical point of view a distribution would be expected where ^{220}Rn and ^{216}Po contribute each 1/3 and ^{212}Bi plus ^{212}Po also account for 1/3 of the total counts. However, Table 5.4 indicates that the dimension of the diffusion chamber influences the contribution of each decay part to the whole spectrum. This can be explained by looking at a simple example of a cuboid chamber with length d . When the dimensions are increased, the inner surface increases proportional to $\propto d^2$ while the volume increases with $\propto d^3$, thus the amount of deposited progeny on the detector surface actually increases $\propto d$. The opposite is true for decreasing dimensions. The total number of registered counts is smaller for Geo2 since the number of simulated events N_{sim} was again the same in both cases, but due to the larger volume of the latter, the concentration was smaller.

5.3.3 Radon: calibration factor environmental dependence

While the previous section focused on the comparison between measurement and simulation, for a selection of results, this section focuses purely on simulation results and on a wider range of environmental parameters. In particular the dependence of the calibration

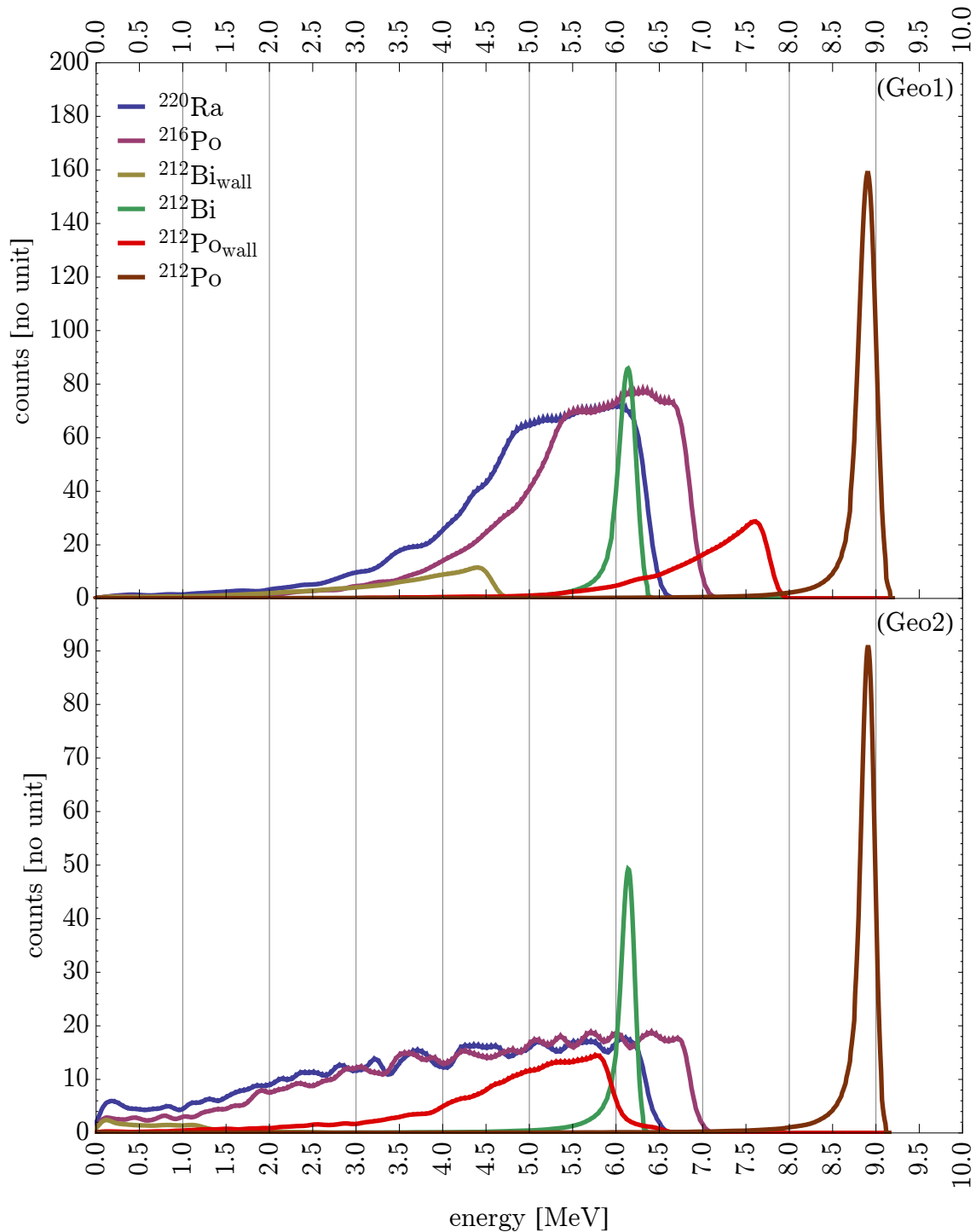


Figure 5.8: Individual contributions to simulated spectrum in a ^{220}Rn environment for standard housing (Geo1) and large housing (Geo2). Larger alpha particle path causes energy shift to the left for decays traversing the volume. Index *wall* denominates contributions of progeny decays from surfaces of the housing.

factor on the relative humidity, pressure (height) and temperature is discussed.

Relative humidity

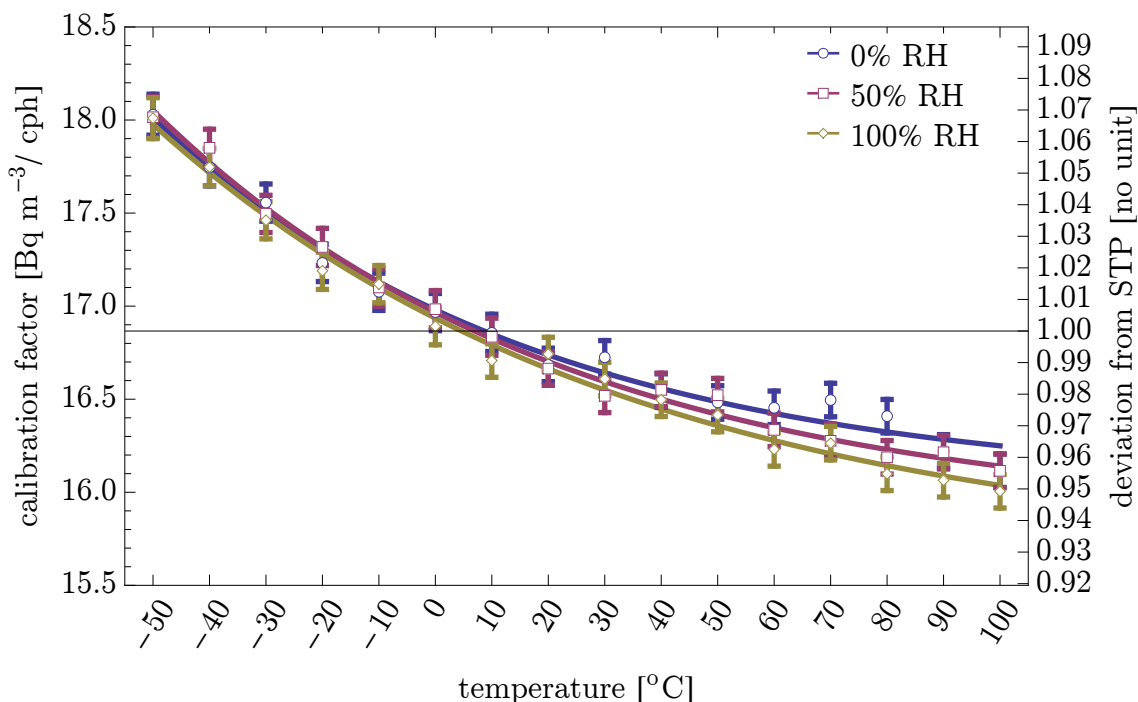


Figure 5.9: Radon calibration factor dependence on temperature and humidity for ex-posimeter with standard dimension (Geo1). Right scale indicates the relative deviation from the calibration factor at standard temperature and pressure (STP, 50% RH, 101,325 Pa and 20 °C). Error bars include 1σ statistical uncertainty only.

In general the most representative relative humidity level indoors is considered to be in the range of 40% to 60% [186]. In order to quantify the effect of changing the relative humidity, three levels with varying ambient temperature have been analyzed. The investigated temperature range between -50 to 100 °C can be deemed extreme and therefore not applicable to real world conditions. However, it demonstrates the maximal achievable difference. Three relative humidity levels, namely 0%, 50% and 100%, have been taken into account. One also has to note that the simulation, according to the proposed model, concentrates only on the energy absorption in the diffusion chamber and does not include the diffusion properties of the gas or decay products. While the mean free path and density of air can be assumed to be independent of the RH, the settling velocities and diffusion coefficients of particles in stagnant air are significantly affected by these factors [59]. This is, however, only relevant when volumes many times larger than those considered here are simulated, and thus their effects are neglected.

Figure 5.9 reveals that the change of humidity doesn't influence the calibration factor

Table 5.5: Fit parameter estimation with calculated standard error u ($\sqrt{\sigma^2}$) for the data given in Figure 5.9 and fitted by Equation 5.22.

RH	a	u(a)	b	u(b)	c	u(c)	R^2
%	$Bq\ m^{-3}/cph$		$Bq\ m^{-3}/cph$		$^{\circ}C$	$^{\circ}C$	
0	16.03	0.10	0.95	0.12	67.79	8.57	0.99999
50	15.86	0.08	1.11	0.10	73.49	6.48	0.99999
100	15.64	0.12	1.30	0.14	84.93	9.50	0.99999

much. The obtained simulation results have been fitted by a nonlinear function via the least squares method,

$$cf(x)_i = a + b \exp^{(-x/c)} \quad (5.22)$$

where x is for example the temperature in Celsius and the index i denominates the respective constant parameter such as humidity (or temperature), while cf is the calibration factor $Bq\ m^{-3}/cph$. Therefore also the unit of parameters a and b is the same as for cf , while c has the unit of the parameter under investigation. The parameter values for the three humidity levels are given in Table 5.5, where the coefficient of determination R^2 is also stated. The standard error u of a parameter is defined as the square root of the estimated error variance σ^2 . The parameter values of a , b and c are significantly different for each humidity level, though when comparing absolute results, the calibration factors differ less than 1% among each other in the range of -50 to $60\ ^{\circ}C$ for RH between 0% and 100% at the same temperature. This is in well agreement with results from a recent publication where it was found that the relative humidity does not change the calibration factor of alpha-track radon detectors significantly [211]. In this study the calibration factor was simulated for a RH range from 0%-100% but only at a constant temperature of $25\ ^{\circ}C$. At this condition no influence on the calibration factor is to be expected since at $25\ ^{\circ}C$ and 100% RH the partial mass fraction of hydrogen and oxygen in air is only about 3.5% and 25%, respectively, according to Equation 5.9, thus hardly changing the air composition (Table 5.1) and its alpha particle absorption behavior. However, with 100% RH and increasing temperatures the air composition is significantly affected, for example at an ambient temperature of $100\ ^{\circ}C$ air consist completely of water vapor, ie. 89% oxygen and 11% hydrogen. Accordingly one notices an increased relative deviation of the calibration factor between 0% and 100% RH with higher temperatures. However, the deviation can be considered negligible as it is at most about 1.3%. This indicates that the influence of the humidity in air on the calibration factor can be neglected. Therefore all further simulations within the framework of this thesis were performed at a 50% RH . The results obtained are of course only valid if no condensation of water vapor occurs, since any dew on the detectors would introduce an additional layer and therefore significantly alter alpha particle absorption.

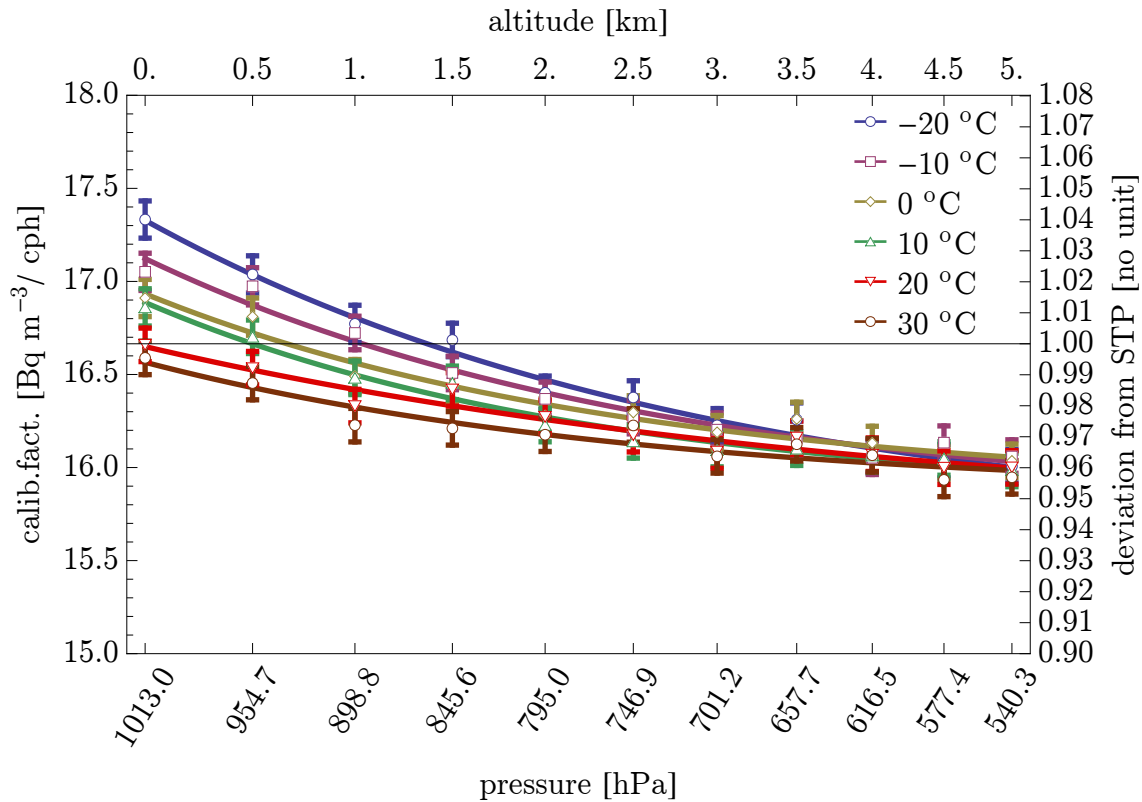


Figure 5.10: Radon calibration factor dependence on temperature and pressure for ex-posimeter with standard dimension (Geo1). Right scale indicates the relative deviation from the calibration factor at standard temperature and pressure (STP, 50% RH , 101,325 Pa and 20 °C). Error bars include 1σ statistical uncertainty only.

Temperature and pressure

Temperature and altitude increase, corresponding to a decrease in pressure, reduce the density of air and thus increase the range of alpha particles. Therefore, in general, more alpha particles can reach the detectors at decreased air density, which in turn lowers the calibration factor. A smaller calibration factor means that the device is more sensitive to ^{222}Rn or ^{220}Rn because equal concentrations generate a higher count rate thus improving the statistical uncertainty. Figure 5.10 shows the results of a simulation for different ambient conditions where the RH was fixed at 50%, the temperature ranged between -20 to 30 °C and the altitudes between 0 and 5,000 m , corresponding to a range in pressure from 101,325 to 54,030 Pa . The pressure was calculated via the international barometric formula [58] that takes also into account temperature decrease per altitude. The simulation results indicate an exponential dependence of the calibration factor with pressure (Equation 5.22). The corresponding parameters are stated in Table 5.6, where $x = dP$ is the pressure difference in Pa compared to standard pressure of 101,325 Pa at sea level.

The largest influence of the temperature on the calibration factor can be observed at sea

level where the relative difference between -20 and 30 $^{\circ}C$ is about 4.6%. The maximum relative difference of the cf between the lowest temperature and altitude (-20 $^{\circ}C$, 0 m) and the highest temperature and altitude (30 $^{\circ}C$, $5,000$ m) is about 8.6%. In general, the lower the pressure the less important is a temperature change. This is due to the fact that at higher altitudes already most of the alpha particles are able to reach the detectors, thus a further decrease of the air density is less significant. These results are in accordance with other findings where small volume monitors were barely affected by temperature or pressure changes [100, 211]. The parameters in Table 5.6 can be used to calculate the relative difference of the calibration factor at a certain condition, as a function of pressure and temperature, compared to the calibration factor at STP which is about 16.65 $Bq\ m^{-3}/cph$. Table 5.7 shows the resulting values and quantitatively demonstrates the little influence of changing environmental parameters for the standard housing.

When the volume of the diffusion chamber increases the effect of environmental changes

Table 5.6: Fit parameter estimation for ^{222}Rn calibration factor with calculated standard error u ($\sqrt{\sigma^2}$) for the data given in Figure 5.10 for geometry 1 and fitted by Equation 5.22.

Temp. $^{\circ}C$	a $Bq\ m^{-3}/cph$	u(a)	b $Bq\ m^{-3}/cph$	u(b)	c $\cdot 10^3\ Pa$	u(c)	R^2
-20	15.63	0.16	1.7	0.14	31.02	5.77	0.99999
-10	15.77	0.16	1.35	0.14	28.55	7.04	0.99999
0	15.88	0.15	1.05	0.13	26.29	8.13	0.99999
10	15.84	0.1	1.05	0.09	24.73	5.14	0.99999
20	15.69	0.3	0.96	0.28	41.85	22.35	0.99999
30	15.86	0.16	0.71	0.15	27.49	13.63	0.99999

Table 5.7: Relative difference of ^{222}Rn calibration factors compared to STP conditions calculated via Equation 5.22 employing values of Table 5.6 for standard housing (Geo1).

Altitude m	Pressure Pa	-20 $^{\circ}C$ %	-10 $^{\circ}C$ %	0 $^{\circ}C$ %	10 $^{\circ}C$ %	20 $^{\circ}C$ %	30 $^{\circ}C$ %
0	101,325	4.1	2.8	1.7	1.4	0.0	-0.5
500	95,461	2.3	1.3	0.4	0.1	-0.8	-1.3
1000	89,875	0.9	0.2	-0.5	-0.9	-1.4	-2.0
1500	84,557	-0.2	-0.8	-1.3	-1.7	-1.9	-2.4
2000	79,496	-1.1	-1.5	-1.9	-2.3	-2.4	-2.8
2500	74,684	-1.8	-2.1	-2.3	-2.7	-2.7	-3.1
3000	70,110	-2.4	-2.5	-2.7	-3.1	-3.0	-3.4
3500	65,766	-2.9	-2.9	-3.0	-3.4	-3.3	-3.6
4000	61,642	-3.3	-3.2	-3.2	-3.6	-3.5	-3.8
4500	57,730	-3.6	-3.5	-3.4	-3.8	-3.7	-3.9
5000	54,022	-3.9	-3.7	-3.6	-3.9	-3.9	-4.0

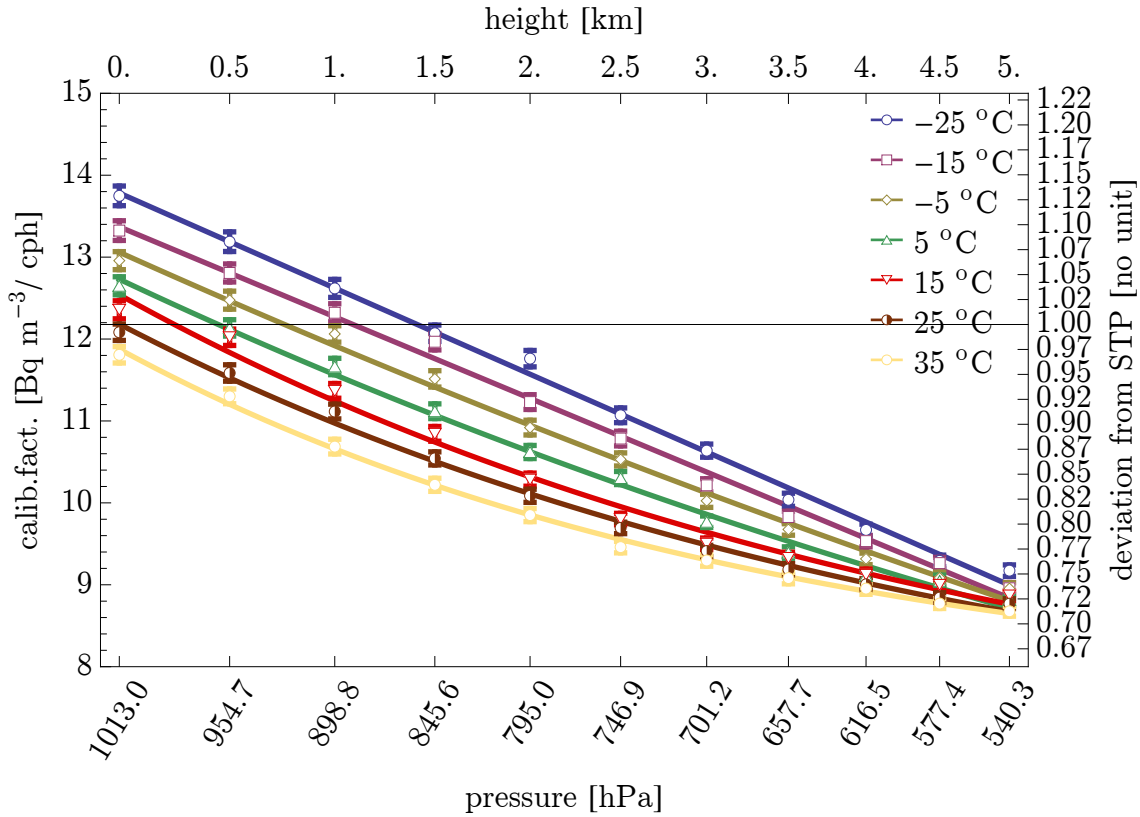


Figure 5.11: Radon calibration factor dependence on temperature and pressure for exposimeter with larger dimension (Geo2). Right scale indicates the relative deviation from the calibration factor at standard temperature and pressure (STP, 50% RH , 101,325 Pa and 25 °C). Error bars include 1σ statistical uncertainty only.

on the calibration factor is, however, expected to be more dominant. Responsible are the longer paths the alpha particles have to reach the detectors, hence changes in the stopping power of air have considerable consequence for the energy loss. Figure 5.11 shows the results of a simulation for geometry 2 and different ambient conditions with RH fixed at 50%, the temperature range between -25 to 35 °C and the altitudes from 0 to 5,000 m in 500 m steps. Clearly a much larger variation of the calibration factor compared to Figure 5.10 is visible, with a maximum difference of 63% between largest and smallest cf values. A least squares fit of the simulation values results in the parameters stated Table 5.8, where $x = dP$ of Equation 5.22 is the pressure difference in Pa compared to standard pressure of 101,325 Pa .

Apparently in the temperature domain of -25 to -5 °C the dependence of the calibration factor is almost linear, while for 5 to 35 °C it is again exponential. The influence of the temperature is now much clearer visible between -25 to 35 °C than in Figure 5.10 and is largest at 1,000 m altitude with a relative difference of about 18%. This is in correspondence with results from simulations with cylindrical monitors ($\varnothing = 60$ mm , $h =$

Table 5.8: Fit parameter estimation for ^{222}Rn calibration factor with calculated standard error $u(\sqrt{\sigma^2})$ for the data given in Figure 5.11 for geometry 2 and fitted by Equation 5.22.

Temp. $^{\circ}\text{C}$	a $Bq\ m^{-3}/cph$	u(a) $Bq\ m^{-3}/cph$	b $Bq\ m^{-3}/cph$	u(b) $Bq\ m^{-3}/cph$	c $\cdot 10^3\ Pa$	u(c) $\cdot 10^3\ Pa$	R^2
-25	-873.97	$26.79 \cdot 10^3$	887.75	$26.79 \cdot 10^3$	$8.75 \cdot 10^3$	$264.8 \cdot 10^3$	0.99993
-15	-854.23	$29.84 \cdot 10^3$	867.6	$29.84 \cdot 10^3$	$9.03 \cdot 10^3$	$311.5 \cdot 10^3$	0.99991
-5	-4.42	9.26	17.48	9.21	169.54	103.25	0.99993
5	2.58	2.79	10.15	2.74	93.91	33.	0.99993
15	6.67	0.91	5.87	0.85	45.84	11.54	0.99987
25	6.77	0.55	5.42	0.52	45.3	7.53	0.99995
35	7.53	0.22	4.34	0.2	34.8	3.25	0.99998

Table 5.9: Relative difference of ^{222}Rn calibration factors compared to STP conditions calculated via Equation 5.22 employing values of Table 5.8 for large housing (Geo2).

Altitude m	Pressure Pa	$-25\ ^{\circ}\text{C}$ %	$-15\ ^{\circ}\text{C}$ %	$-5\ ^{\circ}\text{C}$ %	$5\ ^{\circ}\text{C}$ %	$15\ ^{\circ}\text{C}$ %	$25\ ^{\circ}\text{C}$ %	$35\ ^{\circ}\text{C}$ %
0	101,325	13.1	9.7	7.2	4.5	2.9	0.0	-2.5
500	95,461	8.3	5.1	2.3	-0.5	-2.8	-5.4	-8.0
1000	89,875	3.6	0.7	-2.2	-5.1	-7.7	-9.9	-12.5
1500	84,557	-0.8	-3.5	-6.3	-9.1	-11.8	-13.8	-16.1
2000	79,496	-5.0	-7.4	-10.1	-12.8	-15.3	-17.0	-19.1
2500	74,684	-9.0	-11.2	-13.7	-16.1	-18.3	-19.8	-21.6
3000	70,110	-12.8	-14.8	-16.9	-19.1	-20.9	-22.1	-23.6
3500	65,766	-16.4	-18.2	-19.9	-21.8	-23.1	-24.2	-25.3
4000	61,642	-19.8	-21.5	-22.7	-24.2	-25.0	-25.9	-26.8
4500	57,730	-23.1	-24.5	-25.3	-26.4	-26.6	-27.5	-28.0
5000	54,022	-26.2	-27.5	-27.7	-28.5	-28.1	-28.8	-29.0

60 mm) published recently where a temperature change of 40°C resulted in an increase of sensitivity of about 12% [145]. Table 5.9 shows the relative deviations of the calibration factors from the STP (50% RH, 101,325 Pa and $25\ ^{\circ}\text{C}$) value of $12.18\ Bq\ m^{-3}/cph$ for geometry 2, based on Equation 5.22 and parameters given in Table 5.8. Again the result is in good agreement with those of other researchers who found that for a monitor with even larger dimension in height, cf changes by about 42% for an air pressure decrease of $34.7\ kPa$ (3400 m) [198]. According to the present results the effect of temperature and pressure on the calibration factor must be considered for exposimeter with large dimensions, as for example those of Geo2, when accurate determination of the activity concentration is required.

Table 5.10: Fit parameter estimation for ^{220}Rn calibration factor with calculated standard error $u(\sqrt{\sigma^2})$ for the data given in Figure 5.12 for geometry 1 and fitted by Equation 5.22.

Temp. $^{\circ}\text{C}$	a $\text{Bq m}^{-3}/\text{cph}$	u(a)	b $\text{Bq m}^{-3}/\text{cph}$	u(b)	c $\cdot 10^3 \text{ Pa}$	u(c)	R^2
-20	14.65	0.17	0.66	0.15	28.64	15.27	0.99999
-10	14.77	0.08	0.52	0.10	14.13	7.68	0.99997
0	14.78	0.04	0.48	0.06	13.12	4.19	0.99999
10	14.76	0.05	0.44	0.08	12.15	5.72	0.99998
20	14.71	0.10	0.33	0.09	24.65	16.89	0.99999
30	13.25	10.55	1.73	10.53	258.04	1,724.16	0.99999

5.3.4 Thoron: calibration factor environmental dependence

In order to determine the dependence of the calibration factor for ^{220}Rn , similar simulations as in Section 5.3.3 have been performed. Figure 5.12 shows the obtained results, revealing that the calibration factor for geometry 1 is again less affected by environmental changes than that for the larger housing (Geo2). Fitting the data for Geo1 results in parameters for Equation 5.22 given in Table 5.10, where $x = dP$ is the pressure change in Pascal. The relative difference of the calibration factor due to temperature changes at constant altitude levels is varying between +1.8% to -2.3% compared to the STP cf and thus is not important. The maximum spread of the calibration factor is observed between sea level and lowest temperature (-25°C , 0 m) compared to both highest (35°C , $5,000 \text{ m}$), where cf differs only about 4.5%. Thus the ^{220}Rn calibration factor dependence on environmental changes is negligible for the standard housing.

This is the contrary for the larger housing (Geo2). The fitting parameters for Geo2 of the data plotted in Figure 5.12 are stated in Table 5.11. These allow to describe the calibration factor as a function of the pressure for each temperature via Equation 5.22. Based on Equation 5.22 and parameters given in Table 5.11 the relative deviations of the calibration factors from the STP (50% RH , $101,325 \text{ Pa}$ and 25°C) value of $10.43 \text{ Bq m}^{-3}/\text{cph}$ for geometry 2 have been calculated and are shown in Table 5.12.

The relative difference of the calibration factor at constant altitude due to temperature changes is varying between 26.5% at 0 m to 1.7% at $5,000 \text{ m}$ and thus shows that temperature needs to be considered when measuring with large dimension monitors. The maximum relative difference of the cf between the lowest temperature and altitude (-25°C , 0 m) and the highest temperature and altitude (35°C , $5,000 \text{ m}$) is about 55%. This shows that the environmental conditions have considerable influence on the calibration factor of monitors with large diffusion chamber dimensions such as in this case with geometry 2 (Geo2). Parameters in Table 5.10 can be employed in conjunction with Equation 5.22 to estimated the expected change of the calibration factor compared to STP conditions as a function of the temperature, altitude and geometry, just as shown in Table 5.12 for Geo2. This allows to correct the calibration factor eventually for different conditions at field measurements in the case that the calibration was performed in a significantly different environment.

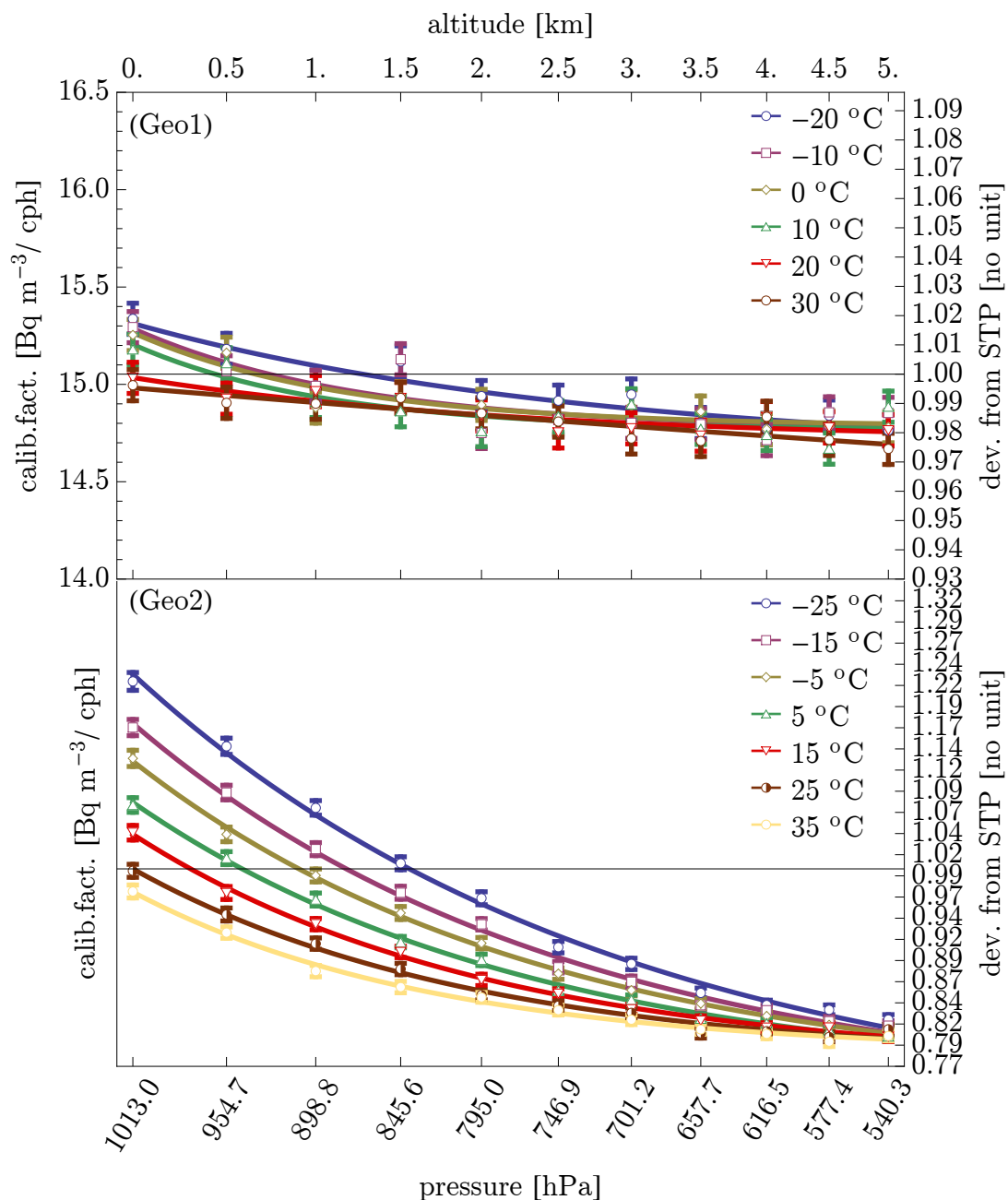


Figure 5.12: Thoron calibration factor dependence on temperature and pressure for ex-posimeter with standard (Geo1) and large (Geo2) dimension. Right scale indicates the relative deviation from the calibration factor at standard temperature and pressure (STP, 50% RH, 101,325 Pa and 20/25 °C). Error bars include 1σ statistical uncertainty only.

Region of interest dependence

In order to distinguish ^{222}Rn and ^{220}Rn spectroscopically it is necessary to choose energy regions in which the alpha particle decays from either have least interference. Such a region of interest (ROI) for ^{216}Po would be ranging from 6.5 – 7.0 MeV (see Figure 5.8), named ROI_2 , and for ^{212}Po from about 8.0 to 10.0 MeV, which is denominated ROI_4 . There will be a radon contribution to ROI_2 which in turn needs to be corrected for. A method is by using counts acquired in ROI_3 (7.0 – 8.0 MeV), attributable to ^{214}Po radon progeny decays, and subtracting the expected background counts in ROI_2 according to rule of proportion. ROI_4 does not experience any influence due to ^{222}Rn since none of its progeny has decay energy beyond 8 MeV. Figure 5.13 shows the result of a simulation with respect to both ^{222}Rn and ^{220}Rn calibration factors in ROI_2 . Clearly there is again a strong temperature dependence of the ^{220}Rn calibration factor at constant altitude levels where relative deviations between 17% at 0 m and 8% at 4,500 m are observable. This dependence can be attributed mainly to counts generated by alpha particles originating from $^{212}\text{Po}_{wall}$ sources, which happen to contribute to the background in ROI_2 (see Figure 5.8) for Geo1. The maximum deviation from the calibration factor at STP of about $240.4 \text{ Bq m}^{-3}/\text{cph}$ is approximately -36% at 30 °C and 5,000 m. This relative difference of the *cf* could be manageable, however, one has to keep in mind the influence of ^{222}Rn on ROI_2 . For a correction algorithm to work a constant relationship between measured ^{214}Po counts in ROI_3 and the background due to the decays originating from chamber walls registered in ROI_2 , has to be established. Ideally radon should thus have a very high calibration factor in ROI_2 , i.e. very little counts due to radon are to be expected per unit radon activity concentration. Additionally the calibration factor should be marginally influenced by changing environmental parameters.

Quite the contrary is true for the ^{222}Rn calibration factor in ROI_2 , as illustrated by Figure 5.13. The temperature and pressure dependence of the calibration factor is the most considerable revealed so far. The maximum relative difference per constant pressure due to temperature changes is about 81% at 1,500 m to 6% at 5,000 m. The deviation from

Table 5.11: Fit parameter estimation for ^{220}Rn calibration factor with calculated standard error u ($\sqrt{\sigma^2}$) for the data given in Figure 5.12 for geometry 2 and fitted by Equation 5.22.

Temp. °C	a $\text{Bq m}^{-3}/\text{cph}$	u(a)	b $\text{Bq m}^{-3}/\text{cph}$	u(b)	c $\cdot 10^3 \text{ Pa}$	u(c)	R^2
-25	7.31	0.3	5.52	0.26	30.36	3.27	0.99993
-15	7.60	0.19	4.62	0.17	27.24	2.35	0.99996
-5	7.77	0.10	3.99	0.09	25.72	1.37	0.99998
5	7.81	0.11	3.44	0.10	25.16	1.82	0.99998
15	8.03	0.07	2.83	0.07	22.17	1.37	0.99998
25	8.08	0.11	2.35	0.10	21.34	2.50	0.99996
35	8.17	0.06	1.98	0.06	19.00	1.63	0.99998

Table 5.12: Relative difference of ^{220}Rn calibration factors compared to STP conditions calculated via Equation 5.22 employing values of Table 5.11 for large housing (Geo2).

Altitude	Pressure	-25 °C	-15 °C	-5 °C	5 °C	15 °C	25 °C	35 °C
<i>m</i>	<i>Pa</i>	%	%	%	%	%	%	%
0	101,325	5.3	0.4	-3.5	-7.6	-10.9	-14.4	-16.7
500	95,461	-2.6	-7.0	-10.1	-13.5	-16.3	-19.0	-21.0
1000	89,875	-8.9	-12.7	-15.2	-18.	-20.2	-22.4	-24.0
1500	84,557	-13.9	-17.1	-19.2	-21.4	-23.2	-24.9	-26.2
2000	79,496	-17.9	-20.6	-22.2	-24.0	-25.4	-26.7	-27.8
2500	74,684	-21.1	-23.3	-24.6	-26.1	-27.1	-28.1	-28.9
3000	70,110	-23.8	-25.5	-26.5	-27.7	-28.4	-29.2	-29.8
3500	65,766	-25.9	-27.3	-28.	-29.0	-29.4	-30.0	-30.4
4000	61,642	-27.7	-28.7	-29.2	-30.0	-30.2	-30.6	-30.9
4500	57,730	-29.2	-29.9	-30.2	-30.9	-30.8	-31.1	-31.3
5000	54,022	-30.4	-30.9	-31.0	-31.6	-31.3	-31.5	-31.6

the STP calibration factor of $3,856.7 \text{ Bq m}^{-3}/\text{cph}$ is about 94% at 5,000 *m*. This means it is not impossible that the radon calibration factor reaches the same order of magnitude as the thoron calibration factor in ROI_2 . This undesired effect and the strong environmental parameter dependence of the calibration factor renders it therefore quite impossible to distinguish counts from either source, especially since the device does not monitor temperature nor pressure. Results from the evaluation of a simulation, employing the larger geometry 2, show a stable calibration factor for ^{222}Rn of $2,330 \pm 40 \text{ Bq m}^{-3}/\text{cph}$ in ROI_2 , where the error is the standard deviation. However the influence of the parameters on the calibration factor for ^{220}Rn is even stronger for the this housing (Geo2), in accordance with the previous results. Thus ROI_2 is considered to be an impossible evaluation option for either geometry.

A reasonable choice for thoron concentration determination is then ROI_4 , which shows no interference with radon and its calibration factor is almost not influenced by temperature or pressure changes, as indicated in Figure 5.14. Up to an altitude of 1.5 *km* the variation of the *cf* is less than 0.5% which in turn can be considered as negligible. When the pressure decreases further an influence of the temperature is observable, which introduces a variation of the calibration factor of 3% at 2.0 *km* and about 13% at 3.0-5.0 *km*. The relative difference compared to the STP calibration factor of $148.5 \text{ Bq m}^{-3}/\text{cph}$ is at 5.0 *km* altitude (540.4 *Pa*) between -16% and -26%. The calibration factor decreases, ie. the sensitivity increases, due to additional counts generated by decays originating from $^{212}\text{Po}_{\text{wall}}$, attached to the chamber walls, which are able to reach the detector in the designated energy ROI_4 , due to the reduced air density. This effect, however, depends on the geometry of the device and is not found for the monitor with the larger geometry (Geo2). Absolutely no dependence of the calibration factor on the environmental parameters is observed in that case in ROI_4 . For the standard housing this means that as long as the altitude difference

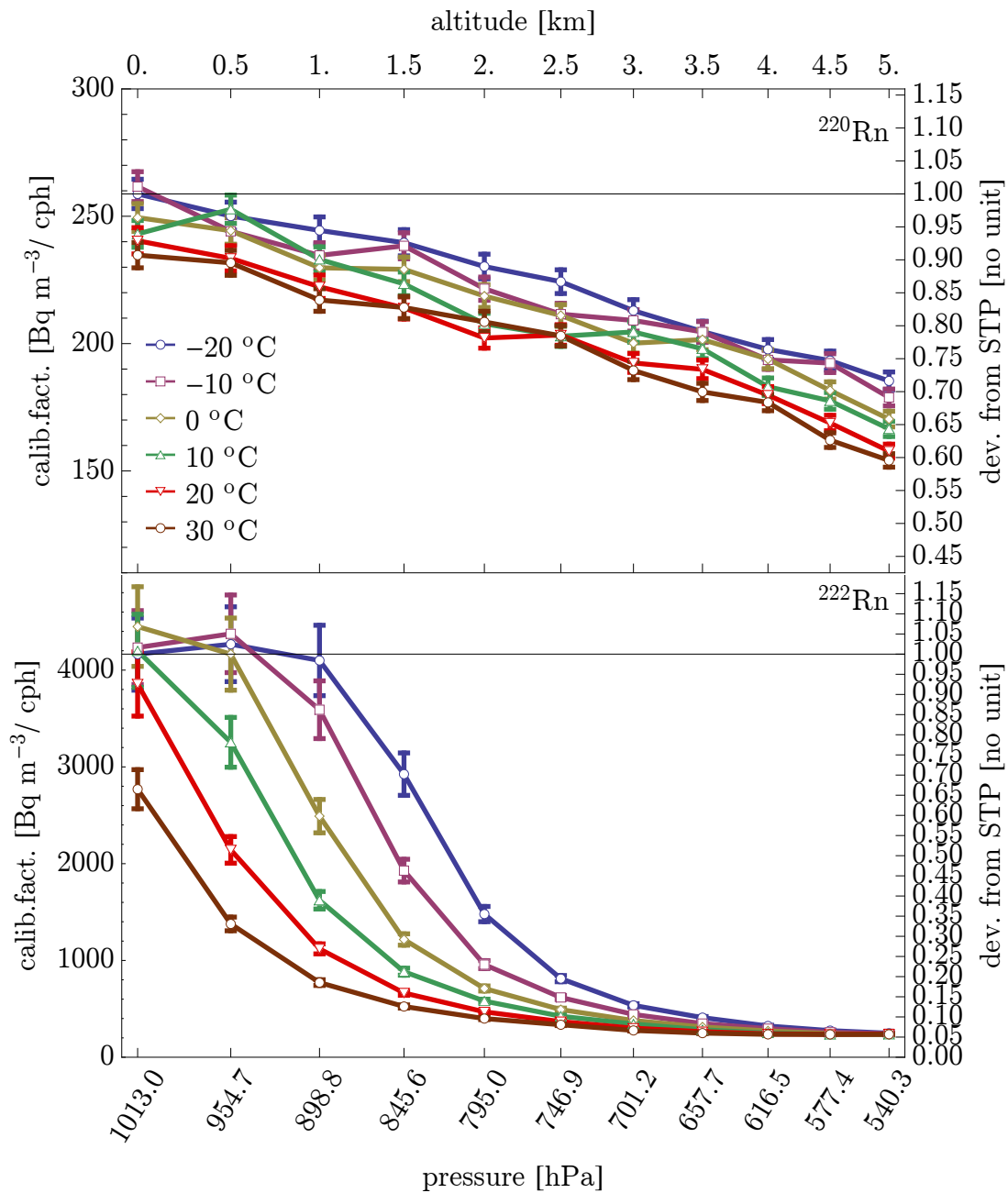


Figure 5.13: ^{220}Rn and ^{222}Rn calibration factor dependence in ROI_2 on temperature and pressure for exosimeter with standard dimension (Geo1). Right scale indicates the relative deviation from the calibration factor at standard temperature and pressure (STP, 50% RH, 101,325 Pa and 20 °C). Error bars include 1σ statistical uncertainty only.

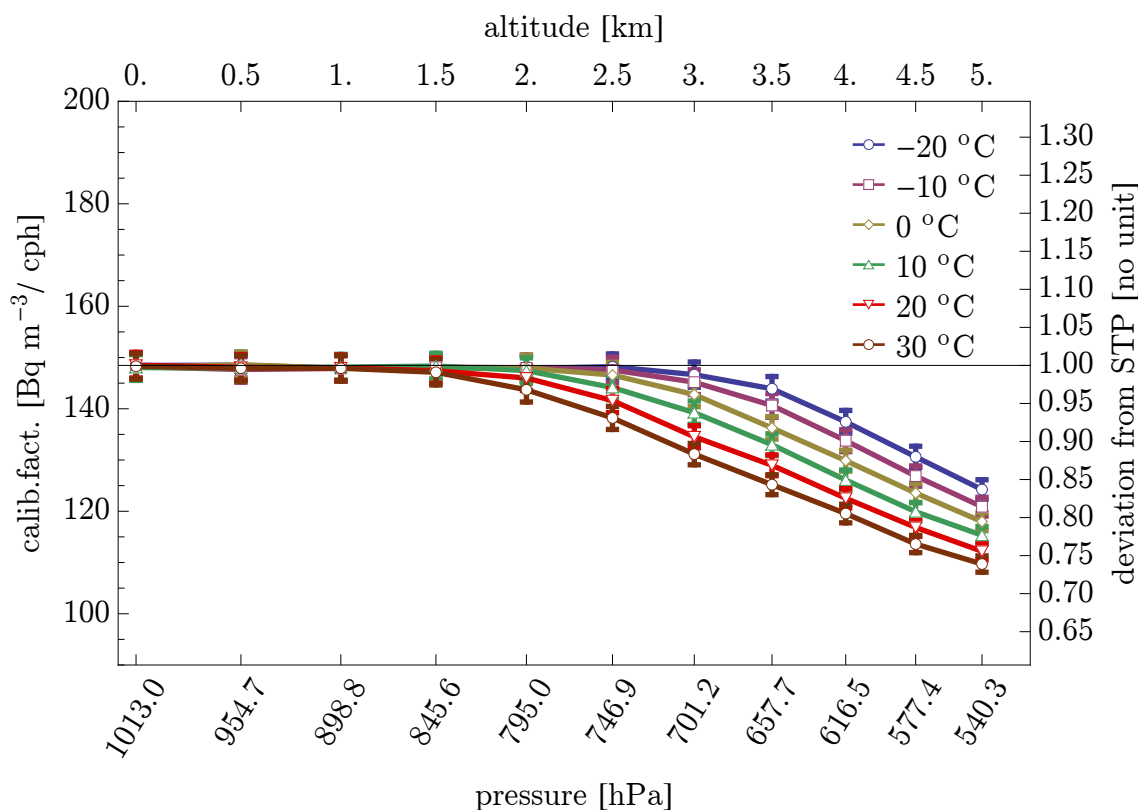


Figure 5.14: Thoron (^{212}Po) calibration factor dependence in ROI_4 on temperature and pressure for exposimeter with standard dimension (Geo1). Right scale indicates the relative deviation from the calibration factor at standard temperature and pressure (STP, 50% RH , 101,325 Pa and 20 °C). Error bars include 1σ statistical uncertainty only.

compared to the level where the calibration was performed is not more than 2,000 m, which only introduces a difference of about 3% for the calibration factor, humidity, temperature and pressure changes have not to be considered.

Conclusion

In summary all results imply that smaller chamber dimensions are preferable with respect to the influence of environmental changes on the calibration factor, but also due to better portability and therefore use as an individual exposure-meter. In general, for the standard housing the influence of the environment can be assumed to be negligible and hence the introduced parameters do not have to be monitored. This is an important requirement to allow for the construction of a cost-effective measurement device, since it reduces necessary hardware components to a minimum.

5.3.5 Geometry dependence

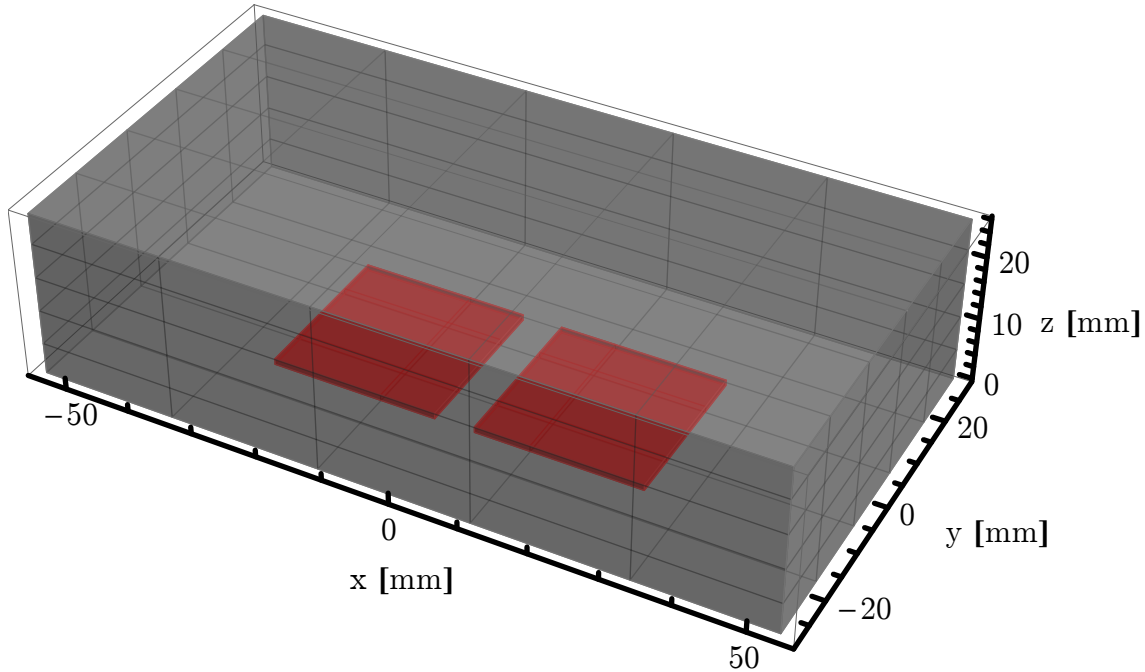


Figure 5.15: Schematic representation of exposimeter geometry 1 with two detectors symmetrically placed at the center (red area). The inlet area for gas diffusion is at the top, which is only relevant for the ^{220}Rn simulation.

In sections 5.3.1 and 5.3.2 the obtained results showed that the influence of atmospheric parameters such as humidity, temperature and pressure on the calibration factor are dependent on the dimensions of the diffusion chamber. In general, it can be stated that the smaller the chamber volume the smaller the dependence of the calibration factor on environmental parameter changes. Hence there exists a tradeoff between housing size and the sensitivity of the device, where a lower calibration factor means higher sensitivity due a larger count rate per unit activity concentration. In order to determine the optimal size systematic simulations changing the geometry of the detection volume have been performed. The starting condition were the dimensions of geometry 1, which is described in Section 5.1.4 and shown in Figure 5.15:

- Geometry 1: $108\text{ mm} \times 57\text{ mm} \times 26\text{ mm}$ (*length* \times *width* \times *height*, $l \times w \times h$)

Two independent simulation sequences have been performed, one changing the original height h by a distance dz , resulting in a series of devices with different heights $h' = h + dz$ and thus volumes. Then the height was held constant but the base area was changed via adding a distance to width and length, where $l' = l + 2 dx$ and $w' = w + dy$ to ensure the ratio between both dimensions was kept the same. In all simulations the detector surface was constant and the detectors were positioned symmetrically at the center of the device. As additional distances for dx , dy and dz the following values were chosen:

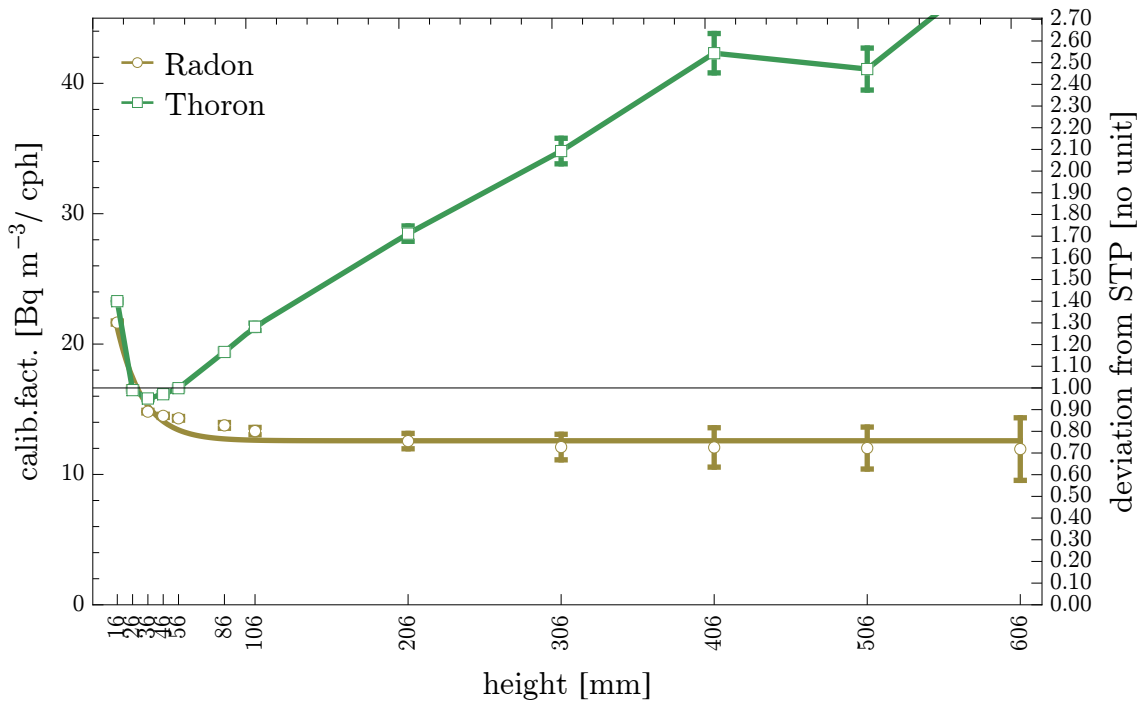


Figure 5.16: ^{220}Rn and ^{222}Rn calibration factor dependence on diffusion chamber height with starting dimensions of Geo1. Right scale indicates the relative deviation from the calibration factor at standard dimension ($h = 26 \text{ mm}$). Error bars include 1σ statistical uncertainty only.

- dx, dy, dz : -10, 0, 10, 20, 30, 60, 80, 180, 280, 380, 480, 580 mm

Hence each series had 12 different simulation runs and thus a total of 48 calibration factors for radon and thoron were calculated. In all simulations the environmental conditions were set to STP, ie. 50% RH , 20 $^{\circ}C$ and 101,325 Pa .

Figure 5.16 shows the calibration factor as function of the height z . An change in height results in a smaller or larger detection volume, where naturally a smaller volume means less sensitivity. For ^{222}Rn a larger volume increases the sensitivity, ie. lowers the calibration factor, but only up to a certain saturation region. Increasing the height further doesn't affect the calibration factor anymore significantly, since the decays in the additional volume are not able to reach the detector. Only a minor increase in the sensitivity is observed, due

Table 5.13: Fit parameter estimation for ^{222}Rn calibration factor with calculated standard error u ($\sqrt{\sigma^2}$) for the data given in Figure 5.16 for geometry 1 and fitted by Equation 5.22.

a	u(a)	b	u(b)	c	u(c)	R^2
$Bq \text{ m}^{-3}/cph$		$Bq \text{ m}^{-3}/cph$		mm	mm	
12.58	0.28	22.18	4.51	17.05	2.99	0.99811

to the fact that the larger volume allows for more progeny to be collected on the detectors, but this effect is only due to the static behavior of the simulation. For very large volumes the assumption of homogenous progeny distribution is not longer valid, thus no increase of the sensitivity is actually possible. The trend of the radon calibration factor in Figure 5.16 can be described by Equation 5.22, where $x = h$ is the height of the device mm . The fitting parameters are stated in Table 5.13, valid for standard width and length of geometry 1. For $dz = -10 mm$ one sees a 30% decrease of the sensitivity compared to the one for standard dimensions, while for $dz = 80 mm$ the cf increases about 20%. The radon calibration factor at STP and $dz = 0$ was determined to be $16.6 Bq m^{-3}/cph$ and is thus in agreement with previous simulation results. Further height increases over $100 mm$ hardly decrease the calibration factor.

This is the contrary for ^{220}Rn , which shows a strong dependence of the calibration factor on dz . The reason is, of course, that increasing the detector-inlet distance reduces the amount of thoron gas which is able diffuse to the bottom on the housing, thus actually lowering the concentration within detection reach. For $h = 16 mm$ we see a decrease in sensitivity of about 41% while for $dz = 10 mm$ and $dz = 20 mm$ the sensitivity increases by about 4% and 2% compared to $dz = 0 mm$. Further height increases lead to a drastic decrease of the sensitivity of up to 200% for $h = 606 mm$. The thoron calibration factor at STP was determined to be about $16.5 Bq m^{-3}/cph$. Thus a small height increase of about $20 mm$ compared to the standard dimension, only slightly improves the calibration factor. A further increment significantly decreases the sensitivity, as expected, since the ^{220}Rn diffusion length is only about $3 cm$. These results indicate that the employed standard geometry (Geo1), is in the sweet spot for radon and thoron sensitivity, where changes either lead to drastic reduction or marginal increase of the sensitivity.

Next the height was left at the constant value of $26 mm$ and just the base area A of the device was changed according to $A = (l + 2 dx) (w + dy)$, where the calibration factor dependence is illustrated in Figure 5.17. For both ^{220}Rn and ^{222}Rn the calibration factor reaches a stable plateau and a further volume gain does not improve significantly the devices' sensitivity. An exponential dependence of the calibration factor cf with the dimension change is observable, which can be described via Equation 5.22, where $x = dx = dy$ is the applied distance variation, and resulting parameters are stated in Table 5.14. The coefficient of determination R^2 for fitting functions is also included, indicating a well agreement of the applied model (Eq. 5.22) and the data. The maximum sensitivity

Table 5.14: Fit parameter estimation for ^{222}Rn and ^{220}Rn calibration factors with calculated standard error $u(\sqrt{\sigma^2})$ for the data given in Figure 5.17 for geometry 1 and fitted by Equation 5.22.

Gas	a	u(a)	b	u(b)	c	u(c)	R^2
	$Bq m^{-3}/cph$		$Bq m^{-3}/cph$		mm	mm	
^{222}Rn	13.72	0.14	3.66	0.20	56.27	7.63	0.99974
^{220}Rn	14.18	0.20	2.44	0.32	33.35	9.38	0.99931

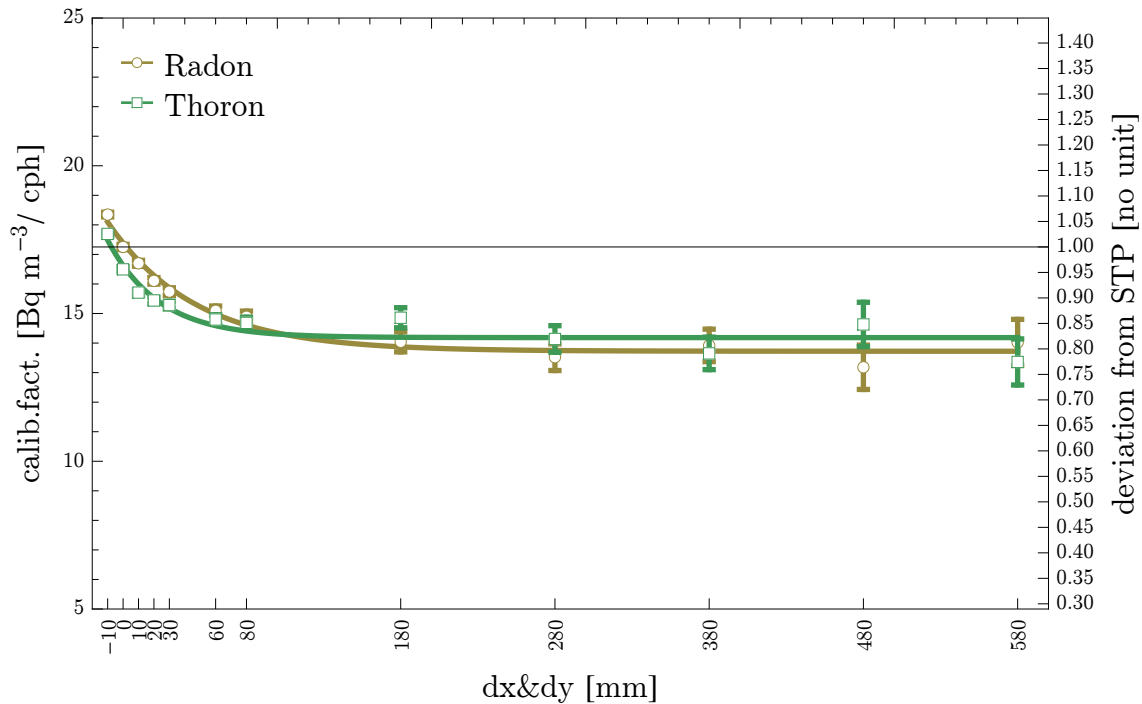


Figure 5.17: ^{220}Rn and ^{222}Rn calibration factor dependence on diffusion chamber base area $A = (l + 2 dx)(w + dy)$ change. Right scale indicates the relative deviation from the calibration factor at standard dimension ($dx = dy = 0$). Error bars include 1σ statistical uncertainty only.

decrease for radon is about 6% at $dx = dy = -10 \text{ mm}$ and the mean saturation gain is about 17%. For thoron it is 7% and 13% respectively. The tendency in the results was to be expected as an higher detection volume increase the effective volume which is within alpha particle range of the sensors, however as the distances grow to large the alpha particles cannot reach these anymore and are stopped in mid air. So there is a certain threshold where a further increase does not significantly improve the calibration factor. According to Figure 5.17 this threshold would be about 106 mm for this setup, since at this point the fitting functions intersect.

This indicates there is some optimization possibility with respect to the base area of the device, where an increase would provide slightly better sensitivity, on the expense of portability of the device.

Chapter 6

Application

The newly developed prototypes have been tested in a variety of environments, in order to validate their functionality in practice and outside the standardized laboratory condition. Furthermore intercomparison measurements have been performed to verify measurement accuracy.

6.1 Prague 2013 Intercomparison

The accuracy and quality of the developed device was checked via intercomparison of measurement instruments during the 7th *European Conference on Protection Against Radon at Home and at Work* in Prague. Intercomparison measurements are a necessary tool to improve and standardize the available measurement methods and verify quality of participation laboratories [72]. A total number of 14 laboratories from 11 different countries participated in the National Radiation Protection Institute (NRPI) intercomparison. The radon intercomparison revealed an average deviation of only 5% from the NRPI reference for more than 50% of the exposed monitors while for the mixed radon/thoron gas exposure the average deviation was up to 15 % [74] of the participating instruments. One device developed in the framework of this thesis participated in the radon intercomparison *D*, which tested continuous monitors or electronic detectors in a pure radon atmosphere within the big NRIP radon chamber (48 m^3). During the test the average environmental conditions were 44.3%RH and 27.4 °C with a ^{222}Rn reference concentration of about $C_{Ref} = 8,300 \pm 480 \text{ Bq m}^{-3}$. Ambient pressure was not given, but according to the height above mean sea level (AMSL) of Prague (399 m) the pressure, not considering climate effects, was about 966.2 hPa. Thus the pressure difference to Munich is at least 137.9 hPa, which introduces a change of the calibration factor of about 0.1% according to Equation 5.22 and Table 5.6, which is insignificant. Figure 6.1 shows the sequence of acquired counts and the corresponding ^{222}Rn activity concentration of V315. The first 6 hours of the measurement are disregarded, as equilibrium was to be reached first. The calibration factor for this device was determined to be about $15.5 \pm 2.1 \text{ Bq m}^{-3}/\text{cph}$ (Section 4.3.2), and the calculated mean concentration was $C_{V315} = 8,940 \pm 650 \text{ Bq m}^{-3}$ with the measurement

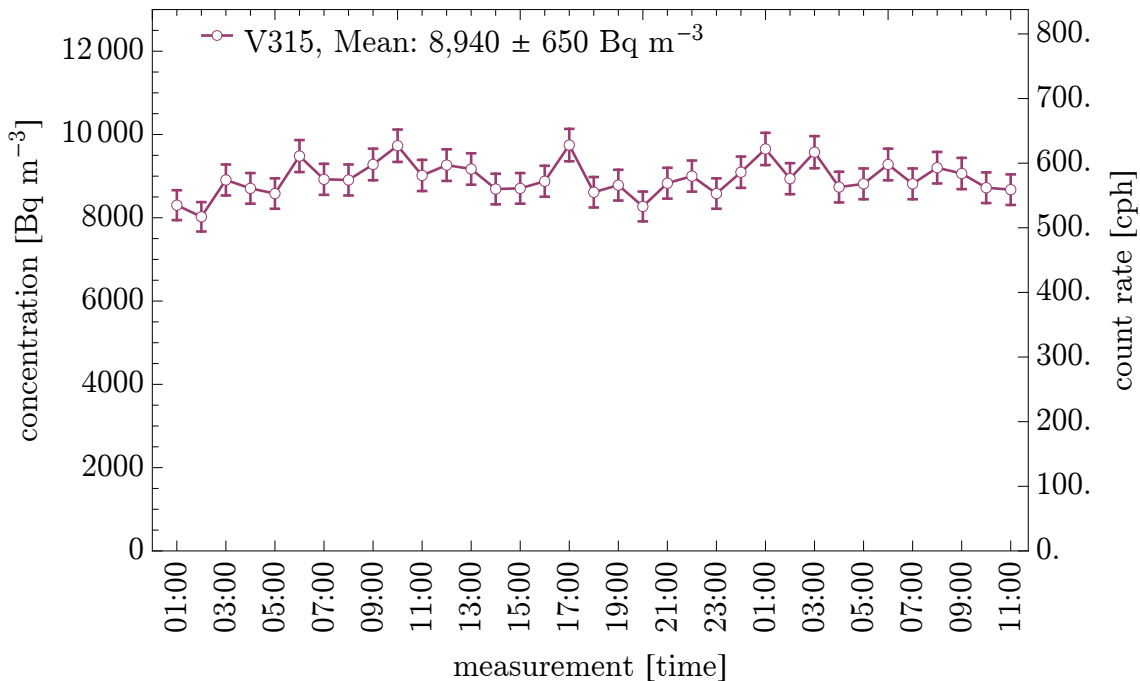


Figure 6.1: Radon activity concentration recorded during the intercomparison measurement in Prague. The integration time of device V315 was set to 10 *min*, but here hourly values are shown. Error bars include 1 σ statistical uncertainty only.

uncertainty calculated according to Section 4.6.3. The standard deviation was determined to be $\sigma_{C_{V315}} = 400 \text{ Bq m}^{-3}$, ie. the relative deviation is about 4.5%. The mean deviation from the reference value $R = C_{V315}/C_{Ref}$ is about 7.7%, which is slightly higher than the average deviation of 5% for most devices. However, the measured and the reference value agree within their confidence intervals. This means that the device demonstrates a quite high precision, i.e. reproducibility of a quasi constant measurand, since the relative standard deviation is only about 4.5%, while the accuracy, which denominates the systematic deviation from the reference value, of the measurement could be improved. The requirement for this is the recalibration of the reference device, in this case the AlphaGuard. The results, however, show that the activity concentrations obtained from these devices are valid within their stated error boundaries and are well below an acceptable deviation of 10%.

6.2 Radon galleries Bad Gastein

A field test was conducted in a spa resort, known by the name Bad Gastein, which is famous for its hydrothermal radioactive springs. Environmental conditions were rather extreme and can reach up to 99% *RH*, 41° *C* and ²²²*Rn* activity concentrations of maximal

100 $kBq\ m^{-3}$ [99]. These conditions were considered suitable to verify the stability of the developed measurement device. The time dependence of the activity concentration were of special interest and, thus, during the visit a protocol with time and location has been recorded:

Time	Comment
11:11	Start of devices by plugging in batteries
11:22	Introduction in cafeteria
11:52	Boarding train and leaving for treatment area
12:15	Arriving at treatment area
12:27	Enter radon free chamber
12:38	Enter station one to expect train
13:15	Leaving the therapy area
13:30	Arriving at starting station
13:53	Final discussion in cafeteria

The radon concentration trend is directly correlated to the course of this record.

6.2.1 Comparison to AlphaGuard

Three devices have been carried on person in a backpack. Two of the exposimeters designed at HMGU, one within the frame of this thesis newly developed radon monitor with improved sensitivity, one previous version with just one detector, and an AlphaGuard for reference. Unfortunately no humidity, temperature and pressure was recorded during the visit. However, the direct comparison to the reference device is sufficient for validating the HMGU exposimeter measurements. Figure 6.2 shows the acquired concentration curve, which demonstrates results of the newly the developed radon monitor, that is in good agreement with those of the previous version and the AlphaGuard. A close look reveals a much better agreement between the reading of the new device V306 and the AlphaGuard than that of the older V102, which is more susceptible to statistical fluctuations. Entering the radon free chamber, which is regularly used by employees, ie. the train driver, for rest during patients treatment, is clearly observable in a decrease of the concentration at about 12:15 o'clock. Leaving the mine at 13:15 immediately results in a reduction of the radon concentration as measured by the AlphaGuard. The count rates in the HMGU exposimeters, however, decreases more slowly. This is due to the decay chain of ^{222}Rn , thus indicating a higher activity concentration than really present in outdoor air. The AlphaGuard corrects for this effect via an algorithm, which is however not yet implemented in the HMGU exposimeter, and thus has to be considered when evaluating the data.

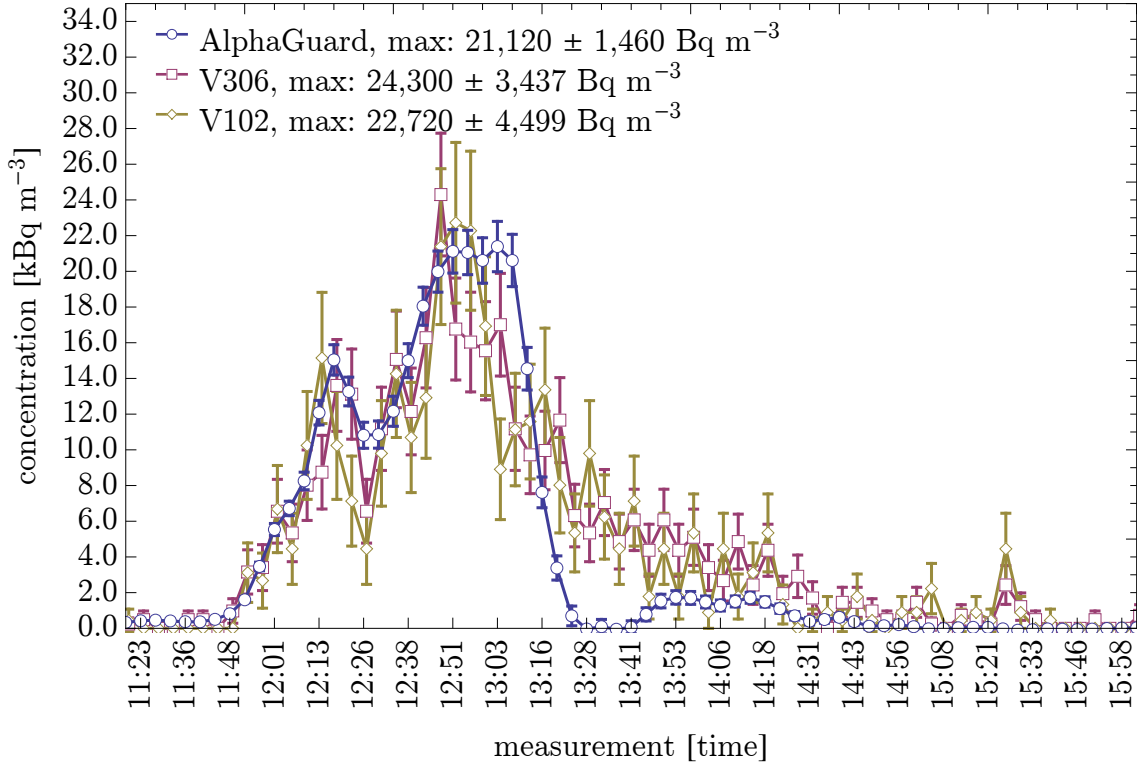


Figure 6.2: Radon activity concentration recorded during a visit at the *Heilstollen Bad Gastein*. The integration time of device V306 and V102 was set to 2 *min*. A general agreement with the AlphaGuard is observable. Error bars include 1σ statistical uncertainty only.

6.2.2 Exposure

The equilibrium equivalent exposure E during the visit to the mine is calculated via Equation 6.1,

$$E(T) = \int_0^T F C(t) dt \quad (6.1)$$

where T represents the end of the exposure and F the equilibrium factor of about 0.4 (see Sec. 2.6.3). The visit duration was about 1 hour and 52 minutes. The following exposures and effective doses have been calculated from the observation shown in Figure 6.2,

- $E_{Alpha} = 9470 \pm 290 \text{ Bq h m}^{-3}$, $D_{eff} = 98 \pm 3.0 \mu\text{Sv}$
- $E_{V305} = 8,550 \pm 1,980 \text{ Bq h m}^{-3}$, $D_{eff} = 89 \pm 2.1 \mu\text{Sv}$
- $E_{V104} = 8,270 \pm 1,970 \text{ Bq h m}^{-3}$, $D_{eff} = 86 \pm 2.1 \mu\text{Sv}$

For the calculation of effective dose the dose conversion factor for occupational exposure of $10.4 \text{ nSv/Bq h m}^{-3}$ was used. Based on these measurements and estimates a train driver

therefore can enter the *Heilstollen* with two drives per day about 100 times per year, in order to stay below the ICRP recommendation for an effective dose of 20 mSv a^{-1} [65]. In a previous measurement a much higher radon exposure was observed in the radon spa (up to 63 kBq h m^{-3}) for two drives into the gallery, leading to a much higher estimated effective lung dose [80]. However such a high radon exposure can be seen as a singular event, and generally the daily occupational exposure is much lower.

6.3 Salt mine Berchtesgaden

Another field test with the newly developed exposure monitors was performed during a visit to Berchtesgaden with colleagues from Bhabha Atomic Research Centre (BARC), India. Three devices were carried on person, two of them using geometry a 1 diffusion chamber with 2 detectors, and additionally, as reference, an AlphaGuard. All three devices were simultaneously started at the beginning of the trip in Munich and had the integral time set to 1 hour. Only during the visit to the salt mine the measurement interval of the AlphaGuard was set to 10 minutes, yielding a better time resolution.

6.3.1 Comparison to AlphaGuard

Figure 6.3 shows the acquired radon concentration trend during the weekend trip from Saturday till Sunday. Clearly a radon build up during night, starting at around 20:00 o'clock on Saturday can be observed where all three devices were stored in the bedroom at the accommodation. The maximum concentration at night reached about $350 \pm 30 \text{ Bq m}^{-3}$, while it has to be noted that the windows of the habitation were closed and it was at ground level with no basement present. During Sunday afternoon the devices were left in the car, where, naturally, almost no radon was present. V302 showed, in general, a somewhat higher radon concentration than the other devices in low concentration environments, indicating that there was probably a background problem with this device. At about 17:00 the visit to the *Berchtesgaden salt mine* [2] started, which is an historic mine and museum open for the public for educational purpose. Before entering the mine the time interval of the AlphaGuard was set to 10 minutes, which was not possible for the HMGU exposimeter, since they do not allow to change this online. Clearly a steep increase of the ^{222}Rn activity concentration is observable at around 17:15 followed by a decrease when leaving the mine at 18:00. The maximum radon concentration measured by the AlphaGuard was about $1,000 \pm 60 \text{ Bq m}^{-3}$, which is reasonable, since generally a mean concentration of about 980 Bq m^{-3} is observed in the public area of the salt mine¹. The better time resolution and sensitivity of the AlphaGuard leads to a more accurate trend in Figure 6.3. This test demonstrates that the developed devices operated also reliable under rough conditions, since at several occasions one has to enter the mine via sliding.

¹Private communication with R. Springl, Salzbergwerk Berchtesgaden

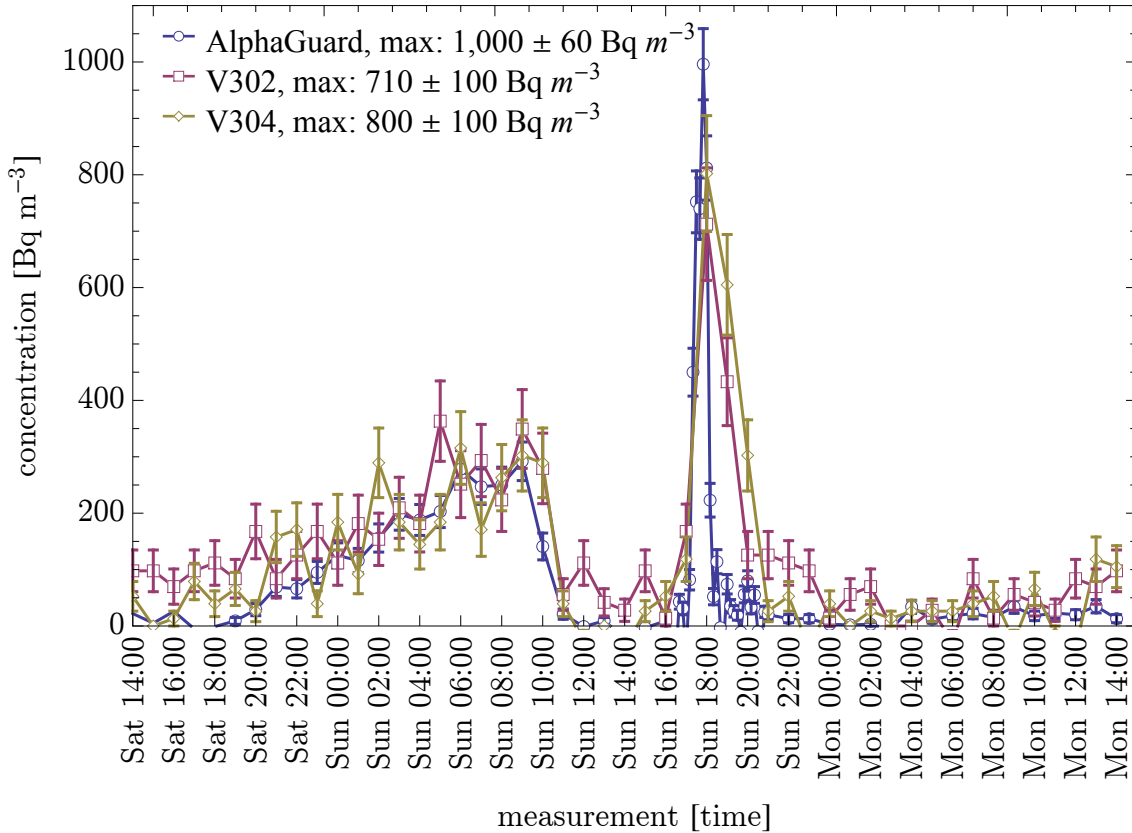


Figure 6.3: Radon activity concentration recorded during the visit to the *Berchtesgaden salt mine*. The integration time of device V306 and V102 was set to 1 *h*. Error bars include 1 σ statistical uncertainty only.

6.3.2 Exposure

The exposure during the trip can be estimated by using the concentration values with high temporal resolution of the AlphaGuard, or the maximum concentration value of the HMGU exposimeter, during the 1 hour visit via Equation 6.1.

- $E_{Alpha} = 137 \pm 58 \text{ Bq h m}^{-3}$, $D_{eff} = 1.1 \pm 0.5 \mu\text{Sv}$
- $E_{V302} = 142 \pm 20 \text{ Bq h m}^{-3}$, $D_{eff} = 1.1 \pm 0.2 \mu\text{Sv}$
- $E_{V305} = 160 \pm 21 \text{ Bq h m}^{-3}$, $D_{eff} = 1.2 \pm 0.2 \mu\text{Sv}$

For the calculation of effective dose the equilibrium factor of $F = 0.2$ and the dose conversion factor for the general public of $7.7 \text{ nSv/Bq h m}^{-3}$ was used. Thus, even when staying in the mine 8 hours per day during the working days of 40 weeks per year, one receives an additional annual effective dose of only about 1.7 mS a^{-1} .

6.4 Thoron field measurements

In order to demonstrate the functionality of the developed radon/thoron monitor beyond standardized laboratory conditions, where its ability to determine correct activity concentrations in mixed $^{222}\text{Rn}/^{220}\text{Rn}$ environments was already validated (see Section 4.6.2), also long term field measurements were performed.

6.4.1 HMGU thoron house

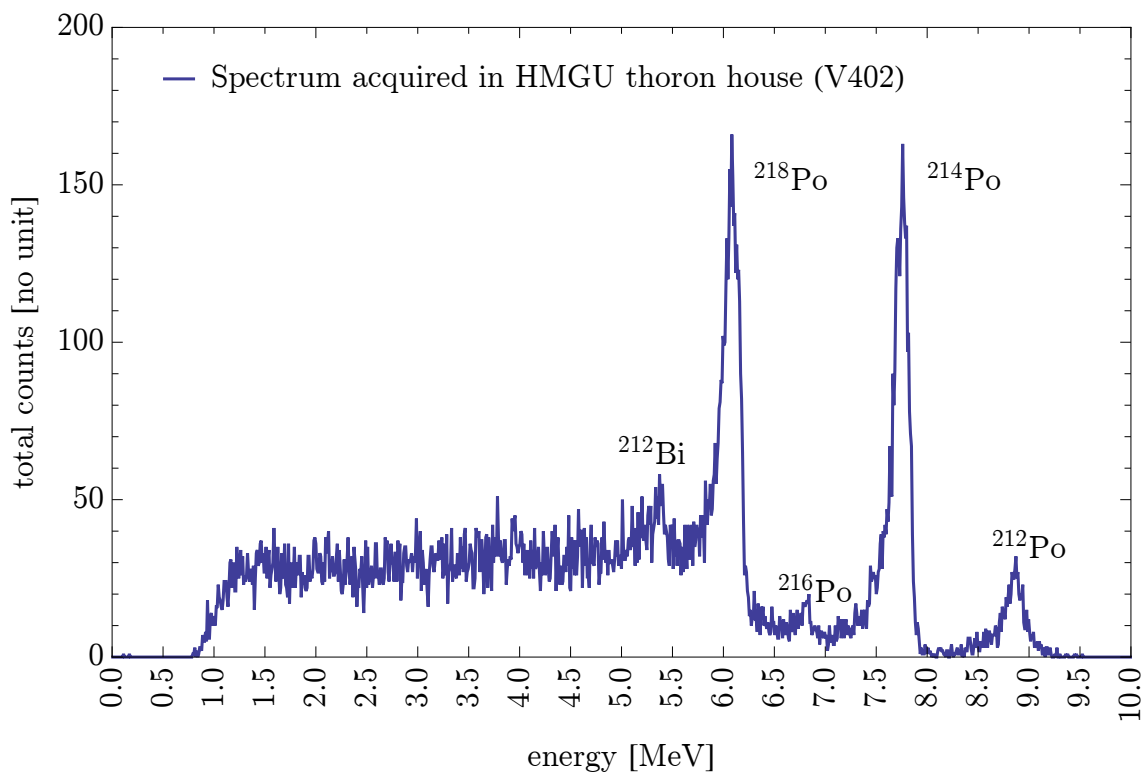


Figure 6.4: Spectrum acquired during a one month measurement in the HMGU thoron house (712 h). Main contribution originates from ^{222}Rn and its progenies, while also ^{220}Rn is clearly present (indicated by the ^{212}Po peak).

The first field measurement was performed in the HMGU thoron experimental house [188]. This house is a miniature model (7.3 m^3) of a traditional Chinese clay house usually found in the Gansu region, China. Built from unfired clay stones and plaster it offers the possibility to control several environmental parameters important for progeny concentration measurements, such as air exchange rate and aerosol concentration. The specific ^{232}Th activity concentration of the building material is about 50 Bq kg^{-1} with an exhalation rate of about $2.2\text{ Bq m}^{-2}\text{ s}^{-1}$ at 40% RH. The measurements were performed at a completely sealed state, i.e. windows and door closed, where the air exchange rate is about 0.6 h^{-1}

[188].

In total six different devices were employed during the measurement. Two HMGU monitors for ^{222}Rn and ^{220}Rn discrimination, developed within the scope of this thesis, four HMGU dual chamber cup exosimeters, which have similar characteristics as other cup exosimeters [53, 206] and further, an AlphaGuard was employed. Additionally, for one week, a Rad7 was used to measure the thoron activity concentration by active sampling. Figure 6.4 shows a typical equilibrium spectrum acquired by device V402 during the 712 h time interval. Obviously the main contribution to the total counts originates from ^{222}Rn and progeny decays, where the two characteristic peaks of ^{218}Po and ^{214}Po are clearly visible. Also the ^{220}Rn contribution is observable, but only within ROI_4 (8-10 MeV) without interference from radon. For determination of the individual respective activity concentrations, the region-of-interest method (Section 4.6.2) was employed using Equations 4.7. The necessary calibration factors and the f factor for device V402 have been determined from four different thoron and three radon calibrations, while for device V404 one calibration each was evaluated. The resulting values were:

- V402: $cf_{^{222}\text{Rn}} = 12.3 \pm 0.8 \text{ Bq m}^{-3}/\text{cph}$, $cf_{^{220}\text{Rn}} = 134.1 \pm 26.9 \text{ Bq m}^{-3}/\text{cph}$
and $f = 13.1 \pm 1.8$
- V404: $cf_{^{222}\text{Rn}} = 12.9 \pm 1.9 \text{ Bq m}^{-3}/\text{cph}$, $cf_{^{220}\text{Rn}} = 98.4 \pm 12.9 \text{ Bq m}^{-3}/\text{cph}$
and $f = 13.9 \pm 1.9$

where the errors refer to the 1σ standard deviation. In case of V402, the standard deviation was calculated from the results of the different calibration measurements, while for V404 it was calculated from the values of one calibration measurement. Device V404 has slightly better sensitivity since its detectors are placed at the top of the housing, thus the inlet-detector distance is decreased. Otherwise the device has the same volume (Geo2), filters and effective diffusion area as V402, although the holes are positioned at the side of the top plate, instead of in circular shape at the center, as compared to V402. This has the further advantage that any light that might enter through the filter at the inlet holes can not directly illuminate the detectors. The background count rate in ROI_4 has also been measured at a low thoron environment and with sealed diffusion inlets. For V402 and V404 the background count rate was determined to be about $cr_0 = 0.02 \text{ cph}$, and thus can be considered negligible.

The measurement period in the house was from the 09/02/2014 until the 10/02/2014, thus approximately one month. During this time 5 devices were continuously measuring (V402, V404, cup exosimeters, AlphaGuard), while the Rad7 was only employed for the first 9 days. The mean environmental conditions during the measurement were 50% RH, 21 °C and 961.7 hPa, monitored by the AlphaGuard. All devices were placed at the opposite wall to the entrance in the middle, with a distance of about 5 cm from the wall, with the diffusion inlets facing the wall. The Rad7 sniffer pipe was also fixed at that distance from the wall with a mechanical arm.

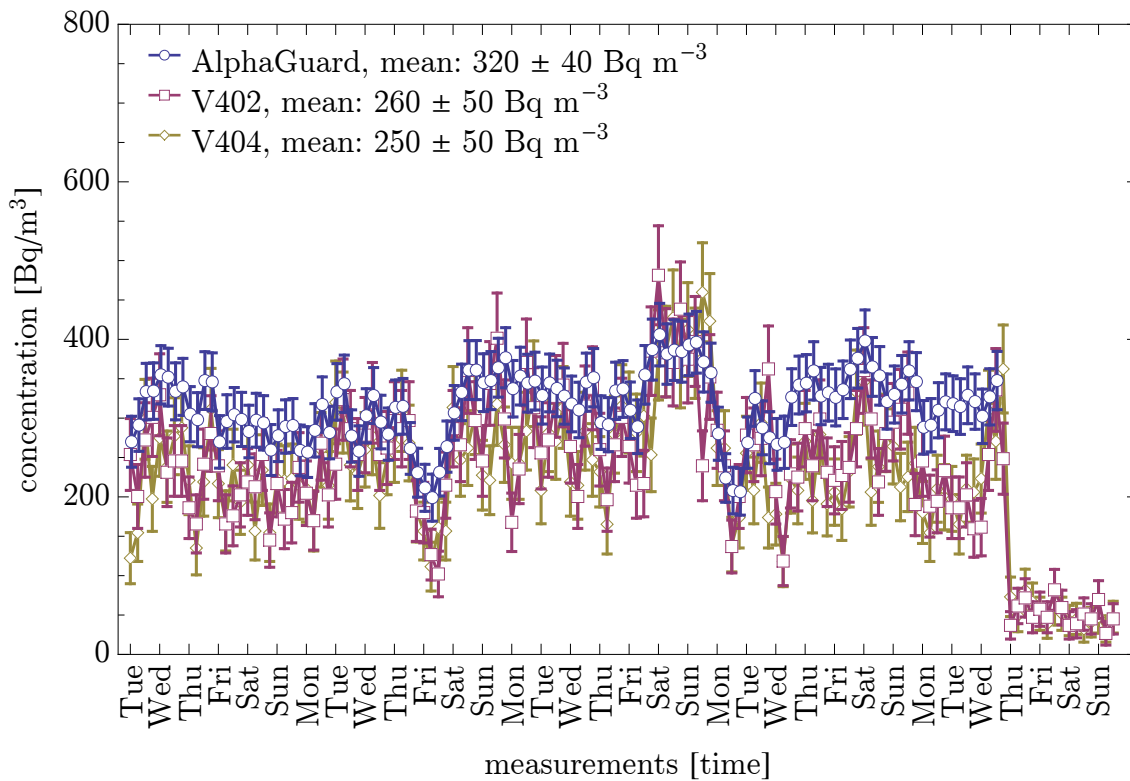


Figure 6.5: Radon concentrations measured in the HMGU thoron house during an one-month time period (712 h). Although the integration time of the devices was 1 h , here the mean of every six hours is shown. A general agreement with the AlphaGuard is observable. Error bars include 1σ statistical uncertainty only.

Figure 6.5 shows the acquired ^{222}Rn activity concentrations for devices V402 and V404, and the radon reference device. Clearly the temporal course of the concentration as well as absolute values determined by V402 and V404 agree quite well with the AlphaGuard. The count rate due to radon has been calculated by subtracting the mean count rate attributable to thoron in ROI_1 (Equation 4.7b). The ^{220}Rn concentration as a function of time is not plotted since the ROI_4 count rate is only about $cr_{ROI_4} = 1.8 \text{ cph}$, and thus shows too high statistical fluctuations.

The determined mean activity concentration values are shown in Table 6.1. The ^{222}Rn activity concentrations are in reasonable agreement within their uncertainties, where the AlphaGuard indicated the largest value. However, an influence of the AlphaGuard due to thoron exposure can be assumed unlikely, due to its low thoron sensitivity of only about 5% to 10% [67, 85, 170]. The measured ^{220}Rn activity concentrations show also reasonable agreement for passive sampling methods, however the Rad7 active sampling device indicates a much higher thoron concentration. This indicates that active and passive sampling results are not comparable when the ^{220}Rn activity concentration is not homogeneously

Table 6.1: Measured ^{222}Rn and ^{220}Rn activity concentrations in the HMGU thoron house, for the different devices employed. Stated errors refer to a 1σ uncertainty.

Gas	AlphaGuard $Bq\ m^{-3}$	Rad7 $Bq\ m^{-3}$	V402 $Bq\ m^{-3}$	V404 $Bq\ m^{-3}$	Cups 1 $Bq\ m^{-3}$	Cups 2 $Bq\ m^{-3}$
^{222}Rn	320 ± 40	250 ± 50	260 ± 50	250 ± 50	192 ± 40	200 ± 40
^{220}Rn		860 ± 100	180 ± 40	170 ± 40	210 ± 60	310 ± 90

distributed. This originates from the effective sampling distance of the Rad7, which was not 5 cm as for the passive devices, but - due to its high flow rate of $650\ \text{cm}^2\ \text{min}^{-1}$ - virtually comparable to a passive device that was positioned at zero distance from the wall in this case. The expected ^{220}Rn concentration as a function of distance cm from a side wall is actually about $C_{220\text{Rn}}(0) = 900 \pm 100\ \text{Bq}\ \text{m}^{-3}$, $C_{220\text{Rn}}(5) = 220 \pm 50\ \text{Bq}\ \text{m}^{-3}$ and $C_{220\text{Rn}}(80) = 20 \pm 7\ \text{Bq}\ \text{m}^{-3}$ [188]. Thus the thoron concentration determined by the Rad7 resembles the value as reported in literature. Devices V402, V404 and Cups 1 measured quite similar concentrations, while Cups 2 shows a 50% deviation compared to the $C_{220\text{Rn}}$ concentration determined by Cups 1. This seems, however, to be an intrinsic problem of the employed measurement and evaluation method, where large variations have already been reported for a intercomparison measurement for this type of device [71]. The found concentrations measured with the new radon/thoron monitors developed in the frame of this thesis, on the other hand, are very similar, as to be expected. This is another verification of the validity of the results determined by the HMGU radon/thoron monitors.

6.4.2 Bavarian clay house

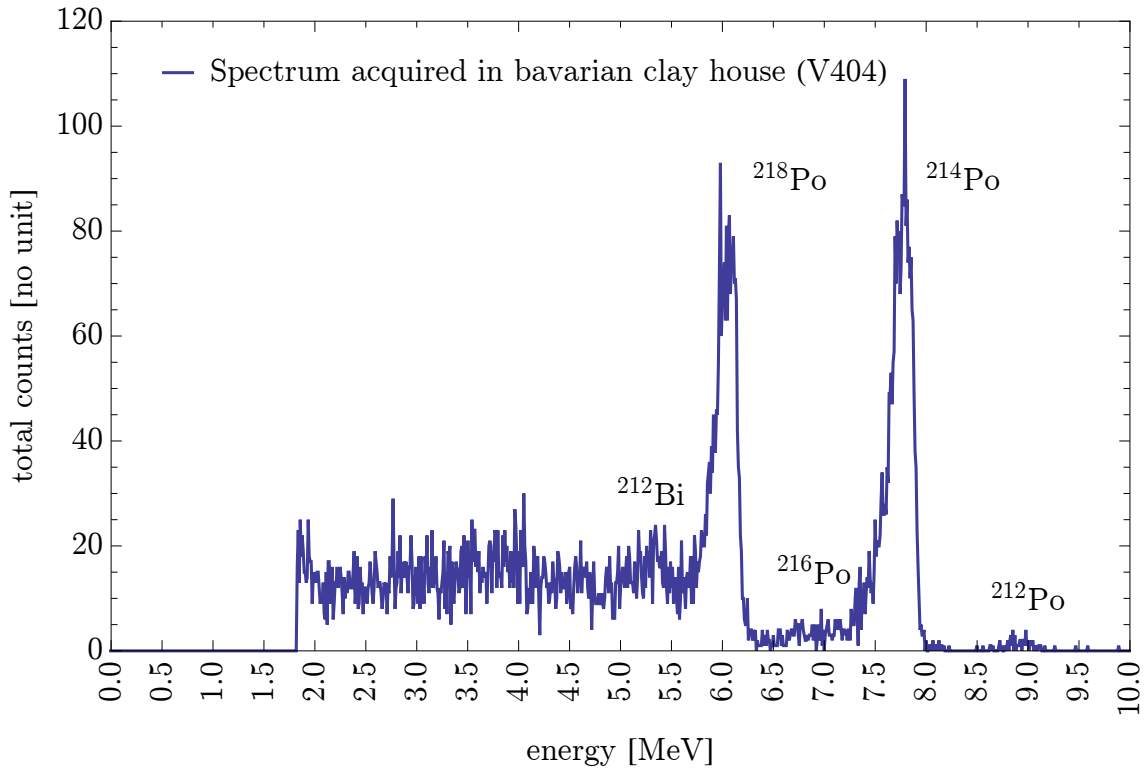


Figure 6.6: Spectrum acquired during a 600 *h* measurement in a modern Bavarian clay house. Main contribution originates from ^{222}Rn and its progenies, while ^{220}Rn is almost not present, indicated by the low ^{212}Po peak.

Due to recent reports of elevated ^{212}Po concentrations levels in German clay houses [49], a field measurement was performed in a modern clay house, where clay is used as wall plastering for ecological and aesthetic reasons. The measurement period was in spring (04/28/2014 till 05/22/2014) and two radon and one radon/thoron monitors were placed in a basement bedroom. One radon monitor (V311) was placed next to the mixed gas exosimeter at 4.2 *cm* distance from the wall, while the other was placed in the middle of the room (V315). Both devices measured a mean radon concentration of $180 \pm 70 \text{ Bq m}^{-3}$ and $190 \pm 70 \text{ Bq m}^{-3}$, indicating a trend in the concentration level with a period of about 12 days (see Figure 6.7). In Figure 6.6 the acquired spectrum of the combined monitor (V404) is shown with a total number of 78 counts in the energy ROI_4 (8 to 10 *MeV*), that are purely attributable to ^{212}Po decays. In this measurement a software threshold was set that only decays which generated signal amplitudes larger than 1.8 *MeV* (channel 200) were recorded, which manifests in a clear edge at this point. This was done in order to reduce possible counts generated by vibrations due to shock of device. Figure 6.6 demonstrates that even at this very low thoron concentration level it is still possible to measure the mean ^{220}Rn activity concentration reliably based on the single

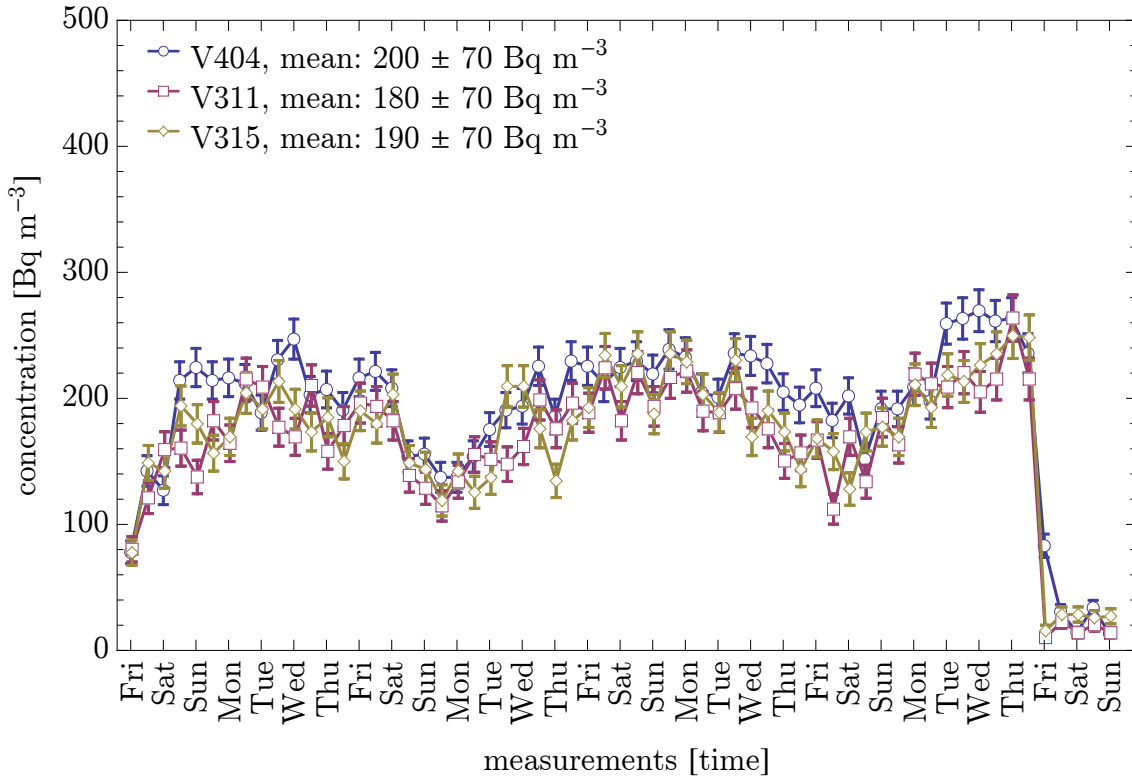


Figure 6.7: Radon concentrations acquired during a measurement in a clay house during a time interval of one month . The integration time of the devices was 1 h but here the mean of every 12th hour is shown. Error bars include 1σ statistical uncertainty only.

^{212}Po peak which is not influenced by radon. According to Section 4.6.3, the decision threshold and the detection limit for device V404, for a $t_m = 600 h$ measurement time and a $cr_0 = 0.02 cph$ ($t_0 = 308 h$) background count rate, is about $C^* = 1.6 Bq m^{-3}$ and $C^\# = 3.8 Bq m^{-3}$, respectively. The mean ^{220}Rn concentration during the measurement period was determined to be about $C_{220Rn} = 13.0 \pm 3.0 Bq m^{-3}$, where the error has been calculated by standard error propagation considering the statistical uncertainty of about 11% and the uncertainty of the calibration factor. Thus about 2 counts each hour in the radon energy ROI_1 are attributable to thoron. When considering this the resulting mean radon concentration measured by V404 was about $C_{222Rn} = 200 \pm 70 Bq m^{-3}$, in agreement with the other radon monitors. In case no correction for thoron is applied the resulting ^{222}Rn concentration would be about $240 \pm 70 Bq m^{-3}$, thus about 20% more than the actual value, yielding a quite significant overestimation. Figure 6.7 shows the acquired ^{222}Rn activity concentrations for the devices. Clearly the temporal course of the concentration as well as absolute values determined agree reasonably well. The measurement devices were removed from the basement and placed in a car on Monday the 05/26/2014 at 11:00 o'clock, after which a steep concentration decrease is observable.

Chapter 7

Conclusions and outlook

In the framework of this thesis several new and unique techniques for the general topic of radon and thoron monitoring were developed. These developments include both, development of new hardware for actual measurement equipment, and detailed characterization with respect to the employed diffusion filter, sensitivity and geometry. Further software tools for simulating the calibration factor dependence on environmental parameters were established based on the Geant4 toolkit. This led to a sound understanding of the intrinsic mechanisms determining the functionality of the device.

More specifically the sensitivity of the new radon exposimeter was improved by about a factor two compared to the previous prototype. Additionally, the sensitivity is about 3-5 times higher than that of other comparable commercially available devices. In order to improve the sensitivity and allow the discrimination of ^{222}Rn and ^{220}Rn , a new amplifier and digital circuit for alpha particle spectroscopy was developed. The electronics feature low power consumption resulting in a life time of up to one month when running on battery. SPICE simulations performed for the analog circuit allowed reproduction of the actual signal behavior and revealed for established thresholds a minimum tolerance for certain electrical components, while also indicating a negligible influence on temperature. The thoron sensitivity of the newly developed device was determined to be in the same range as for radon when using an appropriate filter and diffusion chamber design.

It was shown in this thesis that thoron calibrations are less reproducible compared to radon calibrations with respect to the acquired calibration factor which shows a relative standard deviation of about 5% for radon. Participation in an international radon intercomparison campaign proofed the accuracy of the developed device to be sufficient, since the results obtained were in the range of a 7% relative deviation from the reference. After optimization of the calibration chamber, a relative standard deviation of the thoron calibration factor of about 17% was found. This increase in uncertainty is mainly attributed to an inhomogeneous thoron distribution in the calibration chamber caused by the short half-life of ^{220}Rn , and therefore its limited diffusion length. Several filters have been investigated to identify the one most effective for thoron diffusion. This part of the study demonstrated

that the employed polyurethane foam filter features about a factor two larger diffusion velocity than other cellulose based filters. Thus, similar to stagnant air, it almost introduces no obstacle for thoron gas diffusion, while it effectively stops progeny from entering the diffusion chamber. This is a necessary requirement since otherwise the calibration factor would depend additionally on the progeny deposition rates influenced by humidity, aerosol concentration, airflow and equilibrium factor of the environment. However, this also constraints the wearability of the device, since it has to be ensured that no additional layer of material (clothes) masks the inlets.

The device measures the activity concentrations of either ^{222}Rn or ^{220}Rn according to the recently released ISO 11665 standards for measurement of radioactivity in the environment. Measurements in mixed radon/thoron environments were performed at laboratory as well as naturally thoron rich environments, where a reasonable agreement with reference devices was found. The results verified the employed evaluation method. With the measured calibration factors, the detection threshold for a new device with standard housing was determined to be $C_{^{222}\text{Rn}}^{\#} = 44.0 \text{ Bq m}^{-3}$ and $C_{^{220}\text{Rn}}^{\#} = 40.0 \text{ Bq m}^{-3}$ for radon and thoron respectively, in a one hour measurement interval. Therefore, the developed handheld device offers the unique feature to determine radon and thoron activity concentrations simultaneously with a single diffusion chamber design.

For the first time, the high energy resolution of the alpha particle spectroscopy allowed to study the effects of changing air density or housing dimension on the spectral shape. In order to theoretically verify the observed changes, both an analytic and a Geant4 based Monte-Carlo simulation was developed to compute spectra, allowing comparison to those spectra acquired experimentally with the devices. It was shown that a simple static model, taking only alpha-particle decays into account and assuming an homogenous progeny distribution within the diffusion chamber, is sufficient to obtain reasonable agreement between simulated and measured spectra for both ^{222}Rn and ^{220}Rn environments, thus validating the developed simulations. The Geant4 simulation was then utilized to systematically study the dependence of the calibration factors for both ^{222}Rn and ^{220}Rn on environmental parameters such as relative humidity, ambient temperature and pressure. The results obtained revealed that a device with smaller housing dimension is less affected by air density changes and that the relative change of the calibration factors is below 4% for an ample altitude and temperature range. In contrast, for the larger housing the calibration factor changes can exceed 31%, and thus environmental conditions have to be considered. Additionally, simulations to investigate the calibration factor as a function of the housing dimensions were used to identify the optimal housing size, while demonstrating a clear saturation region where any further increase does not enhance the sensitivity. Hence, the developed and validated simulation proofed to be a valuable and fundamental tool for the further development of radon/thoron monitors.

With the provided results and simulation tools it is now possible to further optimize the portable radon/thoron monitor, with respect to size and sensitivity. More specifically, a

compromise has to be found between usability and wearability, between housing size and detection limit. A reduced housing size allows for a decreased dependence of the calibration factors on environmental parameters, while losing sensitivity. Furthermore despite the developed evaluation method including alpha particle spectroscopy, which was demonstrated to be a useful method to investigate the influence of air density changes and the housing size, an alternative method for signal acquisition can be developed, including a comparator with two channels. This would allow to reduce development and production costs and, as surplus, also would ensure that the thoron influence on future diffusion-chamber-based radon monitor devices can be measured and a radon concentration overestimation is avoided. Note also that the diffusion constant of the employed filter is a major factor determining the calibration coefficient for thoron. Thus, the effect of layers of clothes that may cover the diffusion filter needs to be investigated. In any case, different approaches for wearing the device on a person have to be evaluated. Further, the thoron detection limit can be increased by exposimeters with dual diffusion chamber design, where one chamber only enables radon diffusion while the other allows for radon and thoron to enter. This method allows for a better thoron sensitivity compared to the limited region of interest evaluation method applied with spectroscopy, since the calibration factor for both isotopes is almost the same in the energy domain between 1 and 10 MeV . When integrating the dual chamber in the standard housing, the smaller individual chamber size also reduces the influence of environmental parameters on the calibration factors as well as the production costs.

Finally, a very promising possible future development, based on the methods developed in the frame of this thesis, is the design of a stationary progeny monitor, employing electrostatic progeny collection and solid state detectors for exposure measurements. According to the recently released European council directive *2013/59/EURATOM*, member states shall establish national reference levels for indoor radon concentrations not higher than $300 Bq m^{-3}$, and ensure that an effective annual lung dose of $6 mSv$ due to radon or thoron progeny is not exceeded. Electrostatic progeny collection and spectroscopic measurement resolves the issue of inhomogeneous indoor thoron gas distribution, since the decay products responsible for the lung dose are homogeneously distributed, and the equilibrium factor can be determined exactly. Thus, this new development could provide the ideal means of ensuring the new directive.

Bibliography

- [1] S. Agostinelli et al. ‘Geant4—a simulation toolkit’. In: *Nuclear Instruments and Methods in Physics Research Section A: Accelerators, Spectrometers, Detectors and Associated Equipment* 506.3 (July 2003), pp. 250–303. ISSN: 0168-9002. DOI: [10.1016/S0168-9002\(03\)01368-8](https://doi.org/10.1016/S0168-9002(03)01368-8).
- [2] P. Ambatiello and P. Ney. ‘The Berchtesgaden Salt Mine’. en. In: *Mineral Deposits of the Alps and of the Alpine Epoch in Europe*. Ed. by Professor Dr Hans-J. Schneider. Special Publication No. 3 of the Society for Geology Applied to Mineral Deposits 3. Springer Berlin Heidelberg, Jan. 1983, pp. 146–154. ISBN: 978-3-642-68990-1, 978-3-642-68988-8.
- [3] J. C. Anthony. ‘Lung dosimetry’. In: *Radon and its decay products in indoor air*. Wiley-Interscience, 1988, pp. 259–309. ISBN: 978-0-471-62810-1.
- [4] J. Apostolakis et al. ‘Geometry and physics of the Geant4 toolkit for high and medium energy applications’. In: *Radiation Physics and Chemistry* 78.10 (Oct. 2009), pp. 859–873. ISSN: 0969-806X. DOI: [10.1016/j.radphyschem.2009.04.026](https://doi.org/10.1016/j.radphyschem.2009.04.026).
- [5] D. Arnold and K. N. Yu. ‘Uncertainty in radon measurements with CR39 detector due to unknown deposition of ^{218}Po ’. In: *Nuclear Instruments and Methods in Physics Research Section A: Accelerators, Spectrometers, Detectors and Associated Equipment* 450.2–3 (Aug. 2000), pp. 568–572. ISSN: 0168-9002. DOI: [10.1016/S0168-9002\(00\)00309-0](https://doi.org/10.1016/S0168-9002(00)00309-0).
- [6] A. Aurand, W. Jacobi, and A. Schraub. ‘Zur biologischen Strahlenwirkung des Radons und seiner Folgeprodukte’. In: *Sonderband zur Strahlentherapie*. 35. 1955, pp. 237–243.
- [7] W.F. Bale and J.V Shapiro. ‘Radiation dosage to lungs from radon and its daughter products’. In: vol. 13. New York: United Nations, 1956, pp. 233–236.
- [8] H. Bateman. *Partial Differential Equations*. en. Read Books, Nov. 2008. ISBN: 9781443726702.
- [9] Klaus Becker. ‘Health effects of high radon environments in central Europe: another test for the LNT hypothesis?’ In: *Nonlinearity in Biology, Toxicology, and Medicine* 1.1 (2003), pp. 3–35.
- [10] BEIR. *Health effects of exposure to radon (BEIR VI)*. Vol. 6. Washington, D.C.: National Academies Press, 1999.

- [11] M. J. Berger et al. ‘Stopping-power and range tables for electrons’. In: *Positrons, and Helium Ions* (2005).
- [12] L. Bi et al. ‘Age and sex dependent inhalation doses to members of the public from indoor thoron progeny’. eng. In: *Journal of radiological protection: official journal of the Society for Radiological Protection* 30.4 (Dec. 2010), pp. 639–658. ISSN: 1361-6498. DOI: [10.1088/0952-4746/30/4/001](https://doi.org/10.1088/0952-4746/30/4/001).
- [13] J. Bigu and R. Raz. ‘Passive radon/thoron personal dosimeter using an electrostatic collector and a diffused junction detector’. In: *Review of Scientific Instruments* 56.1 (Jan. 1985), pp. 146–153. ISSN: 0034-6748, 1089-7623. DOI: [10.1063/1.1138482](https://doi.org/10.1063/1.1138482).
- [14] BIPM. *Bureau International des Poids et Mesures - standards*. June 2014.
- [15] Irene Brüske-Hohlfeld and Lothar Kreienbock H.-Erich Wichmann. ‘Lungenkrebs durch Radon’. In: *mensch und umwelt* 18 (Aug. 2006).
- [16] K. Brudecki et al. ‘Age-dependent inhalation doses to members of the public from indoor short-lived radon progeny’. en. In: *Radiation and Environmental Biophysics* (May 2014), pp. 1–15. ISSN: 0301-634X, 1432-2099. DOI: [10.1007/s00411-014-0543-8](https://doi.org/10.1007/s00411-014-0543-8).
- [17] Jerzy Cetnar. ‘General solution of Bateman equations for nuclear transmutations’. In: *Annals of Nuclear Energy* 33.7 (May 2006), pp. 640–645. ISSN: 0306-4549. DOI: [10.1016/j.anucene.2006.02.004](https://doi.org/10.1016/j.anucene.2006.02.004).
- [18] R. P. Chauhan, Mahabir Nain, and K. Kant. ‘Radon diffusion studies through some building materials: Effect of grain size’. In: *Radiation Measurements*. Proceedings of the 23rd International Conference on Nuclear Tracks in Solids 43, Supplement 1 (Aug. 2008), S445–S448. ISSN: 1350-4487. DOI: [10.1016/j.radmeas.2008.03.013](https://doi.org/10.1016/j.radmeas.2008.03.013).
- [19] B. L. Cohen. ‘Lung cancer rate vs. mean radon level in U.S. counties of various characteristics’. eng. In: *Health Physics* 72.1 (Jan. 1997), pp. 114–119. ISSN: 0017-9078.
- [20] B. L. Cohen. ‘Test of the linear-no threshold theory of radiation carcinogenesis for inhaled radon decay products’. eng. In: *Health Physics* 68.2 (Feb. 1995), pp. 157–174. ISSN: 0017-9078.
- [21] Geant4 Collaboration. ‘Geant4 User’s Guide for Application Developers’. In: *Accessible from the GEANT4 web page*. 10.0 (Dec. 2013).
- [22] Geant4 Collaboration. ‘Physics reference manual’. In: *Version geant4* 9.5 (Dec. 2011).
- [23] Geant4 Collaboration. ‘Physics reference manual’. In: *Version geant4* 10 (Dec. 2013).
- [24] C. R. Cothorn and J. E. Smith. *Environmental Radon*. en. Springer, Nov. 1987. ISBN: 9780306427077.

- [25] C.R. Phillips, A. Khan, and H.M.Y Leung. ‘The nature and determination of the unattached fraction of radon and thoron progeny’. en. In: *Radon and its decay products in indoor air*. J. Wiley, Feb. 1988. ISBN: 9780471628101.
- [26] Marie Curie. *Die Radioaktivität*. Salzwasser-Verlag GmbH, 2012. ISBN: 3864449138.
- [27] E. L. Cussler. *Diffusion: Mass Transfer in Fluid Systems*. en. Cambridge University Press, Jan. 2009. ISBN: 9780521871211.
- [28] S. Darby et al. ‘Radon and Cancers Other Than Lung Cancer in Underground Miners: a Collaborative Analysis of 11 Studies’. en. In: *Journal of the National Cancer Institute* 87.5 (Jan. 1995), pp. 378–384. ISSN: 0027-8874, 1460-2105. DOI: [10.1093/jnci/87.5.378](https://doi.org/10.1093/jnci/87.5.378).
- [29] S. Darby et al. ‘Radon in homes and risk of lung cancer: collaborative analysis of individual data from 13 European case-control studies’. en. In: *BMJ* 330.7485 (Jan. 2005), p. 223. ISSN: 0959-8138, 1468-5833. DOI: [10.1136/bmj.38308.477650.63](https://doi.org/10.1136/bmj.38308.477650.63).
- [30] S. Darby et al. ‘Residential radon and lung cancer—detailed results of a collaborative analysis of individual data on 7148 persons with lung cancer and 14,208 persons without lung cancer from 13 epidemiologic studies in Europe.’ eng. In: *Scandinavian journal of work, environment & health* 32 Suppl 1 (2006), pp. 1–83. ISSN: 0355-3140.
- [31] DDBST. *Vapor Pressure of Water from Dortmund Data Bank*. 2014.
- [32] R. Dersch and U. Schötzig. ‘Production and measurement of ^{222}Rn standards’. In: *Applied Radiation and Isotopes* 49.9–11 (Aug. 1998), pp. 1171–1174. ISSN: 0969-8043. DOI: [10.1016/S0969-8043\(97\)10040-9](https://doi.org/10.1016/S0969-8043(97)10040-9).
- [33] J. B. Dixit. *Solutions to Programming in C and Numerical Analysis*. en. Firewall Media, Aug. 2006. ISBN: 9788170088769.
- [34] T. Domanski, W. Chruscielewski, and K. Dobrzynska. ‘Equilibrium between radon and its daughters in the atmosphere of certain mines’. In: (1979).
- [35] Ernst Dorn. ‘Über die von radioaktiven Substanzen ausgesandte Emanation’. In: *Abhandlungen der Naturforschenden Gesellschaft zu Halle* 23 (1901), pp. 1–15.
- [36] G. Dubois. *An Overview of Radon Surveys in Europe*. Radioactivity Environmental Monitoring Emissions and Health Unit. Italy: Office for Official Publication of the European Communities, 2005.
- [37] G. Dubois et al. ‘First steps towards a European atlas of natural radiation: status of the European indoor radon map’. In: *Journal of Environmental Radioactivity*. Advances in radon mapping 101.10 (Oct. 2010), pp. 786–798. ISSN: 0265-931X. DOI: [10.1016/j.jenvrad.2010.03.007](https://doi.org/10.1016/j.jenvrad.2010.03.007).
- [38] William L. Dunn and J. Kenneth Shultis. *Exploring Monte Carlo Methods*. en. Elsevier, May 2011. ISBN: 9780080930619.
- [39] DurrIDGE. *RAD7 RADON DETECTOR User Manual*. 2014.

- [40] K. Eckerman and A. Endo. ‘ICRP Publication 107. Nuclear decay data for dosimetric calculations.’ In: *Annals of the ICRP* 38.3 (2007), pp. 7–96.
- [41] G.J. Enderle and K. Friedrich. ‘East German uranium miners (Wismut)–exposure conditions and health consequences.’ eng. In: *Stem cells (Dayton, Ohio)* 13 Suppl 1 (May 1995), pp. 78–89. ISSN: 1066-5099.
- [42] EPA. ‘Radon Decay Product Measurement Device Protocols’. In: *Document EPA 402* (1992).
- [43] R. B. Firestone. *The Berkeley Laboratory Isotopes Project*. May 2000.
- [44] Heinz-Martin Fischer. *Lutz, Lehrbuch der Bauphysik*. de. Springer-Verlag, Apr. 2008. ISBN: 9783834894670.
- [45] A. Fröjdth et al. ‘An optimized system for measurement of radon levels in buildings by spectroscopic measurement of radon progeny’. en. In: *Journal of Instrumentation* 6.12 (Dec. 2011), p. C12018. ISSN: 1748-0221. DOI: [10.1088/1748-0221/6/12/C12018](https://doi.org/10.1088/1748-0221/6/12/C12018).
- [46] Mitchell H. Gail. *Encyclopedia of Epidemiologic Methods*. en. John Wiley & Sons, Nov. 2000. ISBN: 9780471866411.
- [47] Eduardo García-Toraño. ‘Current status of alpha-particle spectrometry’. In: *Applied Radiation and Isotopes* 64.10–11 (Oct. 2006), pp. 1273–1280. ISSN: 0969-8043. DOI: [10.1016/j.apradiso.2006.02.034](https://doi.org/10.1016/j.apradiso.2006.02.034).
- [48] Andreas C. George. ‘State-of-the-art instruments for measuring radon/thoron and their progeny in dwellings—a review’. In: *Health Physics* 70.4 (1996), pp. 451–463.
- [49] S. Gierl et al. ‘Thoron and Thoron Progeny Measurements in German Clay Houses’. en. In: *Radiation Protection Dosimetry* (Apr. 2014), ncu076. ISSN: 0144-8420, 1742-3406. DOI: [10.1093/rpd/ncu076](https://doi.org/10.1093/rpd/ncu076).
- [50] M. Greenberg and I. J. Selikoff. ‘Lung Cancer in the Schneeberg Mines: A Reappraisal of the Data Reported by Harting and Hesse in 1879’. en. In: *Annals of Occupational Hygiene* 37.1 (Jan. 1993), pp. 5–14. ISSN: 0003-4878, 1475-3162. DOI: [10.1093/annhyg/37.1.5](https://doi.org/10.1093/annhyg/37.1.5).
- [51] E. Gruber. *Messung der zeitaufgelösten Radonexposition an ausgewählten Personen*. Diploma Thesis. LMU München, 2009.
- [52] J.A. Gunby et al. ‘Factors affecting indoor radon concentrations in the United Kingdom.’ eng. In: *Health Physics* 64.1 (Jan. 1993), pp. 2–12. ISSN: 0017-9078.
- [53] Qiuju GUO et al. ‘Measurements of Thoron Concentration by Passive Cup Method and Its Application to Dose, Assessment’. In: *Journal of Nuclear Science and Technology* 32.8 (1995), pp. 794–803. ISSN: 0022-3131. DOI: [10.1080/18811248.1995.9731775](https://doi.org/10.1080/18811248.1995.9731775).
- [54] Mustafa G. Guvench. ‘SPICE Parameter Extraction from Automated Measurement of JFET and MOSFET Characteristics in The Computer-Integrated-Electronics Laboratory’. In: *Proc. of ASEE*. Vol. 94. 1994, pp. 879–884.

- [55] Thomas Haninger. *Messungen der Größenverteilungen von Radon-Folgeprodukten zur Verbesserung der Quantifizierung des durch Radonexpositionen verursachten Lungenkrebsrisikos*. GSF-Forschungszentrum für Umwelt und Gesundheit, 1997.
- [56] Harald Hartl et al. *Elektronische Schaltungstechnik: mit Beispielen in PSpice*. de. Pearson Deutschland GmbH, 2008. ISBN: 9783827373212.
- [57] C. W. Heath Jr. et al. ‘Residential radon exposure and lung cancer risk: commentary on Cohen’s county-based study’. eng. In: *Health Physics* 87.6 (Dec. 2004), 647–655; discussion 656–658. ISSN: 0017-9078.
- [58] Ekbert Hering, Rolf Martin, and Martin Stohrer. *Physik für Ingenieure*. de. Springer DE, 2004. ISBN: 9783540351481.
- [59] Gottfried Hänel. ‘Humidity effects on gravitational settling and Brownian diffusion of atmospheric aerosol particles’. en. In: *Pure and Applied Geophysics* 115.4 (July 1977), pp. 775–797. ISSN: 0033-4553, 1420-9136. DOI: [10.1007/BF00881210](https://doi.org/10.1007/BF00881210).
- [60] Robert Hull. *Properties of Crystalline Silicon*. en. IET, 1999. ISBN: 9780852969335.
- [61] Nezahat Hunter et al. ‘Joint Analysis of Three European Nested Case-control Studies of Lung Cancer among Radon Exposed Miners: Exposure Restricted to Below 300 WLM’. In: *Health Physics* 104.3 (2013), pp. 282–292. ISSN: 0017-9078. DOI: [10.1097/HP.0b013e3182765857](https://doi.org/10.1097/HP.0b013e3182765857).
- [62] ICRP. ‘Exposure and dose to lung tissues’. In: *Annals of the ICRP* 17.1 (1987), pp. 11–17. ISSN: 0146-6453. DOI: [10.1016/0146-6453\(87\)90041-8](https://doi.org/10.1016/0146-6453(87)90041-8).
- [63] ICRP. *Human respiratory tract model for radiological protection: A report of a task group of the International Commission on Radiological Protection*. 66. Elsevier Health Sciences, 1994.
- [64] ICRP. ‘Radon-222 at Home and at Work’. In: *ICRP Publication* 65 (1993).
- [65] ICRP. ‘The 2007 recommendations of the international commission on radiological protection’. In: *ICRP Publication* 103 (2007).
- [66] ICRU. ‘Ranges for Protons and Alpha Particles’. In: *International Commission on Radiation Units and Measurements. Report* 49 (1993).
- [67] T. Ishikawa. ‘Effects of thoron on a radon detector of pulse-ionization chamber type’. en. In: *Radiation Protection Dosimetry* 108.4 (Jan. 2004), pp. 327–330. ISSN: 0144-8420, 1742-3406. DOI: [10.1093/rpd/nch037](https://doi.org/10.1093/rpd/nch037).
- [68] ISO. *Determination of the Characteristic Limits (Decision Threshold, Detection Limit and Limits of the Confidence Interval) for Measurements of Ionizing Radiation—Fundamentals and Application*. 11929. 2010.
- [69] ISO. *Standards to help manage risk of exposure to radon*. 11665 5. International Organization for Standardization, July 2012.
- [70] W. Jacobi. ‘Activity and Potential Alpha-energy of ²²²Radon and ²²⁰Radon daughters in Different Air Atmospheres’. In: *Health Physics* 22.5 (1972), pp. 441–450.

- [71] M. Janik et al. ‘Invited Article: Radon and thoron intercomparison experiments for integrated monitors at NIRS, Japan’. In: *Review of Scientific Instruments* 85.2 (Feb. 2014), p. 022001. ISSN: 0034-6748, 1089-7623. DOI: [10.1063/1.4865159](https://doi.org/10.1063/1.4865159).
- [72] Mirosław Janik et al. ‘International intercomparisons of integrating radon detectors in the NIRS radon chamber’. In: *Applied Radiation and Isotopes* 67.9 (Sept. 2009), pp. 1691–1696. ISSN: 0969-8043. DOI: [10.1016/j.apradiso.2009.03.006](https://doi.org/10.1016/j.apradiso.2009.03.006).
- [73] M. Jiránek and A. Froňka. ‘New technique for the determination of radon diffusion coefficient in radon-proof membranes’. en. In: *Radiation Protection Dosimetry* 130.1 (Jan. 2008), pp. 22–25. ISSN: 0144-8420, 1742-3406. DOI: [10.1093/rpd/ncn121](https://doi.org/10.1093/rpd/ncn121).
- [74] K. Jílek et al. ‘International Intercomparison of Measuring Instruments for Radon Thoron Gas and Radon Short-Lived Daughter Products in the NRPi Prague’. en. In: *Radiation Protection Dosimetry* (Apr. 2014), ncu079. ISSN: 0144-8420, 1742-3406. DOI: [10.1093/rpd/ncu079](https://doi.org/10.1093/rpd/ncu079).
- [75] Luetzelschwab Jw, Hastings L, and Ellis Sm. ‘Adsorption of ^{222}Rn by open-faced and diffusion-barrier canisters at different conditions of temperature and humidity.’ eng. In: *Health Physics* 66.1 (Jan. 1994), pp. 63–71. ISSN: 0017-9078.
- [76] SANTIRAM KAL. *BASIC ELECTRONICS: DEVICES, CIRCUITS AND IT FUNDAMENTALS*. en. PHI Learning Pvt. Ltd., Jan. 2009. ISBN: 9788120319523.
- [77] S. S. Kapoor and V. Ramamurthy. *Nuclear Radiation Detectors*. en. New Age International, Apr. 1986. ISBN: 9780852264966.
- [78] F. L. Karinda. ‘Verbesserung und Einsatz von Echtzeit-Exposimetern zur Bestimmung individueller Radonexpositionen’. PhD thesis. 2009.
- [79] F. L. Karinda, B. Haider, and W. Rühm. ‘A new electronic personal exposure meter for radon gas’. In: *Radiation Measurements*. Proceedings of the 15th Solid State Dosimetry (SSD15) 43.2–6 (Feb. 2008), pp. 1170–1174. ISSN: 1350-4487. DOI: [10.1016/j.radmeas.2007.10.012](https://doi.org/10.1016/j.radmeas.2007.10.012).
- [80] F. L. Karinda, C. Köstinger, and W. Rühm. ‘Realtime assessment of individual radon exposure in the Gasteiner Heilstollen, Austria’. In: *In preparation* (2015).
- [81] G. Keller, K. H. Folkerts, and H. Muth. ‘Activity concentrations of ^{222}Rn , ^{220}Rn , and their decay products in German dwellings, dose calculations and estimate of risk’. en. In: *Radiation and Environmental Biophysics* 20.4 (Dec. 1982), pp. 263–274. ISSN: 0301-634X, 1432-2099. DOI: [10.1007/BF01323752](https://doi.org/10.1007/BF01323752).
- [82] J. Kemski et al. ‘Mapping the geogenic radon potential in Germany’. In: *Science of The Total Environment*. Radon in the Living Environment 272.1–3 (May 2001), pp. 217–230. ISSN: 0048-9697. DOI: [10.1016/S0048-9697\(01\)00696-9](https://doi.org/10.1016/S0048-9697(01)00696-9).
- [83] Haybatolah Khakzár. *Entwurf und Simulation von Halbleiterschaltungen mit PSPICE mit 79 Tabellen [Anleitung zur sachkundigen Planung und Ausführung]*. de. Expert Verlag, 2006. ISBN: 9783816924715.

- [84] Glenn F. Knoll. *Radiation detection and measurement*. Wiley, 2010.
- [85] E. Kochowska et al. ‘Test measurements of thoron concentration using two ionization chambers AlphaGuard vs. radon monitor RAD7’. English. In: (2009).
- [86] M. Konrad. ‘Detector Pulse Shaping for High Resolution Spectroscopy’. In: *IEEE Transactions on Nuclear Science* 15.1 (Feb. 1968), pp. 268–282. ISSN: 0018-9499. DOI: [10.1109/TNS.1968.4324864](https://doi.org/10.1109/TNS.1968.4324864).
- [87] Jean Kovalevsky. ‘The consequences of the mutual recognition of measurement standards for international metrology’. en. In: *Accreditation and Quality Assurance* 5.10-11 (Nov. 2000), pp. 409–413. ISSN: 0949-1775, 1432-0517. DOI: [10.1007/s007690000228](https://doi.org/10.1007/s007690000228).
- [88] Lothar Kreienbrock and A. Siehl. ‘Multiple statistische Analyse von Radon Erhebungsmessungen in der Bundesrepublik Deutschland’. In: *Umweltradioaktivität Geologie und Ökologie im Kontext. Ernst & Sohn, VCH, Berlin* (1996), pp. 299–310.
- [89] M. Kreuzer et al. ‘Mortality from cancers of the extra-thoracic airways in relation to radon progeny in the WISMUT cohort, 1946-2008’. In: *International Journal of Radiation Biology* (Mar. 2014), pp. 1–15. ISSN: 0955-3002. DOI: [10.3109/09553002.2014.909074](https://doi.org/10.3109/09553002.2014.909074).
- [90] M. Kreuzer et al. ‘Radon and risk of death from cancer and cardiovascular diseases in the German uranium miners cohort study: follow-up 1946–2003’. en. In: *Radiation and Environmental Biophysics* 49.2 (May 2010), pp. 177–185. ISSN: 0301-634X, 1432-2099. DOI: [10.1007/s00411-009-0249-5](https://doi.org/10.1007/s00411-009-0249-5).
- [91] Michaela Kreuzer et al. ‘Characteristics of the German uranium miners cohort study’. In: *Health Physics* 83.1 (2002), pp. 26–34.
- [92] Daniel Krewski et al. ‘A Combined Analysis of North American Case-Control Studies of Residential Radon and Lung Cancer’. In: *Journal of Toxicology and Environmental Health, Part A* 69.7-8 (2006), pp. 533–597. ISSN: 1528-7394. DOI: [10.1080/15287390500260945](https://doi.org/10.1080/15287390500260945).
- [93] Daniel Krewski et al. ‘Residential Radon and Risk of Lung Cancer: A Combined Analysis of 7 North American Case-Control Studies’. In: *Epidemiology March 2005* 16.2 (2005), pp. 137–145. ISSN: 1044-3983. DOI: [10.1097/01.ede.0000152522.80261.e3](https://doi.org/10.1097/01.ede.0000152522.80261.e3).
- [94] Georg Kropat et al. ‘Major influencing factors of indoor radon concentrations in Switzerland’. In: *Journal of Environmental Radioactivity* 129 (Mar. 2014), pp. 7–22. ISSN: 0265-931X. DOI: [10.1016/j.jenvrad.2013.11.010](https://doi.org/10.1016/j.jenvrad.2013.11.010).
- [95] Santosh Kumar Singh et al. ‘Parameter extraction and calorimetric validation for a silicon carbide JFET PSpice model’. In: *5th IET International Conference on Power Electronics, Machines and Drives (PEMD 2010)*. Apr. 2010, pp. 1–6. DOI: [10.1049/cp.2010.0121](https://doi.org/10.1049/cp.2010.0121).

- [96] Michael F. L'Annunziata. *Handbook of Radioactivity Analysis*. en. Academic Press, Sept. 2012. ISBN: 9780123848741.
- [97] Jong-Man Lee et al. 'Development of radon calibration chamber at KRISS'. In: *Applied Radiation and Isotopes*. Low Level Radionuclide Measurement Techniques - ICRM 61.2-3 (Aug. 2004), pp. 237-241. ISSN: 0969-8043. DOI: [10.1016/j.apradiso.2004.03.052](https://doi.org/10.1016/j.apradiso.2004.03.052).
- [98] William R. Leo. *Techniques for Nuclear and Particle Physics Experiments: A How-To Approach*. en. Springer, Feb. 1994. ISBN: 9783540572800.
- [99] H. Lettner et al. 'Occupational exposure to radon in treatment facilities of the radon-spa Badgastein, Austria'. In: *Environment International*. The Natural Radiation Environment VI 22, Supplement 1 (1996), pp. 399-407. ISSN: 0160-4120. DOI: [10.1016/S0160-4120\(96\)00138-9](https://doi.org/10.1016/S0160-4120(96)00138-9).
- [100] Chen Ling et al. 'Monte-Carlo computation of the calibration factor of solid state nuclear track detector for radon and the effect by atmospheric pressure'. Chinese. In: (2004).
- [101] D. Linzmaier and A. Röttger. 'Development of a low-level radon reference atmosphere'. In: *Applied Radiation and Isotopes*. 6th International Conference on Radionuclide Metrology - Low Level Radioactivity Measurement Techniques 81 (Nov. 2013), pp. 208-211. ISSN: 0969-8043. DOI: [10.1016/j.apradiso.2013.03.032](https://doi.org/10.1016/j.apradiso.2013.03.032).
- [102] Jay H. Lubin. *Radon and lung cancer risk: a joint analysis of 11 underground miners studies*. 94. US Dept. of Health and Human Services, Public Health Service, National Institutes of Health, 1994.
- [103] Jay H. Lubin and John D. Boice. 'Lung Cancer Risk From Residential Radon: Meta-analysis of Eight Epidemiologic Studies'. en. In: *Journal of the National Cancer Institute* 89.1 (Jan. 1997), pp. 49-57. ISSN: 0027-8874, 1460-2105. DOI: [10.1093/jnci/89.1.49](https://doi.org/10.1093/jnci/89.1.49).
- [104] Jay H. Lubin et al. 'Risk of lung cancer and residential radon in China: Pooled results of two studies'. en. In: *International Journal of Cancer* 109.1 (Mar. 2004), pp. 132-137. ISSN: 1097-0215. DOI: [10.1002/ijc.11683](https://doi.org/10.1002/ijc.11683).
- [105] P. Ludewig and E. Lorenzer. 'Untersuchung der Grubenluft in den Schneeberger Gruben auf den Gehalt an Radiumemanation'. de. In: *Zeitschrift für Physik* 22.1 (Dec. 1924), pp. 178-185. ISSN: 0044-3328. DOI: [10.1007/BF01328120](https://doi.org/10.1007/BF01328120).
- [106] Joseph Magill and Jean Galy. *Radioactivity Radionuclides Radiation*. en. Springer, Dec. 2005. ISBN: 9783540268819.
- [107] A. Malki et al. 'Measurement of radon diffusion length in thin membranes'. en. In: *Radiation Protection Dosimetry* 150.4 (Jan. 2012), pp. 434-440. ISSN: 0144-8420, 1742-3406. DOI: [10.1093/rpd/ncr421](https://doi.org/10.1093/rpd/ncr421).

- [108] James W. Marsh et al. ‘DOSE CONVERSION FACTORS FOR RADON: RECENT DEVELOPMENTS.’ en. In: *Health Physics* 99.4 (Oct. 2010), pp. 511–516. ISSN: 0017-9078. DOI: [10.1097/HP.0b013e3181d6bc19](https://doi.org/10.1097/HP.0b013e3181d6bc19).
- [109] J. McLaughlin et al. ‘Long-term measurements of thoron, its airborne progeny and radon in 205 dwellings in Ireland’. en. In: *Radiation Protection Dosimetry* 145.2-3 (Jan. 2011), pp. 189–193. ISSN: 0144-8420, 1742-3406. DOI: [10.1093/rpd/ncr067](https://doi.org/10.1093/rpd/ncr067).
- [110] O. Meisenberg and J. Tschiersch. ‘Specific properties of a model of thoron and its decay products in indoor atmospheres’. In: *Nukleonika* Vol. 55, No. 4 (2010), pp. 463–469.
- [111] O. Meisenberg and J. Tschiersch. ‘Thoron in indoor air: modeling for a better exposure estimate’. en. In: *Indoor Air* 21.3 (June 2011), pp. 240–252. ISSN: 1600-0668. DOI: [10.1111/j.1600-0668.2010.00697.x](https://doi.org/10.1111/j.1600-0668.2010.00697.x).
- [112] S. Menzler et al. ‘Abschätzung des attributablen Lungenkrebsrisikos in Deutschland durch Radon in Wohnungen’. In: *ecomед Medizin* (2006).
- [113] Rosaline Mishra and Y. S. Mayya. ‘Study of a deposition-based direct thoron progeny sensor (DTPS) technique for estimating equilibrium equivalent thoron concentration (EETC) in indoor environment’. In: *Radiation Measurements* 43.8 (Sept. 2008), pp. 1408–1416. ISSN: 1350-4487. DOI: [10.1016/j.radmeas.2008.03.002](https://doi.org/10.1016/j.radmeas.2008.03.002).
- [114] Rosaline Mishra, B. K. Sapra, and Y. S. Mayya. ‘Multi-parametric approach towards the assessment of radon and thoron progeny exposures’. In: *Review of Scientific Instruments* 85.2 (Feb. 2014), p. 022105. ISSN: 0034-6748, 1089-7623. DOI: [10.1063/1.4865165](https://doi.org/10.1063/1.4865165).
- [115] Hans Möre, Rolf Falk, and Leif Nyblom. ‘A bench-top calibration chamber for ^{220}Rn activity in air’. In: *Environment International*. The Natural Radiation Environment VI 22, Supplement 1 (1996), pp. 1147–1153. ISSN: 0160-4120. DOI: [10.1016/S0160-4120\(96\)00231-0](https://doi.org/10.1016/S0160-4120(96)00231-0).
- [116] D. M. Murphy and T. Koop. ‘Review of the vapour pressures of ice and supercooled water for atmospheric applications’. en. In: *Quarterly Journal of the Royal Meteorological Society* 131.608 (2005), pp. 1539–1565. ISSN: 1477-870X. DOI: [10.1256/qj.04.94](https://doi.org/10.1256/qj.04.94).
- [117] Niren Laxmichand Nagda. *Radon: Prevalence, Measurements, Health Risks, and Control*. en. ASTM International, Jan. 1994. ISBN: 9780803120570.
- [118] A. K. Narula et al. ‘Calculation of radon diffusion coefficient and diffusion length for different building construction materials’. In: *Indian Journal of Physics* 83.8 (2009), pp. 1171–1175. DOI: [10.1007/s12648-009-0097-9](https://doi.org/10.1007/s12648-009-0097-9).
- [119] W. W. Nazaroff and Anthony V. Nero. *Radon and its decay products in indoor air*. en. J. Wiley, Feb. 1988. ISBN: 9780471628101.

- [120] D. Nikezić and K. N. Yu. ‘The influence of thoron and its progeny on radon measurements with CR39 detectors in diffusion chambers’. In: *Nuclear Instruments and Methods in Physics Research Section A: Accelerators, Spectrometers, Detectors and Associated Equipment* 419.1 (Dec. 1998), pp. 175–180. ISSN: 0168-9002. DOI: [10.1016/S0168-9002\(98\)01152-8](https://doi.org/10.1016/S0168-9002(98)01152-8).
- [121] D. Nikezic and K. N. Yu. ‘Computer simulation of radon measurements with nuclear track detectors’. In: *Computer physics research trends* 3 (2007), pp. 119–150.
- [122] NRPP. *National Radon Proficiency Program - Measurement & Lab Calibration*. June 2014.
- [123] C. Nuccetelli and F. Bochicchio. ‘The Thoron Issue: Monitoring Activities, Measuring Techniques and Dose Conversion Factors’. en. In: *Radiation Protection Dosimetry* 78.1 (Jan. 1998), pp. 59–64. ISSN: 0144-8420, 1742-3406.
- [124] ON Semiconductor. *2SK932 Datasheet*. 2014.
- [125] Phillip F. Ostwald and Jairo Munoz. *Manufacturing Processes And Systems, 9Th Ed.* en. Wiley India Pvt. Limited, Oct. 2008. ISBN: 9788126518937.
- [126] Feng Pan and Tapan Samaddar. *Charge Pump Circuit Design*. en. McGraw Hill Professional, July 2006. ISBN: 9780071491426.
- [127] J. R. Partington. ‘Discovery of radon’. In: (1957).
- [128] A. Paul et al. ‘Measurement of radon and radon progenies at the German radon reference chamber’. English. In: *Applied Radiation and Isotopes* 52.3 (2000), pp. 369–375. ISSN: 0969-8043. DOI: [10.1016/S0969-8043\(99\)00180-3](https://doi.org/10.1016/S0969-8043(99)00180-3).
- [129] Helmut Paul. ‘The Stopping Power of Matter for Positive Ions’. In: *Johannes Kepler University Linz* (2012).
- [130] J. E. Peter. ‘Analysis of Radon and Thoron Daughter Concentrations in Air by Continuous Alpha Spectroscopy’. en. In: *Radiation Protection Dosimetry* 56.1-4 (Jan. 1994), pp. 267–270. ISSN: 0144-8420, 1742-3406.
- [131] A. Picard et al. ‘Revised formula for the density of moist air (CIPM-2007)’. In: *Metrologia* 45.2 (2008), p. 149.
- [132] J. L. Picolo. ‘Absolute measurement of radon 222 activity’. In: *Nuclear Instruments and Methods in Physics Research Section A: Accelerators, Spectrometers, Detectors and Associated Equipment* 369.2–3 (Feb. 1996), pp. 452–457. ISSN: 0168-9002. DOI: [10.1016/S0168-9002\(96\)80029-5](https://doi.org/10.1016/S0168-9002(96)80029-5).
- [133] Russell A. Poldrack, Jeanette A. Mumford, and Thomas E. Nichols. *Handbook of Functional MRI Data Analysis*. en. Cambridge University Press, Aug. 2011. ISBN: 9781139498364.
- [134] J. Porstendörfer. ‘Behaviour of Radon Daughter Products in Indoor Air’. en. In: *Radiation Protection Dosimetry* 7.1-4 (Jan. 1984), pp. 107–113. ISSN: 0144-8420, 1742-3406.

- [135] J. Porstendörfer. ‘Properties and behaviour of radon and thoron and their decay products in the air’. In: *Journal of Aerosol Science* 25.2 (Mar. 1994), pp. 219–263. ISSN: 0021-8502. DOI: [10.1016/0021-8502\(94\)90077-9](https://doi.org/10.1016/0021-8502(94)90077-9).
- [136] J. Porstendörfer, G. Röbig, and A. Ahmed. ‘Experimental determination of the attachment coefficients of atoms and ions on monodisperse aerosols’. In: *Journal of Aerosol Science* 10.1 (1979), pp. 21–28. ISSN: 0021-8502. DOI: [10.1016/0021-8502\(79\)90132-0](https://doi.org/10.1016/0021-8502(79)90132-0).
- [137] J. Porstendörfer and A. Reineking. ‘Radon: characteristics in air and dose conversion factors’. eng. In: *Health Physics* 76.3 (Mar. 1999), pp. 300–305. ISSN: 0017-9078.
- [138] J. Porstendörfer, A. Wicke, and A. Schraub. ‘The influence of exhalation, ventilation and deposition processes upon the concentration of radon (^{222}Rn), thoron (^{220}Rn) and their decay products in room air’. In: *Health Physics* 34.5 (1978), pp. 465–473.
- [139] D. Pressyanov, I. Rusinov, and G. Simeonov. ‘Radon progeny deposition in track-detection diffusion chambers’. In: *Nuclear Instruments and Methods in Physics Research Section A: Accelerators, Spectrometers, Detectors and Associated Equipment* 435.3 (Oct. 1999), pp. 509–513. ISSN: 0168-9002. DOI: [10.1016/S0168-9002\(99\)00578-1](https://doi.org/10.1016/S0168-9002(99)00578-1).
- [140] Louie Pylarinos. ‘Charge pumps: An overview’. In: *in Proceedings of the IEEE International Symposium on Circuits and Systems*. 2003.
- [141] T. V. Ramachandran, B. Y. Lalit, and U. C. Mishra. ‘Measurement of radon permeability through some membranes’. In: *International Journal of Radiation Applications and Instrumentation. Part D. Nuclear Tracks and Radiation Measurements* 13.1 (1987), pp. 81–84. ISSN: 1359-0189. DOI: [10.1016/1359-0189\(87\)90012-4](https://doi.org/10.1016/1359-0189(87)90012-4).
- [142] Daniel Reger, Scott Goode, and David Ball. *Chemistry: Principles and Practice*. en. Cengage Learning, Jan. 2009. ISBN: 0534420125.
- [143] A. Reineking and J. Porstendörfer. ‘Unattached fraction of short-lived Rn decay products in indoor and outdoor environments: an improved single-screen method and results.’ eng. In: *Health Physics* 58.6 (June 1990), pp. 715–727. ISSN: 0017-9078.
- [144] K.J. Renken and T. Rosenberg. ‘Laboratory measurements of the transport of radon gas through concrete samples.’ eng. In: *Health Physics* 68.6 (June 1995), pp. 800–808. ISSN: 0017-9078.
- [145] Jorge Rickards, Jose-Ignacio Golzarri, and Guillermo Espinosa. ‘A Monte Carlo study of radon detection in cylindrical diffusion chambers’. In: *Journal of Environmental Radioactivity* 101.5 (May 2010), pp. 333–337. ISSN: 0265-931X. DOI: [10.1016/j.jenvrad.2010.01.003](https://doi.org/10.1016/j.jenvrad.2010.01.003).

- [146] Katerina Rovenska and Martin Jiránek. ‘1st International comparison measurement on assessing the diffusion coefficient of radon’. en. In: *Radiation Protection Dosimetry* 145.2-3 (Jan. 2011), pp. 127–132. ISSN: 0144-8420, 1742-3406. DOI: [10.1093/rpd/ncr079](https://doi.org/10.1093/rpd/ncr079).
- [147] A. Röttger and A. Honig. ‘Recent developments in radon metrology: new aspects in the calibration of radon, thoron and progeny devices’. en. In: *Radiation Protection Dosimetry* 145.2-3 (Jan. 2011), pp. 260–266. ISSN: 0144-8420, 1742-3406. DOI: [10.1093/rpd/ncr047](https://doi.org/10.1093/rpd/ncr047).
- [148] A. Röttger, Anja Honig, and Dirk Arnold. ‘The German thoron progeny chamber—Concept and application’. In: *Applied Radiation and Isotopes*. 5th International Conference on Radionuclide Metrology - Low-Level Radioactivity Measurement Techniques 67.5 (May 2009), pp. 839–842. ISSN: 0969-8043. DOI: [10.1016/j.apradiso.2009.01.043](https://doi.org/10.1016/j.apradiso.2009.01.043).
- [149] A. Röttger et al. ‘A primary standard for activity concentration of ^{220}Rn (thoron) in air’. In: *Applied Radiation and Isotopes*. Proceedings of the 17th International Conference on Radionuclide Metrology and its Applications (ICRM 2009) 68.7–8 (July 2010), pp. 1292–1296. ISSN: 0969-8043. DOI: [10.1016/j.apradiso.2010.01.004](https://doi.org/10.1016/j.apradiso.2010.01.004).
- [150] A. Röttger et al. ‘Comparison of calibration facilities for radon activity concentration: Euromet Project 657’. en. In: *Metrologia* 42.1A (Jan. 2005), p. 06003. ISSN: 0026-1394. DOI: [10.1088/0026-1394/42/1A/06003](https://doi.org/10.1088/0026-1394/42/1A/06003).
- [151] E. Rutherford. ‘I. A radio-active substance emitted from thorium compounds’. In: *Philosophical Magazine Series 5* 49.296 (1900), pp. 1–14. ISSN: 1941-5982. DOI: [10.1080/14786440009463821](https://doi.org/10.1080/14786440009463821).
- [152] Bibudhendra Sarkar. *Heavy Metals In The Environment*. en. CRC Press, Mar. 2002. ISBN: 9780824706302.
- [153] S. D. Schery. ‘Thoron in the Environment’. In: *Journal of the Air & Waste Management Association* 40.4 (1990), pp. 493–497. ISSN: 1047-3289. DOI: [10.1080/10473289.1990.10466704](https://doi.org/10.1080/10473289.1990.10466704).
- [154] R. Randall Schumann. ‘The radon emanation coefficient: An important tool for geologic radon potential estimations’. In: *Proceedings of the 1993 International Radon Conference, Sept 20-22, Denver Colorado*. 1993.
- [155] Bing Shang et al. ‘Radon survey in dwellings of Gansu, China: the influence of thoron and an attempt for correction’. en. In: *Radiation and Environmental Biophysics* 47.3 (July 2008), pp. 367–373. ISSN: 0301-634X, 1432-2099. DOI: [10.1007/s00411-008-0163-2](https://doi.org/10.1007/s00411-008-0163-2).
- [156] Jacob Shapiro. *An evaluation of the pulmonary radiation dosage from radon and its daughter products*. Tech. rep. Atomic Energy Project, Univ. of Rochester, 1954.

- [157] Jens Sogaard-Hansen and Anders Damkjaer. ‘Determining ^{222}Rn Diffusion Lengths in Soils and Sediments’. In: *Health Physics* 53.5 (1987), pp. 455–459. ISSN: 0017-9078.
- [158] G. Somogyi, B. Paripás, and Zs. Varga. ‘Measurement of radon, radon daughters and thoron concentrations by multi-detector devices’. In: *Nuclear Tracks and Radiation Measurements (1982)*. Special Volume: Solid State Nuclear Track Detectors 8.1–4 (1984), pp. 423–427. ISSN: 0735-245X. DOI: [10.1016/0735-245X\(84\)90135-2](https://doi.org/10.1016/0735-245X(84)90135-2).
- [159] A. Sorimachi, Hiroyuki Takahashi, and Shinji Tokonami. ‘Influence of the presence of humidity, ambient aerosols and thoron on the detection responses of electret radon monitors’. In: *Radiation Measurements* 44.1 (Jan. 2009), pp. 111–115. ISSN: 1350-4487. DOI: [10.1016/j.radmeas.2008.10.009](https://doi.org/10.1016/j.radmeas.2008.10.009).
- [160] A. Sorimachi et al. ‘Performance test of passive radon–thoron discriminative detectors on environmental parameters’. In: *Radiation Measurements* 47.6 (June 2012), pp. 438–442. ISSN: 1350-4487. DOI: [10.1016/j.radmeas.2012.04.003](https://doi.org/10.1016/j.radmeas.2012.04.003).
- [161] A. Sorimachi et al. ‘Quality assurance and quality control for thoron measurement at NIRS’. en. In: *Radiation Protection Dosimetry* 141.4 (Jan. 2010), pp. 367–370. ISSN: 0144-8420, 1742-3406. DOI: [10.1093/rpd/ncq245](https://doi.org/10.1093/rpd/ncq245).
- [162] Helmuth Spieler. *Semiconductor Detector Systems*. en. Oxford University Press, Aug. 2005. ISBN: 9780191523656.
- [163] M. Sreenath Reddy et al. ‘Thoron levels in the dwellings of Hyderabad city, Andhra Pradesh, India’. In: *Journal of Environmental Radioactivity* 73.1 (2004), pp. 21–28. ISSN: 0265-931X. DOI: [10.1016/j.jenvrad.2003.07.002](https://doi.org/10.1016/j.jenvrad.2003.07.002).
- [164] Ronald G. Stafford and Harry J. Ettinger. ‘Filter efficiency as a function of particle size and velocity’. In: *Atmospheric Environment (1967)* 6.5 (May 1972), pp. 353–362. ISSN: 0004-6981. DOI: [10.1016/0004-6981\(72\)90201-6](https://doi.org/10.1016/0004-6981(72)90201-6).
- [165] John Stanford and Stepen Vardeman. *Statistical Methods for Physical Science*. en. Academic Press, Dec. 1994. ISBN: 9780080860169.
- [166] F. Steinhäusler, W. Hofmann, and H. Lettner. ‘Thoron Exposure of Man: A Negligible Issue?’ en. In: *Radiation Protection Dosimetry* 56.1-4 (Jan. 1994), pp. 127–131. ISSN: 0144-8420, 1742-3406.
- [167] Christine A. Stidley and Jonathan M. Samet. ‘A Review of Ecologic Studies of Lung Cancer and Indoor Radon.’ en. In: *Health Physics* 65.3 (Sept. 1993), pp. 234–251. ISSN: 0017-9078. DOI: [10.1097/00004032-199309000-00001](https://doi.org/10.1097/00004032-199309000-00001).
- [168] Christine A. Stidley and Jonathan M. Samet. ‘Assessment of Ecologic Regression in the Study of Lung Cancer and Indoor Radon’. en. In: *American Journal of Epidemiology* 139.3 (Jan. 1994), pp. 312–322. ISSN: 0002-9262, 1476-6256.
- [169] Strahlenschutzkommission. ‘Attributives Lungenkrebsrisiko durch Radon Expositionen in Wohnungen’. In: *SSK* (June 2006).

- [170] C. G. Sumesh et al. ‘Comparison study and thoron interference test of different radon monitors’. en. In: *Radiation Protection Dosimetry* 153.3 (Jan. 2013), pp. 309–315. ISSN: 0144-8420, 1742-3406. DOI: [10.1093/rpd/ncs118](https://doi.org/10.1093/rpd/ncs118).
- [171] C. G. Sumesh et al. ‘Impact of flow rate on sensitivity of semiconductor type thoron monitor’. In: *Radiation Measurements* 59 (Dec. 2013), pp. 241–244. ISSN: 1350-4487. DOI: [10.1016/j.radmeas.2013.07.007](https://doi.org/10.1016/j.radmeas.2013.07.007).
- [172] M. K. Sundaresan. *Handbook of Particle Physics*. en. CRC Press, Apr. 2001. ISBN: 9781420042054.
- [173] J. W. Thomas and P. C. LeClare. ‘A study of the two-filter method for radon-222.’ In: *Health Physics* 18.2 (1970), pp. 113–22. ISSN: 0017-9078.
- [174] TI. *MSP430 Competitive Benchmarking*. slaa205c. Texas Instruments, 2009.
- [175] TI. *MSP430F2416 Datasheet*. Texas Instruments, 2014.
- [176] TI. *MSP430x2xx Family User’s Guide (Rev. J)*. slau144j. Texas Instruments, 2013.
- [177] Ulrich Tietze, Christoph Schenk, and Eberhard Gamm. *Halbleiter-Schaltungstechnik*. de. Springer-Verlag GmbH, Nov. 2012. ISBN: 9783642310256.
- [178] M. Tirmarche et al. ‘Lung Cancer Risk from Radon and Progeny and Statement on Radon’. In: *Annals of the ICRP*. ICRP PUBLICATION 115 Lung Cancer Risk from Radon and Progeny and Statement on Radon 40.1 (Feb. 2010), pp. 1–64. ISSN: 0146-6453. DOI: [10.1016/j.icrp.2011.08.011](https://doi.org/10.1016/j.icrp.2011.08.011).
- [179] M. Tirmarche et al. ‘Risk of lung cancer from radon exposure: contribution of recently published studies of uranium miners’. In: *Annals of the ICRP*. Proceedings of the First ICRP Symposium on the International System of Radiological Protection 41.3–4 (Oct. 2012), pp. 368–377. ISSN: 0146-6453. DOI: [10.1016/j.icrp.2012.06.033](https://doi.org/10.1016/j.icrp.2012.06.033).
- [180] Shinji Tokonami. ‘Why is ^{220}Rn (thoron) measurement important?’ en. In: *Radiation Protection Dosimetry* 141.4 (Jan. 2010), pp. 335–339. ISSN: 0144-8420, 1742-3406. DOI: [10.1093/rpd/ncq246](https://doi.org/10.1093/rpd/ncq246).
- [181] Shinji Tokonami, Mingli Yang, and Tetsuya Sanada. ‘CONTRIBUTION FROM THORON ON THE RESPONSE OF PASSIVE RADON DETECTORS’. In: *Health Physics* 80.6 (2001), pp. 612–615. ISSN: 0017-9078.
- [182] Shinji Tokonami et al. ‘Simple, discriminative measurement technique for radon and thoron concentrations with a single scintillation cell’. In: *Review of Scientific Instruments* 73.1 (Jan. 2002), pp. 69–72. ISSN: 0034-6748, 1089-7623. DOI: [10.1063/1.1416121](https://doi.org/10.1063/1.1416121).
- [183] Shinji Tokonami et al. ‘Up-to-date radon-thoron discriminative detector for a large scale survey’. In: *Review of Scientific Instruments* 76.11 (Nov. 2005), p. 113505. ISSN: 0034-6748, 1089-7623. DOI: [10.1063/1.2132270](https://doi.org/10.1063/1.2132270).

- [184] L. Tomasek et al. ‘Lung cancer in French and Czech uranium miners: Radon-associated risk at low exposure rates and modifying effects of time since exposure and age at exposure’. English. In: *Radiation Research* 169.2 (2008), pp. 125–137. ISSN: 0033-7587. DOI: [10.1667/RR0848.1](https://doi.org/10.1667/RR0848.1).
- [185] L. Tommasino, S. Tokonami, and P. M. Tommasino. ‘The measurements of thoron, radon and their decay products thanks to Pinocchio, Tengu and Trolls’. en. In: *Radiation Protection Dosimetry* 141.4 (Jan. 2010), pp. 340–345. ISSN: 0144-8420, 1742-3406. DOI: [10.1093/rpd/ncq248](https://doi.org/10.1093/rpd/ncq248).
- [186] Fernando Pacheco Torgal and Said Jalali. *Eco-efficient Construction and Building Materials*. en. Springer Science & Business Media, July 2011. ISBN: 9780857298928.
- [187] J. Tschiersch, W. B. Li, and O. Meisenberg. ‘Increased indoor thoron concentrations and implication to inhalation dosimetry’. en. In: *Radiation Protection Dosimetry* 127.1-4 (Jan. 2007), pp. 73–78. ISSN: 0144-8420, 1742-3406. DOI: [10.1093/rpd/ncm341](https://doi.org/10.1093/rpd/ncm341).
- [188] J. Tschiersch and O. Meisenberg. ‘The HMGU thoron experimental house: a new tool for exposure assessment’. en. In: *Radiation Protection Dosimetry* 141.4 (Jan. 2010), pp. 395–399. ISSN: 0144-8420, 1742-3406. DOI: [10.1093/rpd/ncq249](https://doi.org/10.1093/rpd/ncq249).
- [189] Jagdish K. Tuli. *Nuclear wallet cards*. BNL. N.-Y, 2005.
- [190] UNSCEAR. *Effects of Ionizing Radiation: United Nations Scientific Committee on the Effects of Atomic Radiation-UNSCEAR 2006 Report, Volume II-Report to the General Assembly, with Scientific Annexes C, D, and E*. Vol. 2. United Nations Publications, 2009.
- [191] UNSCEAR. *Sources and effects of ionizing radiation: sources*. Vol. 1. New York: United Nations Publications, 2000.
- [192] UNSCEAR. *UNSCEAR 2008 Report, Vol. I: Sources of ionizing radiation. Annex A: Medical Radiation Exposures*. New York, NY: United Nations, 2010.
- [193] M. P. Unterweger. ‘The NIST Primary Radon-222 Measurement System’. In: *Journal of Research of the National Institute of Standards and Technology* 95.2 (1990).
- [194] M. Urban. ‘Passive one-element track etch dosimeter for simultaneous measurement of radon, thoron and decay products in air’. In: *International Journal of Radiation Applications and Instrumentation. Part D. Nuclear Tracks and Radiation Measurements*. Special Volume Solid State Nuclear Track Detectors 12.1–6 (1986), pp. 685–688. ISSN: 1359-0189. DOI: [10.1016/1359-0189\(86\)90679-5](https://doi.org/10.1016/1359-0189(86)90679-5).
- [195] V. Urošević and D. Nikezić. ‘Radon transport through concrete and determination of its diffusion coefficient’. en. In: *Radiation Protection Dosimetry* 104.1 (Jan. 2003), pp. 65–70. ISSN: 0144-8420, 1742-3406.
- [196] V. Urošević, D. Nikezić, and S. Vulović. ‘A theoretical approach to indoor radon and thoron distribution’. In: *Journal of Environmental Radioactivity* 99.12 (Dec. 2008), pp. 1829–1833. ISSN: 0265-931X. DOI: [10.1016/j.jenvrad.2008.07.010](https://doi.org/10.1016/j.jenvrad.2008.07.010).

- [197] A. Vargas and X. Ortega. ‘Influence of environmental changes on integrating radon detectors: results of an intercomparison exercise’. en. In: *Radiation Protection Dosimetry* 123.4 (Jan. 2007), pp. 529–536. ISSN: 0144-8420, 1742-3406. DOI: [10.1093/rpd/nc1161](https://doi.org/10.1093/rpd/nc1161).
- [198] Latha Vasudevan and Milton McLain. ‘Atmospheric Pressure Effects on the Calibration Constant of Alpha-track Radon Detectors’. In: *Health Physics* 66.3 (1994), pp. 318–326. ISSN: 0017-9078.
- [199] Linda Walsh et al. ‘The influence of radon exposures on lung cancer mortality in German uranium miners, 1946-2003’. In: *Radiation Research* 173.1 (2010), pp. 79–90.
- [200] Maciej Wegrzecki et al. ‘Design and properties of silicon charged-particle detectors developed at the Institute of Electron Technology (ITE)’. In: *Proc. SPIE*. Vol. 8902. 2013, pp. 890212–890212–11. DOI: [10.1117/12.2031041](https://doi.org/10.1117/12.2031041).
- [201] Peter Westphal. *Signalübertragung analoger Schaltungen: Schwerpunkt: Operationsverstärkerschaltungen*. de. BoD – Books on Demand, 2008. ISBN: 9783837061154.
- [202] H. Erich Wichmann et al. ‘Increased lung cancer risk due to residential radon in a pooled and extended analysis of studies in Germany.’ en. In: *Health Physics* 88.1 (Jan. 2005), pp. 71–79. ISSN: 0017-9078. DOI: [10.1097/01.HP.0000142497.31627.86](https://doi.org/10.1097/01.HP.0000142497.31627.86).
- [203] Jens Wiegand et al. ‘Radon and thoron in cave dwellings (Yan’an, China)’. In: *Health Physics* 78.4 (2000), pp. 438–444.
- [204] M. Wielunski et al. ‘Study of the sensitivity of neutron sensors consisting of a converter plus Si charged-particle detector’. In: *Nuclear Instruments and Methods in Physics Research Section A: Accelerators, Spectrometers, Detectors and Associated Equipment* 517.1–3 (Jan. 2004), pp. 240–253. ISSN: 0168-9002. DOI: [10.1016/j.nima.2003.07.032](https://doi.org/10.1016/j.nima.2003.07.032).
- [205] M. Wilkening. ‘Radon - Soil to Air’. en. In: *Radon in the Environment*. Elsevier, Aug. 1990, p. 46. ISBN: 9780080874999.
- [206] Yunyun Wu et al. ‘Intercomparisons for Integrating the Radon/Thoron Detector of Nirp, China with Nirs, Japan’. en. In: *Radiation Protection Dosimetry* (Sept. 2014), ncu286. ISSN: 0144-8420, 1742-3406. DOI: [10.1093/rpd/ncu286](https://doi.org/10.1093/rpd/ncu286).
- [207] Xie George Xu and Keith F. Eckerman. *Handbook of Anatomical Models for Radiation Dosimetry*. en. CRC Press, Sept. 2009. ISBN: 9781420059809.
- [208] T. Yamasaki, Q. Guo, and T. Iida. ‘Distributions of Thoron Progeny Concentrations in Dwellings’. en. In: *Radiation Protection Dosimetry* 59.2 (Jan. 1995), pp. 135–140. ISSN: 0144-8420, 1742-3406.
- [209] Y. Yoshtoa et al. ‘Comparison of performance characteristics of some filters using Thoron daughters as radioactive aerosol’. In: (1968).

-
- [210] H. Zeeb and F. Shannoun. *Handbook on indoor radon: a public health perspective*. WHO, 2009.
- [211] C. Zhao et al. ‘Effects of atmospheric parameters on radon measurements using alpha-track detectors’. In: *Review of Scientific Instruments* 85.2 (Feb. 2014), p. 022101. ISSN: 0034-6748, 1089-7623. DOI: [10.1063/1.4865155](https://doi.org/10.1063/1.4865155).
- [212] Weihai Zhou et al. ‘Simulation of the Concentrations and Distributions of Indoor Radon and Thoron’. en. In: *Radiation Protection Dosimetry* 93.4 (Jan. 2001), pp. 357–367. ISSN: 0144-8420, 1742-3406.
- [213] Weihai Zhuo et al. ‘A simple passive monitor for integrating measurements of indoor thoron concentrations’. In: *Review of Scientific Instruments* 73.8 (Aug. 2002), pp. 2877–2881. ISSN: 00346748. DOI: [doi:10.1063/1.1493233](https://doi.org/10.1063/1.1493233).
- [214] James F. Ziegler, Matthias D. Ziegler, and Jochen P. Biersack. ‘SRIM–The stopping and range of ions in matter (2010)’. In: *Nuclear Instruments and Methods in Physics Research Section B: Beam Interactions with Materials and Atoms* 268.11 (2010), pp. 1818–1823.

List of Figures

2.1	Simplified ^{238}U decay series, including radon ^{222}Rn and its progenies. Only the major decay branches with the respective decay modes, energies and half-lives are shown. See also Table 2.2.	7
2.2	Relative activities of ^{222}Rn and its immediate progenies. Here it is assumed that only ^{222}Rn is present initially and is also constant. Lines of bismuth and polonium overlap due to the short half-life of ^{214}Po	10
2.3	Part of the thorium ^{232}Th decay series immediately preceding and following ^{220}Rn , also showing rounded half-lives, alpha and beta particle decays. See also Table 2.2	11
2.4	Relative activities of ^{220}Rn and its immediate progenies. Here it is assumed that only thoron is present initially and at a constant level. Lines of thoron and polonium overlap due to the short half-life of ^{216}Po	12
2.5	Average ^{222}Rn concentration in dwellings in the Federal Republic of Germany [112], adapted from [15].	16
3.1	Categories for radon and thoron measurement methods, adapted from [71]. The developed device belongs to the blue group.	28
3.2	Schematic of voltage generator used in current exposimeter version.	30
3.3	Schematic drawing of charge sensitive preamplifier.	32
3.4	Schematic drawing of pulse shaper stage.	34
3.5	Schematic of Schmitt-trigger circuit with microcontroller pin designators.	35
3.6	Functional block diagram with pin assignment of most important components (red) and optional future features (green), adapted from [175].	36
3.7	Comparison of simulated and measured voltage output of amplifier.	41
3.8	Dependence of amplifier output amplitude, for a signal corresponding to a 10 MeV alpha, on tolerance of coupling components. Threshold (red) should not be exceeded.	42
3.9	Simulated signals for preamplifier, shaper and final output, corresponding to an input signal of an 1 MeV alpha particle.	43
3.10	Rendered CAD drawing of both geometries showing size and PCB position differences. In final setup the side walls are complete, and the top inlets are covered with a filter.	44

4.1	Reference device comparison, absolute radon activity concentrations determined by an AlphaGuard and a Rad7. Error bars include 1σ statistical uncertainty only.	51
4.2	Distribution of calibration factors with bin width of 0.7 and Gaussian fit (solid line), resulting from a measurement with 22 radon monitors.	52
4.3	Typical alpha particle spectrum acquired in a radon environment for the small housing (geometry 1). In the summed spectrum (hours 10-50) the characteristic alpha peaks of two progeny are clearly visible.	55
4.4	Radon calibration factors obtained by three devices for a linear increasing radon concentration. Error bars include 1σ statistical uncertainty only. The mean was found to be $12.8 \pm 0.6 \text{ Bq m}^{-3}/\text{cph}$ (red line, standard deviation as gray shade), hence a 4.5% relative standard deviation.	56
4.5	Thoron calibration factors obtained by three similar devices under varying conditions (Table 4.2). Error bars include 1σ statistical uncertainty only. The mean was found to be $8.4 \pm 1.6 \text{ Bq m}^{-3} / \text{cph}$ (red line, standard deviation as gray shade).	59
4.6	Typical alpha particle spectrum acquired in a thoron environment for the standard housing (geometry 1). In the summed spectrum (hours 60-85) the characteristic alpha peaks of two progeny are clearly visible.	61
4.7	Typical alpha particle spectrum acquired in a thoron environment for the monitor with large housing (geometry 2). In the summed spectrum (hours 60-85) with no filter applied the characteristic alpha peaks of two progeny are clearly visible.	62
4.8	Spectra in mixed ^{222}Rn and ^{220}Rn concentrations acquired by device V305 with standard housing (Geo1) and improved ADC circuit. Spectra are normalized with respect to total count number.	67
4.9	Comparison of reference activity concentration with calculated values from device V305 with standard housing (Geo1). Note that concentration is plotted on a logarithmic scale. Uncertainties refer to 1σ	70
4.10	Experimentally acquired spectra in mixed ^{222}Rn and ^{220}Rn concentrations and fit of linear combination of normalized spectra. Trend shows good agreement, however, calculated concentrations differ largely.	72
5.1	Goff-Gratch approximation (Equation 5.10) used for the simulation described below and experimental data [31] of saturated vapor pressure are in well agreement.	84
5.2	Schematic representation of exposimeter geometry 1 with random decay origins from volume and walls. Decays from the bottom area are not calculated since these cannot hit the detectors.	86
5.3	Simulated spectra for ^{222}Rn (A) and ^{220}Rn (B) environments at STP for geometry 1, show reasonable agreement between Geant4 and Analytic transport code.	89

5.4	Simulated and measured spectra in a ^{222}Rn environment for geometries 1 (Geo1) and 2 (Geo2).	91
5.5	Simulated and measured spectra in a ^{222}Rn environment at an altitude equivalent of about 2229 m for geometries 1 (Geo1) and 2 (Geo2).	93
5.6	Individual contributions to simulated spectrum in a ^{222}Rn environment at equal concentrations but different ambient pressures (96,836 Pa and 77,259 Pa) for standard housing (Geo1). Lower air density causes energy shift to the right for decays traversing the volume. Index <i>wall</i> denominates contributions of progeny decays from surfaces of the housing.	95
5.7	Simulated and measured spectra in a ^{220}Rn environment for geometries 1 (Geo1) and 2 (Geo2).	97
5.8	Individual contributions to simulated spectrum in a ^{220}Rn environment for standard housing (Geo1) and large housing (Geo2). Larger alpha particle path causes energy shift to the left for decays traversing the volume. Index <i>wall</i> denominates contributions of progeny decays from surfaces of the housing.	99
5.9	Radon calibration factor dependence on temperature and humidity for exposimeter with standard dimension (Geo1). Right scale indicates the relative deviation from the calibration factor at standard temperature and pressure (STP, 50% RH, 101,325 Pa and 20 °C). Error bars include 1σ statistical uncertainty only.	100
5.10	Radon calibration factor dependence on temperature and pressure for exposimeter with standard dimension (Geo1). Right scale indicates the relative deviation from the calibration factor at standard temperature and pressure (STP, 50% RH, 101,325 Pa and 20 °C). Error bars include 1σ statistical uncertainty only.	102
5.11	Radon calibration factor dependence on temperature and pressure for exposimeter with larger dimension (Geo2). Right scale indicates the relative deviation from the calibration factor at standard temperature and pressure (STP, 50% RH, 101,325 Pa and 25 °C). Error bars include 1σ statistical uncertainty only.	104
5.12	Thoron calibration factor dependence on temperature and pressure for exposimeter with standard (Geo1) and large (Geo2) dimension. Right scale indicates the relative deviation from the calibration factor at standard temperature and pressure (STP, 50% RH, 101,325 Pa and 20/25 °C). Error bars include 1σ statistical uncertainty only.	107
5.13	^{220}Rn and ^{222}Rn calibration factor dependence in ROI_2 on temperature and pressure for exposimeter with standard dimension (Geo1). Right scale indicates the relative deviation from the calibration factor at standard temperature and pressure (STP, 50% RH, 101,325 Pa and 20 °C). Error bars include 1σ statistical uncertainty only.	110

5.14	Thoron (^{212}Po) calibration factor dependence in ROI_4 on temperature and pressure for exposimeter with standard dimension (Geo1). Right scale indicates the relative deviation from the calibration factor at standard temperature and pressure (STP, 50% RH, 101,325 Pa and 20 °C). Error bars include 1σ statistical uncertainty only.	111
5.15	Schematic representation of exposimeter geometry 1 with two detectors symmetrically placed at the center (red area). The inlet area for gas diffusion is at the top, which is only relevant for the ^{220}Rn simulation.	112
5.16	^{220}Rn and ^{222}Rn calibration factor dependence on diffusion chamber height with starting dimensions of Geo1. Right scale indicates the relative deviation from the calibration factor at standard dimension ($h = 26\text{ mm}$). Error bars include 1σ statistical uncertainty only.	113
5.17	^{220}Rn and ^{222}Rn calibration factor dependence on diffusion chamber base area $A = (l + 2\ dx) (w + dy)$ change. Right scale indicates the relative deviation from the calibration factor at standard dimension ($dx = dy = 0$). Error bars include 1σ statistical uncertainty only.	115
6.1	Radon activity concentration recorded during the intercomparison measurement in Prague. The integration time of device V315 was set to 10 min, but here hourly values are shown. Error bars include 1σ statistical uncertainty only.	118
6.2	Radon activity concentration recorded during a visit at the <i>Heilstollen Bad Gastein</i> . The integration time of device V306 and V102 was set to 2 min. A general agreement with the AlphaGuard is observable. Error bars include 1σ statistical uncertainty only.	120
6.3	Radon activity concentration recorded during the visit to the <i>Berchtesgaden salt mine</i> . The integration time of device V306 and V102 was set to 1 h. Error bars include 1σ statistical uncertainty only.	122
6.4	Spectrum acquired during a one month measurement in the HMGU thoron house (712 h). Main contribution originates from ^{222}Rn and its progenies, while also ^{220}Rn is clearly present (indicated by the ^{212}Po peak).	123
6.5	Radon concentrations measured in the HMGU thoron house during an one-month time period (712 h). Although the integration time of the devices was 1 h, here the mean of every six hours is shown. A general agreement with the AlphaGuard is observable. Error bars include 1σ statistical uncertainty only.	125
6.6	Spectrum acquired during a 600 h measurement in a modern Bavarian clay house. Main contribution originates from ^{222}Rn and its progenies, while ^{220}Rn is almost not present, indicated by the low ^{212}Po peak.	127
6.7	Radon concentrations acquired during a measurement in a clay house during a time interval of one month. The integration time of the devices was 1 h but here the mean of every 12 th hour is shown. Error bars include 1σ statistical uncertainty only.	128

List of Tables

2.1	Radioactive decay relative change	9
2.2	Radon/Thoron Decay Series	12
2.3	Typical diffusion coefficients	14
2.4	Dose conversion factors (DCFs) for exposure of adults to ^{222}Rn daughters .	21
2.5	Summary of excess relative risk (ERR)for lung cancer incidence per working level month (WLM) from combined analysis of miner studies [179].	24
2.6	Summary of ERR per unit concentration or exposure from combined residential ^{222}Rn studies [190].	25
3.1	Design and electrical parameters of detector	31
3.2	Energy loss difference $\Delta E = dE_{60^\circ} - dE_{0^\circ}$ MeV for alpha particles incident under two different angles (60° and 0°) for different energies E_α	31
3.3	JFET SPICE parameters	40
4.1	Device calibration factors (<i>cf</i>) with 1σ standard deviation as uncertainty (<i>std</i>) for exposimeters of first (<i>V1xx</i>) and third (<i>V3xx</i>) generation in a ^{222}Rn environment.	54
4.2	Mean thoron calibration measurement conditions	58
4.3	Calibration factors for ^{222}Rn and ^{220}Rn for radon (V311, V315) and combined radon/thoron (V305) exposimeter.	60
4.4	Mean radon and thoron mixed concentrations measurement conditions . .	66
4.5	Relative difference of $N_{210\text{Po}}$ atoms calculated with Equation 4.12 and with the decay chain implementation in <i>Mathematica</i>	74
5.1	Composition of dry air and water vapor at standard temperature and pressure (STP)	83
5.2	Individual contributions to the sum spectra of Figure 5.3 for the two different transport codes in Geant4 (G4) and Analytic (AN) (ASTAR based) simulation.	87
5.3	Individual contributions to the spectra of Figure 5.6 for the standard housing and different pressures, as well as for geometry 2.	96
5.4	Individual contributions to the spectra of Figure 5.6 for the different housings.	98
5.5	Fit parameter estimation with calculated standard error u ($\sqrt{\sigma^2}$) for the data given in Figure 5.9 and fitted by Equation 5.22.	101

5.6	Fit parameter estimation for ^{222}Rn calibration factor with calculated standard error $u(\sqrt{\sigma^2})$ for the data given in Figure 5.10 for geometry 1 and fitted by Equation 5.22.	103
5.7	Relative difference of ^{222}Rn calibration factors compared to STP conditions calculated via Equation 5.22 employing values of Table 5.6 for standard housing (Geo1).	103
5.8	Fit parameter estimation for ^{222}Rn calibration factor with calculated standard error $u(\sqrt{\sigma^2})$ for the data given in Figure 5.11 for geometry 2 and fitted by Equation 5.22.	105
5.9	Relative difference of ^{222}Rn calibration factors compared to STP conditions calculated via Equation 5.22 employing values of Table 5.8 for large housing (Geo2).	105
5.10	Fit parameter estimation for ^{220}Rn calibration factor with calculated standard error $u(\sqrt{\sigma^2})$ for the data given in Figure 5.12 for geometry 1 and fitted by Equation 5.22.	106
5.11	Fit parameter estimation for ^{220}Rn calibration factor with calculated standard error $u(\sqrt{\sigma^2})$ for the data given in Figure 5.12 for geometry 2 and fitted by Equation 5.22.	108
5.12	Relative difference of ^{220}Rn calibration factors compared to STP conditions calculated via Equation 5.22 employing values of Table 5.11 for large housing (Geo2).	109
5.13	Fit parameter estimation for ^{222}Rn calibration factor with calculated standard error $u(\sqrt{\sigma^2})$ for the data given in Figure 5.16 for geometry 1 and fitted by Equation 5.22.	113
5.14	Fit parameter estimation for ^{222}Rn and ^{220}Rn calibration factors with calculated standard error $u(\sqrt{\sigma^2})$ for the data given in Figure 5.17 for geometry 1 and fitted by Equation 5.22.	114
6.1	Measured ^{222}Rn and ^{220}Rn activity concentrations in the HMGU thoron house, for the different devices employed. Stated errors refer to a 1σ uncertainty.	126

Acknowledgments

I wish to express my thanks to all those who contributed to the success of this work.

In particular, I would like to thank Prof. Dr. Werner Rühm who allowed me to work on such an interesting and demanding topic. His keen interest, critical review and valuable suggestions and advice were of great help.

Further I thank Dr. Marek Wielunski, whose advice and help especially in the field of electronics was always more than welcome. Also I send gratitude's to Norbert Kochanski, who provided through his excellent work on the amplification system a significant contribution to the success of this work.

Without my office mate and PHD fellow Sebastian Trinkl, who helped develop the GEANT4 Monte Carlo simulation, the achieved results would have not been possible.

My colleagues Mattias Volnhals, Ferdinand Bergmaier and Christian Pioch also have to be mentioned, because they have made my work much more enjoyable. Many thanks also to Martin Schmid for proofreading parts of my thesis.

I thank my parents for their constant help and support, especially during the years of study, without which I would not be here today. Especially my mother insisted on the importance of higher education, while my elementary school teacher would have like me to attend school for mentally handicapped children.

I thank my brother from whom I very early learned that life is not handed to one on a silver tablet.

Special thanks also goes to my girl friend Marina Hoheneder, who has always managed to cheer me up when I was down.

This study was supported by the German Federal Ministry of Education and Research (contract 02NUK015B). Its contents are solely the responsibility of the authors.

Publications

Publications of this work in peer reviewed Journals and Proceedings

J. Irlinger, S. Trinkl, M. Wielunski, and W. Rühm. Monte Carlo study of environmental parameter effects on the calibration factor of a radon/thoron exposure meter. *In preparation*, Q1 2015.

J. Irlinger, M. Wielunski, and W. Rühm. Thoron detection with an active radon exposure meter. *Review of Scientific Instruments*, 85(2):022106, February 2014.

Oral format publications of this work

Kompetenzverband Strahlenforschung, Development of active detectors for the determination of individual radon and thoron exposure, *KVSF final report*, Hannover, March 2014.

Kompetenzverband Strahlenforschung, Development of active detectors for the determination of individual radon and thoron exposure, *KVSF 3rd progress report*, Neuherberg, June 2013.

Kompetenzverband Strahlenforschung, Development of active detectors for the determination of individual radon and thoron exposure, *KVSF 2nd progress report*, Jena, October 2012.

Kompetenzverband Strahlenforschung, Development of active detectors for the determination of individual radon and thoron exposure, *KVSF 1st progress report*, Rheinbach, September 2011.

Bhabha Atomic Research Centre, Introduction to the HMGU individual radon and thoron exposure monitor, principle and development, *BARC*, Mumbai, October 2012.

Poster format publications of this work

The HMGU Personal Radon and Thoron Exposure Meter, *7th Conference of Protection against Radon at Home and at Work*, Prague, Czech Republic, September 2013.

The HMGU Personal Radon and Thoron Exposure Meter, Bayerisches Landesamt für Umwelt, *2. Bayerisches Radon-Netzwerk-Treffen*, München, Germany, September 2013.

The HMGU Personal Radon and Thoron Exposure Meter, *WE- Heraeus Advance Physics School on Ionizing Radiation and Protection of Man and his Environment*, Bad Honnef, Germany, August 2012.

Eidesstattliche Versicherung

Irlinger, Josef

Name, Vorname

Ich erkläre hiermit an Eides statt,

dass ich die vorliegende Dissertation mit dem Thema

Development of an electronic monitor for the determination of individual radon and thoron exposure

selbständig verfasst, mich außer der angegebenen keiner weiteren Hilfsmittel bedient und alle Erkenntnisse, die aus dem Schrifttum ganz oder annähernd übernommen sind, als solche kenntlich gemacht und nach ihrer Herkunft unter Bezeichnung der Fundstelle einzeln nachgewiesen habe.

Ich erkläre des Weiteren, dass die hier vorgelegte Dissertation nicht in gleicher oder in ähnlicher Form bei einer anderen Stelle zur Erlangung eines akademischen Grades eingereicht wurde.

Ort, Datum

Unterschrift Doktorandin/Doktorand